

# Dynamical modelling and numerical simulation of grain-fluid mixture flows

Vom Fachbereich Maschinenbau  
an der Technischen Universität Darmstadt  
zur Erlangung des akademischen Grades  
eines Doktor-Ingenieurs (Dr.-Ing.)  
genehmigte

## **D i s s e r t a t i o n**

von

Xiannan Meng, M. Sc.

aus Yi An, China

Berichterstatter:	apl. Prof. Dr.-Ing. habil. Yongqi Wang
Mitberichterstatter:	Prof. Dr.-Ing. habil. Martin Oberlack apl. Prof. Dr.-Ing. habil. Amsini Sadiki
Tag der Einreichung:	22.11.2016
Tag der mündlichen Prüfung:	08.02.2017

Darmstadt, 2017

D17



# Abstract

Flows of grain-fluid mixtures are commonly observed in nature and in industry. However, comprehensive understanding of the physics behind them is to date out of reach. This thesis aims to investigate the mechanism underlying flowing grain-fluid mixtures by both analytical and numerical methods.

The work of this thesis starts with introducing standard mixture theory to describe the balance equations of mass and momentum for the fluid and the granular phases of grain-fluid mixtures. As the first step, the flowing mixtures are idealized to be saturated media, indicating that the fluid phase fills all the voids between the particles. Accordingly, the granular phase is treated as a frictional Coulomb-like media, while the fluid phase is modelled as a Newtonian fluid. The interaction forces between the two phases include buoyancy force and drag force. Taking into account the flow characteristics that the flow depth is much smaller than the flow length, the thin-layer approximation and the depth-averaged technique are employed to eliminate the dependency of the governing equations on the vertical coordinate, so that a set of depth-averaged equations are derived. The depth-averaged equations are analyzed in terms of steady flows down an inclined plane. It is found that the present model equations can interpret the classical cross-stream profiles of the downslope velocity, the blunt shape of the flowing front, and roll waves. Additionally, the depth-averaged equations are numerically resolved by using a high-resolution scheme with respect to a large-scale unsteady flow, and the numerical results are compared with the experimental data. The comparison demonstrates that this model is capable to describe dynamics of a grain-fluid mixture flow, such as the evolutions of the mixture height and volume fractions.

Moreover, unsaturated grain-fluid mixtures are considered, in which the fluid phase cannot fill all interstices of the granular medium. To investigate their dynamic process, it is assumed that the fluid percolates easily down through the interstices of the granular medium and as a result the air is extruded. To describe such a kind of unsaturated mixtures, a two-layer approach is proposed, in which the fluid-saturated granular layer is overlaid by the pure granular material. The upper granular mass is treated as a frictional Coulomb-like medium, and the lower layer is described by the standard mixture theory. The lower and upper layers interact at an interface which is a material surface for the fluid phase, but across which the mass exchange for the granular phase may take place. The proposed model equations are numerically resolved, and the numerical solutions demonstrate that the proposed two-layer model can provide reasonable predictions with respect to dynamic process of unsaturated mixture flows.

The last part of this thesis focuses on the improvement of the saturated depth-averaged model, presented in the first part of the thesis, by taking the granular dilatancy into account. The granular dilatancy is described by the critical-state theory. By coupling critical-state theory and mixture theory, we uncover the coupling between the granular dilatancy and the pore fluid pressure, i.e., the granular dilatancy yields the deviation of the pore fluid pressure from the hydrostatic value that, in turn, affects the motion of the granular phase. The formulated model equations describe the coupling of flow thickness, depth-averaged volume fractions and depth-averaged velocities, and the pore fluid pressure. Moreover, a numerical simulation is performed, and quantitative comparison with experimental data is reported. The comparison demonstrates that the proposed depth-averaged equations can provide reasonable predictions on the evolutions of dynamic quantities for a grain-fluid mixture flow.

It is noted that this thesis is based on the accepted publications (see Meng & Wang (2015a) and Meng & Wang (2015b)) and manuscripts in review process (see Meng, Wang, Wang & Fischer (2016) and Meng & Wang (2016)).

# Zusammenfassung

In Natur wie Industrie lassen sich gleichermaßen häufig Granulat-Fluid Strömungen beobachten. Trotzdem sind die sie bestimmenden physikalischen Zusammenhänge zur Zeit nicht umfassend erforscht und verstanden. Diese Arbeit widmet sich deshalb den für Granulat-Fluid Strömungen wesentlichen Mechanismen, sowohl mit analytischen wie auch mit numerischen Methoden.

Den Einstieg dieser Arbeit bildet eine Einführung in die Mischungs-Theorie, mit der die Bilanz-Gleichungen für Masse und Impuls einer Fluid- und einer Granulat-Phase beschrieben werden. Die fließende Mischung wird hierbei als gesättigt angenommen, die Fluid-Phase füllt also vollständig die Zwischenräume aus. Hierbei wird auch die granulare Phase als reibungsbehaftetes Coulombsches Material verstanden, während die Fluid-Phase als Newtonsches Fluid modelliert wird. Die Wechselwirkungs-Kräfte zwischen den zwei Phasen beinhalten Auftrieb und Widerstand. Unter Berücksichtigung der gegenüber der Länge sehr geringen Höhe, die für diese Strömung charakteristisch ist, wird die Flachwasser-Annahme zusammen mit Tiefenmittelung angewandt, um die Unabhängigkeit der Gleichungen von der vertikalen Komponente zu erreichen. Die so tiefengemittelten Gleichungen werden für stationäre Strömungen an der schiefen Ebene analysiert. Die Gleichungen des Modells können die klassischerweise auftretenden Querschnitts-Profile der Geschwindigkeiten reproduzieren, wie auch auftretende Wanderwellen und die stumpfe Frontform. Zusätzlich werden mit einem hoch-auflösenden numerischen Schema die tiefengemittelten Gleichungen berechnet und die Ergebnisse für eine instationären Strömung von großem Umfang mit experimentellen Daten verglichen. Der Vergleich zeigt, dass dieses Modell die Dynamik von Granulat-Fluid Strömungen hinsichtlich etwa der Mischungshöhe und der Volumenanteile beschreiben kann.

Außerdem werden auch ungesättigte Granulat-Fluid Mischungen untersucht, in welchen die Fluid-Phase nicht alle Zwischenräume des Granulats füllen kann. Um deren dynamischen Prozess zu beschreiben wird angenommen, dass das Fluid einfach durch die Zwischenräume des granularen Materials sickern kann und dabei auch die enthaltene Luft herauspresst. Für die Beschreibung solcher ungesättigter Granulat-Fluid Mischungen wird ein Zwei-Schichten Ansatz vorgestellt, in welchem eine gesättigte Granulat-Fluid Mischung von einer Schicht aus purem Granulat überlagert wird. Die obere Granulat-Schicht wird als reibungsbehaftetes Coulombsches Material behandelt, die untere mit der Mischungstheorie. Die obere und die untere Schicht interagieren über eine Grenzfläche, die für die Fluid-Phase eine materielle Oberfläche darstellt, über welche jedoch ein Massenaustausch des Granulats stattfinden kann. Die vorgeschlagenen Gleichungen des Modells werden numerisch gelöst; die numerischen Ergebnisse zeigen, dass das vorgestellte Zwei-Schichten Modell sinnvolle Ergebnisse hinsichtlich der Dynamik solcher ungesättigter Mischungen erzeugen kann.

Der letzte Teil der Thesis wendet sich der Verbesserung des tiefengemittelten Modells für gesättigte Mischungen zu, welches im ersten Teil der Arbeit vorgestellt wurde, indem nun auch granulare Dilatanz berücksichtigt wird. Granulare Dilatanz wird durch die critical-state Theorie beschrieben. Durch die Verknüpfung von Mischungs-  
theorie und critical-state Theorie wird die Wechselwirkung zwischen granularer Dilatanz und Fluid-Porendruck sichtbar gemacht, das heißt die die granulare Dilatanz bedingt die Abweichung des Fluid-Porendrucks von seinem hydrostatischen Wert, was wiederum die Bewegung der granularen Phase beeinflusst. Die aufgestellten Modellgleichungen beschreiben die Kopplung Fluss-Höhe, tiefengemittelten Volumenanteilen, tiefengemittelten Geschwindigkeiten und Fluid-Porendruck. Außerdem wird mit Hilfe einer numerischen Simulation ein quantitativer Vergleich mit experimentellen Daten ermöglicht. Dieser Vergleich zeigt, dass die vorgeschlagenen tiefengemittelten Gleichungen sinnvolle Vorhersagen der Entwicklung der dynamischen Größen für Granulat-Fluid Strömungen ermöglichen.

Wir vermerken, dass die vorliegende Arbeit auf anerkannten Publikationen (siehe Meng & Wang (2015a) und Meng & Wang (2015b)), wie auch auf Manuskripten (siehe Meng et al. (2016)) und Meng & Wang (2016), die sich noch im Prozess der Nachprüfung befinden, beruht.

# Acknowledgements

This work was financially supported by People Programme (Marie Curie Actions) of the European Union's Seventh Framework Programme FP7/2007-2013 through the grant No.289911.

I would like to thank my supervisor Prof. Dr.-Ing. habil. Yongqi Wang for the opportunity to do this PhD thesis at the Chair of Fluid Dynamics and the support he put into my work during the last four years. I also would like to thank Prof. Dr.-Ing. habil. Martin Oberlack for providing me with a freedom scientific environment and being one of my second supervisors. Additionally, I am grateful to Prof. Dr.-Ing. habil. Amsini Sadiki for being the other second supervisor.

I am deeply grateful to all my colleagues at the Chair of Fluid Dynamics for their help in my work and my life.

Last but not least, I want to express my sincere gratitude to my family, especially my parents for their support and patience.





# Contents

<b>List of Figures</b>	<b>xiv</b>
<b>Nomenclature</b>	<b>xv</b>
<b>1 Introduction</b>	<b>1</b>
<b>2 Fundamentals of mixture theory</b>	<b>5</b>
2.1 Kinematics . . . . .	5
2.2 Reynolds Transport Theorem . . . . .	7
2.3 Mixture theory . . . . .	9
2.3.1 Mass conservation law . . . . .	10
2.3.2 Momentum conservation law . . . . .	11
2.4 Jump conditions at the interface . . . . .	12
2.4.1 Mass jump condition at the interface . . . . .	14
2.4.2 Momentum jump condition at the interface . . . . .	14
2.5 Constitutive relations . . . . .	15
2.6 Reduction to Darcy law and hydrostatic balance . . . . .	16
2.7 Conclusion . . . . .	17
<b>3 Dynamical modelling of grain-fluid mixtures: preliminary theory</b>	<b>19</b>
3.1 Field Equations . . . . .	20
3.1.1 Governing Equations . . . . .	20
3.1.2 Boundary Conditions . . . . .	20
3.2 Coordinate System and Scaling . . . . .	21
3.2.1 Coordinate System . . . . .	21
3.2.2 Scalings . . . . .	23
3.3 Nondimensionalization . . . . .	23
3.3.1 Non-dimensional conservation equations . . . . .	24
3.3.2 Non-dimensional Boundary Conditions . . . . .	26
3.4 Ordering . . . . .	27
3.5 Depth-averaged theory . . . . .	28
3.5.1 Evaluation of the pore pressure and shear stress . . . . .	31
3.5.2 Evaluation of the granular stresses . . . . .	32
3.5.3 Assumption of velocity profiles . . . . .	34
3.6 Summary of depth-averaged equations . . . . .	35
3.7 Theoretical analysis for steady flows . . . . .	37
3.7.1 Steady flow in a rectangular channel . . . . .	37
3.7.2 Characteristic shape of flow front and roll waves . . . . .	39
3.8 Conclusion . . . . .	45

<b>4</b>	<b>Dynamical modelling of grain-fluid mixtures: simulation part</b>	<b>47</b>
4.1	Review of high-resolution shock-capturing schemes . . . . .	47
4.2	Standard form of the model equations . . . . .	49
4.3	The scheme of Nessyahu and Tadmor (1990) . . . . .	50
4.3.1	Strategy of N-T scheme . . . . .	50
4.3.2	Remarks . . . . .	52
4.4	Central-upwind scheme . . . . .	54
4.4.1	Strategy of the central-upwind scheme . . . . .	54
4.4.2	Remarks of the central-upwind scheme . . . . .	59
4.5	Numerical tests . . . . .	60
4.6	Numerical simulations of grain-fluid mixture flows . . . . .	61
4.6.1	A typical simulation of a grain-fluid mixture flow . . . . .	61
4.6.2	Validation of the present model . . . . .	65
4.7	Conclusion . . . . .	68
<b>5</b>	<b>Dynamical modelling of unsaturated grain-fluid mixtures: preliminary theory</b>	<b>69</b>
5.1	Field equations . . . . .	69
5.1.1	Governing equations . . . . .	70
5.1.2	Boundary conditions . . . . .	71
5.2	Scalings and Nondimensionalization . . . . .	73
5.2.1	Scalings . . . . .	73
5.2.2	Non-dimensional governing equations for the upper layer . . . . .	74
5.2.3	Non-dimensional boundary conditions . . . . .	74
5.3	Ordering and Depth-averaged theory . . . . .	77
5.3.1	Ordering . . . . .	77
5.3.2	Depth-averaged theory . . . . .	77
5.3.3	Evaluation of the unknown terms . . . . .	80
5.3.4	Evaluation of the mass-exchange rate $\mathcal{M}$ . . . . .	83
5.4	Summary of depth-averaged equations . . . . .	84
5.4.1	Assumption of velocity profiles . . . . .	84
5.4.2	Depth-averaged model equations . . . . .	84
5.5	Conclusion . . . . .	88
<b>6</b>	<b>Dynamical modelling of unsaturated grain-fluid mixtures: simulation part</b>	<b>89</b>
6.1	Transition of an initially saturated mixture into unsaturated state . . . . .	89
6.2	Dynamics of an initially unsaturated mixture . . . . .	93
6.3	Conclusion . . . . .	96
<b>7</b>	<b>Dynamical modelling of grain-fluid mixtures by considering dilatancy</b>	<b>97</b>
7.1	Field equations . . . . .	97
7.1.1	Governing equations . . . . .	97
7.1.2	Dilatancy law . . . . .	97
7.1.3	Boundary conditions . . . . .	98
7.2	Depth-averaged theory . . . . .	100
7.2.1	Non-dimensional boundary conditions . . . . .	100

7.2.2	Mass balances . . . . .	102
7.2.3	Slope-normal components of the momentum balances . . . . .	103
7.2.4	Slope-align components of the momentum balances . . . . .	105
7.2.5	Mathematical closure . . . . .	107
7.2.6	Summary of depth-averaged equations . . . . .	108
7.3	Numerical simulation of unsteady flows . . . . .	109
7.3.1	Comparison between the model results with $p_e^{(b)}$ and without $p_e^{(b)}$	110
7.3.2	Comparison with experimental data . . . . .	111
7.3.3	Conclusion . . . . .	113
<b>8</b>	<b>Conclusion and Outlook</b>	<b>115</b>
<b>9</b>	<b>Bibliography</b>	<b>117</b>
<b>A</b>	<b>Comparison between mixture theory and averaging theories</b>	<b>123</b>
	<b>Lebenslauf</b>	<b>125</b>



# List of Figures

2.1	Relationship between the reference and the present configurations . . .	6
2.2	Mapping of a material line element . . . . .	7
2.3	Mapping of a material volume . . . . .	8
2.4	The sketch of a two-phase grain-fluid mixture . . . . .	9
2.5	A material volume with a singular surface inside . . . . .	13
3.1	The sketch of a saturated grain-fluid mixture flow down a slope . . .	19
3.2	Definition of a curvilinear coordinate system . . . . .	21
3.3	The velocity profile in plug flows . . . . .	35
3.4	Velocity profiles in wide and narrow channels . . . . .	38
3.5	Profile of the mixture depth . . . . .	41
3.6	Profiles of roll waves . . . . .	45
4.1	The sketch of N-T scheme . . . . .	51
4.2	The strategy of the central-upwind scheme . . . . .	54
4.3	Comparison between numerical predictions and analytical solutions	62
4.4	The profiles of height and solid volume fraction . . . . .	63
4.5	3-D overview of the predicted debris flows-1 . . . . .	64
4.6	3-D overview of the predicted debris flows-2 . . . . .	64
4.7	The profiles of height and solid volume fraction for smaller viscosity fluid . . . . .	65
4.8	The profile of initial mass . . . . .	66
4.9	The profiles of height and solid volume fraction . . . . .	67
4.10	Comparison between numerical prediction and experimental data .	68
5.1	Sketch of an unsaturated mixture flow . . . . .	70
6.1	The predicted profiles of height by the two-layer and single-layer model . . . . .	90
6.2	Comparison of height profiles between two-layer and single-layer models . . . . .	91
6.3	The predicted profiles of solid volume fraction . . . . .	91
6.4	Contour plots of the predicted flowing heights . . . . .	92
6.5	Predicted profiles of both layer heights . . . . .	93
6.6	Predicted profiles of height and solid volume fraction . . . . .	94
6.7	Predicted profiles of heights for an initially two-layer mixture . . . .	95
6.8	Predicted profiles of heights and solid volume fraction . . . . .	95
6.9	Three-dimensional overview of an unsaturated mixture flow . . . .	96
7.1	The variance of the position of a virtual surface due to dilatancy . .	99
7.2	Long-term evolutions of the height and solid volume fraction . . . .	111

7.3 Comparison of the numerical predictions with the experimental data 112

# Nomenclature

$\mathcal{X}$	Function of motion
$\Psi_s$	The granular surface-force density
$\sigma_e$	The solid effective stress tensor
$\sigma_f$	The fluid stress tensor
$\sigma_g$	The granular stress tensor in the upper layer
$\sigma_s$	The granular stress tensor in the lower-layer mixture
$\tau_f$	The fluid partial shear stress tensor
$F$	Downslope numerical flux
$f_f$	Interaction force exerted on the fluid phase
$f_s$	Interaction force exerted on the granular phase
$g$	Gravitational acceleration
$n^b$	The normal vector at the bed surface
$n^i$	The normal vector at the interface
$n^s$	The normal vector at the top surface
$Q_1$	Nonconservative term
$Q_2$	Nonconservative term
$S$	Numerical source
$U$	Conservative vector
$v_f$	The fluid velocity
$v_g$	The granular velocity
$v_s$	The granular velocity in the lower-layer mixture
$X$	Coordinate in the reference configuration
$x$	Coordinate in the present configuration
$\delta$	Bed friction angle
$\Delta_n$	Normalization factor
$\Delta_t$	Timestep
$\Delta_x$	Space step
$\dot{\gamma}$	Scalar for shear rate

$\epsilon$	Aspect ratio
$\eta$	Index for the fluid or the granular phase
$\gamma$	Density ratio
$\hat{\mu}_s^b$	Bed friction coefficient with dilatancy into account
$\kappa$	The bed curvature
$\lambda$	Nondimensional geometrical parameter
$\lambda^{(n)}$	Maximum eigenvalue of the matrix $\partial \mathbf{F} / \partial \mathbf{U}$
$\mathcal{B}$	Initial material body
$\mathcal{B}_R$	Material body at the reference configuration
$\mathcal{B}_t$	Material body at the present configuration
$\mathcal{F}^b$	Bed surface
$\mathcal{F}^i$	Interface
$\mathcal{F}^s$	Top free surface
$\mathcal{H}$	The typical height
$\mathcal{J}$	The granular mass-exchange rate across the virtual surface
$\mathcal{L}$	The typical length
$\mathcal{M}$	The granular mass-exchange rate across the interface
$\mathcal{R}$	The characteristic radius
$\mathcal{U}$	Interfacial velocity
$\mathbf{g}$	Arbitrary quantity
$\mathfrak{X}$	Particle label
$\mu_f$	Fluid viscosity
$\mu_s^b$	Bed friction coefficient without dilatancy into account
$\Omega$	Material volume in the reference configuration
$\omega$	Material volume in the present configuration
$\phi_c$	Critical solid volume fraction
$\phi_f$	Fluid volume fraction in the lower-layer mixture
$\phi_g$	Solid volume fraction in the upper layer
$\phi_s$	Solid volume fraction in the lower-layer mixture
$\phi_{eq}$	Equilibrium solid volume fraction
$\phi_{max}$	Solid maximum packing fraction
$\pi$	Dilatancy angle
$\rho$	The mixture density



$\rho_f$	Partial fluid mass density
$\rho_s$	Partial solid mass density
$\varphi$	Internal friction angle
$\vartheta$	Non-dimensional drag coefficient
$\tilde{\boldsymbol{\tau}}_f$	The fluid intrinsic shear stress tensor
$\tilde{\rho}_f$	Intrinsic fluid mass density
$\tilde{\rho}_s$	Intrinsic solid mass density
$\zeta$	Slope angle
$b$	The bed surface
$C_d$	Drag force coefficient
$Fr$	Froude number
$h_g$	The upper-layer depth
$h_m$	The mixture depth
$I_v$	Viscous number
$J$	Determinant of the deformation gradient
$k$	Solid permeability
$k_1$	Dilatancy parameter-I
$k_2$	Dilatancy parameter-II
$k_f^b$	Fluid bed friction coefficient
$k_s^i$	The granular friction coefficient at the bed
$k_s^i$	The granular friction coefficient at the interface
$K_x^g$	Upper-layer earth pressure coefficient in the downslope direction
$K_x^s$	Lower-layer earth pressure coefficient in the downslope direction
$K_y^g$	Upper-layer earth pressure coefficient in the crossslope direction
$K_y^s$	Lower-layer earth pressure coefficient in the crossslope direction
$N_R$	Non-dimensional parameter
$p_f$	The pore fluid pressure
$Re$	Reynolds number
$s_{x(f)}$	Fluid downslope source
$s_{x(s)}$	Solid downslope source
$s_{y(f)}$	Fluid crossslope source
$s_{y(s)}$	Solid crossslope source
$t$	Time

$u_\eta$  The downslope velocity for  $\eta$  phase

$v_\eta$  The crossslope velocity for  $\eta$  phase

$w_\eta$  The normal velocity for  $\eta$  phase

# 1 Introduction

Grain-fluid mixture flows are ubiquitous in nature, e.g. debris flows, landslides, and submarine avalanche etc, and they attract scientists' attention due to possible catastrophic consequences. Various efforts have been made in recent decades to account for some mechanism underlying dynamic flow of a grain-fluid mixture.

Three kinds of theoretical models are primarily used in fluid dynamics for describing dynamic processes of flowing grain-fluid mixtures: single-phase flow models, two-phase one-velocity models and two-phase two-velocity models. Single-phase flow models, represented by Bagnold (1954) and Chen (1988), treat mixtures as a single-phase non-Newtonian fluid material. The dynamic behaviour of the bulk can be to some extent described by single-phase flow models. However, such simple models are unable to account for complex interactive coupling between the fluid and granular phases, dynamic behaviours of each phase, and variations of volume fractions in a grain-fluid mixture flow.

The two-phase one-velocity models treat a grain-fluid mixture as a heterogeneous medium but the two phases, i.e. the granular and fluid phases, are idealized to move with the same slope-align velocity. The variations of the volume fractions are implicitly accounted for by taking the evolution of the pore fluid pressure into account. The evolution of the pore fluid pressure in such flows is initially stipulated, but not dynamically. For instance, in Iverson & Denlinger (2001) and its slightly modified model by Pudasaini, Wang & Hutter (2005), an advection-diffusion equation for the pore fluid pressure is postulated according to experimental results. Such a hypothesis lacks a theoretical justification. Recent works overcome the deficiencies for the equation of the pore fluid pressure, see e.g. Kowalski & McElwaine (2013) and Iverson & George (2014). Kowalski & McElwaine (2013) developed a model interpreting the granular internal sedimentation and resuspension by the dissipation and elevation of the pore pressure. Moreover, Iverson & George (2014) presented a model, in which the evolutions of the flow depth, the volume fractions, and the bulk velocity are influenced by the pore fluid pressure. The pore fluid pressure is evolved by an advection-diffusion equation that is derived by combining the critical-state theory with the consolidation theory well established in soil mechanics. Making use of the postulation that the two phases in a grain-fluid mixture approximately move with the same slope-align velocities, the derived model equations are tractable mathematically.

Taking into account the velocity differences between both phases, Pitman & Le (2005) proposed a pioneering two-phase two-velocity model, in which each phase satisfies its own balance equations for mass and momentum. The two phases are explicitly coupled by the interaction forces between each other, including buoyancy force and viscous drag force. The derived model equations cannot only describe the mixture

bulk velocity as the quasi-single phase flow models do, but also delineate the velocity of each phase and the volume fractions. A slightly modified work by Pelanti, Bouchut & Mangeney (2008), starting from the conservative forms of mass and momentum equations, formulated a set of depth-averaged equations similar to those derived by Pitman & Le (2005). The depth-averaged equations established by Pelanti et al. (2008) have the property of recovering a conservative depth-averaged equation for the mixture. Additionally, Pitman, Patra, Kumar, Nishimura & Komori (2013), based on Pitman & Le (2005), added a Navier's bed slip term in the fluid momentum equation. Still based on Pitman & Le (2005), Bouchut, Fernandez-Nieto, Mangeney & Narbona-Reina (2014) postulated an additional equation indicating that the granular phase is incompressible during flows, so that the derived model equations are capable to account for dissipative energy balance. In these models, the fluid viscosity and the granular dilatancy are not taken into account. In addition, these models are based on a Cartesian coordinate system, which prevents from interpreting the bed curvature.

Another two-phase two-velocity model, proposed by Pudasaini (2012) and starting from different governing equations, considers more complex interaction forces including viscous drag force that linearly or quadratically depends on the velocity difference of both phases, buoyancy force, and virtual mass force. Moreover, Pudasaini & Miller (2012) applied this model to examine the effects of buoyancy force on dynamics of the granular phase. Pudasaini (2014), based on the model of Pudasaini (2012), investigated submarine debris flows. A deficiency needs to be noted for Pudasaini (2012) and its applications Pudasaini & Miller (2012) and Pudasaini (2014) that the static balance cannot be satisfied at static state, see Meng & Wang (2015b).

This thesis aims to overcome the aforementioned shortcomings. The first part of this thesis focuses on proposing a two-velocity depth-averaged model based on standard continuum-mechanical mixture theory presented in Chap. 2. In this model, the grain-fluid mixture is treated as a saturated media, in which we postulate that the fluid phase fills all the voids between particles. A frictional Coulomb-like granular phase and a Newtonian fluid phase are taken into account, and the two phases are coupled by the interaction forces including buoyancy force and viscous drag force. The derived depth-averaged model extends the model of Pitman & Le (2005) by including fluid viscous forces and considering the curvature of the topography. Furthermore, the depth-averaged equations are analyzed in terms of steady flows down an inclined plane. It is found that the present model equations can account for classical cross-stream profiles of the downslope velocity, the blunt shape of the flowing front, and roll waves. These aspects are indicated in Chap. 3.

To numerically resolve this model, two typical high-resolution schemes, the N-T scheme of Nessyahu & Tadmor (1990) and the central-upwind scheme of Kurganov, Noelle & Petrova (2001), are introduced in Chap. 4. These two schemes are compared with an analytical solution with respect to a simple convection-dominated flow. It is found that both schemes can give sufficiently accurate solutions. Consequently, the N-T scheme is used to numerically resolve the depth-averaged equations presented in Chap. 3 in order to save computational time. The numerical solutions demonstrate

---

that the proposed model is capable to describe dynamic processes of grain-fluid mixture flows.

It is necessary to note that the saturated hypothesis that the fluid phase fills all the voids between particles cannot always hold for grain-fluid mixture flows, especially when the velocity difference between the two phases is apparent. When the saturated hypothesis does not hold, it means that an unsaturated mixture develops. The second part of this thesis, presented in Chap. 5, aims to tackle unsaturated flows by assuming that the fluid percolates easily down through the interstices of the granular medium and as a result the air is extruded. It implies that a two-layer approach is proposed. In the sketch of two-layer flows, the grain-fluid saturated layer is overlain by a pure granular layer, and the two layers interact at the interface which is a material surface for the fluid but not for the granular phase. The granular mass exchange may occur at the interface between the two layers. The lower layer is dealt with by standard mixture theory, and the upper layer is described by the pure granular model (see Savage & Hutter (1989)). By performing depth-averaged technique, a set of tractable depth-averaged equations are derived.

To validate the proposed two-layer model, we employ N-T scheme to numerically resolve the model equations. The numerical simulations focus on two typical cases. In the first case, a finite mass of initially saturated grain-fluid mixture sliding down a slope that merges into a horizontal plane by a smooth transition zone is investigated. Numerical results demonstrate that the proposed model can reproduce and interpret some phenomena commonly observed in nature and experiments, for instance, the elongation of the mixture body, the development and evolution of blunt head, etc. The numerical results also demonstrate that the two-layer model can give more reasonable investigations on the profiles of the flow height and volume fractions than the previous saturated model, when the transition process of a saturated mixture into an unsaturated state occurs. In the second case, the present model is implemented to investigate the flow of an initially unsaturated mixture that cannot be simulated by the previous saturated models. Numerical results indicate that the two-layer model can predict the phenomenon of phase separation between the fluid and the granular phases, but a further research is warranted to test the predictions. These aspects are presented in Chap. 6.

The third part of this thesis still idealizes the flowing grain-fluid mixtures as saturated media, in which the fluid fills all the voids between the particles. Distinguishing from the saturated model presented in Chap. 3, this part takes into account the granular dilatancy that is ignored in the preceding Chapters. Based on the model of Pailha & Pouliquen (2009), we couple mixture theory and critical-state theory, which describes the relation between shear rate and dilatancy, to derive a depth-averaged model. The derived model describes the mass and momentum balances, and an additional relation between the excess pore fluid pressure (hydrostatic pressure extracted from the pore fluid pressure) and the granular dilatancy. The derived model equations are numerically resolved by the central-upwind scheme presented in Chap. 4. The numerical simulation is to visit to a large-scale flow reported by Iverson, Logan, LaHusen & Berti (2010). The comparison with experimental data demonstrates that the proposed

model taking the granular dilatancy into account can give a better prediction than the saturated model without the dilatancy into account. The aforementioned aspects are described in Chap. 7.

Finally, a conclusion and an outlook are given in Chap. 8.

## 2 Fundamentals of mixture theory

This chapter presents foundations of the mixture theory. The kinematics, conservation equations, and jump conditions for granular mixture are discussed in Sections 2.1-2.4. In Section 2.5, constitutive relations for incompressible mixtures are given. Moreover, we scrutinize the formulated governing equations by reproducing them to Darcy law and hydrostatic balances, which is presented Section 2.6.

### 2.1 Kinematics

Let us consider a *material body*  $\mathcal{B}$ , which consists of an infinite number of material particles labelled  $\mathfrak{X}$ . For each arbitrary particle  $\mathfrak{X}$  in a material body, there exists a position vector  $\mathbf{X}$  at a given time  $t_0$  identifying individual particle of the material body. The set of position vectors  $\mathcal{B}_R = \{\mathbf{X}(\mathfrak{X}) \mid \mathfrak{X} \in \mathcal{B}\}$  in a material body  $\mathcal{B}$  represents the *reference configuration*. The reference configuration can be visualized as the positions of the body at time  $t_0$ . We assume that the initial configuration is the reference configuration, i.e.  $t_0 = 0$ .

When the material body moves, then a particle  $\mathfrak{X}$  found at the position  $\mathbf{X}$  in the reference configuration reaches a new position  $\mathbf{x}$  at time  $t \in \mathcal{R}^+$ . The set of new position vectors  $\mathcal{B}_t = \{\mathbf{x}(\mathfrak{X}, t) \mid \mathfrak{X} \in \mathcal{B}\}$  constitutes the configuration of the body  $\mathcal{B}$  at time  $t$  and it is called *present configuration*. The motion of the particle can be traced mathematically by virtue of a mapping

$$\begin{aligned} \mathcal{X} : \mathcal{B}_R \times \mathcal{R}^+ &\rightarrow \mathcal{B}_t \\ (\mathbf{X}, t) &\mapsto \mathbf{x} = \mathcal{X}(\mathbf{X}, t), \end{aligned} \quad (2.1)$$

where  $\mathcal{X}$  is the function of motion. When the function of motion  $\mathcal{X}$  is continuously differentiable in the entire material body, the mapping (2.1) is invertible

$$\mathbf{X} = \mathcal{X}^{-1}(\mathbf{x}, t). \quad (2.2)$$

Relation (2.2) indicates that any particle in  $\mathcal{B}_t$  can be traced back to its position in  $\mathcal{B}_R$ , as long as the position  $\mathbf{x}$  and the function of motion  $\mathcal{X}$  are known. The relationship between the body  $\mathcal{B}$ , its reference configuration  $\mathcal{B}_R$ , and its present configuration  $\mathcal{B}_t$  is demonstrated in Fig. 2.1. As reflected in Fig. 2.1, the motion of a body can be described by either the present configuration coordinate  $\mathbf{x}$  or the reference configuration

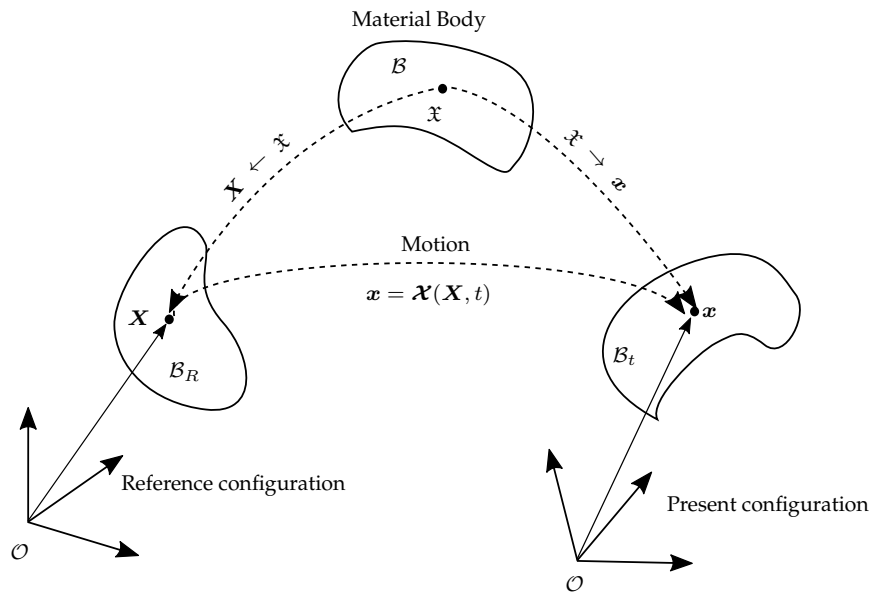


Figure 2.1: Relationship between the body  $\mathcal{B}$ , its reference configuration  $\mathcal{B}_R$ , and its present configuration  $\mathcal{B}_t$ . This figure reproduces Fig.1.1 of Hutter and Jöhnk (2004).

coordinate  $\mathbf{X}$ . If the motion is described by the reference configuration coordinate, then

$$\mathbf{x} = \boldsymbol{\mathcal{X}}(\mathbf{X}, t), \quad \mathbf{X} = (X_1, X_2, X_3), \quad (2.3)$$

where the coordinates  $\mathbf{X} = (X_1, X_2, X_3)$  are called *material* or *Lagrangian coordinates*. If the motion is interpreted with the present configuration coordinates, then

$$\mathbf{X} = \boldsymbol{\mathcal{X}}^{-1}(\mathbf{x}, t), \quad \mathbf{x} = (x_1, x_2, x_3), \quad (2.4)$$

where  $\mathbf{x} = (x_1, x_2, x_3)$  is called *Eulerian coordinates*.

When a material body is experiencing motion  $\mathbf{x} = \boldsymbol{\mathcal{X}}(\mathbf{X}, t)$ , the following relation,

$$d\mathbf{x} = \mathbf{F} \cdot d\mathbf{X}, \quad (2.5)$$

holds for a material line element of the body described by  $d\mathbf{X}$  in the reference configuration and by  $d\mathbf{x}$  in the present configuration, see Fig. 2.2. The tensor  $\mathbf{F}$  is the gradient of the function of motion with respect to the material coordinates, i.e.  $\mathbf{F} = \text{Grad}\boldsymbol{\mathcal{X}}(\mathbf{X}, t)$ , and it is known as *deformation gradient*. The components of deformation gradient are

$$F_{i\alpha} = \frac{\partial \mathcal{X}_i(\mathbf{X}, t)}{\partial X_\alpha}. \quad (2.6)$$

As we assume that the motion is invertible, the determinant of the deformation gra-



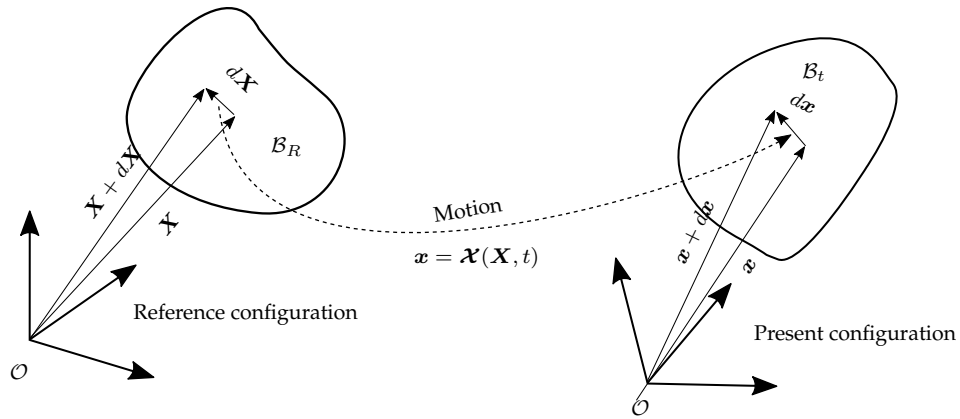


Figure 2.2: The material line element indicated by  $d\mathbf{X}$  in the reference configuration evolves into  $d\mathbf{x}$  at time  $t$  in the present configuration. This figure reproduces Fig.1.2 of Hutter and Jöhnk (2004).

dient is always non-zero, i.e.,

$$J := \det \mathbf{F} \neq 0. \quad (2.7)$$

The determinant of the deformation gradient tensor is responsible for mapping an infinitesimal volume element  $d\Omega$  in the reference configuration onto the infinitesimal volume element  $d\omega$  in the present configuration (see Fig. 2.3), i.e.,

$$d\omega = J d\Omega, \quad (2.8)$$

see Hutter & Jöhnk (2004).

## 2.2 Reynolds Transport Theorem

An arbitrary material volume  $\omega$  of a material body  $\mathcal{B}_t$  in the present configuration at any time  $t$  is taken into account, see Fig. 2.3. We prescribe that an arbitrary material volume is deforming with a velocity  $\mathbf{v}$ , and a physical quantity  $\mathfrak{g}(\mathbf{x}, t)$  is assigned to it. This quantity  $\mathfrak{g}(\mathbf{x}, t)$  can be a scalar, or a vector function of space and time. The function  $\mathfrak{g}(\mathbf{x}, t)$  can be written as  $\hat{\mathfrak{g}}(\mathbf{X}, t)$  in terms of the material coordinate. The time derivative of an arbitrary physical quantity  $\mathfrak{g}$  in this material volume  $\omega$  can be given by

$$\begin{aligned} \frac{d}{dt} \int_{\omega} \mathfrak{g} d\omega &= \int_{\Omega} \frac{\partial}{\partial t} \left( \hat{\mathfrak{g}}(\mathbf{X}, t) J \right) d\Omega \\ &= \int_{\Omega} \left( \frac{\partial \hat{\mathfrak{g}}}{\partial t} + \hat{\mathfrak{g}} \nabla \cdot \mathbf{v} \right) J d\Omega = \int_{\omega} \left( \frac{d\mathfrak{g}}{dt} + \mathfrak{g} \nabla \cdot \mathbf{v} \right) d\omega, \end{aligned} \quad (2.9)$$

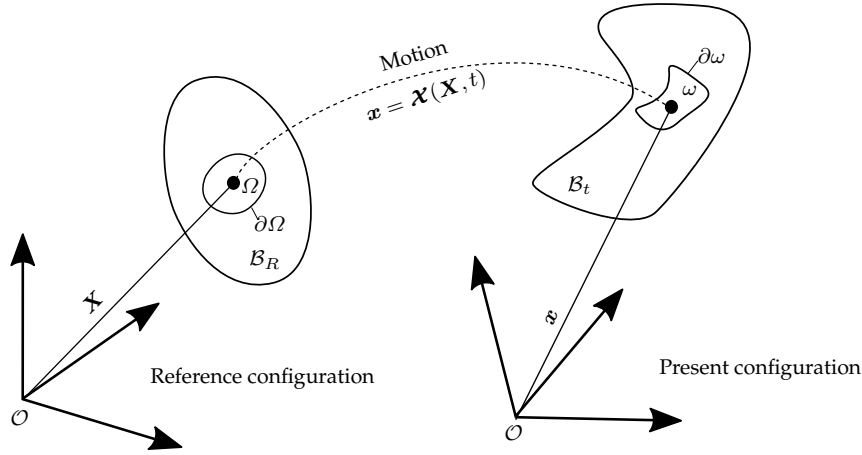


Figure 2.3: A material domain  $\Omega$  in the reference configuration, bounded by surface  $\partial\Omega$ , evolves into the domain  $\omega$  bounded by surface  $\partial\omega$  in the present configuration after time  $t$ . This figure reproduces Fig. 2.1 of Hutter and Jöhnk (2004).

where the identity  $\partial J/\partial t = J\nabla \cdot \mathbf{v}$  (see e.g. Hutter & Jöhnk (2004)) was used. The material derivative  $d\mathbf{g}/dt$ , appearing in equation (2.9), can be further expressed as follows,

$$\frac{d\mathbf{g}(\mathbf{x}, t)}{dt} = \frac{d}{dt}\mathbf{g}(\mathcal{X}(\mathbf{X}, t), t) = \frac{\partial\mathbf{g}}{\partial t} + \mathbf{v} \cdot \nabla\mathbf{g}. \quad (2.10)$$

Combining relations (2.9) with (2.10) can give the Reynolds transport theorem

$$\begin{aligned} \frac{d}{dt} \int_{\omega} \mathbf{g} d\omega &= \int_{\omega} \left[ \frac{\partial\mathbf{g}}{\partial t} + \mathbf{v} \cdot \nabla\mathbf{g} + \mathbf{g}\nabla \cdot \mathbf{v} \right] d\omega \\ &= \int_{\omega} \left[ \frac{\partial\mathbf{g}}{\partial t} + \nabla \cdot (\mathbf{g}\mathbf{n}) \right] d\omega \\ &= \int_{\omega} \frac{\partial\mathbf{g}}{\partial t} d\omega + \oint_{\partial\omega} \mathbf{g}(\mathbf{v} \cdot \mathbf{n}) ds. \end{aligned} \quad (2.11)$$

Furthermore, the Reynolds transport theorem (2.11) can also be extended for non-material volumes. For this purpose, an arbitrary non-material volume  $\hat{\omega}$  is chosen, in which the boundary is moving with the velocity  $\mathbf{w}$ . By referring to Wang (2016), the time rate of change of the quantity  $\mathbf{g}$  assigned to this non-material volume  $\hat{\omega}$  can be expressed as follows

$$\frac{d}{dt} \int_{\hat{\omega}} \mathbf{g} d\omega = \int_{\hat{\omega}} \frac{\partial\mathbf{g}}{\partial t} d\omega + \oint_{\partial\hat{\omega}} \mathbf{g}(\mathbf{w} \cdot \mathbf{n}) ds. \quad (2.12)$$

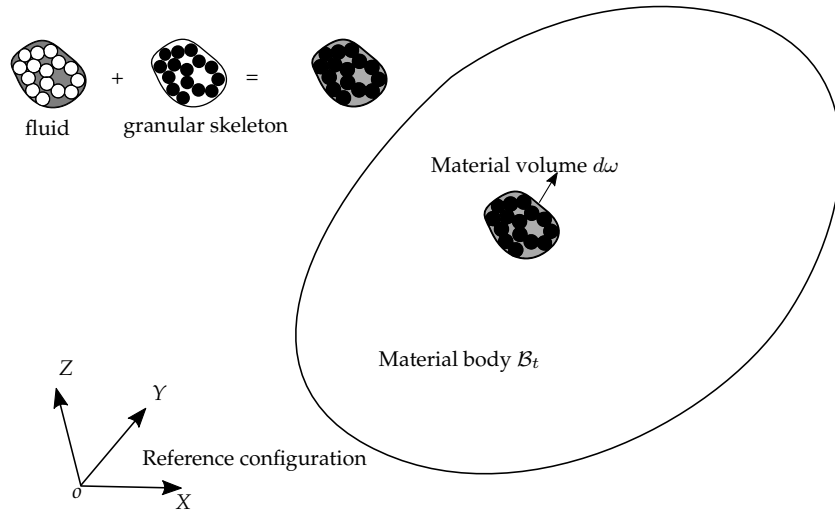


Figure 2.4: A grain-fluid mixture medium as the superposition of two continuous media: a granular skeleton and fluid occupy simultaneously each point of space.

## 2.3 Mixture theory

When a material body composed of several different components or phases, is taken into account, the classical mixture theory is commonly applied (see Hutter & Jöhnk (2004) and Truesdell (1984)). The central idea for the mixture theory is the supposition that each spatial point, at any time, is simultaneously occupied by material of all phases (say, “ $n > 1$ ” phases) with individual volume fraction  $\phi_\eta$ , where  $\eta \in \{1, 2, \dots, n\}$ . In this way, the mixture can be idealized as a superposition of continuous media, each following its own motion with the coupling of interaction forces between the phases. To derive rigorously the conservation laws of the mixture theory, a number of useful concepts are worth mentioning. We focus on a two-phase saturated grain-fluid mixture, where  $\eta = s$  represents the solid phase, and  $\eta = f$  denotes the fluid phase. If we take an infinitesimal volume  $d\omega$  in the present configuration at any time  $t$  into account, it is composed of a skeleton matrix of grains and interstitial fluid filling in the porous space of granular skeleton matrix, see Fig. 2.4. In this material volume  $d\omega$ , the granular phase (granular skeleton) occupies the volume  $d\omega_s$  and the fluid phase occupies the volume  $d\omega_f$ . Therefore, the volume fractions for each phase are defined as

$$\phi_s = \frac{d\omega_s}{d\omega}, \quad \phi_f = \frac{d\omega_f}{d\omega}, \quad (2.13)$$

where for a saturated two-phase mixture the summation of volume fractions satisfies

$$\phi_s + \phi_f = 1. \quad (2.14)$$

Moreover, in this volume  $d\omega$ , we define the mass of the granular phase as  $dm_s$  and the mass of the fluid phase as  $dm_f$ . There are two mass density fields that can be assigned to each phase. The intrinsic mass density of each phase is the individual mass divided by the volume occupied by the phase in consideration in  $d\omega$ , i.e.,

$$\tilde{\rho}_s = \frac{dm_s}{d\omega_s}, \quad \tilde{\rho}_f = \frac{dm_f}{d\omega_f}. \quad (2.15)$$

The other density of each phase, the partial mass density  $\rho_\eta$ , is the individual mass divided by the volume  $d\omega$ , i.e.,

$$\rho_s = \frac{dm_s}{d\omega}, \quad \rho_f = \frac{dm_f}{d\omega}. \quad (2.16)$$

Through relations (2.15) and (2.16), the partial mass density of each phase is related to the intrinsic mass density by

$$\rho_s = \tilde{\rho}_s \phi_s, \quad \rho_f = \tilde{\rho}_f \phi_f. \quad (2.17)$$

### 2.3.1 Mass conservation law

This part aims to formulate the conservation law of the mass for each phase. Taking an arbitrary material volume  $\omega$  in the present configuration at any time  $t$  into account, and tracing the deformation of granular skeleton in domain  $\omega$  with time, its mass will neither increase, nor decrease when chemical reactions and phase changes are absent. Therefore, one can formulate

$$\frac{d}{dt} \int_{\omega} \rho_s d\omega = 0. \quad (2.18)$$

By virtue of the Reynolds transport theorem (2.11), equation (2.18) can be rewritten as

$$\int_{\omega} \left[ \frac{\partial \rho_s}{\partial t} + \nabla \cdot (\rho_s \mathbf{v}_s) \right] d\omega = 0. \quad (2.19)$$

As equation (2.19) holds for any material volume of a material body  $\mathcal{B}_t$  at any time  $t$ , the integrand should be always zero at any spatial point, i.e.,

$$\frac{\partial \rho_s}{\partial t} + \nabla \cdot (\rho_s \mathbf{v}_s) = 0. \quad (2.20)$$

Similarly, the conservation law of mass for the fluid phase is derived as

$$\frac{\partial \rho_f}{\partial t} + \nabla \cdot (\rho_f \mathbf{v}_f) = 0. \quad (2.21)$$

Summation of equations (2.20) and (2.21) yields the conservation equation of mass for the mixture as a whole

$$\frac{\partial \rho}{\partial t} + \nabla \cdot (\rho \mathbf{v}) = 0, \quad (2.22)$$

where the mixture density  $\rho$  and the mixture velocity  $\mathbf{v}$  are defined by

$$\rho = \rho_s + \rho_f, \quad \mathbf{v} = (\rho_s \mathbf{v}_s + \rho_f \mathbf{v}_f) / \rho. \quad (2.23)$$

### 2.3.2 Momentum conservation law

Let us consider an arbitrary material volume  $\omega$  bounded by surface  $\partial\omega$  in the present configuration at any time  $t$ . Tracing the deformation of the granular skeleton in domain  $\omega$ , the time rate of change of its momentum is equal to the sum of the forces acting on the granular phase. The forces include volume forces, surface force through surface  $\partial\omega$ , and interaction forces exerted by the other phase. Based on these descriptions for the granular phase, the following equation can be formulated

$$\frac{d}{dt} \int_{\omega} \rho_s \mathbf{v}_s d\omega = \int_{\omega} \rho_s \mathbf{g} d\omega + \int_{\partial\omega} \boldsymbol{\Psi}_s(\mathbf{x}, t, \mathbf{n}) ds + \int_{\omega} \mathbf{f}_s d\omega, \quad (2.24)$$

where  $\mathbf{g}$  denotes gravitational acceleration,  $\mathbf{f}_s$  the density of the interaction force exerted on the granular phase by the fluid phase,  $\boldsymbol{\Psi}_s$  the granular surface-force density, and  $\mathbf{n}$  the unit external normal vector to the surface  $\partial\omega$ . By referring to the Cauchy Lemma (see Hutter & Jöhnk (2004), page 55), the surface-force density  $\boldsymbol{\Psi}_s$  can be linearized into a second-order stress tensor contracting with the normal vector  $\mathbf{n}$  of the surface, i.e.,

$$\boldsymbol{\Psi}_s(\mathbf{x}, t, \mathbf{n}) = \boldsymbol{\sigma}_s(\mathbf{x}, t) \mathbf{n}, \quad (2.25)$$

where  $\boldsymbol{\sigma}_s$  is commonly named as the solid partial stress tensor.

Substituting (2.25) into (2.24), and rewriting the surface integral into the volume integral by the divergent theorem, and reformulating the left-hand side terms by making use of the Reynolds transport theorem (2.11), one can obtain

$$\int_{\omega} \left[ \frac{\partial}{\partial t} (\rho_s \mathbf{v}_s) + \nabla \cdot (\rho_s \mathbf{v}_s \otimes \mathbf{v}_s) - \rho_s \mathbf{g} - \nabla \cdot \boldsymbol{\sigma}_s - \mathbf{f}_s \right] d\omega = 0. \quad (2.26)$$

As equation (2.26) holds for any arbitrary material volume  $\omega(t)$ , the integrand of the volume integral must vanish identically, i.e.,

$$\frac{\partial}{\partial t} (\rho_s \mathbf{v}_s) + \nabla \cdot (\rho_s \mathbf{v}_s \otimes \mathbf{v}_s) = \rho_s \mathbf{g} + \nabla \cdot \boldsymbol{\sigma}_s + \mathbf{f}_s. \quad (2.27)$$

Similarly, the conservation law of momentum for the fluid phase is given by

$$\frac{\partial}{\partial t}(\rho_f \mathbf{v}_f) + \nabla \cdot (\rho_f \mathbf{v}_f \otimes \mathbf{v}_f) = \rho_f \mathbf{g} + \nabla \cdot \boldsymbol{\sigma}_f + \mathbf{f}_f, \quad (2.28)$$

where the interaction force should satisfy  $\mathbf{f}_s + \mathbf{f}_f = 0$ , according to the Newtonian third law.

Summation of equations (2.27) and (2.28) leads to the conservation law of momentum for the mixture as a whole,

$$\frac{\partial}{\partial t}(\rho \mathbf{v}) + \nabla \cdot (\rho \mathbf{v} \otimes \mathbf{v}) = \nabla \cdot (\boldsymbol{\sigma}_s + \boldsymbol{\sigma}_f - \boldsymbol{\sigma}') + \rho \mathbf{g}, \quad (2.29)$$

where  $\boldsymbol{\sigma}' = \rho_s(\mathbf{v}_s - \mathbf{v}) \otimes (\mathbf{v}_s - \mathbf{v}) + \rho_f(\mathbf{v}_f - \mathbf{v}) \otimes (\mathbf{v}_f - \mathbf{v})$ .

## 2.4 Jump conditions at the interface

If an interface, especially a discontinuous interface, exists in the flowing domain, the physical quantities will not be continuously differentiable across this interface. In this case, the conservation equations (2.20), (2.21), (2.27), and (2.28) do not hold any more. Some new conditions, so-called jump conditions, must be formulated at a discontinuous interface instead. To this end, this section aims to formulate the jump conditions including mass and momentum jump conditions.

To derive jump conditions, an arbitrary material volume  $\omega$  containing the grain-fluid mixture in the present configuration at any time is taken into account (see Fig. 2.5), in which there exists an orientable interface labelled as  $\mathfrak{s}$  and the material volume is separated into two parts by this interface, which are indicated by  $+$  and  $-$ . The part  $\omega^+$  (or  $\omega^-$ ) is bounded by the material surface  $\partial\omega^+$  (or  $\partial\omega^-$ ) plus the interface  $\mathfrak{s}$  moving with the velocity  $\mathbf{w}$  with unit normal vector  $\mathbf{n}_s$ . Across this interface, the physical quantities, e.g. density, velocity, pressure etc., may be discontinuous, but in the remaining parts of the material volume they are supposed to be continuously differentiable.

The time rate of change of the quantity  $\mathbf{g}$  assigned to this material volume  $\omega$  is given by

$$\frac{d}{dt} \int_{\omega} \mathbf{g} \, d\omega = \frac{d}{dt} \int_{\omega^+} \mathbf{g} \, d\omega + \frac{d}{dt} \int_{\omega^-} \mathbf{g} \, d\omega. \quad (2.30)$$

The transport theorem (2.12) can be used for the parts on the right-hand side of (2.30) (note the direction of the normal vector of the singular surface). It turns out to be

$$\frac{d}{dt} \int_{\omega^\pm} \mathbf{g} \, d\omega = \int_{\omega^\pm} \frac{\partial \mathbf{g}}{\partial t} \, d\omega + \int_{\partial\omega^\pm} \mathbf{g}(\mathbf{v} \cdot \mathbf{n}) \, ds \mp \int_{\mathfrak{s}} \mathbf{g}^\pm(\mathbf{w} \cdot \mathbf{n}_s) \, ds. \quad (2.31)$$

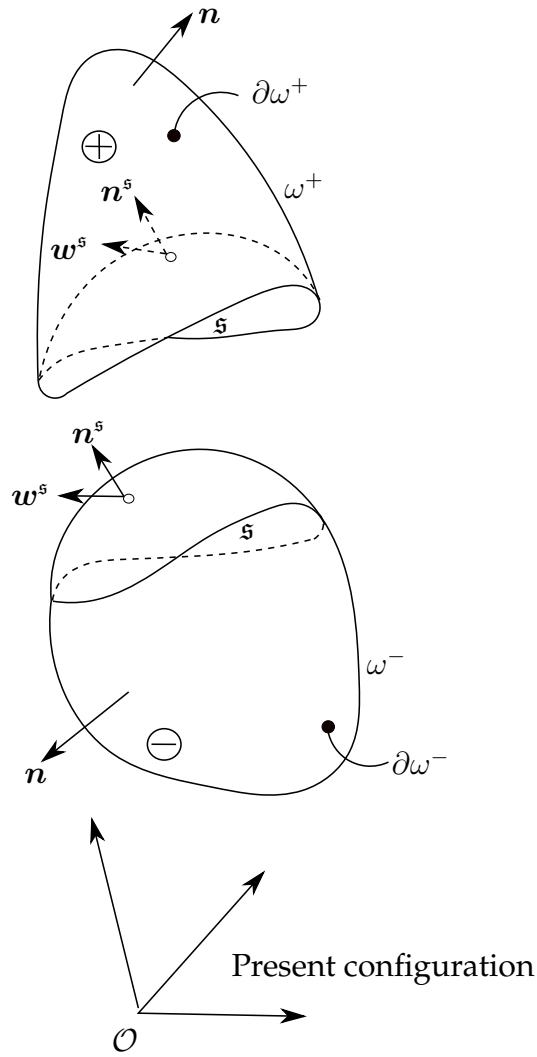


Figure 2.5: An arbitrary material volume,  $\omega = \omega^+ + \omega^-$ , which is bounded by the surface  $\partial\omega = \partial\omega^+ + \partial\omega^-$  and is divided into two continuous parts by a singular surface labelled as  $\mathfrak{s}$ . This figure reproduces the figure 3.5 in Wang (2016).

By adding the two identities of (2.31), one can obtain

$$\begin{aligned}
 \frac{d}{dt} \int_{\omega} \mathbf{g} \, d\omega &= \int_{\omega^+} \frac{\partial \mathbf{g}}{\partial t} \, d\omega + \int_{\omega^-} \frac{\partial \mathbf{g}}{\partial t} \, d\omega + \int_{\partial\omega^+ \cup \mathfrak{s}} \mathbf{g}(\mathbf{v} \cdot \mathbf{n}) \, ds + \int_{\partial\omega^- \cup \mathfrak{s}} \mathbf{g}(\mathbf{v} \cdot \mathbf{n}) \, ds \\
 &\quad + \int_{\mathfrak{s}} \llbracket \mathbf{g}(\mathbf{v} \cdot \mathbf{n}_s) \rrbracket \, ds - \int_{\mathfrak{s}} \llbracket \mathbf{g}(\mathbf{w} \cdot \mathbf{n}_s) \rrbracket \, ds \\
 &= \int_{\omega^+} \left( \frac{\partial \mathbf{g}}{\partial t} + \nabla \cdot (\mathbf{g}\mathbf{v}) \right) d\omega + \int_{\omega^-} \left( \frac{\partial \mathbf{g}}{\partial t} + \nabla \cdot (\mathbf{g}\mathbf{v}) \right) d\omega - \int_{\mathfrak{s}} \llbracket \mathbf{g}(\mathbf{w} - \mathbf{v}) \cdot \mathbf{n}_s \rrbracket \, ds,
 \end{aligned} \tag{2.32}$$

where the divergent theorem is used to derived the last-line terms, and the notation  $\llbracket q \rrbracket$  stands for the jump of  $q$  across a singular surface with  $\llbracket q \rrbracket = q^+ - q^-$ .

### 2.4.1 Mass jump condition at the interface

Tracing the material volume  $\omega$  described above, the mass of the grain-fluid mixture will neither increase nor decrease when chemical reactions and phase changes are absent. Therefore one can formulate

$$\frac{d}{dt} \int_{\omega} \rho d\omega = 0. \quad (2.33)$$

By virtue of the Reynolds transport theorem (2.32), one can rewrite (2.33) as

$$\int_{\omega^+} \left( \frac{\partial \rho}{\partial t} + \nabla \cdot (\rho \mathbf{v}) \right) d\omega + \int_{\omega^-} \left( \frac{\partial \rho}{\partial t} + \nabla \cdot (\rho \mathbf{v}) \right) d\omega - \int_{\mathfrak{s}} \llbracket \rho(\mathbf{w} - \mathbf{v}) \cdot \mathbf{n}_{\mathfrak{s}} \rrbracket ds = 0. \quad (2.34)$$

The boundary condition at the interface indicates that the volume integrals in relation (2.34) will vanish. Additionally, an arbitrary material volume is chosen in the formulation above, such that the integrand of surface integral must vanish identically. Consequently, the mass jump condition holding at the interface can be derived and it turns out to be

$$\llbracket \rho(\mathbf{w} - \mathbf{v}) \cdot \mathbf{n}_{\mathfrak{s}} \rrbracket = 0. \quad (2.35)$$

### 2.4.2 Momentum jump condition at the interface

Tracing such an arbitrary material volume  $\omega$ , the time rate of change of its internal mixture momentum is equal to the sum of the forces acting on the mixture. These forces include volume forces, and surface forces through material surfaces  $\partial\omega^+$  and  $\partial\omega^-$  and through the interface (singular surface)  $\mathfrak{s}$ . It is necessary to note that for the problems we will investigate in the subsequent chapters, the surface tension has a negligible effect. Consequently, we will not consider the surface tension in the following. Based on the descriptions above, one can formulate

$$\frac{d}{dt} \int_{\omega} \rho \mathbf{v} d\omega = \int_{\omega} \rho \mathbf{g} d\omega + \int_{\partial\omega^+} \Psi(\mathbf{x}, t, \mathbf{n}) ds + \int_{\partial\omega^-} \Psi(\mathbf{x}, t, \mathbf{n}) ds, \quad (2.36)$$

where  $\Psi$  represents the surface-force density of the mixture.

By virtue of the Reynolds transport theorem (2.32), one can rewrite the left-hand side term of relation (2.36) such that relation (2.36) is rewritten as

$$\begin{aligned} & \int_{\omega^+} \left( \frac{\partial(\rho \mathbf{v})}{\partial t} + \nabla \cdot (\rho \mathbf{v} \mathbf{v}) \right) d\omega + \int_{\omega^-} \left( \frac{\partial(\rho \mathbf{v})}{\partial t} + \nabla \cdot (\rho \mathbf{v} \mathbf{v}) \right) d\omega \\ & \quad - \int_{\mathfrak{s}} \llbracket \rho \mathbf{v}(\mathbf{w} - \mathbf{v}) \cdot \mathbf{n}_{\mathfrak{s}} \rrbracket ds \\ & = \int_{\omega} \rho \mathbf{g} d\omega + \int_{\partial\omega^+} \Psi(\mathbf{x}, t, \mathbf{n}) ds + \int_{\partial\omega^-} \Psi(\mathbf{x}, t, \mathbf{n}) ds. \end{aligned} \quad (2.37)$$



By referring to Cauchy theorem, the surface-force density  $\Psi$  can be linearized as follows

$$\Psi(\mathbf{x}, t, \mathbf{n}) = \boldsymbol{\sigma}(\mathbf{x}, t)\mathbf{n}, \quad (2.38)$$

similar to relation (2.25), where  $\boldsymbol{\sigma} = \boldsymbol{\sigma}_s + \boldsymbol{\sigma}_f - \boldsymbol{\sigma}'$ .

Substituting (2.38) into the integral  $\int_{\partial\omega^\pm} \Psi ds$ , one can formulate

$$\begin{aligned} \int_{\partial\omega^+} \Psi(\mathbf{x}, t, \mathbf{n}) ds + \int_{\partial\omega^-} \Psi(\mathbf{x}, t, \mathbf{n}) ds &= \int_{\partial\omega^+} \boldsymbol{\sigma}\mathbf{n} ds - \int_{\mathfrak{s}} \boldsymbol{\sigma}^+ \mathbf{n}_s ds \\ &+ \int_{\partial\omega^-} \boldsymbol{\sigma}\mathbf{n} ds + \int_{\mathfrak{s}} \boldsymbol{\sigma}^- \mathbf{n}_s ds + \int_{\mathfrak{s}} \boldsymbol{\sigma}^+ \mathbf{n}_s ds - \int_{\mathfrak{s}} \boldsymbol{\sigma}^- \mathbf{n}_s ds \\ &= \int_{\omega^+} \nabla \cdot \boldsymbol{\sigma} ds + \int_{\omega^-} \nabla \cdot \boldsymbol{\sigma} ds + \int_{\mathfrak{s}} \llbracket \boldsymbol{\sigma} \rrbracket \mathbf{n}_s ds. \end{aligned} \quad (2.39)$$

Substituting (2.39) into (2.37), one can derive the following relation

$$\begin{aligned} \int_{\omega^+} \left( \frac{\partial(\rho\mathbf{v})}{\partial t} + \nabla \cdot (\rho\mathbf{v}\mathbf{v}) \right) d\omega + \int_{\omega^-} \left( \frac{\partial(\rho\mathbf{v})}{\partial t} + \nabla \cdot (\rho\mathbf{v}\mathbf{v}) \right) d\omega \\ - \int_{\mathfrak{s}} \llbracket \rho\mathbf{v}(\mathbf{w} - \mathbf{v}) \cdot \mathbf{n}_s \rrbracket ds \\ = \int_{\omega} \rho\mathbf{g} d\omega + \int_{\omega^+} \nabla \cdot \boldsymbol{\sigma} ds + \int_{\omega^-} \nabla \cdot \boldsymbol{\sigma} ds + \int_{\mathfrak{s}} \llbracket \boldsymbol{\sigma} \rrbracket \mathbf{n}_s ds. \end{aligned} \quad (2.40)$$

The boundary condition at the interface indicates that the volume integrals in relation (2.40) will vanish. Additionally, an arbitrary material volume is chosen in the formulation above, such that the integrand of the surface integral must vanish identically. Consequently, the momentum jump condition holding at the interface can be derived and it turns out to be

$$\llbracket \rho\mathbf{v}(\mathbf{w} - \mathbf{v}) \cdot \mathbf{n}_s + \boldsymbol{\sigma}\mathbf{n}_s \rrbracket = 0 \quad (2.41)$$

## 2.5 Constitutive relations

The formulation of constitutive relations involves the description of material properties. To this end, we postulate that the fluid and granular phases are incompressible as commonly used in literatures, see e.g. Boer & Ehlers (1990), Franco (2012), and Liu (2014). Within the framework of thermodynamical analysis, the solid partial stress tensor  $\boldsymbol{\sigma}_s$  and the fluid partial stress tensor  $\boldsymbol{\sigma}_f$  are formulated as

$$\boldsymbol{\sigma}_s = -\phi_s p_f \mathbf{I} - \boldsymbol{\sigma}_e, \quad \boldsymbol{\sigma}_f = -\phi_f p_f \mathbf{I} + \boldsymbol{\tau}_f, \quad (2.42)$$

(see Boer & Ehlers (1990) and Liu (2014)), where  $p_f$  is the pore fluid pressure,  $\mathbf{I}$  the unit isotropic stress tensor,  $\boldsymbol{\sigma}_e$  the solid effective stress tensor, and  $\boldsymbol{\tau}_f$  the fluid partial shear stress tensor. The solid effective stress represents the stress between grains

transmitted by the contact between the solid particles. The negative sign presented in the solid effective stress lies in the fact that compressive stress is counted as positive in soil mechanics. Moreover, the fluid partial shear stress  $\boldsymbol{\tau}_f$  can connect with the intrinsic shear stress  $\tilde{\boldsymbol{\tau}}_f$  by the fluid volume fraction, i.e.  $\boldsymbol{\tau}_f = \phi_f \tilde{\boldsymbol{\tau}}_f$ . A Newtonian fluid is assumed for the fluid phase, such that  $\tilde{\boldsymbol{\tau}}_f = \mu_f (\nabla \mathbf{v}_f + \nabla^T \mathbf{v}_f)$ , where  $\mu_f$  stands for the fluid viscosity. When one adds  $\boldsymbol{\sigma}_s$  and  $\boldsymbol{\sigma}_f$ , the total stress tensor,  $\boldsymbol{\sigma}_t = -p_f \mathbf{I} - \boldsymbol{\sigma}_e + \phi_f \tilde{\boldsymbol{\tau}}_f$  is derived. The formulation of  $\boldsymbol{\sigma}_t$  can be seen as an extension of classical effective stress principle of Terzaghi (1925) in soil mechanics by including the fluid shear stress.

Following Iverson (1997), the interaction force  $\mathbf{f}_s$  exerted on the granular phase by the fluid phase is postulated by

$$\mathbf{f}_s = p_f \nabla \phi_s + \mu_f \phi_f^2 (\mathbf{v}_f - \mathbf{v}_s) / k, \quad (2.43)$$

where the term  $p_f \nabla \phi_s$  is the buoyancy force (see Drew (1983)), and the term  $\mu_f \phi_f^2 (\mathbf{v}_f - \mathbf{v}_s) / k$  is the viscous drag force with  $k$  being permeability of the solid skeleton.

## 2.6 Reduction to Darcy law and hydrostatic balance

So far the conservation equations for incompressible fluid and granular phases in a mixture have been derived and given by

$$\frac{\partial \rho_f}{\partial t} + \nabla \cdot (\rho_f \mathbf{v}_f) = 0, \quad (2.44)$$

$$\frac{\partial \rho_s}{\partial t} + \nabla \cdot (\rho_s \mathbf{v}_s) = 0, \quad (2.45)$$

$$\frac{\partial (\rho_f \mathbf{v}_f)}{\partial t} + \nabla \cdot (\rho_f \mathbf{v}_f \otimes \mathbf{v}_f) = -\phi_f \nabla p_f + \nabla \cdot \boldsymbol{\tau}_f + \rho_f \mathbf{g} - \frac{\mu_f \phi_f^2}{k} (\mathbf{v}_f - \mathbf{v}_s), \quad (2.46)$$

$$\frac{\partial (\rho_s \mathbf{v}_s)}{\partial t} + \nabla \cdot (\rho_s \mathbf{v}_s \otimes \mathbf{v}_s) = -\phi_s \nabla p_f - \nabla \cdot \boldsymbol{\sigma}_e + \rho_s \mathbf{g} + \frac{\mu_f \phi_f^2}{k} (\mathbf{v}_f - \mathbf{v}_s). \quad (2.47)$$

It should be noted that equations (2.44)-(2.47) are comparable with those based on averaging theories (see Appendix A). To scrutinize the equations above, let us take a steady creeping flow and an ideal fluid into account. For such case, the time derivative, the inertial term, and the fluid shear stress, appearing in equation (2.46), can be ignored, such that equation (2.46) reduces to

$$\mathbf{q} = \phi_f (\mathbf{v}_f - \mathbf{v}_s) = -\frac{k}{\mu_f} (\nabla p_f - \tilde{\rho}_f \mathbf{g}), \quad (2.48)$$

where  $\mathbf{q}$  is usually called specific discharge of the fluid relative to the solid. It is worth mentioning that the form of equation (2.48) is exactly the same as the Darcy law.

In addition to the ability of recovering to the Darcy law, the governing equations (2.46) and (2.47) can also reproduce the hydrostatic balance of a grain-fluid mixture. In the static state, equations (2.46) and (2.47) transform into the forms,

$$\nabla p_f = \tilde{\rho}_f \mathbf{g}, \quad (2.49)$$

$$(\tilde{\rho}_s - \tilde{\rho}_f) \phi_s \mathbf{g} = \nabla \cdot \boldsymbol{\sigma}_e, \quad (2.50)$$

where relation (2.49) asserts that the equilibrium pore pressure is the hydrostatic pressure. It agrees with the observation in soil mechanics that the manometric pressure in the soil is the pressure as if the medium were bulk fluid, unaffected by the presence of the solid constituent in the medium. Equation (2.50) indicates that the contact force of the particles equals the difference of gravity and buoyancy force, and it agrees with the static balance.

## 2.7 Conclusion

In this Chapter, the fundamentals of mixture theory is presented, including kinematics, conservation equations, jump conditions, and constitutive relations. These fundamental knowledge aids to derive the two-phase conservation equations which will be used to formulate depth-averaged equations in the next chapters.



### 3 Dynamical modelling of grain-fluid mixtures: preliminary theory

When a grain-fluid mixture is flowing down a slope, it is commonly treated as a two-phase saturated material. For such a saturated mixture whose depth is much smaller than its length, a depth-averaged model, which gains advantage of less computation burden compared with a three-dimensional model, can be derived. To derive a depth-averaged model, we use the following steps. First, the standard two-phase mixture theory, presented in Chap. 2, can be applied. We present the conservation equations together with the boundary conditions in Section 3.1. Moreover, a curvilinear coordinate system and the scalings of dynamic quantities are introduced. These aspects are presented in Section 3.2. Then, the process of non-dimensionalizing the conservation equations by virtue of the scalings, is necessary to derive a depth-averaged model, which is presented in Section 3.3. The last procedure is to follow Savage & Hutter (1989) to simplify the non-dimensionalized equations by using depth-integration technique, which is presented from Section 3.4 till Section 3.7.

Investigating steady flows can gain some insights into complex flow. Additionally, it can also scrutinize the correctness of the derived depth-averaged model. Consequently, we will perform theoretical analyses on some simple steady flows. These analyses will be presented in Section 3.8 and Section 3.9.

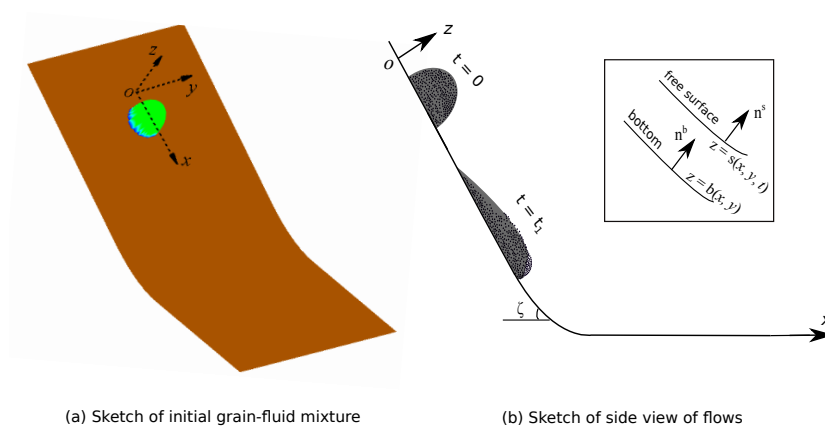


Figure 3.1: Sketch of a saturated grain-fluid mixture flow, where the mixture is assumed to be always saturated.

## 3.1 Field Equations

### 3.1.1 Governing Equations

We take into account a two-phase grain-fluid mixture, which is described in Fig. 3.1. Such a mixture is idealized to be a saturated medium, i.e. the interstitial fluid fills all the voids between grains. Therefore, the mixture theory, presented in the last chapter, can be applied. In the framework of the mixture theory, all phases are present at each point of the field with different volume fractions. Thus, the separate mass and momentum conservation equations can be applied at all locations for the fluid and the granular components of the mixture. The conservation equations are given by relations (2.44)-(2.47). Additionally, the fluid and the granular phases are assumed to be incompressible, which indicate that the intrinsic densities  $\tilde{\rho}_f$  and  $\tilde{\rho}_s$  are constant. Last for saturated media, the volume fractions satisfy the condition (2.14).

### 3.1.2 Boundary Conditions

- (i) The **top free surface**  $\mathcal{F}^s(x, y, z, t) = z - s(x, y, t) = 0$ , is assumed to be material for both fluid and granular phases. It implies that the kinematic boundary conditions hold for each component of the mixture, which are

$$\frac{\partial \mathcal{F}^s}{\partial t} + \mathbf{v}_f^s \cdot \nabla \mathcal{F}^s = 0 \quad \text{and} \quad \frac{\partial \mathcal{F}^s}{\partial t} + \mathbf{v}_s^s \cdot \nabla \mathcal{F}^s = 0. \quad (3.1)$$

Moreover, the ambient air is ignored such that the following traction-free dynamic conditions hold at the free surface,

$$\boldsymbol{\sigma}_f^s \cdot \mathbf{n}^s = 0 \quad \text{and} \quad \boldsymbol{\sigma}_e^s \cdot \mathbf{n}^s = 0, \quad (3.2)$$

where  $\mathbf{n}^s = \nabla \mathcal{F}^s / |\nabla \mathcal{F}^s|$  indicates the exterior unit normal vector of the free surface. The superscript “s” in (3.1) and (3.2), and in the following part of this thesis indicates physical quantities at the free surface.

- (ii) At the **bottom**  $\mathcal{F}^b(x, y, z, t) = z - b(x, y) = 0$ , erosion and deposition are not considered. The kinematic boundary condition is therefore satisfied for each component of the mixture,

$$\mathbf{v}_f^b \cdot \mathbf{n}^b = 0 \quad \text{and} \quad \mathbf{v}_s^b \cdot \mathbf{n}^b = 0, \quad (3.3)$$

indicating the vanishing wall-normal velocity components, where  $\mathbf{n}^b = \nabla \mathcal{F}^b / |\nabla \mathcal{F}^b|$ . The superscript “b” in (3.3) and in the following parts of this thesis indicates physical quantities at the bottom.

Frictional boundary conditions, constraining tangential movement of each component at the bottom, are proposed as follows

$$\boldsymbol{\sigma}_f^b \mathbf{n}^b - (\mathbf{n}^b \cdot \boldsymbol{\sigma}_f^b \mathbf{n}^b) \mathbf{n}^b = k_f^b \phi_f^b \mathbf{v}_f^b, \quad (3.4)$$

$$\boldsymbol{\sigma}_e^b \mathbf{n}^b - (\mathbf{n}^b \cdot \boldsymbol{\sigma}_e^b \mathbf{n}^b) \mathbf{n}^b = -\frac{\mathbf{v}_s^b}{|\mathbf{v}_s^b|} (\mathbf{n}^b \cdot \boldsymbol{\sigma}_e^b \mathbf{n}^b) \mu_s^b, \quad (3.5)$$

where  $k_f^b$  represents bed friction coefficient for the fluid. The bed frictional condition for the fluid phase, (3.4), represents Navier bed slip, which covers ideal slip with  $k_f^b = 0$  and no slip with  $k_f^b = \infty$ . Relation (3.5) is the classical Coulomb friction condition, where the bed granular friction coefficient  $\mu_s^b$  is commonly formulated as  $\mu_s^b = \tan \delta$  with “ $\delta$ ” being the bed friction angle.

## 3.2 Coordinate System and Scaling

A coordinate system must be defined in order to properly investigate the dynamics of flowing grain-fluid mixtures. Additionally, scaling arguments involving geometrical quantities and dynamic quantities are also necessary to define. These aspects are presented in this section.

### 3.2.1 Coordinate System

To investigate gravity-driven flows of grain-fluid mixtures down a slope, an orthogonal curvilinear coordinate system  $Oxyz$  is employed as done in Gray, Wieland &

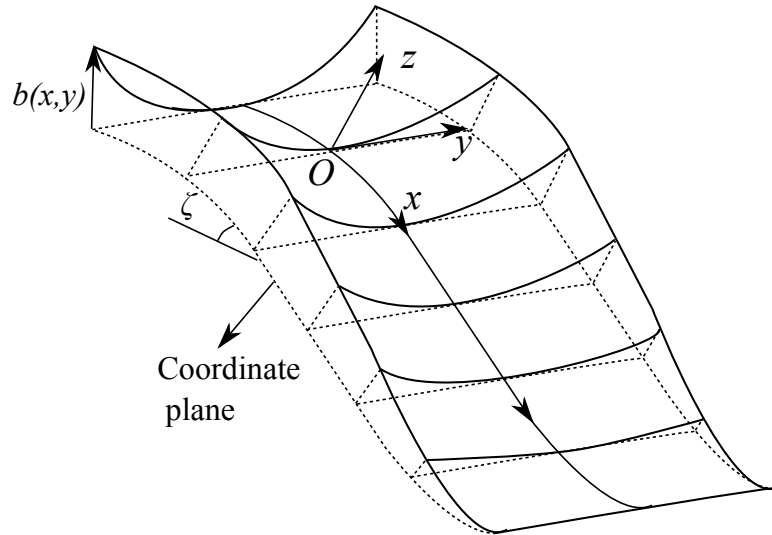


Figure 3.2: Curvilinear coordinate system  $Oxyz$ , where the downslope inclination angle  $\zeta$  relative to the horizontal plane varies as a function of the  $x$ -coordinate. A shallow basal topography with an elevation  $z = b(x, y)$  can be added.

Hutter (1999) and Wang, Hutter & Pudasaini (2004). The  $Ox$  axis follows the mean downslope topography in the main flow direction with an inclination angle  $\zeta$  as a function of the downslope coordinate  $x$ , the  $Oy$  axis is taken to be lateral and straight, and the  $Oz$  axis is normal to the coordinate plane  $Oxy$  (see Fig. 3.2). The curvature of the bed topography is defined as  $\kappa = -d\zeta/dx$ . In addition, a shallow topography with an elevation  $z = b(x, y)$  can be overlapped on the coordinate plane when needed.

The governing equations (2.44)-(2.47) and the prescribed boundary conditions (3.1)-(3.5) need to be explicitly expressed in this orthogonal curvilinear coordinate system. For this purpose, referring to Gray et al. (1999) or Pudasaini & Hutter (2007) who employed a curvilinear coordinate system in the investigation of pure granular flows, the gradient of a scalar field  $F$ , the divergences of a vector field  $\mathbf{l}$  and a symmetry second-order tensor  $\mathbf{N}$  are represented in the present coordinate system in the forms

$$\nabla F = \psi \frac{\partial F}{\partial x} \mathbf{e}_x + \frac{\partial F}{\partial y} \mathbf{e}_y + \frac{\partial F}{\partial z} \mathbf{e}_z, \quad (3.6)$$

$$\nabla \cdot \mathbf{l} = \frac{\partial}{\partial x}(\psi l_x) + \frac{\partial l_y}{\partial y} + \frac{\partial l_z}{\partial z} - \psi^2 \kappa' z l_x - \psi \kappa l_z, \quad (3.7)$$

$$\begin{aligned} \nabla \cdot \mathbf{N} = & \left[ \frac{\partial}{\partial x}(\psi N_{xx}) + \frac{\partial N_{xy}}{\partial y} + \frac{\partial N_{xz}}{\partial z} - \psi^2 \kappa' z N_{xx} - 2\psi \kappa N_{xz} \right] \mathbf{e}_x \\ & + \left[ \frac{\partial}{\partial x}(\psi N_{xy}) + \frac{\partial N_{yy}}{\partial y} + \frac{\partial N_{yz}}{\partial z} - \psi^2 \kappa' z N_{xy} - \psi \kappa N_{yz} \right] \mathbf{e}_y \\ & + \left[ \frac{\partial}{\partial x}(\psi N_{xz}) + \frac{\partial N_{yz}}{\partial y} + \frac{\partial N_{zz}}{\partial z} - \psi^2 \kappa' z N_{xz} - \psi \kappa (N_{zz} - N_{xx}) \right] \mathbf{e}_z, \end{aligned} \quad (3.8)$$

where  $\mathbf{e}_i$  is the unit vector of the  $i$ -axis,  $l_i$  the curvilinear coordinate component of vector  $\mathbf{l}$ , and  $N_{ij}$  ( $i, j \in \{x, y, z\}$ ) the curvilinear coordinate component of the stress tensor  $\mathbf{N}$ . In addition,  $\kappa' = d\kappa/dx$  represents the derivative of the topographic curvature with respect to the downslope coordinate, and the variable

$$\psi = \frac{1}{1 - \kappa z} \quad (3.9)$$

is introduced by the coordinate transformation.

Apart from relations (3.6)-(3.8), the gradient of a vector field  $\mathbf{l}$ , which emerges in the present model due to the Newtonian shear stress for the fluid phase but not in Gray et al. (1999), can be expressed as follows

$$\begin{aligned} \nabla \mathbf{l} = & \left[ \frac{\partial l_x}{\partial x} - \psi \kappa' z l_x - \kappa l_z \right] \psi^{-1} \mathbf{e}_x \otimes \mathbf{e}_x + \psi^{-1} \frac{\partial l_y}{\partial x} \mathbf{e}_x \otimes \mathbf{e}_y \\ & + \left[ \frac{\partial l_z}{\partial x} + \kappa l_x \right] \psi^{-1} \mathbf{e}_x \otimes \mathbf{e}_z + \frac{\partial l_x}{\partial y} \mathbf{e}_y \otimes \mathbf{e}_x + \frac{\partial l_y}{\partial y} \mathbf{e}_y \otimes \mathbf{e}_y \\ & + \frac{\partial l_z}{\partial y} \mathbf{e}_y \otimes \mathbf{e}_z + \left[ \frac{\partial l_x}{\partial z} - \psi \kappa l_x \right] \mathbf{e}_z \otimes \mathbf{e}_x + \frac{\partial l_y}{\partial z} \mathbf{e}_z \otimes \mathbf{e}_y \end{aligned} \quad (3.10)$$



$$+ \frac{\partial t_z}{\partial z} \mathbf{e}_z \otimes \mathbf{e}_z.$$

### 3.2.2 Scalings

To highlight the balance of dominating terms and neglect inessential terms, a set of scaling arguments on the order of physical quantities are necessary. For the convenience of notation, the physical components of velocities  $\mathbf{v}_\eta$  are defined by downslope component  $u_\eta$ , cross-slope  $v_\eta$  and vertical  $w_\eta$ . Similarly, the symmetric components of the solid effective stress tensor are  $\sigma_{e(ii)}$  and  $\sigma_{e(ij)}$  ( $i, j = x, y, z; i \neq j$ ). Then, the following scalings are introduced to non-dimensionalize all the equations

$$\begin{aligned} (x, y, z, t) &= (\mathcal{L}x^*, \mathcal{L}y^*, \mathcal{H}z^*, \sqrt{\mathcal{L}/g}t^*), \\ (u_\eta, v_\eta, w_\eta) &= \sqrt{g\mathcal{L}}(u_\eta^*, v_\eta^*, \epsilon w_\eta^*), \\ (\sigma_{e(ii)}, \sigma_{e(ij)}, p_f) &= \tilde{\rho}_s g \mathcal{H} (\sigma_{e(ii)}^*, \mu_s^b \sigma_{e(ij)}^*, \gamma p_f^*), \\ (\tau_{f(ii)}, \tau_{f(ij)}) &= \mu_f \sqrt{g/\mathcal{L}} (\tau_{f(ii)}^*, \tau_{f(ij)}^*), \\ k_f^b &= (\mu_f/\mathcal{H}) k_f^{b*}, \\ \kappa &= (1/\mathcal{R})\kappa^*, \end{aligned} \tag{3.11}$$

where  $\gamma = \tilde{\rho}_f/\tilde{\rho}_s$  denotes density ratio and the superscript "\*" represents non-dimensional variables. Relation (3.11) indicates that a characteristic horizontal length scale  $\mathcal{L}$ , a characteristic depth scale  $\mathcal{H}$  and a characteristic radius  $\mathcal{R}$  of the curvature are chosen. Assuming a static balance, the bed fluid pressure is of the order  $\tilde{\rho}_f g \mathcal{H}$ , the normal components of the solid effective stress at the base can be estimated to be of order  $\tilde{\rho}_s g \mathcal{H}$ , and the Coulomb shear stress is consequently scaled by  $\tilde{\rho}_s g \mathcal{H} \mu_s^b$  according to the Coulomb friction law. Furthermore, two non-dimensional parameters, the aspect ratio  $\epsilon$  and characteristic curvature  $\lambda$ , are introduced by these scalings, which are

$$\epsilon = \frac{\mathcal{H}}{\mathcal{L}} \quad \text{and} \quad \lambda = \frac{\mathcal{L}}{\mathcal{R}}. \tag{3.12}$$

## 3.3 Nondimensionalization

For the purpose of deriving a set of scale-independent model equations, we non-dimensionalize the governing equations and boundary conditions presented above by applying scalings (3.11). The results are shown below.

### 3.3.1 Non-dimensional conservation equations

The balance equations of mass (2.44) and (2.45) can be represented in the present coordinate system by using (3.7) to explicitly account for  $\nabla \cdot (\phi_\eta \mathbf{v}_\eta)$ . Then, applying (3.11), it follows that the non-dimensional balance equations of mass read

$$\frac{\partial \phi_f}{\partial t} + \frac{\partial}{\partial x}(\phi_f u_f \psi) + \frac{\partial}{\partial y}(\phi_f v_f) + \frac{\partial}{\partial z}(\phi_f w_f) \quad (3.13)$$

$$- \epsilon \lambda \kappa' z \phi_f u_f \psi^2 - \epsilon \lambda \kappa \phi_f w_f \psi = 0,$$

$$\frac{\partial \phi_s}{\partial t} + \frac{\partial}{\partial x}(\phi_s u_s \psi) + \frac{\partial}{\partial y}(\phi_s v_s) + \frac{\partial}{\partial z}(\phi_s w_s) \quad (3.14)$$

$$- \epsilon \lambda \kappa' z \phi_s u_s \psi^2 - \epsilon \lambda \kappa \phi_s w_s \psi = 0,$$

for the fluid and granular components, respectively, where the constant densities  $\tilde{\rho}_f$  and  $\tilde{\rho}_s$  are removed, and the superscript \* indicating non-dimensional quantity is dropped here and in the following for simplicity. The non-dimensional variable  $\psi$ , appearing in (3.13) and (3.14), is written as

$$\psi = \frac{1}{1 - \epsilon \lambda \kappa z}. \quad (3.15)$$

The balance equations of momentum (2.46) and (2.47) can be represented in the present curvilinear coordinates by using (3.10) to express the Newtonian fluid shear stress, (3.6) to transform the fluid pressure gradient, and (3.8) to express  $\nabla \cdot (\phi_\eta \mathbf{v}_\eta \otimes \mathbf{v}_\eta)$ ,  $\nabla \cdot \boldsymbol{\sigma}_e$  and  $\nabla \cdot (\phi_f \tilde{\boldsymbol{\tau}}_f)$ . Applying (3.11), the non-dimensional curvilinear components of the fluid momentum equation (2.46) in the downslope, cross-slope and normal directions are

$$\frac{\partial}{\partial t}(\phi_f u_f) + \frac{\partial}{\partial x}(\phi_f u_f^2 \psi) + \frac{\partial}{\partial y}(\phi_f u_f v_f) + \frac{\partial}{\partial z}(\phi_f u_f w_f) \quad (3.16)$$

$$\begin{aligned} &= \phi_f \sin \zeta - \vartheta \phi_f^2 (u_f - u_s) - \epsilon \psi \phi_f \frac{\partial p_f}{\partial x} + \epsilon \lambda \kappa' z \phi_f u_f^2 \psi^2 + 2\epsilon \lambda \kappa \phi_f u_f w_f \psi \\ &+ \frac{\epsilon}{N_R} \left[ \frac{\partial}{\partial x}(\tau_{f(xx)}) + \frac{\partial}{\partial y}(\tau_{f(xy)}) + \frac{\partial}{\partial z}(\tau_{f(xz)}) \right] \\ &+ \epsilon^2 \lambda \kappa' z (N_R)^{-1} \tau_{f(xx)} \psi^2 + 2\epsilon \lambda \kappa (N_R)^{-1} \tau_{f(xz)} \psi, \end{aligned}$$

$$\frac{\partial}{\partial t}(\phi_f v_f) + \frac{\partial}{\partial x}(\phi_f u_f v_f \psi) + \frac{\partial}{\partial y}(\phi_f v_f^2) + \frac{\partial}{\partial z}(\phi_f v_f w_f) \quad (3.17)$$

$$\begin{aligned} &= -\vartheta \phi_f^2 (v_f - v_s) - \epsilon \phi_f \frac{\partial p_f}{\partial y} + \epsilon \lambda \kappa' z \phi_f u_f v_f \psi^2 + \epsilon \lambda \kappa \phi_f v_f w_f \psi \\ &+ \frac{\epsilon}{N_R} \left[ \frac{\partial}{\partial x}(\tau_{f(yx)}) + \frac{\partial}{\partial y}(\tau_{f(yy)}) + \frac{\partial}{\partial z}(\tau_{f(yz)}) \right] \\ &+ \epsilon^2 \lambda \kappa' z (N_R)^{-1} \tau_{f(yx)} \psi^2 + \epsilon \lambda \kappa (N_R)^{-1} \tau_{f(yz)} \psi, \end{aligned}$$

$$\begin{aligned}
& \epsilon \left[ \frac{\partial}{\partial t}(\phi_f w_f) + \frac{\partial}{\partial x}(\phi_f u_f w_f \psi) + \frac{\partial}{\partial y}(\phi_f v_f w_f) + \frac{\partial}{\partial z}(\phi_f w_f^2) \right] + \lambda \psi \kappa \phi_f u_f^2 \quad (3.18) \\
& = -\phi_f \cos \zeta - \epsilon \vartheta \phi_f^2 (w_f - w_s) - \phi_f \frac{\partial p_f}{\partial z} + \epsilon^2 \lambda \phi_f \psi (\kappa' z u_f \psi + \kappa w_f) w_f \\
& \quad + \frac{\epsilon}{N_R} \left[ \frac{\partial}{\partial x}(\tau_{f(zx)}) + \frac{\partial}{\partial y}(\tau_{f(zy)}) + \frac{\partial}{\partial z}(\tau_{f(zz)}) \right] \\
& \quad + \epsilon^2 \lambda \kappa' z (N_R)^{-1} \tau_{f(zx)} \psi^2 + \epsilon \lambda \kappa (N_R)^{-1} (\tau_{f(zz)} - \tau_{f(xx)}) \psi,
\end{aligned}$$

respectively, where the variable  $\vartheta$  inside the drag force term is expressed as

$$\vartheta = \frac{\mu_f \sqrt{\mathcal{L}}}{\tilde{\rho}_f k \sqrt{g}}, \quad (3.19)$$

and the dynamic parameter  $N_R$  inside the viscous forces is defined as

$$N_R = \frac{\tilde{\rho}_f \mathcal{H} \sqrt{g \mathcal{L}}}{\mu_f \phi_f}, \quad (3.20)$$

whose form is analogous to the Reynolds number in Newtonian fluid mechanics, see Iverson & Denlinger (2001).

Similarly, for the granular phase, by virtue of the scaling (3.11), the downslope, cross-slope and normal non-dimensional components of the momentum equation (2.47) read,

$$\begin{aligned}
& \frac{\partial}{\partial t}(\phi_s u_s) + \frac{\partial}{\partial x}(\phi_s u_s^2 \psi) + \frac{\partial}{\partial y}(\phi_s u_s v_s) + \frac{\partial}{\partial z}(\phi_s u_s w_s) \quad (3.21) \\
& = -\epsilon \frac{\partial}{\partial x}(\sigma_{e(xx)} \psi) - \epsilon \mu_s^b \frac{\partial}{\partial y}(\sigma_{e(xy)}) - \mu_s^b \frac{\partial}{\partial z}(\sigma_{e(xz)}) - \epsilon \psi \gamma \phi_s \frac{\partial p_f}{\partial x} + \gamma \vartheta \phi_f^2 (u_f - u_s) \\
& \quad + \phi_s \sin \zeta + \epsilon \lambda \kappa' z \phi_s u_s^2 \psi^2 + 2\epsilon \lambda \kappa \phi_s u_s w_s \psi + \epsilon^2 \lambda \kappa' z \sigma_{e(xx)} \psi^2 + 2\epsilon \lambda \kappa \mu_s^b \sigma_{e(xz)} \psi,
\end{aligned}$$

$$\begin{aligned}
& \frac{\partial}{\partial t}(\phi_s v_s) + \frac{\partial}{\partial x}(\phi_s u_s v_s \psi) + \frac{\partial}{\partial y}(\phi_s v_s^2) + \frac{\partial}{\partial z}(\phi_s v_s w_s) \quad (3.22) \\
& = -\epsilon \mu_s^b \frac{\partial}{\partial x}(\sigma_{e(yx)} \psi) - \epsilon \frac{\partial}{\partial y}(\sigma_{e(yy)}) - \mu_s^b \frac{\partial}{\partial z}(\sigma_{e(yz)}) - \epsilon \gamma \phi_s \frac{\partial p_f}{\partial y} + \gamma \vartheta \phi_f^2 (v_f - v_s) \\
& \quad + \epsilon \lambda \kappa' z \phi_s u_s v_s \psi^2 + \epsilon \lambda \kappa \phi_s v_s w_s \psi + \epsilon^2 \lambda \mu_s^b \kappa' z \sigma_{e(yx)} \psi^2 + \epsilon \lambda \mu_s^b \kappa \sigma_{e(yz)} \psi,
\end{aligned}$$

$$\begin{aligned}
& \epsilon \left[ \frac{\partial}{\partial t}(\phi_s w_s) + \frac{\partial}{\partial x}(\phi_s u_s w_s \psi) + \frac{\partial}{\partial y}(\phi_s v_s w_s) + \frac{\partial}{\partial z}(\phi_s w_s^2) \right] + \lambda \psi \kappa \phi_s u_s^2 \quad (3.23) \\
& = -\epsilon \mu_s^b \frac{\partial}{\partial x}(\sigma_{e(zx)} \psi) - \epsilon \mu_s^b \frac{\partial}{\partial y}(\sigma_{e(zy)}) - \frac{\partial}{\partial z}(\sigma_{e(zz)}) - \gamma \phi_s \frac{\partial p_f}{\partial z} + \epsilon \gamma \vartheta \phi_f^2 (w_f - w_s) \\
& \quad - \phi_s \cos \zeta + \epsilon^2 \lambda \kappa' z \phi_s u_s w_s \psi^2 + \epsilon^2 \lambda \kappa w_s^2 \psi + \epsilon^2 \lambda \kappa' z \sigma_{e(zx)} \psi^2 + \epsilon \lambda \kappa (\sigma_{e(zz)} - \sigma_{e(xx)}) \psi.
\end{aligned}$$

### 3.3.2 Non-dimensional Boundary Conditions

(i) Non-dimensional boundary conditions at the free surface

By virtue of the scaling (3.11), the non-dimensional forms of the kinematic boundary condition (3.1) at the top free surface read

$$\frac{\partial s}{\partial t} + u_f^s \psi^s \frac{\partial s}{\partial x} + v_f^s \frac{\partial s}{\partial y} - w_f^s = 0, \quad (3.24)$$

$$\frac{\partial s}{\partial t} + u_s^s \psi^s \frac{\partial s}{\partial x} + v_s^s \frac{\partial s}{\partial y} - w_s^s = 0. \quad (3.25)$$

In addition, the downslope, cross-slope and normal non-dimensional components of the dynamic boundary condition (3.2) read, for the fluid component,

$$\epsilon \left[ -\phi_f^s p_f^s N_R^s + \tau_{f(xx)}^s \right] \psi^s \frac{\partial s}{\partial x} + \epsilon \tau_{f(xy)}^s \frac{\partial s}{\partial y} - \tau_{f(xz)}^s = 0, \quad (3.26)$$

$$\epsilon \tau_{f(xy)}^s \psi^s \frac{\partial s}{\partial x} + \epsilon \left[ -\phi_f^s p_f^s N_R^s + \epsilon \tau_{f(yy)}^s \right] \frac{\partial s}{\partial y} - \tau_{f(xz)}^s = 0, \quad (3.27)$$

$$\epsilon \tau_{f(xz)}^s \psi^s \frac{\partial s}{\partial x} + \epsilon \tau_{f(zy)}^s \frac{\partial s}{\partial y} - \left[ -\phi_f^s p_f^s N_R^s + \tau_{f(zz)}^s \right] = 0, \quad (3.28)$$

where  $N_R^s = \tilde{\rho}_f \mathcal{H} \sqrt{g\mathcal{L}} / (\mu_f \phi_f^s)$ , and for the granular component,

$$\epsilon \sigma_{e(xx)}^s \psi^s \frac{\partial s}{\partial x} + \epsilon \mu_s^b \sigma_{e(xy)}^s \frac{\partial s}{\partial y} - \mu_s^b \sigma_{e(xz)}^s = 0, \quad (3.29)$$

$$\epsilon \mu_s^b \sigma_{e(yx)}^s \psi^s \frac{\partial s}{\partial x} + \epsilon \sigma_{e(yy)}^s \frac{\partial s}{\partial y} - \mu_s^b \sigma_{e(yz)}^s = 0, \quad (3.30)$$

$$\epsilon \mu_s^b \sigma_{e(zx)}^s \psi^s \frac{\partial s}{\partial x} + \epsilon \mu_s^b \sigma_{e(zy)}^s \frac{\partial s}{\partial y} - \sigma_{e(zz)}^s = 0, \quad (3.31)$$

respectively.

Consistent with relations (3.26)-(3.28), we postulate that the pore fluid pressure and shear-stress components vanish at the free surface, which are

$$p_f^s = 0, \quad \text{and} \quad \tau_{f(ij)}^s = 0, \quad (3.32)$$

where  $i, j \in (x, y, z)$ .

(ii) Non-dimensional boundary conditions at the bottom

Similarly, at the bottom, the non-dimensional forms of the kinematic boundary condition (3.3) for each constituent can be derived as follows:

$$u_s^b \psi^b \frac{\partial b}{\partial x} + v_s^b \frac{\partial b}{\partial y} - w_s^b = 0 \quad \text{and} \quad u_f^b \psi^b \frac{\partial b}{\partial x} + v_f^b \frac{\partial b}{\partial y} - w_f^b = 0, \quad (3.33)$$

where  $\psi^b = (1 - \epsilon \lambda \kappa b)^{-1}$ .

For the fluid component, the downslope, cross-slope and normal non-dimensional components of the bed friction condition (3.4) are

$$\epsilon \left[ -\phi_f^b p_f^b N_R^b + \tau_{f(xx)}^b \right] \psi^b \frac{\partial b}{\partial x} + \epsilon \tau_{f(xy)}^b \frac{\partial b}{\partial y} - \tau_{f(xz)}^b \quad (3.34)$$

$$= -k_f^b \Delta_b \epsilon^{-1} u_f^b + \epsilon (\mathbf{n}^b \cdot \boldsymbol{\sigma}_f^b \mathbf{n}^b) \psi^b \frac{\partial b}{\partial x},$$

$$\epsilon \tau_{f(xy)}^b \psi^b \frac{\partial b}{\partial x} + \epsilon \left[ -\phi_f^b p_f^b N_R^b + \tau_{f(yy)}^b \right] \frac{\partial b}{\partial y} - \tau_{f(yz)}^b \quad (3.35)$$

$$= -k_f^b \Delta_b \epsilon^{-1} v_f^b + \epsilon (\mathbf{n}^b \cdot \boldsymbol{\sigma}_f^b \mathbf{n}^b) \frac{\partial b}{\partial y},$$

$$\epsilon \tau_{f(zx)}^b \psi^b \frac{\partial b}{\partial x} + \epsilon \tau_{f(zy)}^b \frac{\partial b}{\partial y} - \left[ -\phi_f^b p_f^b N_R^b + \tau_{f(zz)}^b \right] \quad (3.36)$$

$$= -k_f^b \Delta_b w_f^b - (\mathbf{n}^b \cdot \boldsymbol{\sigma}_f^b \mathbf{n}^b),$$

respectively, where  $N_R^b = \tilde{\rho}_f \mathcal{H} \sqrt{g \mathcal{L}} / (\mu_f \phi_f^b)$ , and the normalization factor  $\Delta_b$  is

$$\Delta_b = \left[ 1 + \epsilon^2 (\psi^b)^2 \left( \frac{\partial b}{\partial x} \right)^2 + \epsilon^2 \left( \frac{\partial b}{\partial y} \right)^2 \right]^{1/2}. \quad (3.37)$$

Analogously, the downslope, cross-slope and normal non-dimensional components of the granular bed friction boundary condition (3.5) read

$$\epsilon \sigma_{e(xx)}^b \psi^b \frac{\partial b}{\partial x} + \epsilon \mu_s^b \sigma_{e(xy)}^b \frac{\partial b}{\partial y} - \mu_s^b \sigma_{e(xz)}^b \quad (3.38)$$

$$= (\mathbf{n}^b \cdot \boldsymbol{\sigma}_e^b \mathbf{n}^b) \left[ \Delta_b \frac{u_s^b}{|\mathbf{v}_s^b|} \mu_s^b + \epsilon \psi^b \frac{\partial b}{\partial x} \right],$$

$$\epsilon \mu_s^b \sigma_{e(yx)}^b \psi^b \frac{\partial b}{\partial x} + \epsilon \sigma_{e(yy)}^b \frac{\partial b}{\partial y} - \mu_s^b \sigma_{e(yz)}^b \quad (3.39)$$

$$= (\mathbf{n}^b \cdot \boldsymbol{\sigma}_e^b \mathbf{n}^b) \left[ \Delta_b \frac{v_s^b}{|\mathbf{v}_s^b|} \mu_s^b + \epsilon \frac{\partial b}{\partial y} \right],$$

$$\epsilon \mu_s^b \sigma_{e(zx)}^b \psi^b \frac{\partial b}{\partial x} + \epsilon \mu_s^b \sigma_{e(zy)}^b \frac{\partial b}{\partial y} - \sigma_{e(zz)}^b \quad (3.40)$$

$$= (\mathbf{n}^b \cdot \boldsymbol{\sigma}_e^b \mathbf{n}^b) \left[ \Delta_b \frac{\epsilon w_s^b}{|\mathbf{v}_s^b|} \mu_s^b - 1 \right],$$

respectively.

### 3.4 Ordering

Typical geometry of the flowing grain-fluid mixture indicates that the flow depth is usually much smaller than the flow length. As a result,  $\epsilon = \mathcal{H}/\mathcal{L} \ll 1$  can be reasonably stipulated. In addition,  $0 < \lambda = \mathcal{L}/\mathcal{R} < 1$  can be generally satisfied, though it may be violated locally due to the fact that the downslope inclination angle of the

reference surface  $\zeta$  may change rapidly (Chiou, Wang & Hutter 2005). The typical bed friction angle  $\delta$  is normally between  $20^\circ$  and  $40^\circ$ , therefore  $0 < \mu_s^b = \tan \delta < 1$  holds. With these descriptions, we assume

$$\lambda = \mathcal{O}(\epsilon^\alpha), \quad \mu_s^b = \mathcal{O}(\epsilon^\ell) \quad (3.41)$$

as done in several previous studies (see Chiou et al. (2005), Gray et al. (1999), Pudasaini & Hutter (2007), etc.). In addition, by virtue of (3.41) and Taylor series expansion, the variable  $\psi$  defined in (3.15) can be written as

$$\psi = 1 + \mathcal{O}(\epsilon^{1+\alpha}) \quad (3.42)$$

in terms of aspect ratio  $\epsilon$ . To simplify the fluid and granular momentum equations, the orders of the parameter  $N_R$  and the function  $\Delta_b$  also need to be prescribed. For typical natural geophysical flows,  $\mathcal{H}$  normally exceeds 1 m and  $\mathcal{L}$  normally exceeds tens of meters. Consequently, we stipulate

$$N_R = \mathcal{O}(\epsilon^{-2}). \quad (3.43)$$

Following (3.37), the function  $\Delta_b$  can be written as

$$\Delta_b = 1 + \mathcal{O}(\epsilon^2) \quad (3.44)$$

in terms of aspect ratio.

### 3.5 Depth-averaged theory

Physical reasonings allow further simplification of the three-dimensional non-dimensional governing equations and boundary conditions by performing the depth-integration technique. Before integrating the balance equations, some definitions are described. First, the mixture depth between the bottom  $z = b(x, y, t)$  and the free surface  $z = s(x, y, t)$  is given by

$$h_m(x, y, t) = s - b. \quad (3.45)$$

Then, it is useful to define the mean value of a quantity  $q(x, y, z, t)$  through the mixture depth as

$$\bar{q}(x, y, t) = \frac{1}{h_m} \int_b^s q(x, y, z, t) dz, \quad (3.46)$$

where the overbar denotes the depth-averaged quantities. When depth integration is performed, the Leibnitz rule must be applied that indicates

$$\frac{\partial}{\partial t} \int_b^s q dz = \int_b^s \frac{\partial q}{\partial t} dz + \left[ q \frac{\partial z}{\partial t} \right]_b^s, \quad (3.47)$$

where  $[\cdot]_b^s$  represents the difference of a function between at the free surface and at the bottom.

Additionally, the distribution of the volume fractions along the depth direction need to be prescribed. To this end, motivated by the experimental data of Egashira, Itoh & Takeuchi (2001), we postulate that the volume fraction is uniformly distributed throughout the mixture depth, which indicates

$$\phi_s \approx \bar{\phi}_s, \quad \phi_f \approx \bar{\phi}_f. \quad (3.48)$$

Integrating the mass equations (3.13) and (3.14) over the mixture depth, applying the Leibnitz rule (3.47) to swap the order of integration and differentiation, using the kinematic boundary conditions (3.24), (3.25), and (3.33) to simplify the terms at the free surface and at the bottom, the depth-averaged mass equations for the fluid and granular components can be derived, and take the form

$$\begin{aligned} \frac{\partial}{\partial t}(h_m \bar{\phi}_f) + \frac{\partial}{\partial x}(h_m \bar{\phi}_f \bar{u}_f) + \frac{\partial}{\partial y}(h_m \bar{\phi}_f \bar{v}_f) \\ - h_m \lambda \epsilon \kappa' \overline{\psi^2 z \phi_f u_f} - h_m \lambda \epsilon \kappa \overline{\psi \phi_f w_f} = 0, \end{aligned} \quad (3.49)$$

$$\begin{aligned} \frac{\partial}{\partial t}(h_m \bar{\phi}_s) + \frac{\partial}{\partial x}(h_m \bar{\phi}_s \bar{u}_s) + \frac{\partial}{\partial y}(h_m \bar{\phi}_s \bar{v}_s) \\ - h_m \lambda \epsilon \kappa' \overline{\psi^2 z \phi_s u_s} - h_m \lambda \epsilon \kappa \overline{\psi \phi_s w_s} = 0. \end{aligned} \quad (3.50)$$

Applying the above orderings (3.41) and (3.42), it follows that the depth-averaged mass equations (3.49) and (3.50) reduce to

$$\frac{\partial}{\partial t}(h_m \bar{\phi}_f) + \frac{\partial}{\partial x}(h_m \bar{\phi}_f \bar{u}_f) + \frac{\partial}{\partial y}(h_m \bar{\phi}_f \bar{v}_f) = \mathcal{O}(\epsilon^{1+\alpha}), \quad (3.51)$$

$$\frac{\partial}{\partial t}(h_m \bar{\phi}_s) + \frac{\partial}{\partial x}(h_m \bar{\phi}_s \bar{u}_s) + \frac{\partial}{\partial y}(h_m \bar{\phi}_s \bar{v}_s) = \mathcal{O}(\epsilon^{1+\alpha}). \quad (3.52)$$

Similar to derive (3.49) and (3.50), integrating the momentum equations (3.16)-(3.18), applying Leibnitz rule (3.47) to swap the orders of integration and differentiation, and substituting boundary conditions (3.24), (3.26)-(3.28), and (3.33)- (3.36) into the results lead that the depth-averaged balance equations of the fluid momentum in the downslope, cross-slope, and normal direction are given by

$$\begin{aligned} \frac{\partial}{\partial t}(h_m \bar{\phi}_f \bar{u}_f) + \frac{\partial}{\partial x}(h_m \bar{\phi}_f \overline{u_f^2 \psi}) + \frac{\partial}{\partial y}(h_m \bar{\phi}_f \overline{u_f v_f \psi}) - \epsilon \lambda \kappa' h_m \overline{z \phi_f u_f^2 \psi^2} - 2 \epsilon \lambda \kappa h_m \overline{\phi_f u_f w_f \psi} \\ = \epsilon (\mathbf{n}^b \cdot \boldsymbol{\sigma}_f^b \mathbf{n}^b) \psi^b \frac{\partial b}{\partial x} - h_m \bar{\phi}_f^2 \vartheta (\bar{u}_f - \bar{u}_s) + h_m \bar{\phi}_f \sin \zeta - k_f^b \Delta_b u_f^b / (\epsilon N_R^b) \\ - \epsilon \bar{\phi}_f \frac{\partial}{\partial x}(h_m \overline{p_f \psi}) + \frac{\epsilon}{N_R} \frac{\partial}{\partial x}(h_m \bar{\tau}_{f(xx)}) + \frac{\epsilon}{N_R} \frac{\partial}{\partial y}(h_m \bar{\tau}_{f(xy)}) \\ + \frac{\epsilon^2}{N_R} \lambda \kappa' h_m \overline{z \tau_{f(xx)} \psi^2} + \frac{2\epsilon}{N_R} \lambda \kappa h_m \overline{\tau_{f(xz)} \psi}, \end{aligned} \quad (3.53)$$

$$\begin{aligned}
 & \frac{\partial}{\partial t}(h_m \bar{\phi}_f \bar{v}_f) + \frac{\partial}{\partial x}(h_m \bar{\phi}_f \overline{u_f v_f \psi}) + \frac{\partial}{\partial y}(h_m \bar{\phi}_f \bar{v}_f^2) - \epsilon \lambda \kappa' h_m \overline{z \phi_f u_f v_f \psi^2} - \epsilon \lambda \kappa h_m \overline{\phi_f v_f w_f \psi} \\
 &= \epsilon (\mathbf{n}^b \cdot \boldsymbol{\sigma}_f^b \mathbf{n}^b) \psi^b \frac{\partial b}{\partial y} - h_m \bar{\phi}_f^2 \vartheta (\bar{v}_f - \bar{v}_s) - k_f^b \Delta_b v_f^b / (\epsilon N_R^b) \\
 & \quad - \epsilon \bar{\phi}_f \frac{\partial}{\partial y}(h_m \bar{p}_f) + \frac{\epsilon}{N_R} \frac{\partial}{\partial x}(h_m \bar{\tau}_{f(yx)}) + \frac{\epsilon}{N_R} \frac{\partial}{\partial y}(h_m \bar{\tau}_{f(yy)}) \\
 & \quad + \frac{\epsilon}{N_R} \lambda \kappa \overline{\tau_{f(yz)} \psi} + \frac{\epsilon}{N_R} \epsilon^2 \lambda \kappa' h_m \overline{z \tau_{f(yx)} \psi^2}, \tag{3.54}
 \end{aligned}$$

$$\begin{aligned}
 & \epsilon \left[ \frac{\partial}{\partial t}(h_m \bar{\phi}_f \bar{w}_f) + \frac{\partial}{\partial x}(h_m \bar{\phi}_f \overline{u_f w_f \psi}) + \frac{\partial}{\partial y}(h_m \bar{\phi}_f \overline{v_f w_f \psi}) \right] + \lambda \kappa h_m \bar{\phi}_f \overline{u_f^2 \psi} - \epsilon^2 \lambda \kappa' h_m \bar{\phi}_f \overline{z u_f w_f \psi^2} \\
 &= -(\mathbf{n}^b \cdot \boldsymbol{\sigma}_f^b \mathbf{n}^b) - \epsilon h_m \bar{\phi}_f^2 \vartheta (\bar{w}_f - \bar{w}_s) - h_m \bar{\phi}_f \cos \zeta - k_f^b \Delta_b w_f^b / N_R^b \\
 & \quad + \frac{\epsilon}{N_R} \frac{\partial}{\partial x}(h_m \bar{\tau}_{f(zx)}) + \frac{\epsilon}{N_R} \frac{\partial}{\partial y}(h_m \bar{\tau}_{f(zy)}) + \epsilon^2 \lambda \kappa h_m \bar{\phi}_f \overline{w_f^2 \psi} \\
 & \quad + \frac{\epsilon^2}{N_R} \lambda \kappa' h_m \overline{z \tau_{f(zx)} \psi^2} + \frac{\epsilon^2}{N_R} \lambda \kappa \overline{\tau_{f(zz)} \psi} + \bar{\phi}_f p_f^b. \tag{3.55}
 \end{aligned}$$

Integrating (3.21)-(3.23) leads that the downslope, cross-slope, and normal components of the depth-averaged granular momentum equations take the form

$$\begin{aligned}
 & \frac{\partial}{\partial t}(h_m \bar{\phi}_s \bar{u}_s) + \frac{\partial}{\partial x}(h_m \bar{\phi}_s \overline{u_s^2 \psi}) + \frac{\partial}{\partial y}(h_m \bar{\phi}_s \overline{u_s v_s \psi}) - \epsilon \lambda \kappa' h_m \overline{z \phi_s u_s^2 \psi^2} - 2\epsilon \lambda \kappa h_m \overline{\phi_s u_s w_s \psi} \\
 &= -(\mathbf{n}^b \cdot \boldsymbol{\sigma}_e^b \mathbf{n}^b) \left[ \Delta_b \frac{u_s^b}{|\mathbf{v}_s^b|} \mu_s^b + \epsilon \psi^b \frac{\partial b}{\partial x} \right] + \gamma h_m \bar{\phi}_f^2 \vartheta (\bar{u}_f - \bar{u}_s) + h_m \bar{\phi}_s \sin \zeta \\
 & \quad - \epsilon \frac{\partial}{\partial x}(h_m \overline{\sigma_{e(xx)} \psi}) - \epsilon \mu_s^b \frac{\partial}{\partial y}(h_m \overline{\sigma_{e(xy)} \psi}) - \epsilon \gamma \bar{\phi}_s \frac{\partial}{\partial x}(h_m \overline{p_f \psi}) \\
 & \quad + \epsilon^2 \lambda \kappa' h_m \overline{z \sigma_{e(xx)} \psi^2} + 2\epsilon \lambda \kappa \mu_s^b \overline{\sigma_{e(xz)} \psi} - \epsilon \gamma \bar{\phi}_s p_f^b \psi^b \frac{\partial b}{\partial x}, \tag{3.56}
 \end{aligned}$$

$$\begin{aligned}
 & \frac{\partial}{\partial t}(h_m \bar{\phi}_s \bar{v}_s) + \frac{\partial}{\partial x}(h_m \bar{\phi}_s \overline{u_s v_s \psi}) + \frac{\partial}{\partial y}(h_m \bar{\phi}_s \bar{v}_s^2) - \epsilon \lambda \kappa' h_m \overline{z \phi_s u_s v_s \psi^2} - \epsilon \lambda \kappa h_m \overline{\phi_s v_s w_s \psi} \\
 &= -(\mathbf{n}^b \cdot \boldsymbol{\sigma}_e^b \mathbf{n}^b) \left[ \Delta_b \frac{v_s^b}{|\mathbf{v}_s^b|} \mu_s^b + \epsilon \psi^b \frac{\partial b}{\partial y} \right] + \gamma h_m \bar{\phi}_f^2 \vartheta (\bar{v}_f - \bar{v}_s) \\
 & \quad - \epsilon \mu_s^b \frac{\partial}{\partial x}(h_m \overline{\sigma_{e(yx)} \psi}) - \epsilon \frac{\partial}{\partial y}(h_m \overline{\sigma_{e(yy)} \psi}) - \epsilon \gamma \bar{\phi}_s \frac{\partial}{\partial y}(h_m \bar{p}_f), \\
 & \quad + \epsilon^2 \lambda \mu_s^b \kappa' h_m \overline{z \sigma_{e(yx)} \psi^2} + \epsilon \lambda \mu_s^b \kappa h_m \overline{\sigma_{e(yz)} \psi} - \epsilon \gamma \bar{\phi}_s p_f^b \frac{\partial b}{\partial y}, \tag{3.57}
 \end{aligned}$$

$$\begin{aligned}
 & \epsilon \left[ \frac{\partial}{\partial t}(h_m \bar{\phi}_s \bar{w}_s) + \frac{\partial}{\partial x}(h_m \bar{\phi}_s \overline{u_s w_s \psi}) + \frac{\partial}{\partial y}(h_m \bar{\phi}_s \overline{v_s w_s \psi}) \right] + \lambda \psi \kappa h_m \bar{\phi}_s \overline{u_s^2 \psi} - \epsilon^2 \lambda \kappa' h_m \overline{z \phi_s u_s w_s \psi^2} \\
 &= -(\mathbf{n}^b \cdot \boldsymbol{\sigma}_e^b \mathbf{n}^b) \left[ \Delta_b \frac{\epsilon w_s^b}{|\mathbf{v}_s^b|} \mu_s^b - 1 \right] + \gamma h_m \bar{\phi}_f^2 \vartheta (\bar{w}_f - \bar{w}_s) - h_m \bar{\phi}_s \cos \zeta \\
 & \quad - \epsilon \mu_s^b \frac{\partial}{\partial x}(h_m \overline{\sigma_{e(zx)} \psi}) - \epsilon \mu_s^b \frac{\partial}{\partial y}(h_m \overline{\sigma_{e(zy)} \psi}) + \epsilon^2 \lambda \kappa h_m \overline{w_s^2 \psi}
 \end{aligned}$$



$$+ \epsilon^2 \lambda \mu_s^b \kappa' h_m \overline{z \sigma_{e(zx)} \psi^2} + \epsilon \lambda \kappa h_m \overline{\sigma_{e(zz)} - \sigma_{g(xx)}} \psi + \gamma \bar{\phi}_s p^b. \quad (3.58)$$

### 3.5.1 Evaluation of the pore pressure and shear stress

To streamline the momentum balances (3.53)-(3.55), it is indispensable to explicitly formulate the pore pressure  $p_f$  and the depth-averaged fluid shear stress  $\bar{\tau}_{ij}$  ( $i, j \in \{x, y, z\}$ ), which are presented as follows.

To evaluate the pore fluid pressure, we appeal to the normal component (3.18) of the fluid momentum equations. Equation (3.18) indicates that the inertial terms ( $\sim \mathcal{O}(\epsilon)$ ) and the viscous stresses ( $\sim \mathcal{O}(\epsilon^3)$ ) are small quantities in relation to the gravity normal component and the gradient of the pore fluid pressure ( $\sim \mathcal{O}(1)$ ). Additionally, it is necessary to evaluate the order of the normal component  $-\epsilon \phi_f^2 \vartheta(w_f - w_s)$  of the drag force appearing in (3.18). Provided that the normal velocity difference  $w_f - w_s$  is negligibly small, it is expected that the drag force will have a negligible effect on the evolution of the pore fluid pressure. In this chapter, we postulate  $w_f - w_s \sim \mathcal{O}(\epsilon)$  for simplicity and scrutinize this postulation later by comparing the model predictions with the experimental data. Actually, this postulation is very commonly used in previous literatures (see Pitman & Le (2005) and Pudasaini (2012)). With these descriptions, the normal component (3.18) of the fluid momentum equations reduces to

$$\lambda \kappa \phi_f u_f^2 + \phi_f \cos \zeta + \phi_f \frac{\partial p_f}{\partial z} = \mathcal{O}(\epsilon). \quad (3.59)$$

Vertical integration of (3.59) from the bottom to the position  $z(x, y, t)$  yields

$$p_f(x, y, z, t) = (s - z) \cos \zeta + \lambda \kappa (s - z) \overline{u_f^2} + \mathcal{O}(\epsilon), \quad (3.60)$$

which is corrected to order  $\epsilon$ , or

$$p_f(x, y, z, t) = (s - z) \cos \zeta + \mathcal{O}(\epsilon^\alpha) \quad (3.61)$$

that is corrected to order  $\epsilon^\alpha$ . Moreover, the fluid normal stress ( $\mathbf{n}^b \cdot \boldsymbol{\sigma}_f^b \mathbf{n}^b$ ) corrected to order  $\mathcal{O}(\epsilon)$  at the bottom can be derived by approximating (3.55). It is given by

$$(\mathbf{n}^b \cdot \boldsymbol{\sigma}_f^b \mathbf{n}^b) = h_m \phi_f \cos \zeta + \mathcal{O}(\epsilon^\alpha). \quad (3.62)$$

Substituting (3.61) into the pressure term, arising in (3.53) and (3.54), yields

$$\begin{aligned} \epsilon \bar{\phi}_f \frac{\partial}{\partial x} (h_m \overline{p_f \psi}) &= \epsilon \bar{\phi}_f \frac{\partial}{\partial x} \left( \frac{1}{2} h_m^2 \cos \zeta \right) + \mathcal{O}(\epsilon^{1+\alpha}), \\ \epsilon \bar{\phi}_f \frac{\partial}{\partial y} (h_m \overline{p_f}) &= \epsilon \bar{\phi}_f \frac{\partial}{\partial y} \left( \frac{1}{2} h_m^2 \cos \zeta \right) + \mathcal{O}(\epsilon^{1+\alpha}). \end{aligned} \quad (3.63)$$

For the fluid shear stress, by substituting the constitutive relation into the shear stress terms, we obtain

$$\frac{\partial}{\partial x}(h_m \bar{\tau}_{f(xx)}) \approx 2h_m \frac{\partial^2 \bar{u}_f}{\partial x^2}, \quad \frac{\partial}{\partial y}(h_m \bar{\tau}_{f(xy)}) \approx h_m \frac{\partial^2 \bar{u}_f}{\partial y^2} + h_m \frac{\partial^2 \bar{v}_f}{\partial x \partial y}, \quad (3.64)$$

and

$$\frac{\partial}{\partial y}(h_m \bar{\tau}_{f(yy)}) \approx 2h_m \frac{\partial^2 \bar{v}_f}{\partial y^2}, \quad \frac{\partial}{\partial x}(h_m \bar{\tau}_{f(yx)}) \approx h_m \frac{\partial^2 \bar{v}_f}{\partial x^2} + h_m \frac{\partial^2 \bar{u}_f}{\partial x \partial y}, \quad (3.65)$$

where we used the shallow-water approximations  $\partial h_m / \partial x \approx 0$  and  $\partial h_m / \partial y \approx 0$  which allow to take the depth  $h_m$  out of the differentiation (see Denlinger & Iverson (2001)). To proceed, approximating (3.53) and (3.54) to order  $1 + \mathcal{O}(\epsilon^{1+\alpha})$ , and combining the result with (3.62)-(3.65) allow us to derive the following depth-averaged balance equations of momentum for the fluid phase

$$\begin{aligned} & \frac{\partial}{\partial t}(h_m \bar{\phi}_f \bar{u}_f) + \frac{\partial}{\partial x}(h_m \bar{\phi}_f \bar{u}_f^2) + \frac{\partial}{\partial y}(h_m \bar{\phi}_f \bar{u}_f \bar{v}_f) \\ &= h_m \bar{\phi}_f \sin \zeta + \frac{\epsilon h_m}{N_R} \left[ 2 \frac{\partial^2 \bar{u}_f}{\partial x^2} + \frac{\partial}{\partial y} \left( \frac{\partial \bar{v}_f}{\partial x} + \frac{\partial \bar{u}_f}{\partial y} \right) - \frac{k_f^b u_f^b}{\epsilon^2 h_m} \right] - \epsilon \bar{\phi}_f \frac{\partial}{\partial x} \left( \frac{h_m^2 \cos \zeta}{2} \right) \\ & \quad - h_m \bar{\phi}_f^2 \vartheta (\bar{u}_f - \bar{u}_s) - \epsilon h_m \bar{\phi}_f (\cos \zeta) \frac{\partial b}{\partial x} + \mathcal{O}(\epsilon^{1+\alpha}), \end{aligned} \quad (3.66)$$

$$\begin{aligned} & \frac{\partial}{\partial t}(h_m \bar{\phi}_f \bar{v}_f) + \frac{\partial}{\partial x}(h_m \bar{\phi}_f \bar{u}_f \bar{v}_f) + \frac{\partial}{\partial y}(h_m \bar{\phi}_f \bar{v}_f^2) \\ &= \frac{\epsilon h_m}{N_R} \left[ 2 \frac{\partial^2 \bar{v}_f}{\partial y^2} + \frac{\partial}{\partial x} \left( \frac{\partial \bar{v}_f}{\partial x} + \frac{\partial \bar{u}_f}{\partial y} \right) - \frac{k_f^b v_f^b}{\epsilon^2 h_m} \right] - \epsilon \bar{\phi}_f \frac{\partial}{\partial y} \left( \frac{h_m^2 \cos \zeta}{2} \right) \\ & \quad - h_m \bar{\phi}_f^2 \vartheta (\bar{v}_f - \bar{v}_s) - \epsilon h_m \bar{\phi}_f (\cos \zeta) \frac{\partial b}{\partial y} + \mathcal{O}(\epsilon^{1+\alpha}). \end{aligned} \quad (3.67)$$

### 3.5.2 Evaluation of the granular stresses

Similarly, to simplify the granular momentum balances (3.56)-(3.58), it is necessary to explicitly formulate the depth-averaged stresses  $\bar{\sigma}_{e(ij)}$ , ( $i, j \in \{x, y, z\}$ ), and the normal stress ( $\mathbf{n}^b \cdot \boldsymbol{\sigma}_e^b \mathbf{n}^b$ ) at the bottom, which are presented in the following.

Applying the order arguments (3.41) and (3.42), the normal component (3.23) of the granular momentum equations can reduce to

$$\gamma \phi_s \frac{\partial p_f}{\partial z} + \frac{\partial \sigma_{e(zz)}}{\partial z} + \phi_s \cos \zeta = \mathcal{O}(\epsilon^\alpha), \quad (3.68)$$

The relation (3.68) indicates the following expression for  $\sigma_{e(zz)}$ ,

$$\sigma_{e(zz)} = (s - z)\bar{\phi}_s(1 - \gamma) \cos \zeta + \mathcal{O}(\epsilon^\alpha). \quad (3.69)$$

Moreover, the normal component (3.58) of the granular depth-integrating momentum equations can be simplified as follows

$$(\mathbf{n}^b \cdot \boldsymbol{\sigma}_e^b \mathbf{n}^b) = h_m \bar{\phi}_s \cos \zeta - \gamma \bar{\phi}_s p_f^b + \lambda \kappa h_m \bar{\phi}_s \bar{u}_s^2 + \mathcal{O}(\epsilon), \quad (3.70)$$

which can further yield that  $(\mathbf{n}^b \cdot \boldsymbol{\sigma}_e^b \mathbf{n}^b)$  is

$$(\mathbf{n}^b \cdot \boldsymbol{\sigma}_e^b \mathbf{n}^b) = h_m \bar{\phi}_s (1 - \gamma) \cos \zeta + \lambda \kappa h_m \bar{\phi}_s (\bar{u}_s^2 - \gamma \bar{u}_f^2) + \mathcal{O}(\epsilon). \quad (3.71)$$

to order  $\epsilon$ , or

$$(\mathbf{n}^b \cdot \boldsymbol{\sigma}_e^b \mathbf{n}^b) = h_m \bar{\phi}_s (1 - \gamma) \cos \zeta + \mathcal{O}(\epsilon^\alpha). \quad (3.72)$$

to order  $\epsilon^\alpha$ .

In shallow granular flow models, the bed lateral normal stresses  $\sigma_{e(xx)}^b$  and  $\sigma_{e(yy)}^b$  are usually connected with the bed normal stress  $\sigma_{e(zz)}^b$  by earth pressure coefficients  $K_x$  and  $K_y$  (see Savage & Hutter (1989)). For the bed element satisfying both bed friction and internal yield criterion simultaneously, the following relations hold

$$\sigma_{e(xx)}^b = K_x^s \sigma_{e(zz)}^b + \mathcal{O}(\epsilon^\nu) \quad \text{and} \quad \sigma_{e(yy)}^b = K_y^s \sigma_{e(zz)}^b + \mathcal{O}(\epsilon^\nu), \quad (3.73)$$

where  $\nu = \min(\alpha, \beta)$ , and the coefficients  $K_x$  and  $K_y$  are given by

$$K_x = K_{x_{act/pass}} = 2 \sec^2 \varphi \left( 1 \mp \sqrt{1 - \cos^2 \varphi \sec^2 \delta} \right) - 1, \quad \frac{\partial u_s}{\partial x} \gtrless 0, \quad (3.74)$$

$$K_y = K_{y_{act/pass}} = \frac{1}{2} \left( K_x + 1 \mp \sqrt{(K_x - 1)^2 + 4 \tan^2 \delta} \right), \quad \frac{\partial v_s}{\partial y} \gtrless 0. \quad (3.75)$$

The earth pressure coefficients are active (upper sign) during dilatational motion, and passive (lower sign) during compressional motion. Moreover, following Savage & Hutter (1989), we stipulate that the lateral normal stresses,  $\sigma_{e(xx)}$  and  $\sigma_{e(yy)}$ , vary linearly with the normal stress  $\sigma_{e(zz)}$  throughout the mixture depth, which indicates that relations

$$\sigma_{e(xx)} = K_x^s \sigma_{e(zz)} + \mathcal{O}(\epsilon^\nu) \quad \text{and} \quad \sigma_{e(yy)} = K_y^s \sigma_{e(zz)} + \mathcal{O}(\epsilon^\nu) \quad (3.76)$$

hold at any spatial and temporal points.

Combining (3.69) with (3.76), one can derive  $\sigma_{e(xx)}$  and  $\sigma_{e(yy)}$  whose depth-averaged forms  $\bar{\sigma}_{e(xx)}$  and  $\bar{\sigma}_{e(yy)}$  are written as

$$\begin{aligned} \bar{\sigma}_{e(xx)} &= \frac{K_x^s}{2} (1 - \gamma) h_m \bar{\phi}_s \cos \zeta + \mathcal{O}(\epsilon^\nu), \\ \bar{\sigma}_{e(yy)} &= \frac{K_y^s}{2} (1 - \gamma) h_m \bar{\phi}_s \cos \zeta + \mathcal{O}(\epsilon^\nu), \end{aligned} \quad (3.77)$$

by calculating the integrations  $\bar{\sigma}_{e(xx)} = \int_b^s \sigma_{e(xx)} dz/h_m$  and  $\bar{\sigma}_{e(yy)} = \int_b^s \sigma_{e(yy)} dz/h_m$ .

Similar to (3.63), the buoyancy force involving the fluid pressure can be approximated as

$$\begin{aligned}\epsilon\gamma\bar{\phi}_s\frac{\partial}{\partial x}(h_m\overline{p_f\psi}) &= \epsilon\gamma\bar{\phi}_s\frac{\partial}{\partial x}\left(\frac{1}{2}h_m^2\cos\zeta\right) + \mathcal{O}(\epsilon^{1+\alpha}), \\ \epsilon\gamma\bar{\phi}_s\frac{\partial}{\partial y}(h_m\overline{p_f}) &= \epsilon\gamma\bar{\phi}_s\frac{\partial}{\partial y}\left(\frac{1}{2}h_m^2\cos\zeta\right) + \mathcal{O}(\epsilon^{1+\alpha}).\end{aligned}\quad (3.78)$$

Approximating the depth-averaged downslope (3.56) and cross-slope (3.57) momentum balances to order  $\mathcal{O}(\epsilon^{1+\nu})$ , and then substituting (3.71), (3.77), and (3.78) into the result, one can yield

$$\begin{aligned}\frac{\partial}{\partial t}(h_m\bar{\phi}_s\bar{u}_s) + \frac{\partial}{\partial x}(h_m\bar{\phi}_s\overline{u_s u_s}) + \frac{\partial}{\partial y}(h_m\bar{\phi}_s\overline{u_s v_s}) \\ = h_m\bar{\phi}_s\sin\zeta - \frac{\partial}{\partial x}\left(\frac{\beta_s^x h_m^2 \bar{\phi}_s}{2}\right) - \epsilon\bar{\phi}_s\gamma\frac{\partial}{\partial x}\left(\frac{1}{2}h_m^2\cos\zeta\right) - \epsilon h_m\bar{\phi}_s(\cos\zeta)\frac{\partial b}{\partial x} \\ - \frac{u_s^b}{\sqrt{(u_s^b)^2 + (v_s^b)^2}}h_m\bar{\phi}_s\mu_s^b\left[(1-\gamma)\cos\zeta + \lambda\kappa(\bar{u}_s^2 - \gamma\bar{u}_f^2)\right], \\ + \gamma h_m\bar{\phi}_f^2\vartheta(\bar{u}_f - \bar{u}_s) + \mathcal{O}(\epsilon^{1+\nu}),\end{aligned}\quad (3.79)$$

$$\begin{aligned}\frac{\partial}{\partial t}(h_m\bar{\phi}_s\bar{v}_s) + \frac{\partial}{\partial x}(h_m\bar{\phi}_s\overline{u_s v_s}) + \frac{\partial}{\partial y}(h_m\bar{\phi}_s\bar{v}_s^2) \\ = -\frac{\partial}{\partial y}\left(\frac{\beta_s^y h_m^2 \bar{\phi}_s}{2}\right) - \epsilon\bar{\phi}_s\gamma\frac{\partial}{\partial y}\left(\frac{1}{2}h_m^2\cos\zeta\right) - \epsilon h_m\bar{\phi}_s(\cos\zeta)\frac{\partial b}{\partial y} \\ - \frac{v_s^b}{\sqrt{(u_s^b)^2 + (v_s^b)^2}}h_m\bar{\phi}_s\mu_s^b\left[(1-\gamma)\cos\zeta + \lambda\kappa(\bar{u}_s^2 - \gamma\bar{u}_f^2)\right] \\ + \gamma h_m\bar{\phi}_f^2\vartheta(\bar{v}_f - \bar{v}_s) + \mathcal{O}(\epsilon^{1+\nu}),\end{aligned}\quad (3.80)$$

where the factors  $\beta_s^x$  and  $\beta_s^y$  are written as

$$\beta_s^x = \epsilon(1-\gamma)K_x^s\cos\zeta, \quad \beta_s^y = \epsilon(1-\gamma)K_y^s\cos\zeta. \quad (3.81)$$

### 3.5.3 Assumption of velocity profiles

Due to the depth-averaged procedure, it is impossible to evaluate the depth variation of the velocity. It must rather be postulated. For this purpose, a plug flow is postulated, which indicates that mostly sliding and narrow differential shearing take place near the bottom (see Fig. 3.3). As a result, relations

$$\begin{aligned}u_s &= \bar{u}_s + \mathcal{O}(\epsilon^{1+\nu}), & v_s &= \bar{v}_s + \mathcal{O}(\epsilon^{1+\nu}), \\ u_f &= \bar{u}_f + \mathcal{O}(\epsilon^{1+\nu}), & v_f &= \bar{v}_f + \mathcal{O}(\epsilon^{1+\nu})\end{aligned}\quad (3.82)$$

hold. The plug flow is commonly assumed in the simulations of grain-fluid mixture flows, for instance, see Iverson & Denlinger (2001), Pitman & Le (2005) and Pudasaini (2012), since it can lead to reasonable results. With relation (3.82), the velocity-product

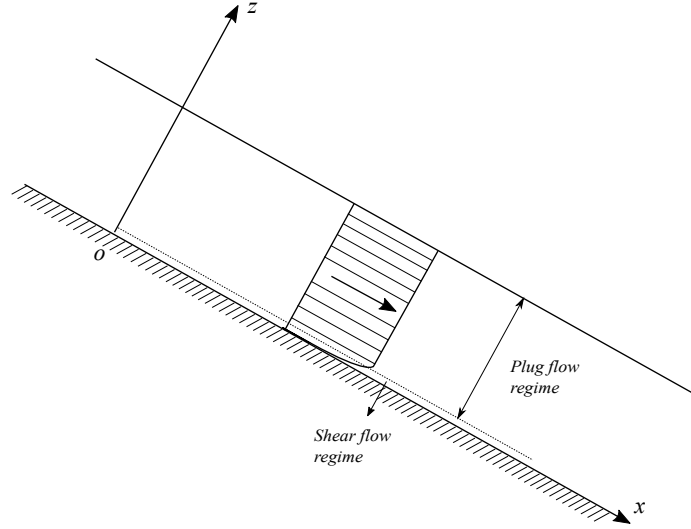


Figure 3.3: Gravity-driven grain-fluid mixture flow with a large plug flow regime lying atop of a thin shear flow regime near the bottom. The shear layer is magnified.

terms can then be factorized as

$$\overline{u_\eta u_\eta} = \overline{u_\eta} \overline{u_\eta} + \mathcal{O}(\epsilon^{1+\nu}), \quad \overline{u_\eta v_\eta} = \overline{u_\eta} \overline{v_\eta} + \mathcal{O}(\epsilon^{1+\nu}), \quad \overline{v_\eta v_\eta} = \overline{v_\eta} \overline{v_\eta} + \mathcal{O}(\epsilon^{1+\nu}) \quad (3.83)$$

### 3.6 Summary of depth-averaged equations

In this section, the final form of the model equations are presented and the physics behind the model equations are interpreted.

By taking advantage of (3.83) to decompose the velocity-product terms arising in the downslope (3.66) and cross-slope (3.67) of the depth-averaged momentum equations, we can derive the final depth-averaged balance equations for the fluid phase. In the depth-averaged equations, we drop the overbar for simplicity and assume that the boundary velocities and boundary volume fractions approximately equal the corresponding depth-averaged ones. They are given by

$$\frac{\partial}{\partial t}(h_m \phi_f) + \frac{\partial}{\partial x}(h_m \phi_f u_f) + \frac{\partial}{\partial y}(h_m \phi_f v_f) = 0, \quad (3.84)$$

$$\frac{\partial}{\partial t}(h_m \phi_f u_f) + \frac{\partial}{\partial x}(h_m \phi_f u_f^2) + \frac{\partial}{\partial y}(h_m \phi_f u_f v_f) = s_{x(f)} - \frac{\partial}{\partial x} \left( \frac{\beta_f^x h_m^2 \phi_f}{2} \right), \quad (3.85)$$

$$\frac{\partial}{\partial t}(h_m \phi_f v_f) + \frac{\partial}{\partial x}(h_m \phi_f u_f v_f) + \frac{\partial}{\partial y}(h_m \phi_f v_f^2) = s_{y(f)} - \frac{\partial}{\partial y} \left( \frac{\beta_f^y h_m^2 \phi_f}{2} \right) \quad (3.86)$$

with the factors  $\beta_f^x$  and  $\beta_f^y$  being defined as

$$\beta_f^x = \epsilon \cos \zeta, \quad \beta_f^y = \epsilon \cos \zeta, \quad (3.87)$$

and the source terms  $s_{x(s)}$  and  $s_{x(f)}$  described as

$$\begin{aligned} s_{x(f)} = & h_m \phi_f \sin \zeta - h_m \phi_f^2 \vartheta (u_f - u_s) - \epsilon h_m \phi_f (\cos \zeta) \frac{\partial b}{\partial x} + \frac{1}{2} \epsilon h_m^2 \cos \zeta \frac{\partial \phi_f}{\partial x} \\ & + \frac{\epsilon h_m}{N_R} \left[ 2 \frac{\partial^2 u_f}{\partial x^2} + \frac{\partial}{\partial y} \left( \frac{\partial v_f}{\partial x} + \frac{\partial u_f}{\partial y} \right) - \frac{k_f^b u_f}{\epsilon^2 h_m} \right] + \mathcal{O}(\epsilon^{1+\nu}), \end{aligned} \quad (3.88)$$

$$\begin{aligned} s_{y(f)} = & -h_m \phi_f^2 \vartheta (v_f - v_s) + \frac{1}{2} \epsilon h_m^2 \cos \zeta \frac{\partial \phi_f}{\partial y} - \epsilon h_m \phi_f (\cos \zeta) \frac{\partial b}{\partial y} \\ & + \frac{\epsilon h_m}{N_R} \left[ 2 \frac{\partial^2 v_f}{\partial y^2} + \frac{\partial}{\partial x} \left( \frac{\partial v_f}{\partial x} + \frac{\partial u_f}{\partial y} \right) - \frac{k_f^b v_f}{\epsilon^2 h_m} \right] + \mathcal{O}(\epsilon^{1+\nu}). \end{aligned} \quad (3.89)$$

Similarly, the final depth-averaged balance equations for the granular phase are given by

$$\frac{\partial}{\partial t} (h_m \phi_s) + \frac{\partial}{\partial x} (h_m \phi_s u_s) + \frac{\partial}{\partial y} (h_m \phi_s v_s) = 0, \quad (3.90)$$

$$\frac{\partial}{\partial t} (h_m \phi_s u_s) + \frac{\partial}{\partial x} (h_m \phi_s u_s^2) + \frac{\partial}{\partial y} (h_m \phi_s u_s v_s) \quad (3.91)$$

$$= s_{x(s)} - \frac{\partial}{\partial x} \left( \frac{\beta_s^x h_m^2 \phi_s}{2} \right) + \frac{\partial}{\partial x} \left( \frac{\gamma \beta_f^x h_m^2 \phi_s}{2} \right),$$

$$\frac{\partial}{\partial t} (h_m \phi_s v_s) + \frac{\partial}{\partial x} (h_m \phi_s u_s v_s) + \frac{\partial}{\partial y} (h_m \phi_s v_s^2) \quad (3.92)$$

$$= s_{y(s)} - \frac{\partial}{\partial y} \left( \frac{\beta_s^y h_m^2 \phi_s}{2} \right) + \frac{\partial}{\partial y} \left( \frac{\gamma \beta_f^y h_m^2 \phi_s}{2} \right),$$

where the source terms  $s_{x(s)}$  and  $s_{y(s)}$  are specified as

$$\begin{aligned} s_{x(s)} = & h_m \phi_s \sin \zeta + \gamma h_m \phi_f^2 \vartheta (u_f - u_s) + \frac{1}{2} \epsilon \gamma h_m^2 \cos \zeta \frac{\partial \phi_s}{\partial x} - \epsilon h_m \phi_s (\cos \zeta) \frac{\partial b}{\partial x} \\ & - \frac{u_s}{\sqrt{u_s^2 + v_s^2}} h_m \phi_s \mu_s^b \left[ (1 - \gamma) \cos \zeta + \lambda \kappa (u_s^2 - \gamma u_f^2) \right] + \mathcal{O}(\epsilon^{1+\nu}), \end{aligned} \quad (3.93)$$

$$\begin{aligned} s_{y(s)} = & \gamma h_m \phi_f^2 \vartheta (v_f - v_s) + \frac{1}{2} \epsilon \gamma h_m^2 \cos \zeta \frac{\partial \phi_s}{\partial y} - \epsilon h_m \phi_s (\cos \zeta) \frac{\partial b}{\partial y} \\ & - \frac{v_s}{\sqrt{u_s^2 + v_s^2}} h_m \phi_s \mu_s^b \left[ (1 - \gamma) \cos \zeta + \lambda \kappa (u_s^2 - \gamma u_f^2) \right] + \mathcal{O}(\epsilon^{1+\nu}). \end{aligned} \quad (3.94)$$

The model equations (3.84)-(3.86) and (3.90)-(3.92), completed by (3.87)-(3.89) and (3.93)-(3.94), constitute the framework of a two-phase grain-fluid mixture flow down a curved plane, which can provide deep insights into natural surficial processes with the following aspects:

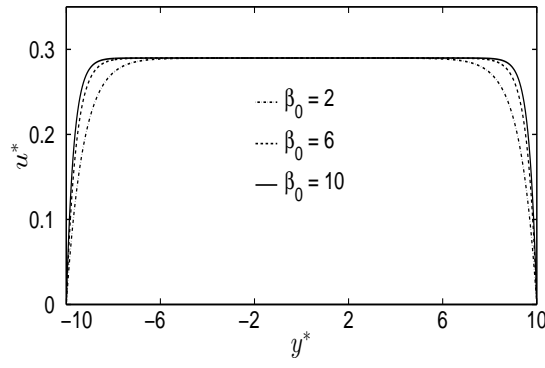
- (i) For the fluid phase, equations (3.85) and (3.86) indicate the balance of inertial terms on the left-hand sides, with the depth-averaged fluid pressure gradients (last terms) and the other source terms (defined in (3.88) and (3.89)) on the right-hand sides. In the fluid pressure gradients, the coefficients  $\beta_f^x$  and  $\beta_f^y$  are equal due to isotropic quality of the fluid pressure. The source terms  $s_{x(f)}$  and  $s_{y(f)}$  are characterised by a gravity term, a drag force term, a topographic term, a buoyancy force term, and viscous stress terms, consecutively. In the viscous stress terms, taking into account the orders of aspect ratio  $\epsilon$  and quasi Reynolds number  $N_R$ , it is found that the fluid diffusion terms (the first two terms in the square bracket) are relatively small compared with the bed friction terms (the last terms in the square bracket).
- (ii) For the granular phase, equations (3.91) and (3.92) describe the balance of inertial terms on the left-hand sides, with granular stress gradient terms (last two terms) and the other source terms (defined in (3.93) and (3.94)) on the right-hand sides. The granular stress gradients include contributions of the solid effective stress (last second terms) and the pore pressure (last terms). The factors  $\beta_s^x$  and  $\beta_s^y$  arising in the solid effective stress incorporate the effects of anisotropy of the normal stresses. The presence of the coefficient  $(1 - \gamma)$  in  $\beta_s^x$  and  $\beta_s^y$  indicates a reduced solid load due to the buoyancy force. The source terms  $s_{x(s)}$  and  $s_{y(s)}$  exhibit a gravity term, a drag force term, a buoyancy force term, a topographic term, and a bed Coulomb friction term, consecutively. The reason for differences of buoyancy and drag force between the fluid and solid phases lies in the fact that the momentum equations are scaled by different densities. The normal traction in bed Coulomb friction comprises of the overburden pressure (the first terms in the square bracket), mitigated by the pore pressure, plus a contribution due to the bed curvature (the second terms in the square bracket).

## 3.7 Theoretical analysis for steady flows

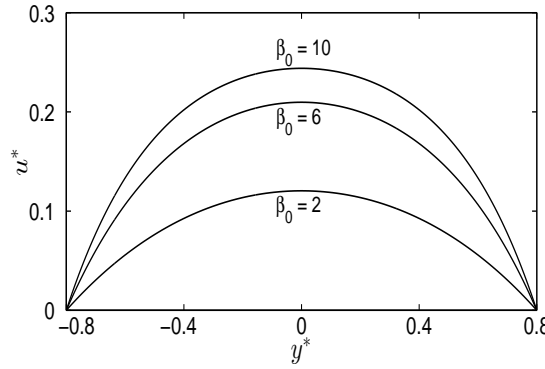
This section focuses on theoretical analysis of steady flows, which are helpful to gain some insights into complex flows. In Section 3.7.1, the steady unidirectional flows in rectangular channels are presented to investigate the cross-stream profile of the downslope velocity. Then, the steady flows in a travelling coordinate system are analyzed to probe into the shape of the flow front and the development of roll waves in Section 3.7.2.

### 3.7.1 Steady flow in a rectangular channel

The investigation of a steady flow can be constructive to scrutinize the correctness of the present model. To this end, steady unidirectional flow of a grain-fluid mixture with constant height  $h = H$  in a uniformly inclined rectangular channel is taken into account here. In steady state, the two components of the mixture are further assumed to move with the same velocity  $u$ . In this case, the balance equations of mass (3.84)



(a) Steady flows in a wide channel



(b) Steady flows in a narrow channel

Figure 3.4: Cross-stream velocity profiles for steady flows in wide and narrow channels

and (3.90) are trivially satisfied. Moreover, let us turn the non-dimensional balance equations of momentum (3.85) and (3.91) into dimensional forms by virtue of scaling (3.11). Summation of the dimensional fluid and granular momentum equations can yield

$$\rho g_x H - (\rho - \tilde{\rho}_f) g_z H \mu_s^b - \phi_f k_f^b u + H \mu_f \phi_f \frac{\partial^2 u}{\partial y^2} = 0. \quad (3.95)$$

Algebraic operation can transform equation (3.95) into the following form

$$\frac{\partial^2 u}{\partial y^2} - \beta_0 u = \frac{\rho g_z}{\mu_f \phi_f} \Psi, \quad (3.96)$$

where  $\beta_0 = k_f^b / (H \mu_f)$  and  $\Psi = g_x / g_z - (1 - \tilde{\rho}_f / \rho) \mu_s^b$ . The solution of equation (3.96) can be written as

$$u^* = \Psi \left[ 1 - \cosh^{-1} \left( \frac{\sqrt{\beta_0}}{H} x_L \right) \cdot \cosh \left( \sqrt{\beta_0} y^* \right) \right] \quad (3.97)$$

when we prescribe no-slip boundary conditions  $u(-x_L) = 0$  and  $u(x_L) = 0$  at the side walls, where  $x_L$  represents half width of a channel. Fig. 3.4(a) corresponds to the



solution of steady flows in a wide channel and it illustrates a narrow shear zone next to a larger plug zone in the cross-stream velocity profile, while Fig. 3.4(b) corresponds to the solution of steady flows in a narrow channel and it exhibits a rounded profile due to the effect of channel restriction.

### 3.7.2 Characteristic shape of flow front and roll waves

When a fluid, a suspension or a system of discrete particles flows downwards on an inclined open channel, for instance natural debris flows, successive wave patterns (roll waves) with blunt shape of fronts, periodic in distance, are often observed (see Iversen (1997) and Schonfeld (1996)). To probe into the underlying physical mechanism, a steady solution in a travelling coordinate system can be constructed to account for the blunt shape of the flow front, and a stability analysis of steady uniform flow can be performed to elucidate roll waves (Hungri 2000, GrayEdwards2014). Moreover, for a clear account of physics, these theoretical analysis are based on the two-dimensional flows corresponding to one-dimensional (1-D) depth-averaged equations.

The 1-D depth-averaged equations are obtained by eliminating the  $y$ -coordinate dependency from the two-dimensional model equations (3.84)-(3.86) and (3.90)-(3.92). As a result, the 1-D equations take the form

$$\frac{\partial}{\partial t}(h_m\phi_f) + \frac{\partial}{\partial x}(h_m\phi_f u_f) = 0, \quad (3.98)$$

$$\frac{\partial}{\partial t}(h_m\phi_s) + \frac{\partial}{\partial x}(h_m\phi_s u_s) = 0, \quad (3.99)$$

$$\frac{\partial}{\partial t}(h_m\phi_f u_f) + \frac{\partial}{\partial x}\left(h_m\phi_f u_f^2 + \frac{\beta_f^x h_m^2 \phi_f}{2}\right) = \hat{s}_{x(f)} + \frac{1}{2}\epsilon h_m^2 \cos \zeta \frac{\partial \phi_f}{\partial x}, \quad (3.100)$$

$$\frac{\partial}{\partial t}(h_m\phi_s u_s) + \frac{\partial}{\partial x}\left(h_m\phi_s u_s^2 + \frac{\beta_s^x h_m^2 \phi_s}{2} - \frac{\gamma \beta_f^x h_m^2 \phi_s}{2}\right) = \hat{s}_{x(s)} + \frac{1}{2}\epsilon \gamma h_m^2 \cos \zeta \frac{\partial \phi_s}{\partial x}, \quad (3.101)$$

where the source terms  $\hat{s}_{x(f)}$  and  $\hat{s}_{x(s)}$  are written as

$$\hat{s}_{x(f)} = h_m\phi_f \sin \zeta - h_m\phi_f^2 \vartheta (u_f - u_s) - \epsilon h_m\phi_f (\cos \zeta) \frac{\partial b}{\partial x} + 2 \frac{\epsilon h_m}{N_R} \frac{\partial^2 u_f}{\partial x^2} - \frac{k_f^b u_f}{\epsilon N_R}, \quad (3.102)$$

$$\begin{aligned} \hat{s}_{x(s)} = & h_m\phi_s \sin \zeta + \gamma h_m\phi_f^2 \vartheta (u_f - u_s) - \epsilon h_m\phi_s (\cos \zeta) \frac{\partial b}{\partial x} - h_m\phi_s \mu_s^b (1 - \gamma) \cos \zeta \\ & - h_m\phi_s \mu_s^b \lambda \kappa (u_s^2 - \gamma u_f^2). \end{aligned} \quad (3.103)$$

#### 1. Characteristic shape of flow front

To demonstrate the blunt shape of the flow front, this part concentrates on the case when a grain-fluid mixture with a uniform steady inflow condition, moving over long distances, attains a constant velocity and well-defined shape, i.e.  $u_s = u_f = u_0$ . In this case, the mass body will not 'passively' compress ( $\partial u_s / \partial x < 0$ ), nor 'actively' extend ( $\partial u_s / \partial x > 0$ ). Moreover, experiments suggest that there is no jump in earth pressure coefficient  $K_x$  at  $\partial u_s / \partial x = 0$ , so a slowly varying

function or a constant earth pressure coefficient is more realistic (see Chugunov, Gray & Hutter (2003)). Hence,  $K_x = 1$  is postulated for simplicity.

Preliminarily, the non-dimensional equations (3.98)-(3.101), completed by (3.102) and (3.103), are transformed into the dimensional ones by virtue of the scaling (3.11). Then, adding the dimensional mass-balance equations together yields the mass-balance equation for the mixture as a whole. By combining the fluid and the granular momentum equations to eliminate the viscous drag force, one can obtain the momentum equation for the mixture as a whole. The mass and momentum equations for the mixture are given by

$$\frac{\partial h_m}{\partial t} + \frac{\partial(h_m u_0)}{\partial x} = 0, \quad (3.104)$$

$$\frac{\partial(h_m u_0)}{\partial t} + \frac{\partial(h_m u_0^2)}{\partial x} = h_m g_x - \frac{\partial}{\partial x} \left( \frac{1}{2} h_m^2 g_z \right) - h_m \mu_s^b (1 - \tilde{\rho}_f / \rho) g_z - k_f^b \phi_f u_0 / \rho, \quad (3.105)$$

where  $g_x = g \sin \zeta$  represents the gravitational downslope component,  $g_z = g \cos \zeta$  the gravitational normal component, and  $\rho$  the mixture depth-averaged density. We take a homogeneous mixture into account here such that  $\rho$  is constant.

It is helpful to transform (3.104) and (3.105) into Lagrangian forms with the following coordinate transformation

$$\varsigma = x - u_0 t, \quad (3.106)$$

where the origin of travelling coordinate system is fixed in the leading edge of the mixture where  $h_m = 0$ . By virtue of (3.106), the balance equation of mass is trivially satisfied, and the balance equation of momentum (3.105) reduces to

$$\frac{dh_m}{d\varsigma} = \tan \zeta - \mu_s^b (1 - \tilde{\rho}_f / \rho) - k_f^b \phi_f u_0 / (\rho h_m g_z), \quad \varsigma \leq 0. \quad (3.107)$$

To proceed, it is reasonable to think the solution is tended toward a steady-uniform flow in far upstream, in which  $h_m = h_0$  and  $u = u_0$  hold. By letting  $dh_m/d\varsigma = 0$  in (3.107), a relation between  $h_m = h_0$  and  $u_0$  can be obtained which is

$$h_0 = \frac{k_f^b \phi_f}{\rho g_z \Gamma} u_0, \quad (3.108)$$

where  $\Gamma = \tan \zeta - \mu_s^b (1 - \tilde{\rho}_f / \rho)$  is considered as a constant here.

Moreover, it is helpful to transform (3.107) into non-dimensional form by

$$(h_m, x, \varsigma) = (h_0 \tilde{h}_m, l_0 \tilde{x}, l_0 \tilde{\varsigma}), \quad t = (l_0 / u_0) \tilde{t}, \quad (3.109)$$

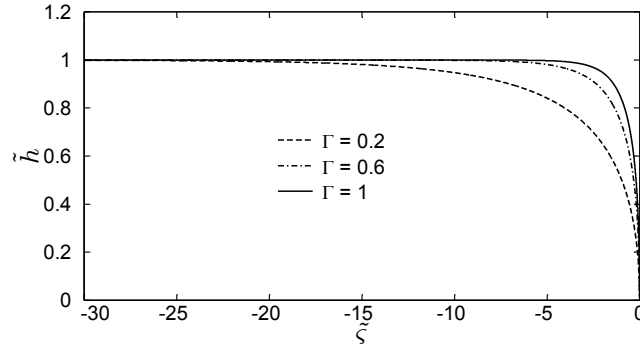


Figure 3.5: Profiles of the depth for homogeneous debris surge with different solid volume fractions, where  $\epsilon_0 = 1$  is chosen.

where  $h_0$  is the typical height,  $l_0$  the typical length,  $u_0$  the typical velocity. The variables with the superscript tilde indicate non-dimensional quantities.

With relations (3.108) and (3.109), relation (3.107) turns into

$$\epsilon_0 \frac{d\tilde{h}_m}{d\tilde{\zeta}} = \Gamma \left( 1 - \frac{1}{\tilde{h}_m} \right), \quad \tilde{\zeta} \leq 0, \quad (3.110)$$

where  $\epsilon_0 = h_0/l_0$ .

In the case that  $\Gamma$  is constant as in the present case, integrating (3.110) at the boundary condition,  $\tilde{h}_m = 0$  at  $\tilde{\zeta} = 0$ , leads to

$$\frac{\epsilon_0}{\Gamma} (\tilde{h}_m + \ln |\tilde{h}_m - 1|) = \tilde{\zeta}. \quad (3.111)$$

The depth profile characterized by (3.111) is demonstrated in Fig. 3.5. It is clearly seen that a blunt shape develops at the front of a surge.

## 2. Development of roll waves

When a grain-fluid mixture is flowing down a channel, a succession of surges can be often observed. The surges most frequently develop following a mechanism similar to water roll waves: instabilities grow up becoming clearly distinguishable waves. A stability analysis for steady uniform flows is commonly performed to investigate the development of roll waves in shallow water and granular flows (see Needham & Merkin (1984), Que & Xu (2006) and Gray & Edwards (2014)). Following this line, the stability analysis is also carried out to observe the development of roll waves herein. In short, this subsection concentrates on the analysis for steady-uniform regions.

1D flows down an inclined plane for simplicity are considered again. Here although the earth pressure coefficient  $K_x$  may be non-constant in small amplitude disturbance, it is accepted to consider isotropic normal stresses as George & Iverson (2011), PoIverson & Forterre (2002), and Bouchut et al. (2014) did. Several numerical tests find only a small difference between the isotropic and

anisotropic normal stresses (see Prochnow, Chevoir & Albertelli (2000)), which motivates to postulate  $K_x = 1$  again. In addition, the same velocity for each constituent  $u_s = u_f = u$  is postulated again, and the volume fractions are assumed to be homogeneously distributed as before, which are justified by small fluctuations. We are aware that these assumptions are only for small amplitude disturbance. With these simplifications, as the same way to formulate (3.104) and (3.105), the dimensional conservation equations are

$$\frac{\partial h_m}{\partial t} + \frac{\partial(h_m u)}{\partial x} = 0, \quad (3.112)$$

$$\begin{aligned} \frac{\partial}{\partial t}(h_m u) + \frac{\partial}{\partial x}(h_m u^2) &= h_m g_x - \frac{\partial}{\partial x} \left( \frac{1}{2} h_m^2 g_z \right) \\ &- h_m g_z (1 - \tilde{\rho}_f / \rho) \mu_s^b + 2\phi_f \mu_f \frac{h_m}{\rho} \frac{\partial^2 u}{\partial x^2} - k_f^b \phi_f u / \rho. \end{aligned} \quad (3.113)$$

It is helpful for further reasoning to transform equations (3.112) and (3.113) into a non-dimensional form. To this end, in addition to relation (3.109), we provide the scalings for the velocity  $u$  and the parameter  $k_f^b$ , which are given by

$$u = u_0 \tilde{u}, \quad k_f^b = \tilde{\rho}_f u_0 \tilde{k}_f^b. \quad (3.114)$$

With these scalings, the dimensional balance equations (3.112) and (3.113) can be transformed into the following non-dimensional forms,

$$\frac{\partial \tilde{h}}{\partial \tilde{t}} + \frac{\partial}{\partial x}(\tilde{h} \tilde{u}) = 0, \quad (3.115)$$

$$\frac{\partial}{\partial \tilde{t}}(\tilde{h} \tilde{u}) + \frac{\partial}{\partial x}(\tilde{h} \tilde{u}^2) + \frac{1}{Fr^2} \tilde{h} \frac{\partial \tilde{h}}{\partial x} = \frac{\gamma \phi_f}{c_n \eta_0} (\tilde{h} - \tilde{u}) + \frac{2\gamma \phi_f}{c_n Re} \tilde{h} \frac{\partial^2 \tilde{u}}{\partial x^2}, \quad (3.116)$$

where  $Fr = u_0 / \sqrt{g_z h_0}$  and  $Re = \tilde{\rho}_f u_0 l_0 / \mu_f$  represent the Froude and Reynolds numbers, respectively. Additionally, the parameter  $c_n$ , appearing here, stands for  $c_n = \rho / \tilde{\rho}_s$  and the parameter  $\eta_0$  represents  $\eta_0 = h_0 / (\tilde{k}_f^b l_0)$ .

Moreover, a temporal stability analysis of the uniform flow to small amplitude disturbances can be performed by letting  $\tilde{h} = 1 + \xi \hat{h}$  and  $\tilde{u} = 1 + \xi \hat{u}$ , where  $\xi \ll 1$ . Substitution into equations (3.115) and (3.116), and retention of terms  $\mathcal{O}(\xi)$  yield the linear equations for the fluctuated quantities  $\hat{h}$  and  $\hat{u}$ , which are given by

$$\frac{\partial \hat{h}}{\partial \tilde{t}} + \frac{\partial \hat{h}}{\partial x} + \frac{\partial \hat{u}}{\partial x} = 0, \quad (3.117)$$

$$\frac{\partial \hat{u}}{\partial \tilde{t}} + \frac{\partial \hat{u}}{\partial x} + \frac{1}{Fr^2} \frac{\partial \hat{h}}{\partial x} = \frac{\gamma \phi_f}{c_n \eta_0} (\hat{h} - \hat{u}) + \frac{2\gamma \phi_f}{c_n Re} \frac{\partial^2 \hat{u}}{\partial x^2}. \quad (3.118)$$

With (3.117), the terms in (3.118) involving velocity  $\hat{u}$  can be cancelled out such that

$$\frac{\partial^2 \hat{h}}{\partial t^2} + 2 \frac{\partial^2 \hat{h}}{\partial t \partial x} + \left(1 - \frac{1}{Fr^2}\right) \frac{\partial^2 \hat{h}}{\partial x^2} + \frac{\gamma \phi_f}{c_n \eta_0} \left(2 \frac{\partial \hat{h}}{\partial x} + \frac{\partial \hat{h}}{\partial t}\right) = \frac{2\gamma \phi_f}{c_n Re} \frac{\partial^2}{\partial x^2} \left(\frac{\partial \hat{h}}{\partial t} + \frac{\partial \hat{h}}{\partial x}\right), \quad (3.119)$$

holds.

For (3.119), the solution is written as  $\hat{h} = A(k_x)e^{ik_x x - \omega t} + c.c.$ , where  $k_x$  means  $2\pi$  wave number and is real,  $c.c.$  means conjugate, and  $\omega = \omega_r + i\omega_i$  ( $\omega_r$  and  $\omega_i$  are real) represents pulsation frequency. For a stability condition,  $\omega_r \geq 0$  is required. Substituting  $\hat{h} = A(k_x)e^{ik_x x - \omega t} + c.c.$  into (3.119), and arranging it, one can lead to the following two equations for real and image parts

$$\omega_r^2 - \omega_i^2 - \omega_r \left(\frac{\gamma \phi_f}{c_n \eta_0} + \frac{2\gamma \phi_f k_x^2}{c_n Re}\right) - k_x^2 \left(1 - \frac{1}{Fr^2}\right) + 2k_x \omega_i = 0, \quad (3.120)$$

$$2\omega_i \omega_r - 2k_x \omega_r - \omega_i \left(\frac{\gamma \phi_f}{c_n \eta_0} + \frac{2\gamma \phi_f k_x^2}{c_n Re}\right) + \frac{2\gamma \phi_f k_x}{c_n \eta_0} + \frac{2\gamma \phi_f k_x^3}{c_n Re} = 0. \quad (3.121)$$

Taking out  $\omega_i$  from (3.120) and (3.121), it comes to

$$\begin{aligned} f(\omega_r) = & 4\omega_r^4 - 8\omega_r^3 \left(\frac{\gamma \phi_f}{c_n \eta_0} + \frac{2\gamma \phi_f k_x^2}{c_n Re}\right) + 5\omega_r^2 \left(\frac{\gamma \phi_f}{c_n \eta_0} + \frac{2\gamma \phi_f k_x^2}{c_n Re}\right) + \frac{4k_x^2}{Fr^2} \omega_r^2 \\ & - \omega_r \left(\frac{\gamma \phi_f}{c_n \eta_0} + \frac{2\gamma \phi_f k_x^2}{c_n Re}\right)^3 - \frac{4k_x^2}{Fr^2} \omega_r \left(\frac{\gamma \phi_f}{c_n \eta_0} + \frac{2\gamma \phi_f k_x^2}{c_n Re}\right) \\ & + \frac{k_x^2}{Fr^2} \left(\frac{\gamma \phi_f}{c_n \eta_0} + \frac{2\gamma \phi_f k_x^2}{c_n Re}\right)^2 - \left(\frac{\gamma k_x \phi_f}{c_n \eta_0}\right)^2 = 0. \end{aligned} \quad (3.122)$$

It is found that three extreme points of the function  $f(\omega_r)$ , obtained by  $f'(\omega_r) = 0$ , lie in

$$\omega_r^{(1)} = \frac{1}{2} \left(\frac{\gamma \phi_f}{c_n \eta_0} + \frac{2\gamma \phi_f k_x^2}{c_n Re}\right) > 0, \quad (3.123)$$

$$\omega_r^{(2,3)} = \frac{1}{2} \left\{ \left(\frac{\gamma \phi_f}{c_n \eta_0} + \frac{2\gamma \phi_f k_x^2}{c_n Re}\right) \pm \sqrt{0.5 \left(\frac{\gamma \phi_f}{c_n \eta_0} + \frac{2\gamma \phi_f k_x^2}{c_n Re}\right)^2 - \frac{2k_x^2}{Fr^2}} \right\} > 0. \quad (3.124)$$

Furthermore it is found that  $f(-\infty) \rightarrow +\infty$  is satisfied in (3.122). All of these indicate that  $f(\omega_r)$  is a monotonic decreasing function for  $-\infty < \omega_r \leq 0$ . In order to assure all the solutions of (3.122) are positive,  $f(0) \geq 0$  must hold that is

$$Fr \leq \left(1 + \frac{k_x^2 \eta_0}{Re}\right). \quad (3.125)$$

Relation (3.125) is the stability condition for steady uniform flows constrained by the bed Coulomb condition for the granular phase and bed Navier slip friction condition for the fluid phase. The critical Froude number  $Fr_c = 1 + k_x^2 \eta_0 / Re$  depends on the geometrical scalings and dynamic conditions of the flow. Consequently, different rheology models and boundary conditions can actually yield

different stability criteria. The stability criteria for Bingham-type and Bagnold-inan dilatant flow models can be found in Arai, Huebl & Kaitna (2013).

To visualize roll waves for the steady state in a moving frame, it is convenient to rewrite the equations (3.115) and (3.116) in a moving system at the constant speed  $u_r$  of roll wave, which can be realized by the following transformation

$$\zeta = x - u_r t. \quad (3.126)$$

Then, the resulted equations are

$$\frac{d}{d\zeta}(\tilde{h}(\tilde{u} - u_r)) = 0, \quad (3.127)$$

$$Fr^2(\tilde{u} - u_r)\frac{d\tilde{u}}{d\zeta} + \frac{d\tilde{h}}{d\zeta} = \frac{Fr^2\gamma\phi_f}{c_n\eta_0}\left(1 - \frac{\tilde{u}}{\tilde{h}}\right) + \frac{2Fr^2\gamma\phi_f}{c_n Re}\frac{d^2\tilde{u}}{d\zeta^2}. \quad (3.128)$$

at a steady state.

The mass-balance equation (3.127) yields  $\tilde{h}(\tilde{u} - u_r) = \text{constant} = c_m$ . To assume that the solution  $(\tilde{h}, \tilde{u}) = (1, 1)$  of steady uniform flows satisfies (3.127), it follows that  $c_m = (1 - u_r)$  is chosen, i.e.,

$$\tilde{h}(\tilde{u} - u_r) = (1 - u_r), \quad (3.129)$$

holds, which means  $\tilde{u} = u_r + (1 - u_r)/\tilde{h}$ . Actually a different choice for  $c_m$  does not affect the following analysis. Substitution  $\tilde{u}$  into (3.128) leads to

$$\begin{aligned} \frac{\partial^2 \tilde{h}}{\partial \zeta^2} = & \quad (3.130) \\ & \frac{2}{\tilde{h}}\left(\frac{\partial \tilde{h}}{\partial \zeta}\right)^2 - \frac{c_n Re}{2Fr^2\gamma\phi_f(1 - u_r)\tilde{h}}\left[\tilde{h}^3 - Fr^2(1 - u_r)^2\right]\frac{\partial \tilde{h}}{\partial \zeta} + \frac{Re(\tilde{h} - 1)(\tilde{h} + 1 - u_r)}{2\eta_0(1 - u_r)}. \end{aligned}$$

To simplify (3.130), let  $\partial \tilde{h}/\partial \zeta = n$  such that (3.130) equals

$$\frac{\partial \tilde{h}}{\partial \zeta} = n, \quad (3.131)$$

$$\frac{\partial n}{\partial \zeta} = \frac{2}{\tilde{h}}n^2 - \frac{c_n Re}{2Fr^2\gamma\phi_f(1 - u_r)\tilde{h}}\left[\tilde{h}^3 - Fr^2(1 - u_r)^2\right]n + \frac{Re(\tilde{h} - 1)(\tilde{h} + 1 - u_r)}{2\eta_0(1 - u_r)}, \quad (3.132)$$

In the unstable regime ( $Fr > 1$ ), the system composed (3.131) and (3.132) is solved through backward Euler scheme solver with a prescribed boundary condition  $(\tilde{h}, n) = (1.2, 0.0)$  at  $\zeta = 0$ . Additionally, to demonstrate stable roll waves with constant wave amplitude,  $u_r = 1.40125846997$  is chosen. The reason of choosing such exact value of  $u_r$  lies in the fact that only limited values in a certain range can exhibit stable roll waves with constant wave amplitude, which is discussed by Needham & Merkin (1984), Gray & Edwards (2014) in details.

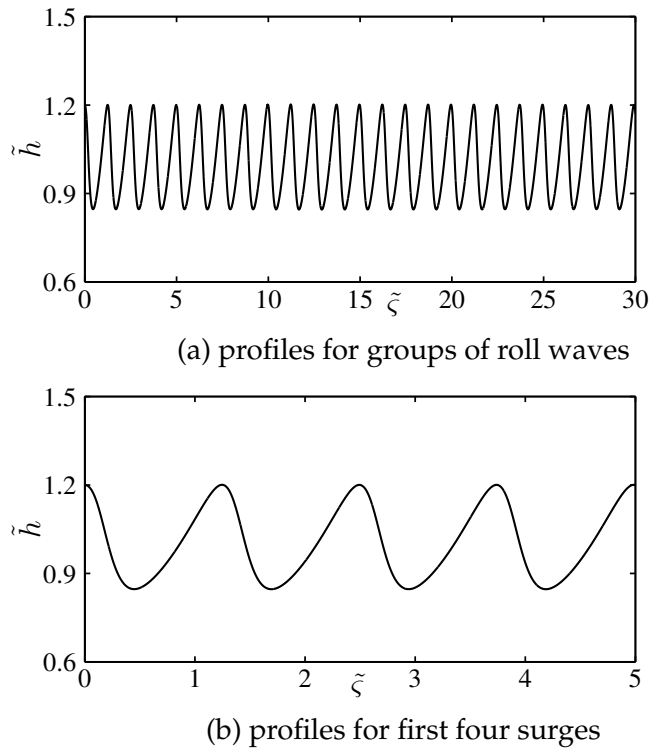


Figure 3.6: Profiles of groups of roll waves (panel (a)) and first four roll waves (panel (b)) obtained by  $Fr = 2.5$ ,  $Re = 20$ ,  $\eta_0 = 0.5$  and  $\phi_f = 0.5$

Here we adjust the appropriate value for  $u_r$  instead of lengthy mathematical formulation to demonstrate the stable roll waves shown in Fig. 3.6.

### 3.8 Conclusion

In this Chapter, a set of depth-averaged equations have been derived, which describe evolutions of flow height, depth-averaged volume fractions, and depth-averaged fluid and granular velocities. To scrutinize the depth-averaged equations, the steady unidirectional flows in rectangular channels are investigated to reveal the cross-stream profile of the downslope velocity. Additionally, the depth-averaged model equations are analyzed in terms of steady flows to demonstrate the blunt shape of the flow front and roll waves. More complex unsteady flows will be numerically simulated next Chapter.





## 4 Dynamical modelling of grain-fluid mixtures: simulation part

Model equations (3.84)-(3.86) and (3.90)-(3.92) comprise a strongly nonlinear partial differentiation equations system. Such a system allows the deformation of shock (large gradients of physical quantities), and as a result, it poses a challenge to numerical simulation. Hence, a sophisticated numerical scheme must be proposed in order to obtain a reliable solution. To this end, it is necessary to apply a non-oscillatory high-resolution numerical scheme as Wang et al. (2004) exhibited. In this Chapter, based on van Leer (2006), we briefly review the progress of high-resolution schemes, discuss the discretizations of two typical high-resolution schemes, and then present some numerical tests for simple and complex configurations.

### 4.1 Review of high-resolution shock-capturing schemes

The development of shock-capturing numerical schemes has a long history starting with the classical paper of Godunov (1959). The key idea of Godunov (1959) is to obtain the flux at the cell interface by virtue of solving Riemann's initial-value problem, that is, the problem of the inviscid interaction of two uniform gases at a plane interface. If the state equation of gas is simple, the exact solution in the perturbed region can be accomplished to any precision with an accepted computational effort, or in an approximate way (approximate Riemann solver) with less effort. Among all the approximate Riemann solvers, the most attracting approximations are developed by Roe (1981) and Harten, Lax & van Leer (1983). The former scheme-Roe (1981)-is based on a local linearization of the conservation equations, whereas the latter one-Harten et al. (1983)-constructs a conservative solution by requiring that two discontinuities propagate at predetermined speeds. Based on these two kinds of approximate Riemann solvers, many extensions have been proposed to investigate shallow granular flows last decades.

Denlinger & Iverson (2001) employed a Harten-Lax-vanLeer-Contact (or HLLC) approximate Riemann solver to generate solutions of a fluid saturated granular flow on a 3D topography. Pelanti et al. (2008) investigated grain-fluid mixture flows by proposing a Roe-type approximate Riemann solver that is based on the framework of high-resolution wave-propagation algorithms of LeVeque (1997). George (2008) presented a novel approximate Riemann solver that possesses the desirable qualities of Roe solver and HLLC-type solver (Einfeldt, Munz, Roe & Sjogreen 1991). These aforementioned schemes, based on approximate Riemann solvers, usually require field-by-

field decomposition that poses a computational burden for complex flows. Hence we will not adopt such schemes in our simulation.

Accompanied with the schemes based on Riemann solvers or approximate Riemann solvers is the history of high-resolution schemes. The development of high-resolution schemes dates back to Harten (1983). Based on the discovery that the total variation of the solution of a scalar 1-D conservation law cannot increase and in fact decreases in a shock, Harten (1983) introduced the total variation of a discrete function as a measure of its oscillation and furthermore formulated a non-oscillatory Total-Variation-Diminishing (TVD) scheme for scalar conservation law. Since then, various kinds of non-oscillatory high-resolution schemes have been proposed, for example the Non-Oscillatory Central scheme (NOC) of Nessyahu & Tadmor (1990), the Essentially Non-Oscillatory (ENO) scheme of Harten, Osher, Engquist & Chakravarthy (1986), and later Weighted version (WENO) of Jiang & Shu (1996).

The first version of NOC scheme is developed by Nessyahu & Tadmor (1990) who used Lax-Friedrichs scheme (Lax 1954) together with TVD-type piecewise linear reconstruction. The derived scheme gains advantage of the simplicity of the Riemann-solver-free approach. Because the scheme of Nessyahu & Tadmor (1990) (N-T) is easy to implement, it was widely adopted to simulate granular flows in the last decades. Tai, Noelle, Gray & Hutter (2001) investigated 2-D flow of a finite granular mass on an inclined plane by combining the N-T scheme with the front-tracking module. Wang et al. (2004) carefully inspected the optimal use of TVD limiters in simulating granular flows on a curved plane. Recently, Meng & Wang (2015b) applied the N-T scheme for grain-fluid mixture flows down a curved plane. A disadvantage of the N-T scheme needs to be mentioned. The N-T scheme suffers from excessive numerical viscosity when a sufficiently small time step is enforced for the sake of stability, see Section 4.3.2.

To overcome the weakness of the N-T scheme, Kurganov & Tadmor (2000) derived a new family of central schemes that suffers from a much smaller numerical viscosity. The main idea is the use of the characteristic structure to predict local propagation speeds of discontinuities at the interface between cells, and integrating conservation equations over Riemann fans of variable sizes. Moreover, Kurganov et al. (2001) extended the scheme of Kurganov & Tadmor (2000) by predicting the local propagation speeds of discontinuity at the interface between cells more precisely. The largest and smallest eigenvalues of the Jacobian  $\partial \mathbf{F} / \partial \mathbf{U}$  are used as one-sided local speeds of propagation, where  $\mathbf{F}$  is a numerical flux and  $\mathbf{U}$  is a conservation vector. The proposed scheme has an upwind nature such that it is often called central-upwind scheme. The applications of the central-upwind scheme for shallow geophysical flows can be found in Kurganov & Petrova (2007), Kurganov & Miller (2014) and Chertock, Kurganov & Wu (2015).

The ENO schemes, based on Harten et al. (1986), select the smoothest stencil among several candidates to reconstruct the conservation vector to a high order. In this way, the formulated schemes can avoid spurious oscillations in shocks. Moreover, the Weighted ENO schemes (see Liu, Osher & Chan (1994) and Jiang & Shu (1996)) use

a convex combination of all stencil candidates to achieve the non-oscillatory nature, while improving the order of accuracy by one. The applications of WENO schemes for geophysical flows can be seen in Xing & Shu (2005) and Sebastian, Xing & Shu (2007).

Below we focus on the discretizations of the NOC schemes due to their simplicity. Precisely, the model equations are rewritten in a conservation form for the convenience of discretization, which is presented in sec. 4.2. Then, the strategies of the N-T scheme and the central-upwind scheme are presented in sections 4.3 and 4.4, respectively. Moreover, we test the numerical solutions of these two schemes with an analytical solution in terms of a homogeneous mass flowing on an inclined plane, which is presented in sec. 4.5. Finally, the simulation of a grain-fluid mixture flowing on a curved plane is presented in sec. 4.6.

## 4.2 Standard form of the model equations

Both N-T and central-upwind schemes require that the model equations are rewritten in a conservation form. Moreover, to clearly show the strategies of the numerical schemes and avoid unnecessary mathematical formulations, 1-D equations (3.98)-(3.101) are taken as an example. We rewrite equations (3.98)-(3.101) in terms of the conservation variables, which are fluid thickness  $h_f = h_m \phi_f$ , granular thickness  $h_s = h_m \phi_s$ , depth-averaged downslope momenta  $m_f^x = h_f u_f$  for the fluid phase, and  $m_s^x = h_s u_s$  for the granular phase. With the vector of the conservation variables,  $\mathbf{U} = (h_f, h_s, m_f^x, m_s^x)$ , the model equations (3.98)-(3.101) can be rewritten as

$$\frac{\partial \mathbf{U}}{\partial t} + \frac{\partial \mathbf{F}(\mathbf{U})}{\partial x} = \mathbf{S}(\mathbf{U}) + \mathbf{Q}_1(\mathbf{U}) \frac{\partial \mathbf{Q}_2}{\partial x}, \quad (4.1)$$

where  $\mathbf{F}$  is the convective flux in the main flow direction,  $\mathbf{S}$  the source term, and  $\mathbf{Q}_1$  and  $\mathbf{Q}_2$  the nonconservative terms in the main flow direction. They are given by

$$\mathbf{U} = \begin{pmatrix} h_f \\ h_s \\ m_f^x \\ m_s^x \end{pmatrix}, \quad \mathbf{F} = \begin{pmatrix} m_f^x \\ m_s^x \\ (m_f^x)^2/h_f + \beta_f^x h_f (h_f + h_s)/2 \\ (m_s^x)^2/h_s + \beta_s^x h_s (h_f + h_s)/2 - \gamma \beta_f^x h_s (h_s + h_f)/2 \end{pmatrix}, \quad (4.2)$$

$$\mathbf{S} = \begin{pmatrix} 0 \\ 0 \\ \hat{s}_{x(f)} \\ \hat{s}_{x(s)} \end{pmatrix}, \quad \mathbf{Q}_1 = \begin{pmatrix} 0 & 0 & 0 & 0 \\ 0 & 0 & 0 & 0 \\ 0 & 0 & \epsilon \cos \zeta (h_s + h_f)^2/2 & 0 \\ 0 & 0 & 0 & \epsilon \gamma \cos \zeta (h_s + h_f)^2/2 \end{pmatrix}, \quad (4.3)$$

and

$$\mathbf{Q}_2 = \begin{pmatrix} 0 \\ 0 \\ h_f/(h_s + h_f) \\ h_s/(h_s + h_f) \end{pmatrix}. \quad (4.4)$$

### 4.3 The scheme of Nessyahu and Tadmor (1990)

#### 4.3.1 Strategy of N-T scheme

The non-oscillatory N-T scheme is a second-order-accuracy extension of the classical Lax (1954) by using a piecewise linear approximation for the reconstruction of the conservation vector  $\mathbf{U}$ . Let us briefly review the N-T scheme:

The vector system (4.1) is considered here, in which we set

$$\bar{\mathbf{U}}_j^n = \int_{x_j}^{x_{j+1}} \mathbf{U}(x, t^n) dx \quad (4.5)$$

to represent the cell average over the interval  $[x_{j-1/2}, x_{j+1/2}]$  at time  $t^n$ , and let

$$\mathbf{U}(x, t^n) = \bar{\mathbf{U}}_j^n + (x - x_j)(\bar{\mathbf{U}}_x)_j^n, \quad x_{j-1/2} \leq x \leq x_{j+1/2} \quad (4.6)$$

be a piecewise linear reconstruction over the cell. In relation (4.6),  $(\bar{\mathbf{U}}_x)_j^n$  represents the cell mean derivative determined by a TVD limiter. For example, a minmod-like limiter involving a parameter  $\theta$  can be used (see Kurganov & Tadmor (2000)),

$$(\bar{\mathbf{U}}_x)_j^n = MM\left(\theta \frac{\bar{\mathbf{U}}_j^n - \bar{\mathbf{U}}_{j-1}^n}{\Delta x}, \frac{\bar{\mathbf{U}}_{j+1}^n - \bar{\mathbf{U}}_{j-1}^n}{2\Delta x}, \theta \frac{\bar{\mathbf{U}}_{j+1}^n - \bar{\mathbf{U}}_j^n}{\Delta x}\right), \quad 1 \leq \theta \leq 2, \quad (4.7)$$

where  $\Delta x = x_{j+1/2} - x_{j-1/2}$  denotes the space step. The parameter  $\theta = 2$  corresponds to the least dissipative limiter, whereas  $\theta = 1$  reproduces the classical minmod limiter that ensures a non-oscillatory nature. The evaluation of  $\theta$  should be related to the physical problems. Alternatively, a UNO limiter of Harten & Osher (1982) can be also used, which is given by

$$(\bar{\mathbf{U}}_x)_j^n = MM\left(\Delta \mathbf{U}_{j-1/2}^n + \frac{1}{2}MM(\Delta^2 \bar{\mathbf{U}}_{j-1}^n, \Delta^2 \bar{\mathbf{U}}_j^n), \Delta \mathbf{U}_{j+1/2}^n - \frac{1}{2}MM(\Delta^2 \bar{\mathbf{U}}_j^n, \Delta^2 \bar{\mathbf{U}}_{j+1}^n)\right), \quad (4.8)$$

where  $\Delta \mathbf{U}_{j+1/2}^n = \bar{\mathbf{U}}_{j+1}^n - \bar{\mathbf{U}}_j^n$ ,  $\Delta^2 \bar{\mathbf{U}}_j^n = \bar{\mathbf{U}}_{j+1}^n - 2\bar{\mathbf{U}}_j^n + \bar{\mathbf{U}}_{j-1}^n$ , and the notion  $MM(\cdot, \cdot)$  stands for the usual limiter

$$MM(x, y) = \frac{1}{2}(\text{sgn}(x) + \text{sgn}(y)) \cdot \min(|x|, |y|). \quad (4.9)$$

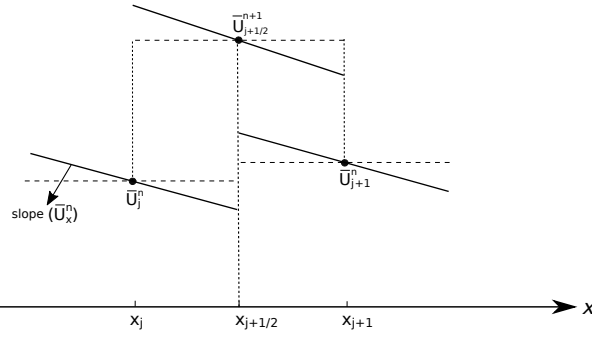


Figure 4.1: The N-T approach: staggered integration

In relation (4.9), the function “sgn” denotes the sign function. Compared to minmod-like limiter (4.7), the UNO limiter (4.8) gains advantage of higher accuracy, see Harten & Osher (1982).

To avoid solving the Riemann problem at the boundaries between the cells, the N-T scheme employs a staggered grid. As Fig. 4.1 shows, the cell average  $\bar{U}_{j+1/2}^{n+1}$  is evaluated over the interval  $[x_j, x_{j+1}]$  at the new time level  $t^{n+1} = t_n + \Delta t$ . The centers of the cells at the old time level  $t^n$  become the boundaries of the cells at  $t^{n+1}$ . With these descriptions, integrating the vector equation (4.1) over the cell  $[x_j, x_{j+1}]$  from  $t^n$  to  $t^{n+1}$ , one has

$$\begin{aligned} \bar{U}_{j+1/2}^{n+1} = & \int_{x_j}^{x_{j+1}} \mathbf{U}(x, t^n) dx - \int_{t_n}^{t^{n+1}} \mathbf{F}(x_{j+1}, t) dt \\ & + \int_{t_n}^{t^{n+1}} \mathbf{F}(x_j, t) dt + \int_{t_n}^{t^{n+1}} \int_{x_j}^{x_{j+1}} \mathbf{S}(x, t) dx dt + \int_{t_n}^{t^{n+1}} \int_{x_j}^{x_{j+1}} \mathbf{Q}_1 \frac{\partial \mathbf{Q}_2}{\partial x} dx dt. \end{aligned} \quad (4.10)$$

The first integration on the right-hand side of (4.10) can be written as

$$\begin{aligned} \int_{x_j}^{x_{j+1}} \mathbf{U}(x, t^n) dx &= \int_{x_j}^{x_{j+1/2}} \mathbf{U}(x, t^n) dx + \int_{x_{j+1/2}}^{x_{j+1}} \mathbf{U}(x, t^n) dx \\ &= \frac{1}{2}(\bar{U}_j^n + \bar{U}_{j+1}^n) - \frac{1}{8} \left[ (\bar{U}_x)_j^n - (\bar{U}_x)_{j+1}^n \right]. \end{aligned} \quad (4.11)$$

To streamline the rest of the integrations arising on the right-hand side of (4.10), it is necessary to ensure that the cell averages  $\bar{U}(x_j, t), \forall j$ , are smooth over the time interval  $[t^n, t^{n+1}]$ . Provided that the timestep  $\Delta t$  is reasonably restricted, the discontinuities at the interface  $x_{j+1/2}, \forall j$ , will not propagate to the cell averages at new time level  $t^{n+1}$ . Consequently, if  $\bar{U}(x_j, t^n), \forall j$ , is smooth, it remains smooth at  $t^{n+1}$ . The N-T scheme restricts the timestep by the Courant-Friedrichs-Lewy (CFL) condition,

$$\Delta t \leq \text{CFL} \frac{\Delta x}{a_{\max}}, \quad a_{\max} = \max_{\text{all } j} (|\lambda_j^{(1)}|, |\lambda_j^{(n)}|), \quad (4.12)$$

where  $a_{\max}$  represents global maximum characteristic speed,  $\lambda_j^{(1)}$  and  $\lambda_j^{(n)}$  are the minimum and maximum eigenvalues of the Jacobian matrix  $(\partial \mathbf{F} / \partial \mathbf{U})_j^n$ , and  $\text{CFL} < 0.5$  is experimentally needed, see Jiang & Tadmor (1998). Once the cell averages  $\bar{\mathbf{U}}(x_j, t)$ ,  $\forall j$ , are assured to be smooth over the time interval  $[t^n, t^{n+1}]$ , the integrations involving convective flux in (4.10) can be approximated by the midpoint quadrature rule, and the conservative vector  $\mathbf{U}$  at the midpoint can be predicted by Taylor expansion. This results in

$$\int_{t^n}^{t^{n+1}} \mathbf{F}(x_j, t) dt = \Delta t \mathbf{F}(\bar{\mathbf{U}}_j^{n+1/2}), \quad \bar{\mathbf{U}}_j^{n+1/2} = \bar{\mathbf{U}}_j^n + \frac{\Delta t}{2} (\partial \bar{\mathbf{U}} / \partial t)_j^n, \quad (4.13)$$

where the temporal derivative  $(\partial \bar{\mathbf{U}} / \partial t)_j^n$  can be determined as

$$(\partial \bar{\mathbf{U}} / \partial t)_j^n = -(\partial \mathbf{F} / \partial x)_j^n + \mathbf{S}_j^n + \left( \mathbf{Q}_1 \frac{\partial \mathbf{Q}_2}{\partial x} \right)_j^n \quad (4.14)$$

by vector equation (4.1). Similarly, the integration of the source term, arising in relation (4.10), is approximated as

$$\int_{t^n}^{t^{n+1}} \int_{x_j}^{x_{j+1}} \mathbf{S} dx dt = \frac{\Delta t}{2} (\mathbf{S}_j^{n+1/2} + \mathbf{S}_{j+1}^{n+1/2}). \quad (4.15)$$

The integration of the nonconservative terms, arising in relation (4.10), is approximated as

$$\int_{t^n}^{t^{n+1}} \int_{x_j}^{x_{j+1}} \mathbf{Q}_1 \frac{\partial \mathbf{Q}_2}{\partial x} dx dt = \frac{\Delta t}{2} \left[ (\mathbf{Q}_1)_j^{n+1/2} + (\mathbf{Q}_1)_{j+1}^{n+1/2} \right] \left[ (\mathbf{Q}_2)_{j+1}^{n+1/2} - (\mathbf{Q}_2)_j^{n+1/2} \right], \quad (4.16)$$

Substituting relations (4.11), (4.13), (4.15), (4.16) into relation (4.10), one has

$$\begin{aligned} \bar{\mathbf{U}}_{j+1/2}^{n+1} = & \frac{1}{2} (\bar{\mathbf{U}}_j^n + \bar{\mathbf{U}}_{j+1}^n) - \frac{1}{8} \left[ (\bar{\mathbf{U}}_x)_{j+1}^n - (\bar{\mathbf{U}}_x)_j^n \right] \\ & - \Delta t \left[ \mathbf{F}(\bar{\mathbf{U}}_{j+1}^{n+1/2}) - \mathbf{F}(\bar{\mathbf{U}}_j^{n+1/2}) \right] + \frac{\Delta t}{2} (\mathbf{S}_j^{n+1/2} + \mathbf{S}_{j+1}^{n+1/2}) \\ & + \frac{\Delta t}{2} \left[ (\mathbf{Q}_1)_j^{n+1/2} + (\mathbf{Q}_1)_{j+1}^{n+1/2} \right] \left[ (\mathbf{Q}_2)_{j+1}^{n+1/2} - (\mathbf{Q}_2)_j^{n+1/2} \right]. \end{aligned} \quad (4.17)$$

### 4.3.2 Remarks

For the N-T scheme, some aspects are worth highlighting. They are listed as follows:

1. The N-T scheme does not require characteristic decomposition and Riemann solvers. Hence, it gains the advantage of simplicity when compared to Godunov type upwind schemes, for example, see Denlinger & Iverson (2001) and George (2008).

2. The N-T scheme is a second-order accurate scheme. It is the extension of the stagger form of the first-order Lax (1954) scheme. When the derivatives of cell averages are zero and the functions at midpoint time  $t^{n+1/2}$  are replaced by the functions at time  $t^n$ , the scheme (4.17) reduces to

$$\begin{aligned} \bar{U}_{j+1/2}^{n+1} = & \frac{1}{2}(\bar{U}_j^n + \bar{U}_{j+1}^n) - \Delta t \left[ \mathbf{F}(\mathbf{U}_{j+1}^n) - \mathbf{F}(\mathbf{U}_j^n) \right] + \frac{\Delta t}{2}(\mathbf{S}_j^n + \mathbf{S}_{j+1}^n) \\ & + \frac{\Delta t}{2} \left[ (\mathbf{Q}_1)_j^n + (\mathbf{Q}_1)_{j+1}^n \right] \left[ (\mathbf{Q}_2)_{j+1}^n - (\mathbf{Q}_2)_j^n \right], \end{aligned} \quad (4.18)$$

which can be seen as the stagger form of the first-order Lax (1954) scheme.

3. The N-T scheme (4.17) does not admit a semi-discrete form. To make this point, we take the first-order form (4.18) as an example. By setting  $\Delta t \rightarrow 0$ , (4.18) reduces to

$$\begin{aligned} \frac{d\bar{U}_{j+1/2}}{dt} = & \frac{(\Delta x)^2}{8\Delta t} \frac{\partial^2 \bar{U}_{j+1/2}}{\partial x^2} - \left[ \mathbf{F}(\mathbf{U}_{j+1}^n) - \mathbf{F}(\mathbf{U}_j^n) \right] + \frac{1}{2}(\mathbf{S}_j^n + \mathbf{S}_{j+1}^n) \\ & + \frac{1}{2} \left[ (\mathbf{Q}_1)_j^n + (\mathbf{Q}_1)_{j+1}^n \right] \left[ (\mathbf{Q}_2)_{j+1}^n - (\mathbf{Q}_2)_j^n \right] + \mathcal{O}(\Delta x^4), \end{aligned} \quad (4.19)$$

where the first term on the right-hand side of (4.19) can be seen as a numerical viscosity, and the numerical viscosity is therefore on the order  $\mathcal{O}((\Delta x)^2/\Delta t)$ . In the presence of degenerate diffusion terms or stiff source terms, a sufficiently small timestep  $\Delta t$  is necessary for the sake of stability. However, the sufficiently small  $\Delta t$  leads to more numerical viscosity. Therefore, the N-T scheme is not suitable for the cases when a small timestep must be used. For our simulation, we will use N-T scheme in Section 4 and Section 6 but not in Section 7, since the simulation cases in Section 4 and Section 6 are convection-dominated problems and the case in Section 7 needs a small timestep for the purpose of stability.

4. The above derivation of the N-T scheme (4.17) is not limited to 1-D case. It can be generalized to 2-D scheme straightforward, which is given by

$$\begin{aligned} \bar{U}_{j+1/2, k+1/2}^{n+1} = & \frac{1}{4}(\bar{U}_{j,k}^n + \bar{U}_{j+1,k}^n + \bar{U}_{j,k+1}^n + \bar{U}_{j+1,k+1}^n) \quad (4.20) \\ & + \frac{1}{16}[(\bar{U}_x)_{j,k}^n - (\bar{U}_x)_{j+1,k}^n] - \frac{\Delta t}{2\Delta x} \left[ \mathbf{F}(\bar{U}_{j+1,k}^{n+1/2}) - \mathbf{F}(\bar{U}_{j,k}^{n+1/2}) \right] \\ & + \frac{1}{16}[(\bar{U}_x)_{j,k+1}^n - (\bar{U}_x)_{j+1,k+1}^n] - \frac{\Delta t}{2\Delta x} \left[ \mathbf{F}(\bar{U}_{j+1,k+1}^{n+1/2}) - \mathbf{F}(\bar{U}_{j,k+1}^{n+1/2}) \right] \\ & + \frac{1}{16}[(\bar{U}_y)_{j,k}^n - (\bar{U}_y)_{j,k+1}^n] - \frac{\Delta t}{2\Delta y} \left[ \mathbf{G}(\bar{U}_{j,k+1}^{n+1/2}) - \mathbf{G}(\bar{U}_{j,k}^{n+1/2}) \right] \\ & + \frac{1}{16}[(\bar{U}_y)_{j+1,k}^n - (\bar{U}_y)_{j+1,k+1}^n] - \frac{\Delta t}{2\Delta y} \left[ \mathbf{G}(\bar{U}_{j+1,k+1}^{n+1/2}) - \mathbf{G}(\bar{U}_{j+1,k}^{n+1/2}) \right] \\ & + \frac{\Delta t}{4} \left[ \mathbf{S}(\mathbf{U}_{i,j}^{n+1/2}) + \mathbf{S}(\mathbf{U}_{i+1,j}^{n+1/2}) + \mathbf{S}(\mathbf{U}_{i,j+1}^{n+1/2}) + \mathbf{S}(\mathbf{U}_{i+1,j+1}^{n+1/2}) \right]. \end{aligned}$$

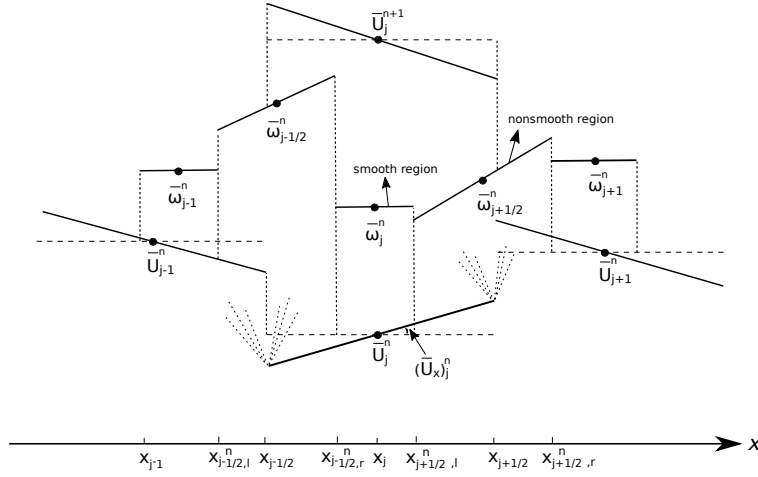


Figure 4.2: The strategy of the central-upwind scheme

## 4.4 Central-upwind scheme

### 4.4.1 Strategy of the central-upwind scheme

Similar to the N-T scheme, the central-upwind scheme also uses relation (4.6) to reconstruct the solution over the cell  $[x_{j-1/2}, x_{j+1/2}]$ . Distinguishing from the N-T scheme, the central-upwind scheme divides the intervals of the integration into the smooth and non-smooth regions, see Fig. 4.2. The non-smooth regions represent the intervals affected by the discontinuities at the interfaces  $x_{j+1/2}, \forall j$ , of cells, and the smooth regions represent the regions unaffected by the discontinuities at the interfaces of cells. The range of non-smooth regions can be estimated by the following. The local propagation speed of the discontinuity at the cell interfaces at the time level  $t^n$  is denoted by  $a_{j+1/2,r}^n$  towards the right side and by  $a_{j+1/2,l}^n$  towards the left side, respectively. The right- and left-sides local speeds  $a_{j+1/2,r}^n$  and  $a_{j+1/2,l}^n$  can be estimated as

$$a_{j+1/2,r}^n = \max(\lambda_{j+1/2,r}^{(n)}, \lambda_{j+1/2,l}^{(n)}, 0), \quad (4.21)$$

$$a_{j+1/2,l}^n = \min(\lambda_{j+1/2,r}^{(1)}, \lambda_{j+1/2,l}^{(1)}, 0) \quad (4.22)$$

where  $\lambda_{j+1/2,r}^{(n)}$  and  $\lambda_{j+1/2,l}^{(n)}$  represent the maximum eigenvalues of the matrix  $(\partial \mathbf{F} / \partial \mathbf{U})$ , respectively, with respect to the right-side value  $\mathbf{U}_{j+1/2,r}^n$  and the left-side value  $\mathbf{U}_{j+1/2,l}^n$ , whereas  $\lambda_{j+1/2,r}^{(1)}$  and  $\lambda_{j+1/2,l}^{(1)}$  represent the minimum eigenvalues of the matrix  $(\partial \mathbf{F} / \partial \mathbf{U})$ , respectively, with respect to  $\mathbf{U}_{j+1/2,r}^n$  and  $\mathbf{U}_{j+1/2,l}^n$ .

Moreover, the central-upwind scheme estimates that the discontinuity at  $x_{j+1/2}$  at  $t^n$  disperses to  $x_{j+1/2,r}^n$  towards the right direction at  $t^{n+1}$ , and to  $x_{j+1/2,l}^n$  towards the left direction, where  $x_{j+1/2,r}^n$  and  $x_{j+1/2,l}^n$  satisfy

$$x_{j+1/2,r}^n \approx x_{j+1/2} + a_{j+1/2,r}^n \Delta t, \quad x_{j+1/2,l}^n \approx x_{j+1/2} + a_{j+1/2,l}^n \Delta t. \quad (4.23)$$



Hence, the non-smooth region is estimated to lie in  $[x_{j+1/2,l}^n, x_{j+1/2,r}^n]$ . Correspondingly, the smooth interval of the cell  $[x_{j-1/2}, x_{j+1/2}]$  is estimated to be  $[x_{j-1/2,r}^n, x_{j+1/2,l}^n]$ .

The non-smooth region  $[x_{j+1/2,l}^n, x_{j+1/2,r}^n]$  is treated as Riemann fans and therefore handled in the same way as in the N-T scheme. Integrating the vector equation (4.1) over the interval  $[x_{j+1/2,l}^n, x_{j+1/2,r}^n] \times [t^n, t^{n+1}]$ , one has

$$\begin{aligned} \bar{\mathbf{w}}_{j+1/2}^{n+1} &= \frac{1}{\Delta x_{j+1/2}} \int_{x_{j+1/2,l}^n}^{x_{j+1/2,r}^n} \mathbf{U}(x, t^{n+1}) dx \\ &= \frac{1}{\Delta x_{j+1/2}} \int_{x_{j+1/2,l}^n}^{x_{j+1/2,r}^n} \mathbf{U}(x, t^n) dx - \frac{1}{\Delta x_{j+1/2}} \int_{t^n}^{t^{n+1}} \left[ \mathbf{F}(\mathbf{U}(x_{j+1/2,r}^n, t)) - \mathbf{F}(\mathbf{U}(x_{j+1/2,l}^n, t)) \right] dt \\ &\quad + \frac{\Delta t}{\Delta x_{j+1/2}} \left\{ \int_{x_{j+1/2,l}^n}^{x_{j+1/2,r}^n} \mathbf{S}(\mathbf{U}(x, t^{n+1/2})) dx + \int_{x_{j+1/2,l}^n}^{x_{j+1/2,r}^n} \left( \mathbf{Q}_1 \frac{\partial \mathbf{Q}_2}{\partial x} \right)^{n+1/2} dx \right\}, \end{aligned} \quad (4.24)$$

where  $\Delta x_{j+1/2} = x_{j+1/2,r}^n - x_{j+1/2,l}^n$ .

The first integration on the second line of relation (4.24) can be written as

$$\begin{aligned} &\frac{1}{\Delta x_{j+1/2}} \int_{x_{j+1/2,l}^n}^{x_{j+1/2,r}^n} \mathbf{U}(x, t^n) dx \\ &= \frac{1}{\Delta x_{j+1/2}} \left[ (a_{j+1/2,r}^n \bar{\mathbf{U}}_{j+1}^n - a_{j+1/2,l}^n \bar{\mathbf{U}}_j^n) \Delta t \right. \\ &\quad \left. - \frac{1}{2} (\bar{\mathbf{U}}_x)_j^n (\Delta x + a_{j+1/2,l}^n \Delta t) a_{j+1/2,l}^n \Delta t + \frac{1}{2} (\bar{\mathbf{U}}_x)_{j+1}^n (-\Delta x + a_{j+1/2,r}^n \Delta t) a_{j+1/2,r}^n \Delta t \right] \end{aligned} \quad (4.25)$$

by substituting relation (4.6).

The integrations of the flux, arising in relation (4.24), can be approximated by the midpoint quadrature rule. It results in

$$\int_{t^n}^{t^{n+1}} \left[ \mathbf{F}(\mathbf{U}(x_{j+1/2,r}^n, t)) - \mathbf{F}(\mathbf{U}(x_{j+1/2,l}^n, t)) \right] dt = \Delta t \left[ \mathbf{F}(\mathbf{U}_{x_{j+1/2,r}^n}^{n+1/2}) - \mathbf{F}(\mathbf{U}_{x_{j+1/2,l}^n}^{n+1/2}) \right]. \quad (4.26)$$

The integrations of source term and nonconservative term can be approximated as follows,

$$\int_{x_{j+1/2,l}^n}^{x_{j+1/2,r}^n} \mathbf{S}(\mathbf{U}(x, t^{n+1/2})) dx = \frac{\Delta x_{j+1/2}}{2} \left[ \mathbf{S}(\mathbf{U}(x_{j+1/2,r}^n, t^{n+1/2})) + \mathbf{S}(\mathbf{U}(x_{j+1/2,l}^n, t^{n+1/2})) \right], \quad (4.27)$$

$$\int_{x_{j+1/2,l}^n}^{x_{j+1/2,r}^n} \left( \mathbf{Q}_1 \frac{\partial \mathbf{Q}_2}{\partial x} \right)^{n+1/2} dx = \frac{\Delta x_{j+1/2}}{2} \left[ \left( \mathbf{Q}_1 \frac{\partial \mathbf{Q}_2}{\partial x} \right)_{x_{j+1/2,r}^n}^{n+1/2} + \left( \mathbf{Q}_1 \frac{\partial \mathbf{Q}_2}{\partial x} \right)_{x_{j+1/2,l}^n}^{n+1/2} \right]. \quad (4.28)$$

Substituting relations (4.25)-(4.28) into relation (4.24), one has

$$\begin{aligned} \bar{\mathbf{w}}_{j+1/2}^{n+1} = & \frac{1}{\Delta x_{j+1/2}} \left\{ (a_{j+1/2,r}^n \bar{\mathbf{U}}_{j+1}^n - a_{j+1/2,l}^n \bar{\mathbf{U}}_j^n) \Delta t \right. \\ & \left. - \frac{1}{2} \Delta t \left[ (\bar{\mathbf{U}}_x)_j^n (\Delta x + a_{j+1/2,l}^n \Delta t) a_{j+1/2,l}^n - (\bar{\mathbf{U}}_x)_{j+1}^n (-\Delta x + a_{j+1/2,r}^n \Delta t) a_{j+1/2,r}^n \right] \right\} \\ & - \frac{\Delta t}{\Delta x_{j+1/2}} \left[ \mathbf{F}(\mathbf{U}_{x_{j+1/2,r}^n}^{n+1/2}) - \mathbf{F}(\mathbf{U}_{x_{j+1/2,l}^n}^{n+1/2}) \right] + \frac{\Delta t}{2} \left[ \mathbf{S}(\mathbf{U}_{x_{j+1/2,r}^n}^{n+1/2}) + \mathbf{S}(\mathbf{U}_{x_{j+1/2,l}^n}^{n+1/2}) \right] \\ & + \frac{\Delta t}{2} \left[ \left( \mathbf{Q}_1 \frac{\partial \mathbf{Q}_2}{\partial x} \right)_{x_{j+1/2,r}^n}^{n+1/2} + \left( \mathbf{Q}_1 \frac{\partial \mathbf{Q}_2}{\partial x} \right)_{x_{j+1/2,l}^n}^{n+1/2} \right]. \end{aligned} \quad (4.29)$$

In the smooth region  $[x_{j-1/2,r}^n, x_{j+1/2,l}^n]$ , integrating the vector equation (4.1) can yield

$$\begin{aligned} \bar{\mathbf{w}}_j^{n+1} = & \bar{\mathbf{U}}_j^n + \frac{\Delta t}{2} (a_{j+1/2,l}^n + a_{j-1/2,r}^n) (\bar{\mathbf{U}}_x)_j^n - \frac{\Delta t}{\Delta x_j} \left[ \mathbf{F}(\mathbf{U}_{x_{j+1/2,l}^n}^{n+1/2}) - \mathbf{F}(\mathbf{U}_{x_{j-1/2,r}^n}^{n+1/2}) \right] \\ & + \frac{\Delta t}{2} \left[ \mathbf{S}(\mathbf{U}(x_{j+1/2,l}^n, t^{n+1/2})) + \mathbf{S}(\mathbf{U}(x_{j-1/2,r}^n, t^{n+1/2})) \right] \\ & + \frac{\Delta t}{2} \left[ \left( \mathbf{Q}_1 \frac{\partial \mathbf{Q}_2}{\partial x} \right)_{x_{j+1/2,l}^n}^{n+1/2} + \left( \mathbf{Q}_1 \frac{\partial \mathbf{Q}_2}{\partial x} \right)_{x_{j-1/2,r}^n}^{n+1/2} \right], \end{aligned} \quad (4.30)$$

where  $\bar{\mathbf{w}}_j^{n+1} = \int_{x_{j-1/2,r}^n}^{x_{j+1/2,l}^n} \bar{\mathbf{U}}(x, t^{n+1}) dx / \Delta x_j$  and  $\Delta x_j = x_{j+1/2,l}^n - x_{j-1/2,r}^n$ .

The values of the conservative vector at midtime  $t^{n+1/2}$ , arising in relations (4.24)-(4.30), can be obtained by Taylor expansion,

$$\mathbf{U}(x_{j+1/2,l}^n, t^{n+1/2}) \quad (4.31)$$

$$\approx \mathbf{U}(x_{j+1/2,l}^n, t^n) - \frac{\Delta t}{2} \frac{\partial \mathbf{F}(\mathbf{U}_{x_{j+1/2,l}^n}^n)}{\partial x} + \frac{\Delta t}{2} \mathbf{S}(\mathbf{U}_{x_{j+1/2,l}^n}^n) + \frac{\Delta t}{2} \left( \mathbf{Q}_1 \frac{\partial \mathbf{Q}_2}{\partial x} \right)_{x_{j+1/2,l}^n}^n,$$

$$\mathbf{U}(x_{j+1/2,r}^n, t^{n+1/2}) \quad (4.32)$$

$$\approx \mathbf{U}(x_{j+1/2,r}^n, t^n) - \frac{\Delta t}{2} \frac{\partial \mathbf{F}(\mathbf{U}_{x_{j+1/2,r}^n}^n)}{\partial x} + \frac{\Delta t}{2} \mathbf{S}(\mathbf{U}_{x_{j+1/2,r}^n}^n) + \frac{\Delta t}{2} \left( \mathbf{Q}_1 \frac{\partial \mathbf{Q}_2}{\partial x} \right)_{x_{j+1/2,r}^n}^n,$$

where  $U(x_{j+1/2,l}^n, t^n)$  and  $U(x_{j+1/2,r}^n, t^n)$  satisfy

$$U(x_{j+1/2,l}^n, t^n) = \bar{U}_j^n + \left( \frac{\Delta x}{2} + a_{j+1/2,l}^n \Delta t \right) (\bar{U}_x)_j^n, \quad (4.33)$$

$$U(x_{j+1/2,r}^n, t^n) = \bar{U}_{j+1}^n + \left( -\frac{\Delta x}{2} + a_{j+1/2,r}^n \Delta t \right) (\bar{U}_x)_{j+1}^n \quad (4.34)$$

according to relation (4.6).

For the convenience of numerical implementation, the central-upwind scheme adopts nonstaggered grids. It projects the averages back onto the uniform nonstaggered grid  $[x_{j-1/2}, x_{j+1/2}]$ ,  $\forall j$ . To this end, based on the cell averages,  $\bar{w}_{j+1/2}^{n+1}$  and  $\bar{w}_j^{n+1}$  given by (4.29) and (4.30), a conserved piecewise-linear approximation can be taken as follows

$$\begin{aligned} w(x, t^{n+1}) = & \sum_j \left\{ \left[ \bar{w}_{j+1/2}^{n+1} + (\bar{w}_x)_{j+1/2}^{n+1} \left( x - \frac{x_{j+1/2,l}^n + x_{j+1/2,r}^n}{2} \right) \right] \chi_{[x_{j+1/2,l}^n, x_{j+1/2,r}^n]} \right. \\ & \left. + \bar{w}_j^{n+1} \chi_{[x_{j-1/2,r}^n, x_{j+1/2,l}^n]} \right\}, \end{aligned} \quad (4.35)$$

where  $\chi$  denotes the characteristic function satisfying

$$\chi_{[x_{j+1/2,l}^n, x_{j+1/2,r}^n]} = \begin{cases} 1, & \text{if } x \in [x_{j+1/2,l}^n, x_{j+1/2,r}^n], \\ 0, & \text{otherwise.} \end{cases} \quad (4.36)$$

To avoid spurious oscillation, the spatial derivative  $(\bar{w}_x)_{j+1/2}^{n+1}$  in relation (4.35) is approximated by

$$(\bar{w}_x)_{j+1/2}^{n+1} = 2MM \left( \frac{\bar{w}_{j+1}^{n+1} - \bar{w}_{j+1/2}^{n+1}}{x_{j+3/2,l}^n - x_{j+1/2,l}^n}, \frac{\bar{w}_{j+1/2}^{n+1} - \bar{w}_j^{n+1}}{x_{j+1/2,r}^n - x_{j-1/2,r}^n} \right). \quad (4.37)$$

Finally, the desired cell averages are obtained by projecting  $w(x, t^{n+1})$  back onto the grid  $[x_{j-1/2}, x_{j+1/2}]$ , namely, computing the cell-averages

$$\bar{U}_j^{n+1} = \frac{1}{\Delta x} \int_{x_{j-1/2}}^{x_{j+1/2}} w(x, t^{n+1}) dx. \quad (4.38)$$

It results in a fully discrete scheme. For the sake of brevity, we do not explicitly indicate the form of fully discrete scheme. Instead, we focus on a much simpler semi-discrete format. The semi-discrete form is then defined by the following limit

$$\begin{aligned} \frac{d\bar{U}_j}{dt} \Big|_{t=t^n} &= \lim_{\Delta t \rightarrow 0} \frac{\bar{U}_j^{n+1} - \bar{U}_j^n}{\Delta t} = \lim_{\Delta t \rightarrow 0} \frac{1}{\Delta t} \left[ \frac{1}{\Delta x} \int_{x_{j-1/2}}^{x_{j+1/2}} w(x, t^{n+1}) dx - \bar{U}_j^n \right] \\ &= \frac{a_{j-1/2,r}}{\Delta x} \lim_{\Delta t \rightarrow 0} \bar{w}_{j-1/2}^{n+1} + \lim_{\Delta t \rightarrow 0} \frac{1}{\Delta t} \left( \frac{x_{j+1/2,l}^n - x_{j-1/2,r}^n}{\Delta x} \bar{w}_j^{n+1} - \bar{U}_j^n \right) \\ &\quad - \frac{a_{j+1/2,l}}{\Delta x} \lim_{\Delta t \rightarrow 0} \bar{w}_{j+1/2}^{n+1}. \end{aligned} \quad (4.39)$$

The three limits in relation (4.39) can be computed separately. The limit  $\lim_{\Delta t \rightarrow 0} \bar{\mathbf{w}}_{j+1/2}^{n+1}$  can be formulated as

$$\lim_{\Delta t \rightarrow 0} \bar{\mathbf{w}}_{j+1/2}^{n+1} = \frac{a_{j+1/2,r} \mathbf{U}_{j+1/2,r}^n - a_{j+1/2,l} \mathbf{U}_{j+1/2,l}^n}{a_{j+1/2,r} - a_{j+1/2,l}} - \frac{\mathbf{F}(\mathbf{U}_{j+1/2,r}^n) - \mathbf{F}(\mathbf{U}_{j+1/2,l}^n)}{a_{j+1/2,r} - a_{j+1/2,l}} \quad (4.40)$$

by substituting (4.29), where we used the following identities

$$\lim_{\Delta t \rightarrow 0} \mathbf{U}(x_{j+1/2,r}^n, t^{n+1/2}) = \mathbf{U}_{j+1/2,r}^n, \quad \lim_{\Delta t \rightarrow 0} \mathbf{U}(x_{j+1/2,l}^n, t^{n+1/2}) = \mathbf{U}_{j+1/2,l}^n. \quad (4.41)$$

Similarly, the second limit, arising in relation (4.39), can be simplified as follows

$$\begin{aligned} & \lim_{\Delta t \rightarrow 0} \frac{1}{\Delta t} \left( \frac{x_{j+1/2,l}^n - x_{j-1/2,r}^n}{\Delta x} \bar{\mathbf{w}}_j^{n+1} - \bar{\mathbf{U}}_j^n \right) \\ &= \frac{a_{j+1/2,l}^n \mathbf{U}_{j+1/2,l}^n - a_{j-1/2,r}^n \mathbf{U}_{j-1/2,r}^n}{\Delta x} - \frac{\mathbf{F}(\mathbf{U}_{j+1/2,l}^n) - \mathbf{F}(\mathbf{U}_{j-1/2,r}^n)}{\Delta x} \\ &+ \frac{1}{2} \left[ \left( \mathbf{Q}_1 \frac{\partial \mathbf{Q}_2}{\partial x} \right)_{j+1/2,l}^n + \left( \mathbf{Q}_1 \frac{\partial \mathbf{Q}_2}{\partial x} \right)_{j-1/2,r}^n \right] \\ &+ \frac{1}{2} \left[ \mathbf{S}(\mathbf{U}_{j+1/2,l}^n) + \mathbf{S}(\mathbf{U}_{j-1/2,r}^n) \right], \end{aligned} \quad (4.42)$$

where the terms involving the source and nonconservative terms can be approximated as follows in practice,

$$\frac{1}{2} \left[ \mathbf{S}(\mathbf{U}_{j+1/2,l}^n) + \mathbf{S}(\mathbf{U}_{j-1/2,r}^n) \right] = \mathbf{S}(\mathbf{U}_j^n), \quad (4.43)$$

$$\frac{1}{2} \left[ \left( \mathbf{Q}_1 \frac{\partial \mathbf{Q}_2}{\partial x} \right)_{j+1/2,l}^n + \left( \mathbf{Q}_1 \frac{\partial \mathbf{Q}_2}{\partial x} \right)_{j-1/2,r}^n \right] = \left( \mathbf{Q}_1 \frac{\partial \mathbf{Q}_2}{\partial x} \right)_j^n. \quad (4.44)$$

Substitution of relations (4.40) and (4.42)-(4.44) into relation (4.39) can lead to the final semi-discrete form,

$$\frac{d\bar{\mathbf{U}}_j}{dt} = - \frac{\mathbf{H}_{j+1/2}(t) - \mathbf{H}_{j-1/2}(t)}{\Delta x} + \mathbf{S}(\mathbf{U}_j) + \left( \mathbf{Q}_1 \frac{\partial \mathbf{Q}_2}{\partial x} \right)_j, \quad (4.45)$$

where the flux  $\mathbf{H}_{j+1/2}$  is given by

$$\begin{aligned} & \mathbf{H}_{j+1/2}(t) \\ &= \frac{a_{j+1/2,r} \mathbf{F}(\mathbf{U}_{j+1/2,l}) - a_{j+1/2,l} \mathbf{F}(\mathbf{U}_{j+1/2,r})}{a_{j+1/2,r} - a_{j+1/2,l}} + \frac{a_{j+1/2,r} a_{j+1/2,l}}{a_{j+1/2,r} - a_{j+1/2,l}} (\mathbf{U}_{j+1/2,r} - \mathbf{U}_{j+1/2,l}). \end{aligned} \quad (4.46)$$

The derivative  $\partial \mathbf{Q}_2 / \partial x$ , arising in relation (4.45), can be determined by a minmod limiter

$$\left( \frac{\partial \mathbf{Q}_2}{\partial x} \right)_j = MM \left( \frac{(\mathbf{Q}_2)_j - (\mathbf{Q}_2)_{j-1}}{\Delta x}, \frac{(\mathbf{Q}_2)_{j+1} - (\mathbf{Q}_2)_j}{\Delta x} \right). \quad (4.47)$$

The semi-discrete scheme (4.45), using (4.46) and (4.47), is an Ordinary Differential Equation (ODE) system which can be solved by a stable ODE solver. To this end, we refer to the second-order Runge-Kutta (RK) method of Shu & Osher (1988) to discretise the temporal derivative. The RK scheme is outlined as follows

$$\begin{aligned}\bar{U}_j^{(1)} &= \bar{U}_j^n + \Delta t C[\bar{U}_j^n] \\ \bar{U}_j^{(2)} &= \frac{1}{2}\bar{U}_j^n + \frac{1}{2}(\bar{U}_j^{(1)} + \Delta t C[\bar{U}_j^{(1)}]) \\ \bar{U}^{n+1} &= \bar{U}_j^{(2)},\end{aligned}\tag{4.48}$$

where  $C[\bar{U}_j^n]$  is given by

$$C[\bar{U}_j^n] = -\frac{H_{j+1/2}^n - H_{j-1/2}^n}{\Delta x} + \mathbf{S}(\mathbf{U}_j^n) + \left( \mathbf{Q}_1 \frac{\partial \mathbf{Q}_2}{\partial x} \right)_j^n.\tag{4.49}$$

#### 4.4.2 Remarks of the central-upwind scheme

For the semi-discrete scheme (4.45), some aspects are worth to be highlighted. They are given as follows,

1. The semi-discrete scheme does not require characteristic decompositions and Riemann solvers. Consequently, similar to the N-T scheme, it possess the advantage of simplicity when compared to the Godunov upwind schemes (see Denlinger & Iverson (2001) and George (2008)).
2. The present semi-discrete scheme (4.45) has second-order accuracy in space. When the slopes of piecewise linear cells are zero, the second-order version reduces to the first-order version. Moreover, the first-order version can reduce to the standard upwind scheme, when the Jacobian matrix  $\mathbf{A} = \partial \mathbf{F} / \partial \mathbf{U}$  is positive or negative definite. For example, if  $\mathbf{A}$  is positive definite, then  $a_{j+1/2,l} = 0, \forall j$ , and the scheme (4.45) reduces to

$$\frac{d\bar{U}_j}{dt} = -\frac{\mathbf{F}(\mathbf{U}_j) - \mathbf{F}(\mathbf{U}_{j-1})}{\Delta x} + \mathbf{S}_j + \left( \mathbf{Q}_1 \frac{\partial \mathbf{Q}_2}{\partial x} \right)_j.\tag{4.50}$$

This is the reason to name this scheme central-upwind scheme.

3. The numerical viscosity of the semi-discrete scheme (4.45) is independent of  $\mathcal{O}(1/\Delta t)$ . Consequently, the scheme (4.45) can be applied to compute steady problems. When compared with the N-T scheme, the present central-upwind scheme estimates the Riemann fans more accurately, and therefore, it suffers from less dissipation. It can be applied when a small timestep is required.

4. The above derivation of the scheme (4.45) is not limited to 1-D situation. It can be generalized to solve 2-D equations (3.84)-(3.86) and (3.90)-(3.92) straightforward. The 2-D semi-discrete scheme takes the form,

$$\begin{aligned} \frac{d\bar{U}_{j,k}}{dt} = & - \frac{\mathbf{H}_{j+1/2,k}^x(t) - \mathbf{H}_{j-1/2,k}^x(t)}{\Delta x} - \frac{\mathbf{H}_{j,k+1/2}^y(t) - \mathbf{H}_{j,k-1/2}^y(t)}{\Delta y} \\ & + \mathbf{S}_{j,k} + \left( \mathbf{Q}_1 \frac{\partial \mathbf{Q}_2}{\partial x} \right)_{j,k} + \left( \mathbf{Q}_1 \frac{\partial \mathbf{Q}_3}{\partial y} \right)_{j,k}. \end{aligned} \quad (4.51)$$

## 4.5 Numerical tests

To inspect the N-T and central-upwind schemes, a simple but helpful numerical test is executed. In this test, a grain-fluid mixture, initially at rest with the height profile ( $h_m$ ) and solid volume fraction profile ( $\phi_s$ ),

$$(h_m, \phi_s) = [h_0(1 - H(x)), \phi_0(1 - H(x))], \quad h_0, \phi_0 > 0, \quad (4.52)$$

is suddenly released at  $t = 0$ , and then slides down an inclined plane with an inclination angle of  $\zeta = 40^\circ$ . In (4.52),  $H(x)$  represents Heavside step function, and  $h_0$  is set  $h_0 = 1$  and  $\phi_0$  is set  $\phi_0 = 0.5$ . Different choices of  $h_0$  and  $\phi_0$  do not affect the following analysis.

The fluid phase in the mixture is assumed to be ideal, and a 2-D flow on a rough inclined plane is investigated. Moreover, we assume that the viscous drag force is strong enough such that the two components of the mixture move downslope with the same velocity  $u$ . In this case, summation of (3.98) and (3.99) can yield the balance equation of mass for the mixture as a whole. Combining (3.100) and (3.101) to eliminate the viscous drag force can yield the balance equation of momentum for the mixture. The balance equations for the mixture as a whole are given by

$$\frac{\partial h_m}{\partial t} + \frac{\partial}{\partial x}(h_m u) = 0, \quad (4.53)$$

$$\frac{\partial}{\partial t}(h_m u) + \frac{\partial}{\partial x} \left( h_m u^2 + \frac{\epsilon \cos \zeta}{2} h_m^2 \right) = h_m s, \quad (4.54)$$

where  $K_x = 1$  is used, and the source term is written as

$$s = \sin \zeta - \tan \delta (\rho - \tilde{\rho}_f) \cos \zeta / \rho. \quad (4.55)$$

Referring to Faccononi & Mangeney (2012), the exact solutions of the height  $h_m$  and the phase equilibrium velocity  $u$  for equations (4.53) and (4.54) can be given by

$$h_m(x, t) = \begin{cases} h_0, & \text{if } x \leq \left(\frac{st}{2} - c_L\right) t, \\ \frac{1}{9 \cos \zeta} \left(2c_L - \frac{x}{t} + \frac{st}{2}\right)^2, & \text{if } \left(\frac{st}{2} - c_L\right) t < x \leq \left(2c_L + \frac{st}{2}\right) t, \\ 0, & \text{if } x > \left(2c_L + \frac{st}{2}\right) t, \end{cases} \quad (4.56)$$

and

$$u(x, t) = \begin{cases} st, & \text{if } x \leq \left(\frac{st}{2} - c_L\right) t, \\ \frac{2}{3} \left(c_L + \frac{x}{t} + st\right), & \text{if } \left(\frac{st}{2} - c_L\right) t < x \leq \left(2c_L + \frac{st}{2}\right) t, \\ 0, & \text{if } x > \left(2c_L + \frac{st}{2}\right) t, \end{cases} \quad (4.57)$$

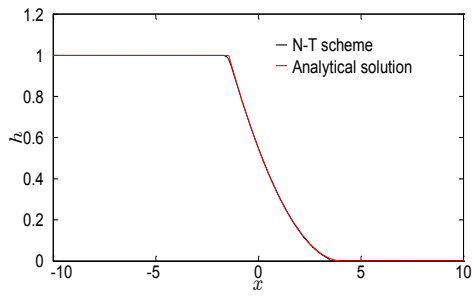
where the non-dimensional wave celerity  $c_L$  is  $c_L = \sqrt{h_0 \cos \zeta}$ .

For this case, we employ N-T scheme and central-upwind scheme to solve the vector equation (4.1), respectively. The numerical simulations are performed with 2000 elements for the computational domain  $x \in [-10, 10]$ , and with CFL = 0.1 to determine the timestep  $\Delta t$  according to relation (4.12). The obtained numerical results are verified by the analytical solutions (4.56) and (4.57), which are presented in Fig. 4.3. The numerical results demonstrate excellent agreements with the analytical solutions, and no visible difference is detected. Both N-T and central-upwind schemes do not show oscillations. Additionally, the case in question is a convection-dominated problem. As a result, there does not exist the excessive numerical dissipation when the N-T scheme is applied, as evidenced in Fig. 4.3. In the following, the N-T scheme is adopted to discretize the present saturated model and the two-layer model presented in next Chapter.

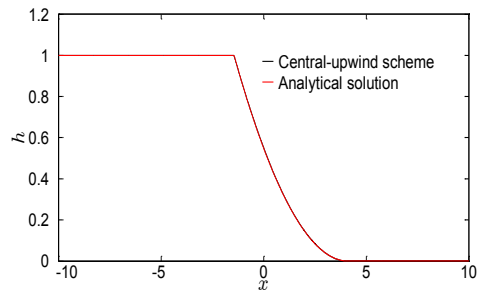
## 4.6 Numerical simulations of grain-fluid mixture flows

### 4.6.1 A typical simulation of a grain-fluid mixture flow

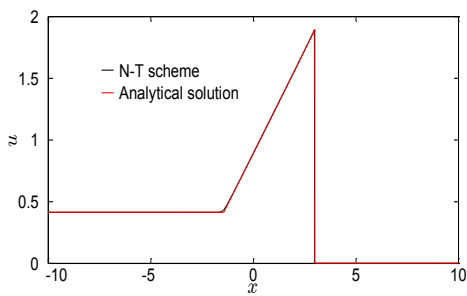
This part aims to demonstrate the general flow pattern, and we consequently take a three-dimensional chute into account. This chute consists of a flat upper part ( $x \leq 24$ ) inclined at an angle of  $40^\circ$  and a horizontal flat part ( $x \geq 40$ ) connected smoothly with the upper inclined plane by a transition zone lying in  $x \in [24, 40]$ . The lateral direction of the chute is assumed to be flat. An overview of this chute is shown in Fig. 3.1. A grain-fluid mixture of a finite mass sliding on this chute is investigated herein. The mixture is released suddenly at  $t = 0$  from an ellipsoidal shell with the following initial height profile,



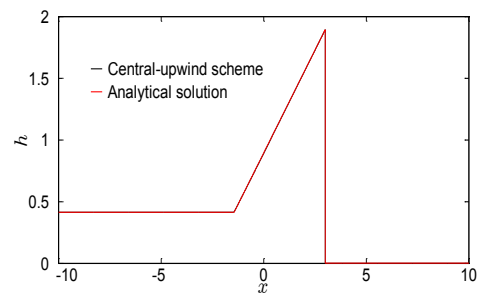
(a)  $t = 2$



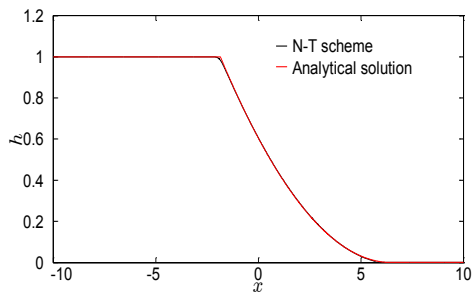
(b)  $t = 2$



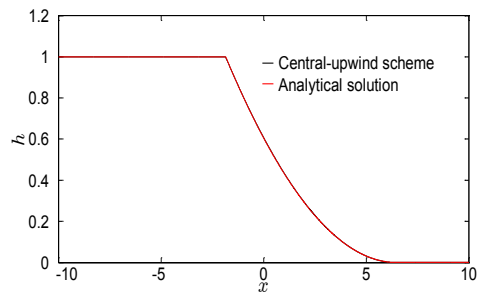
(c)  $t = 2$



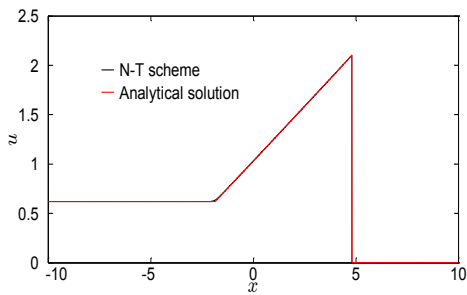
(d)  $t = 2$



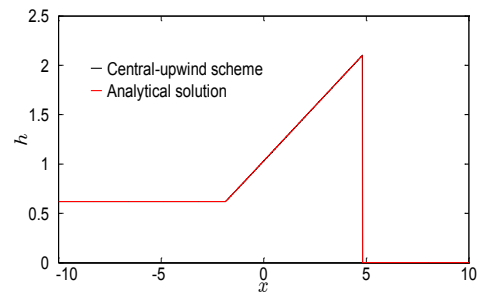
(e)  $t = 3$



(f)  $t = 3$



(g)  $t = 3$



(h)  $t = 3$

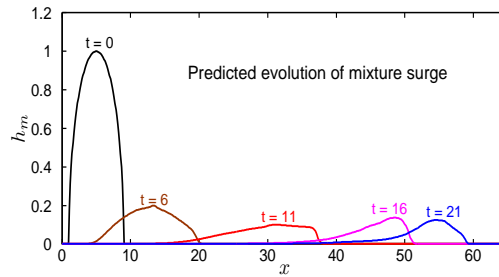
Figure 4.3: Comparison of the height and velocity profiles with the analytical solutions at times  $t = 2$  and  $t = 3$ , where the velocity profiles corresponds to the computational nodes of  $h \geq 0.04$ .



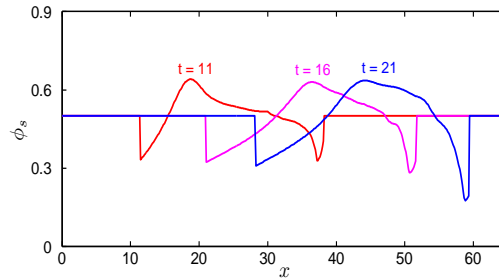
$$h_m(x, y, t = 0) = h_{\max}^{\text{ini}} \left( 1 - \frac{(x - x_0)^2}{a^2} - \frac{(y - y_0)^2}{b^2} \right), \quad (4.58)$$

where the long semi-axis length is  $a = 4$ , the short semi-axis length is  $b = 2$ , and the maximum height is  $h_{\max}^{\text{ini}} = 1$ . The center of the shell is initially located at  $(x_0, y_0) = (5, 0)$ . The initial geometries of the mixture chosen here are very similar to those used to investigate pure granular and grain-fluid mixture flows previously (see Chiou et al. (2005), Pudasaini et al. (2005), etc.). The computational domain (bed topography) is chosen to be a rectangle  $x \in [-10, 70]$  (in the down-slope direction) and  $y \in [-18, 18]$  (in the cross-slope direction), which is sufficiently large that no mass will flow out across the boundary of the domain. The inclination angle of the computational domain is prescribed by

$$\zeta(x) = \begin{cases} \zeta_0, & 0 \leq x \leq 24, \\ \zeta_0(1 - (x - 24)/10), & 24 < x < 40, \\ 0^\circ, & x \geq 40, \end{cases} \quad (4.59)$$



(a) Height profile along the central line of the flow



(b) Solid volume fraction profile along the central line of the flow

Figure 4.4: Height and solid volume fraction profiles obtained by the following parameters,  $\gamma = 0.4$ ,  $\vartheta = 8$ ,  $\delta = 33^\circ$ , and  $k_f^b = 1000$ ,  $N_R = 3 \times 10^5$ ,  $K_x = K_y = 1$  and homogeneous initial volume fractions  $\phi_s = \phi_f = 0.5$ .

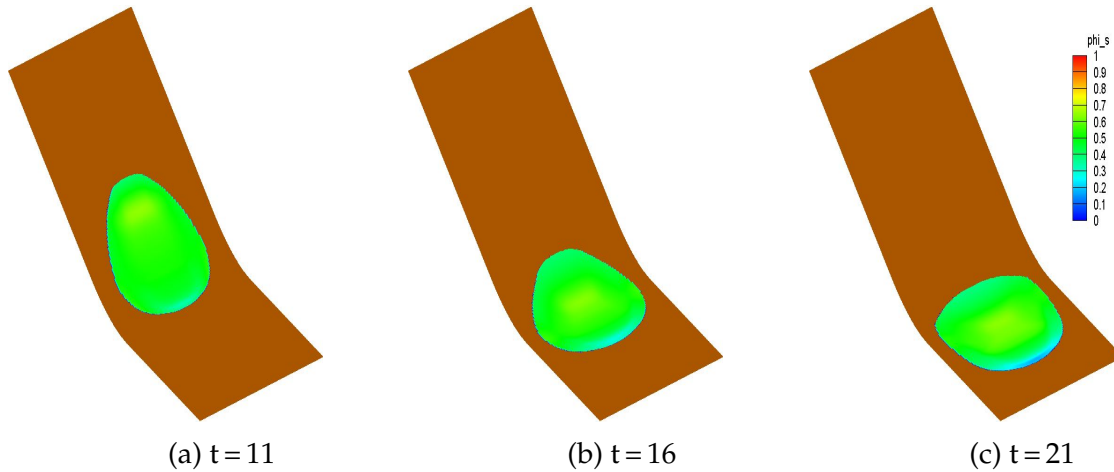


Figure 4.5: Three dimensional geometries of the debris flows at dimensionless times  $t = 11$ , 16 and 21, computed using the same parameters as Figure 4.4. The colors indicate the solid volume fraction.

where  $\zeta_0 = 40^\circ$ . The bed topography chosen here represents a typical, simplified mountain slope. In our simulation, the computational domain is discretized by a number of 600 ( $x$ -axis)  $\times$  100 ( $y$ -axis) elements.

Fig. 4.4 indicates the height and solid volume fraction profiles of a grain-fluid mixture flow along the longitudinal central symmetric section,  $y = 0$ , for various times, respectively. It is clearly seen from Fig. 4.4(a) that when the mixture is initially released, the mass body driven by the gravity force quickly accelerates downslope. The front accelerates more rapidly than the tail, so that the body is constantly elongated until the flow snout approaches a horizontal run-out zone. Then, the main body contracts. Additionally, Fig. 4.4(b) reflects that the fluid phase is transported to the front immediately after the release of the mixture, due to the fact the fluid is experienc-

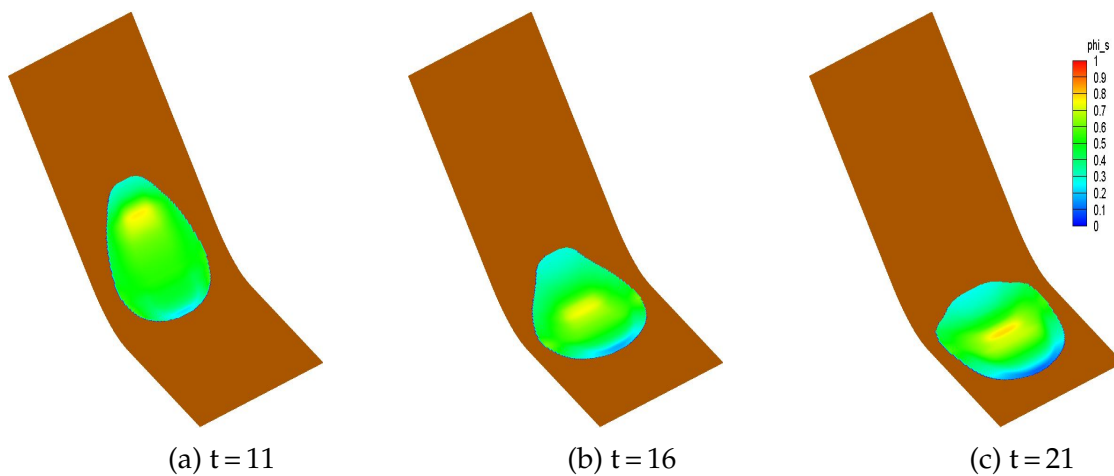
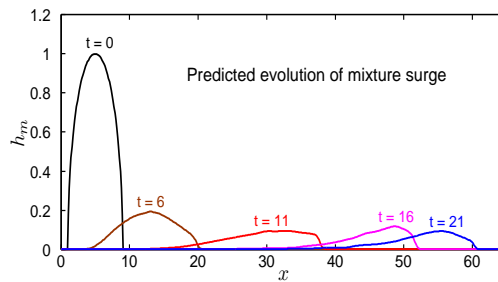
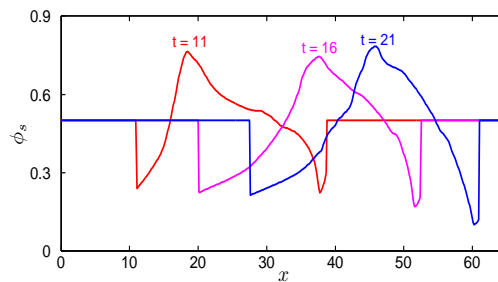


Figure 4.6: Three dimensional geometries of the debris flows at dimensionless times  $t = 11$ , 16 and 21, obtained by the same parameters to Figure 4.5 but with an exception of a smaller drag coefficient  $\vartheta = 4$ .



(a) Height profile along the central line of the flow



(b) Solid volume fraction profile along the central line of the flow

Figure 4.7: Height and solid volume fraction profiles, obtained by the same parameters to Figure 4.6.

ing a smaller bed friction than the granular phase. As the mixture descends further downslope, the accumulation of the fluid in the flow front is more apparent. The evolutions of the mixture shape and volume fractions can be also demonstrated in the three-dimensional overview of the flow pattern in Fig. 4.5. Fig. 4.5 shows that the fluid accumulates not only in the front, but also in the margin of the mixture body. Actually, this phenomenon is more evident when the fluid phase in the mixture is less viscous, indicating a smaller drag coefficient, see Fig. 4.6. Additionally, a notable phenomenon takes place when the fluid phase in the mixture is less viscous, see Fig. 4.7. Fig. 4.7(b) reflects that the solid volume fraction can go beyond the maximum packing fraction  $\phi_{\max} \approx 0.675$  corresponding for the possibly densest packing of the same size spherical particles, which is obviously non-physical. When this non-physical result occurs, it indicates that an unsaturated flow develops. To cope with this difficulty, we will develop a two-layer model presented in Chapter 7.

## 4.6.2 Validation of the present model

To validate the present model, we compare the numerical solutions with experimental data of Iverson et al. (2010). The experiment illustrates a large-scale flow, in which the initial sand-gravel-mud mixture is placed behind a gate with an initial geometry

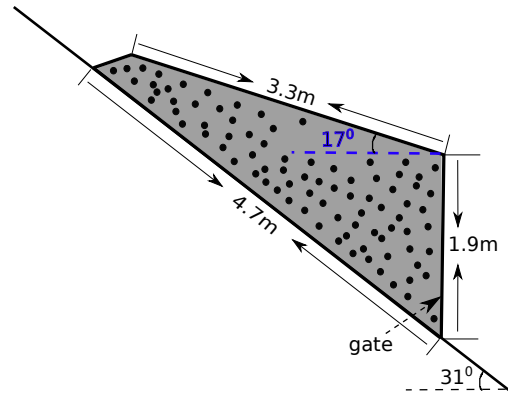


Figure 4.8: Initial homogenous fluid-grain mixture is placed behind a vertical gate at  $x = 0$ .

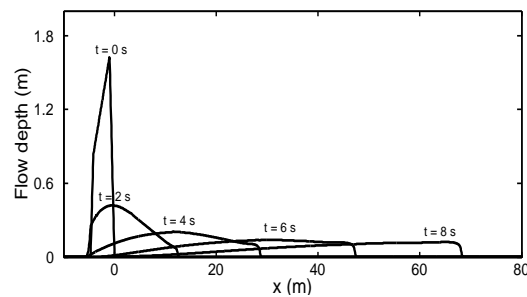
Table 4.1: Material properties used in the experiment and our computation

Property	Experimental values	Model values
Fluid density, $\tilde{\rho}_f$ ( $\text{kg}/\text{m}^3$ )	1100	1100
Solid density, $\tilde{\rho}_s$ ( $\text{kg}/\text{m}^3$ )	2700	2700
Initial solid volume fraction, $\phi_s$	$0.61 \pm 0.04$	0.62
Initial basal pore pressure, $p_f^{(b)}$ (Pa)	hydrostatic	hydrostatic
Basal friction angle, $\delta$	$40.7^\circ \pm 2.1^\circ$	$40.7^\circ$
Initial hydraulic permeability, $k$ ( $\text{m}^2$ )	$4 \times (10^{-12} \sim 10^{-11})$	$7.5 \times 10^{-9}$
Pore fluid viscosity, $\mu_f$ ( $\text{Pa} \cdot \text{s}$ )	$0.001 \sim 0.05$	0.005
Basal frictional coefficient, $k_f^b$ ( $\text{N} \cdot \text{s}/\text{m}^3$ )	--	75

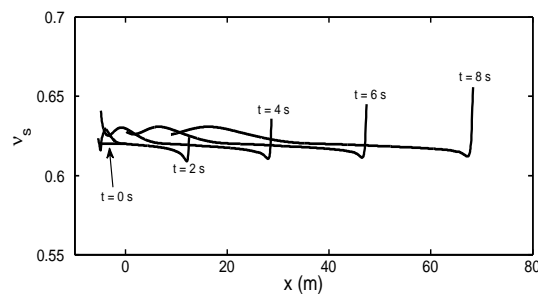
as shown in Fig. 4.8. The mixture was suddenly released as the gate was opened, and then accelerated down the chute until it approached a horizontal run-out plane. The transverse dimension of the chute is wide enough so that the flow across the transverse section can be considered to be uniform. The settings and details of the experiment can be seen in Iverson et al. (2010). For this case, we adopt N-T scheme to discretize dimensional depth-averaged equations, which are obtained by using scaling (3.11) to transform (3.84)-(3.86), and (3.90)-(3.92) into the dimensional form. Moreover, the experimental and computational parameters used to validate the present model are presented in Table 4.1. In the computation, a larger value of permeability than the corresponding experimental value is used due to the fact that the granular matrix in motion is more permeable, caused by rapid shear, than the initial state (see George & Iverson (2014)). Since the experiment does not provide a value for the fluid bed friction coefficients,  $k_f^b = 75 \text{ N} \cdot \text{s}/\text{m}^3$  is chosen. Such condition represents a moderate bed slip for the fluid phase. Fig 4.9 depicts the evolutions of the shape of the grain-fluid mixture and the solid volume fraction along the central line of the flow after the release of the mixture from the gate. Predicted results indicate that the mixture quickly deforms after its release, and a grain-enrichment blunt snout quickly devel-

ops at about  $t = 4$  s. As the mixture advances further downslope, the blunt snout modestly changes. In the meantime, the tail of the mixture begins to attenuate. A tapered thin tail develops at about  $t = 6$  s. These phenomena are consistent with the observations in the experiment (see Iverson et al. (2010)).

Fig. 4.10 compares the measured time series of depth at  $x = 2$  m,  $x = 32$  m, and  $x = 66$  m downslope from the gate with the numerical results. The comparison indicates that the present model can reasonably predict the time series of depth and the speed of the surge, though some discrepancies exist. It can be seen from Fig. 4.10 that the predicted arriving times to the sections of observation are larger than those found by the experiment, which indicates that the computed speed of the flow snout is slower than the real one in the experiment. The reason of the discrepancy of the speed may stem from the hydrostatic pore pressure assumption. In the experiment, the pore pressure quickly elevates from the original hydrostatic pressure throughout the whole mixture body immediately after the mixture is released. The excess pore pressure mitigates the friction of the grains. As a result, the mixture actually descends downslope faster than the prediction. So far the present saturated model, based on the hydrostatic pore pressure assumption, has not taken this aspect into account. In Chap. 7, we aim to improve the present model by taking into account the granular dilatancy that yields the development of excess pore pressure.



(a) Height profile



(b) Solid volume fraction profile

Figure 4.9: Height and solid volume fraction profiles

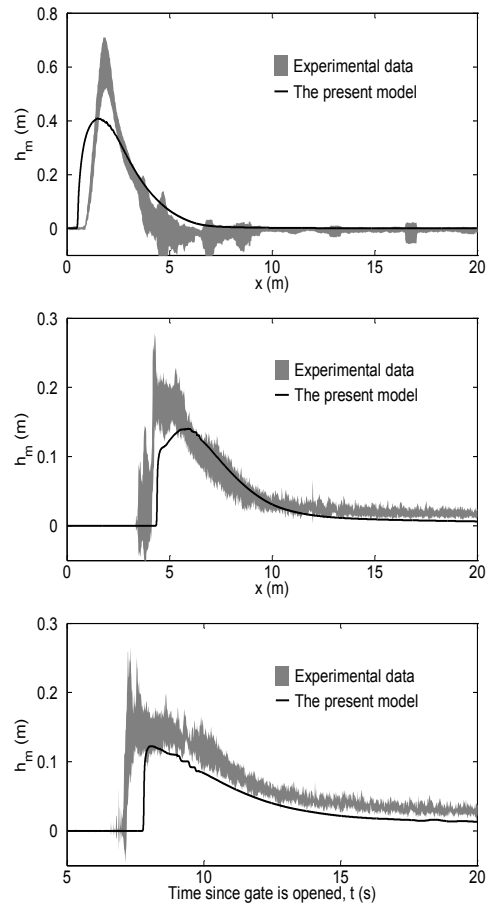


Figure 4.10: Comparison between the measurements and the model predictions. Grey shading represents the mean  $\pm 1$  standard deviation measured in eight experiments. The solid line indicates the predicted result by the present model.

## 4.7 Conclusion

In this Chapter, two shock-capturing schemes are reviewed, i.e. N-T scheme and central-upwind scheme. It is found that both schemes can give accurate enough solutions for the convection-dominated problems. Consequently, N-T scheme will be used to investigate the convection-dominated problems in the following to save computational resource.

Additionally, we apply the present model to numerically investigate the experimental case documented in Iverson et al. (2010). It is found that the present model can give an overall effective prediction on the evolutions of dynamical quantities, though a non-physical result, i.e.  $\phi_s > \phi_{\max}$ , could take place and some discrepancies also exist. The non-physical result could be avoided when a two-layer model is proposed, see next Chapter. Additionally, the discrepancies between the numerical results and the experiment can be minimized when the granular dilatancy is taken into account, which can be seen in Chapter 7.

## 5 Dynamical modelling of unsaturated grain-fluid mixtures: preliminary theory

For flowing grain-fluid materials, unsaturated flows, i.e. the fluid cannot fill all interstices of the granular material, can be observed in many occasions. As a typical representation of partially saturated grain-fluid mixtures, an initially sliding failure occurring in a partially saturated soil can induce an unsaturated flow (see Hungr (2000)). Additionally, even for an initially sliding failure occurring in a fluid-saturated soil, during its motion an unsaturated mixture state can also develop, since the velocities of the solid and fluid phase may deviate substantially, especially when the mixture reaches the horizontal run-out zone. The unsaturated mixture is actually closely linked with phase-separation phenomenon, i.e. the fluid separates from the mixture, see Fig. 5.1. For unsaturated flows, the saturated model, presented in the third Chapter, cannot be applied properly, since a non-physical result may take place, i.e., the solid volume fraction  $\phi_s$  exceeds the volume fraction  $\phi_{\max}$  corresponding to the densest possible packing of the solid particles. For details, see the simulation in the next Chapter. To investigate such unsaturated mixture flows reasonably, more sophisticated models are needed, for instance a two-layer model.

In this Chapter, a two-layer approach is proposed, in which the fluid-saturated granular layer is overlain by the pure granular material. The governing equations and boundary conditions for the two-layer system are described in Section 5.1. The nondimensionalization of the governing equations and boundary conditions are presented in Section 5.2. Moreover, we perform the depth-averaged technique to derive a set of depth-averaged equations, which are presented in Section 5.3 and Section 5.4.

### 5.1 Field equations

For an unsaturated mixture as shown in Fig. 5.1, it is idealized as a two-layer material: the saturated mixture lower layer, in which the granular solid and fluid coexist, and the pure granular upper layer. In this section, we present the rigorous formulation of the governing equations describing this two-layer system and the corresponding boundary conditions.

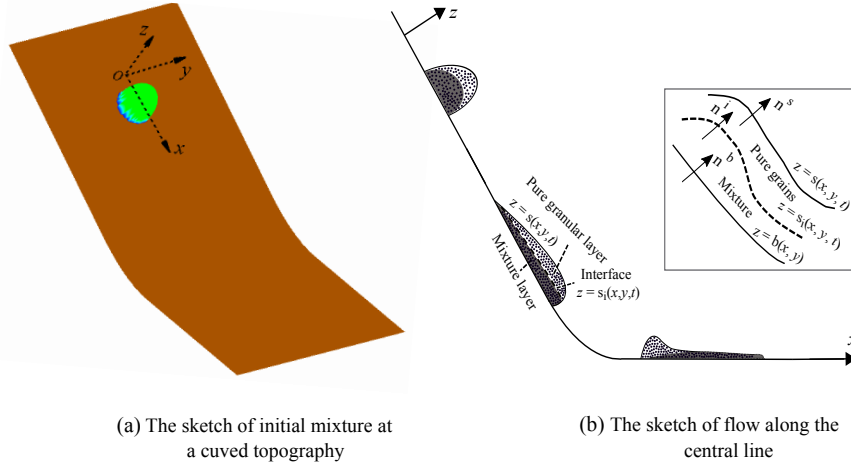


Figure 5.1: Sketch of an unsaturated mixture flow. An initially unsaturated mixture, driven by gravity force, accelerates down a slope until the mixture reaches horizontal run-out zone. Then, the mixture decelerates due to the decreasing of driven force when the phenomenon of phase separation between the solid and the fluid phases is apparently observed, e.g., the fluid phase separates from the mixture.

### 5.1.1 Governing equations

- (i) The **upper layer** is treated as a density preserving medium with a constant volume fraction  $\phi_g$ . The granular dilatancy – a kind of compressibility – will not be accounted for. In this case, the corresponding balance equations for mass and momentum read

$$\nabla \cdot \mathbf{v}_g = 0, \quad (5.1)$$

$$\partial_t \mathbf{v}_g + \nabla \cdot (\mathbf{v}_g \otimes \mathbf{v}_g) = -\frac{1}{\rho_g} \nabla \cdot \boldsymbol{\sigma}_g + \mathbf{g}, \quad (5.2)$$

where  $\boldsymbol{\sigma}_g$  is the pure granular stress tensor, which is the negative Cauchy stress tensor due to the convention that compressive stress is positive in soil mechanics.  $\mathbf{v}_g$  is the corresponding velocity and  $\mathbf{g}$  is the gravity acceleration. In addition,  $\rho_g = \tilde{\rho}_g \phi_g$  denotes the density of the granular medium, where  $\tilde{\rho}_g$  is the intrinsic density of the granular particles assumed to be constant. We postulate  $\phi_g = \phi_{\max}$  here.

- (ii) For the mixture in the **lower layer**, it is described by the standard mixture theory. Consequently, the balance equations for mass are given by

$$\frac{\partial \rho_f}{\partial t} + \nabla \cdot (\rho_f \mathbf{v}_f) = 0, \quad (5.3)$$

$$\frac{\partial \rho_s}{\partial t} + \nabla \cdot (\rho_s \mathbf{v}_s) = 0. \quad (5.4)$$



Additionally, both components are assumed to be density preserving, which is, the intrinsic fluid and solid densities,  $\tilde{\rho}_f$  and  $\tilde{\rho}_s$ , do not vary with space and time. As a result, equations (2.46) and (2.47) can be used for the momentum balances of the lower-layer fluid and solid components. Because the phase separation between the fluid and granular phases takes place in an unsaturated flow, we therefore postulate that the viscous drag between the fluid and solid components is given by  $C_d\phi_s\phi_f(\mathbf{v}_f - \mathbf{v}_s)$  instead of  $\mu_f\phi_f^2(\mathbf{v}_f - \mathbf{v}_s)/k$ , where  $C_d$  is the drag force coefficient. It is due to the fact that the expression  $\mu_f\phi_f^2(\mathbf{v}_f - \mathbf{v}_s)/k$  physically does not hold when  $\phi_s = 0$ . In short, the balance equations of momentum for the fluid and solid components are written as

$$\rho_s \left[ \frac{\partial \mathbf{v}_s}{\partial t} + \nabla \cdot (\mathbf{v}_s \otimes \mathbf{v}_s) \right] = -\nabla \cdot \boldsymbol{\sigma}_e - \phi_s \nabla p_f + \rho_s \mathbf{g} + C_d \phi_s \phi_f (\mathbf{v}_f - \mathbf{v}_s), \quad (5.5)$$

$$\rho_f \left[ \frac{\partial \mathbf{v}_f}{\partial t} + \nabla \cdot (\mathbf{v}_f \otimes \mathbf{v}_f) \right] = -\phi_f \nabla p_f + \nabla \cdot \boldsymbol{\tau}_f + \rho_f \mathbf{g} - C_d \phi_s \phi_f (\mathbf{v}_f - \mathbf{v}_s). \quad (5.6)$$

### 5.1.2 Boundary conditions

- (i) The **top surface**  $\mathcal{F}^s = z - s(x, y, t) = 0$  is a material surface so that the kinematic condition takes the form

$$\frac{\partial}{\partial t} \mathcal{F}^s + \mathbf{v}_g^s \cdot \nabla \mathcal{F}^s = 0. \quad (5.7)$$

Moreover, we assume that the ambient air can be ignored; hence, at the free surface we have

$$\boldsymbol{\sigma}_g^s \cdot \mathbf{n}^s = 0, \quad (5.8)$$

where  $\mathbf{n}^s = \nabla \mathcal{F}^s / |\nabla \mathcal{F}^s|$  is the exterior normal vector of the top free surface.

- (ii) At the **bottom**  $\mathcal{F}^b = z - b(x, y) = 0$ , we do not consider erosion. The kinematic boundary condition (3.3) is therefore satisfied for the fluid and solid components in the mixture.

Additionally, the Navier bed slip condition (3.4) is imposed for the fluid phase, whereas a modified Coulomb friction boundary condition,

$$\boldsymbol{\sigma}_e^b \mathbf{n}^b - (\mathbf{n}^b \cdot \boldsymbol{\sigma}_e^b \mathbf{n}^b) \mathbf{n}^b = -\frac{\mathbf{v}_s^b}{|\mathbf{v}_s^b|} (\mathbf{n}^b \cdot \boldsymbol{\sigma}_e^b \mathbf{n}^b) \mu_s^b - k_s^b \phi_s^b \mathbf{v}_s^b, \quad (5.9)$$

is imposed for the solid phase, where  $\mathbf{n}^b = \nabla \mathcal{F}^b / |\nabla \mathcal{F}^b|$  represents the unit exterior normal vector of the bed surface,  $k_s^b$  the dimensional parameter, and  $\mu_s^b = \tan \delta$  the bed friction coefficient. Relation (5.9) incorporates a rate-dependent term  $k_s^b \phi_s^b \mathbf{v}_s^b$ , when compared to pure Coulomb friction law (3.5). In the absence of such a rate-dependent friction term, the gravity-driven pure granular mass would be accelerated continuously. The inclusion of a rate-dependent term has already been implemented in several avalanche modelings; for example, a

Voellmy-type drag that includes a quadratic function of the velocity was used in Hutter & Greve (1993), Tai et al. (2001) and Bartelt, Salm & Gruber (1999).

- (iii) The **interface**  $\mathcal{F}^i = z - s_i(x, y, t) = 0$ , separating the upper and lower layers, on the one hand, is a material surface for the fluid phase in the lower layer across which no mass flux happens. As a result, the kinematic condition holds in the form

$$\frac{\partial}{\partial t} \mathcal{F}^i + \mathbf{v}_f^i \cdot \nabla \mathcal{F}^i = 0, \quad (5.10)$$

where the superscript “ $i$ ” stands for physical quantities at the interface. On the other hand, the interface is a singular surface for the granular phase with mass flux. The mass jump condition (2.35) holds at the interface. Taking into account the fact that the interface is a material surface for the fluid, i.e.  $\mathbf{v}_f^i \cdot \mathbf{n}^i = \mathbf{w} \cdot \mathbf{n}^i = \mathcal{U}$ , one can rewrite relation (2.35) as

$$\llbracket \rho_s^i (\mathbf{v}_s^i - \mathcal{U} \mathbf{n}^i) \rrbracket \cdot \mathbf{n}^i = 0, \quad (5.11)$$

where  $\mathbf{n}^i = \nabla \mathcal{F}^i / |\nabla \mathcal{F}^i|$  represents the unit normal vector of the interface,  $\mathcal{U}$  the interfacial normal velocity,  $\rho_s^{i+} = \tilde{\rho}_s \phi_g^i$  and  $\rho_s^{i-} = \tilde{\rho}_s \phi_s^i$  the interfacial granular partial densities at the upper and lower sides of the interface, respectively. For simplicity, it is considered that no jump takes place across the interface for the solid volume fraction, which means  $\phi_g^i = \phi_s^i = \phi_g$ . Furthermore,  $\mathcal{U}$  can be determined as  $\mathcal{U} = \partial_t s_i / |\nabla \mathcal{F}^i|$  by relation (5.10). Hence, the mass jump condition (5.11) can be explicitly rewritten as

$$\rho_s^{i+} (\mathbf{v}_g^i \cdot \mathbf{n}^i - \mathcal{U}) = \rho_s^{i-} (\mathbf{v}_s^i \cdot \mathbf{n}^i - \mathcal{U}) \equiv \mathcal{M}, \quad (5.12)$$

where  $\mathcal{M}$  stands for the mass exchange rate of the granular phase across the interface.

At the interface, the momentum balance between the granular material in the upper layer and the mixture in the lower layer must be maintained, i.e. the momentum jump condition (2.41) holds. Taking into account that the interface is a material surface for the fluid phase as indicated by (5.10), we further assume that the traction-free condition holds for the fluid phase at the interface. As a result, the momentum balance between the granular material in the upper layer and the granular phase in the lower layer holds. This yields that relation (2.41) can be decomposed to the following relations

$$\boldsymbol{\sigma}_f^i \cdot \mathbf{n}^i = 0, \quad (5.13)$$

$$\llbracket -\boldsymbol{\sigma}_s^i - \rho_s^i (\mathbf{v}_s^i - \mathcal{U} \mathbf{n}^i) \otimes (\mathbf{v}_s^i - \mathcal{U} \mathbf{n}^i) \rrbracket \cdot \mathbf{n}^i = 0. \quad (5.14)$$

Similar to the condition (5.9) at the bottom, a rate-dependent friction boundary condition is also proposed for the solid constituent at the lower side of the interface, i.e.,

$$\boldsymbol{\sigma}_e^i \mathbf{n}^i - (\mathbf{n}^i \cdot \boldsymbol{\sigma}_e^i \mathbf{n}^i) \mathbf{n}^i = \frac{\mathbf{v}_s^\tau - \mathbf{v}_g^\tau}{|\mathbf{v}_s^\tau - \mathbf{v}_g^\tau|} (\mathbf{n}^i \cdot \boldsymbol{\sigma}_e^i \mathbf{n}^i) \mu_s^i + k_s^i \phi_s^i (\mathbf{v}_s^\tau - \mathbf{v}_g^\tau), \quad (5.15)$$

where  $\mathbf{v}_s^\tau = \mathbf{v}_s^i - (\mathbf{v}_s^i \cdot \mathbf{n}^i) \mathbf{n}^i$  and  $\mathbf{v}_g^\tau = \mathbf{v}_g^i - (\mathbf{v}_g^i \cdot \mathbf{n}^i) \mathbf{n}^i$  are tangential velocities of the granular mass at the lower and upper sides of the interface, respectively. In addition,  $\phi_s^i = \phi_g$  is attained by the continuity assumption of the solid volume fraction across the interface. Moreover,  $\mu_s^i = \tan \varphi$  is assumed and  $k_s^i$  is a dimensional parameter. When the parameter  $k_s^i$  vanishes, relation (5.15) turns into the Coulomb's friction law. In particular applications, the introduction of the parameter  $k_s^b$  in (5.9) and  $k_s^i$  in (5.15) needs to be carefully investigated and calibrated with experiments.

## 5.2 Scalings and Nondimensionalization

This section aims to present the scalings and the non-dimensional forms of the aforementioned governing equations and boundary conditions. Additionally, because the balance equations of mass and momentum for the two components in the mixture of the lower layer are almost the same as those presented in the third Chapter, we will not indicate the non-dimensional forms of balance equations for the lower-layer components below in order to avoid repetition.

### 5.2.1 Scalings

To non-dimensionalize the field equations, the scalings of quantities need to be introduced. In addition to the scalings shown in relation (3.11), we supply the following scalings

$$\begin{aligned} C_d &= \frac{\tilde{\rho}_f \sqrt{g\mathcal{L}}}{\mathcal{L}} C_d^*, \\ \mathcal{M} &= \epsilon \tilde{\rho}_s \sqrt{g\mathcal{L}} \mathcal{M}^*, \\ (k_s^b, k_s^i) &= \epsilon \tilde{\rho}_s \sqrt{g\mathcal{L}} (k_s^{b*}, k_s^{i*}), \\ (\sigma_{g(xx)}, \sigma_{g(yy)}, \sigma_{g(zz)}) &= \tilde{\rho}_s g \mathcal{H} (\sigma_{g(xx)}^*, \sigma_{g(yy)}^*, \sigma_{g(zz)}^*), \\ (\sigma_{g(xy)}, \sigma_{g(xz)}, \sigma_{g(yz)}) &= \tilde{\rho}_s g \mathcal{H} \mu_s^b (\sigma_{g(xy)}^*, \sigma_{g(xz)}^*, \sigma_{g(yz)}^*). \end{aligned} \quad (5.16)$$

In this section, we still focus on the circumstance that a grain-fluid mixture of finite mass slides down an inclined plane that merges into a horizontal plane by a smooth transition. Hence, the coordinate system defined in Fig 3.2 is used here.

## 5.2.2 Non-dimensional governing equations for the upper layer

Applying relation (3.7) to explicitly account for the divergence of the velocity  $\nabla \cdot \mathbf{v}_g$  arising in mass balance (5.1), one can derive the following non-dimensional form

$$\frac{\partial}{\partial x}(u_g \psi) + \frac{\partial v_g}{\partial y} + \frac{\partial w_g}{\partial z} - \epsilon \lambda \kappa' z u_g \psi^2 - \epsilon \lambda \kappa w_g \psi = 0. \quad (5.17)$$

Similarly, applying relation (3.8) to account for the divergence of diadic product  $\nabla \cdot (\mathbf{v}_g \otimes \mathbf{v}_g)$  and the divergence of stress  $\nabla \cdot \boldsymbol{\sigma}_g$  arising in momentum balance (5.2), one can derive the following non-dimensional equations

$$\begin{aligned} & \frac{\partial}{\partial t}(\phi_g u_g) + \frac{\partial}{\partial x}(\phi_g u_g^2 \psi) + \frac{\partial}{\partial y}(\phi_g u_g v_g) + \frac{\partial}{\partial z}(\phi_g u_g w_g) - \epsilon \lambda \kappa' z \phi_g u_g^2 \psi^2 - 2\epsilon \lambda \kappa \phi_g u_g w_g \psi \\ &= \phi_g \sin \zeta - \left[ \epsilon \frac{\partial}{\partial x}(\sigma_{g(xx)} \psi) + \epsilon \mu_s^b \frac{\partial \sigma_{g(xy)}}{\partial y} + \mu_s^b \frac{\partial \sigma_{g(xz)}}{\partial z} \right] + \epsilon^2 \lambda \kappa' z \sigma_{g(xx)} \psi^2 \\ & \quad + 2\epsilon \lambda \mu_s^b \kappa \sigma_{g(xz)} \psi, \end{aligned} \quad (5.18)$$

$$\begin{aligned} & \frac{\partial}{\partial t}(\phi_g v_g) + \frac{\partial}{\partial x}(\phi_g u_g v_g \psi) + \frac{\partial}{\partial y}(\phi_g v_g^2) + \frac{\partial}{\partial z}(\phi_g v_g w_g) - \epsilon \lambda \kappa' z \phi_g u_g v_g \psi^2 - \epsilon \lambda \kappa \phi_g v_g w_g \psi \\ &= - \left[ \epsilon \mu_s^b \frac{\partial}{\partial x}(\sigma_{g(yx)} \psi) + \epsilon \frac{\partial \sigma_{g(yy)}}{\partial y} + \mu_s^b \frac{\partial \sigma_{g(yz)}}{\partial z} \right] + \epsilon^2 \lambda \mu_s^b \kappa' z \sigma_{g(xy)} \psi^2 \\ & \quad + \epsilon \lambda \mu_s^b \kappa \sigma_{g(yz)} \psi, \end{aligned} \quad (5.19)$$

$$\begin{aligned} & \epsilon \left[ \frac{\partial}{\partial t}(\phi_g w_g) + \frac{\partial}{\partial x}(\phi_g u_g w_g \psi) + \frac{\partial}{\partial y}(\phi_g v_g w_g) + \frac{\partial}{\partial z}(\phi_g w_g^2) \right] - \lambda \kappa \phi_g (\epsilon^2 w_g^2 - u_g^2) \psi \\ &= -\phi_g \cos \zeta - \left[ \epsilon \mu_s^b \frac{\partial}{\partial x}(\sigma_{g(zx)} \psi) + \epsilon \mu_s^b \frac{\partial \sigma_{g(zy)}}{\partial y} + \frac{\partial \sigma_{g(zz)}}{\partial z} \right] + \epsilon^2 \lambda \mu_s^b \kappa' z \sigma_{g(xz)} \psi^2 \\ & \quad + \epsilon \lambda \kappa (\sigma_{g(zz)} - \sigma_{g(xx)}) \psi + \epsilon^2 \lambda \kappa' z \phi_g u_g w_g \psi^2. \end{aligned} \quad (5.20)$$

## 5.2.3 Non-dimensional boundary conditions

1. By means of relation (3.11), the non-dimensional form of the kinematic boundary condition (5.7) at the **top free surface** reads

$$\frac{\partial s}{\partial t} + u_g^s \psi^s \frac{\partial s}{\partial x} + v_g^s \frac{\partial s}{\partial y} - w_g^s = 0. \quad (5.21)$$

In addition, the downslope, cross-slope and normal non-dimensional components of the dynamic boundary condition (5.8) are

$$\epsilon \sigma_{g(xx)}^s \psi^s \frac{\partial s}{\partial x} + \epsilon \mu_s^b \sigma_{g(xy)}^s \frac{\partial s}{\partial y} - \mu_s^b \sigma_{g(xz)}^s = 0, \quad (5.22)$$

$$\epsilon \mu_s^b \sigma_{g(yx)}^s \psi^s \frac{\partial s}{\partial x} + \epsilon \sigma_{g(yy)}^s \frac{\partial s}{\partial y} - \mu_s^b \sigma_{g(yz)}^s = 0, \quad (5.23)$$

$$\epsilon \mu_s^b \sigma_{g(zx)}^s \psi^s \frac{\partial s}{\partial x} + \epsilon \mu_s^b \sigma_{g(zy)}^s \frac{\partial s}{\partial y} - \sigma_{g(zz)}^s = 0. \quad (5.24)$$

respectively.

2. **At the bottom**, the non-dimensional forms of the kinematic boundary conditions for each component of the lower layer are presented by relation (3.33). The non-dimensional forms of the bed Navier slip boundary condition for the fluid are presented by relations (3.34)-(3.36). For the solid component of the lower layer, the downslope, cross-slope and normal non-dimensional components of the bed friction boundary condition (5.9) read

$$\epsilon \sigma_{e(xx)}^b \psi^b \frac{\partial b}{\partial x} + \epsilon \mu_s^b \sigma_{e(xy)}^b \frac{\partial b}{\partial y} - \mu_s^b \sigma_{e(xz)}^b \quad (5.25)$$

$$= (\mathbf{n}^b \cdot \boldsymbol{\sigma}_e^b \mathbf{n}^b) \left( \Delta_b \frac{u_s^b}{|\mathbf{v}_s^b|} \mu_s^b + \epsilon \psi^b \frac{\partial b}{\partial x} \right) + (k_s^b \phi_s^b \Delta_b) u_s^b,$$

$$\epsilon \mu_s^b \sigma_{e(yx)}^b \psi^b \frac{\partial b}{\partial x} + \epsilon \sigma_{e(yy)}^b \frac{\partial b}{\partial y} - \mu_s^b \sigma_{e(yz)}^b \quad (5.26)$$

$$= (\mathbf{n}^b \cdot \boldsymbol{\sigma}_e^b \mathbf{n}^b) \left( \Delta_b \frac{v_s^b}{|\mathbf{v}_s^b|} \mu_s^b + \epsilon \frac{\partial b}{\partial y} \right) + (k_s^b \phi_s^b \Delta_b) v_s^b,$$

$$\epsilon \mu_s^b \sigma_{e(zx)}^b \psi^b \frac{\partial b}{\partial x} + \epsilon \mu_s^b \sigma_{e(zy)}^b \frac{\partial b}{\partial y} - \sigma_{e(zz)}^b \quad (5.27)$$

$$= (\mathbf{n}^b \cdot \boldsymbol{\sigma}_e^b \mathbf{n}^b) \left( \Delta_b \frac{\epsilon w_s^b}{|\mathbf{v}_s^b|} \mu_s^b - 1 \right) + (\epsilon k_s^b \phi_s^b \Delta_b) w_s^b,$$

respectively.

**At the interface**, the non-dimensional form of the kinematic boundary condition (5.10) reads

$$\frac{\partial s_i}{\partial t} + u_f^i \psi^i \frac{\partial s_i}{\partial x} + v_f^i \frac{\partial s_i}{\partial y} - w_f^i = 0, \quad (5.28)$$

and the non-dimensional components of the traction-free dynamic boundary condition (5.13) in the downslope, cross-slope and normal directions are given by the following

$$\epsilon \left[ -\phi_f^i p_f^i N_R^i + \tau_{f(xx)}^i \right] \psi^i \frac{\partial s_i}{\partial x} + \tau_{f(xy)}^i \frac{\partial s_i}{\partial y} - \tau_{f(xz)}^i = 0, \quad (5.29)$$

$$\tau_{f(yx)}^i \psi^i \frac{\partial s_i}{\partial x} + \epsilon \left[ -\phi_f^i p_f^i N_R^i + \tau_{f(yy)}^i \right] \frac{\partial s_i}{\partial y} - \tau_{f(yz)}^i = 0, \quad (5.30)$$

$$\tau_{f(zx)}^i \psi^i \frac{\partial s_i}{\partial x} + \tau_{f(zy)}^i \frac{\partial s_i}{\partial y} - \left[ -\phi_f^i p_f^i N_R^i + \tau_{f(zz)}^i \right] = 0, \quad (5.31)$$

respectively, where the parameter  $N_R^i$  is  $N_R^i = \mu_f \phi_f^i / (\tilde{\rho}_f \mathcal{H} \sqrt{g\mathcal{L}})$ , in which  $\phi_f^i = 1 - \phi_g$ . Consistent with relations (5.29)-(5.31), we postulate that the fluid pressure and shear stress vanish at the interface, which indicates

$$p_f^i = 0, \quad \text{and} \quad \tau_{f(j,k)}^i = 0, \quad (5.32)$$

where  $j, k \in \{x, y, z\}$ .

The non-dimensional mass jump condition (5.11) (or (5.12)) is written as

$$\Delta_i \cdot \mathcal{M} = -\phi_g \left( \frac{\partial s_i}{\partial t} + u_s^i \psi^i \frac{\partial s_i}{\partial x} + v_s^i \frac{\partial s_i}{\partial y} - w_s^i \right) = -\phi_g \left( \frac{\partial s_i}{\partial t} + u_g^i \Psi^i \frac{\partial s_i}{\partial x} + v_g^i \frac{\partial s_i}{\partial y} - w_g^i \right). \quad (5.33)$$

where the factor  $\Delta_i$  is

$$\Delta_i = \left[ \epsilon^2 (\psi^i)^2 (\partial s_i / \partial x)^2 + \epsilon^2 (\partial s_i / \partial y)^2 + 1 \right]^{1/2}. \quad (5.34)$$

Similarly, the non-dimensional components of the momentum jump condition (5.14) in the downslope, cross-slope and normal directions are

$$\begin{aligned} -\Delta_i \cdot \mathcal{M}(u_s^i - u_g^i) + \epsilon \sigma_{e(xx)}^i \psi^i \frac{\partial s_i}{\partial x} + \epsilon \mu_s^b \sigma_{e(xy)}^i \frac{\partial s_i}{\partial y} - \mu_s^b \sigma_{e(xz)}^i \\ = \epsilon \sigma_{g(xx)}^i \psi^i \frac{\partial s_i}{\partial x} + \epsilon \mu_s^b \sigma_{g(xy)}^i \frac{\partial s_i}{\partial y} - \mu_s^b \sigma_{g(xz)}^i, \end{aligned} \quad (5.35)$$

$$\begin{aligned} -\Delta_i \cdot \mathcal{M}(v_s^i - v_g^i) + \epsilon \mu_s^b \sigma_{e(yx)}^i \psi^i \frac{\partial s_i}{\partial x} + \epsilon \sigma_{e(yy)}^i \frac{\partial s_i}{\partial y} - \mu_s^b \sigma_{e(yz)}^i \\ = \epsilon \mu_s^b \sigma_{g(yx)}^i \psi^i \frac{\partial s_i}{\partial x} + \epsilon \sigma_{g(yy)}^i \frac{\partial s_i}{\partial y} - \mu_s^b \sigma_{g(yz)}^i, \end{aligned} \quad (5.36)$$

$$\begin{aligned} -\epsilon \Delta_i \cdot \mathcal{M}(w_s^i - w_g^i) + \epsilon \mu_s^b \sigma_{e(zx)}^i \psi^i \frac{\partial s_i}{\partial x} + \epsilon \mu_s^b \sigma_{e(zy)}^i \frac{\partial s_i}{\partial y} - \sigma_{e(zz)}^i \\ = \epsilon \mu_s^b \sigma_{g(zx)}^i \psi^i \frac{\partial s_i}{\partial x} + \epsilon \mu_s^b \sigma_{g(zy)}^i \frac{\partial s_i}{\partial y} - \sigma_{g(zz)}^i, \end{aligned} \quad (5.37)$$

respectively, where we used  $\sigma_{e(jk)}^i = \sigma_{s(jk)}^i$  ( $j, k \in (x, y, z)$ ) that holds due to relation (5.32).

To derive the non-dimensional components of relation (5.15), the tangential velocity  $\mathbf{v}_k^\tau$  ( $k \in \{s, g\}$ ) is rewritten as  $\mathbf{v}_k^\tau = \mathbf{v}_k^i - (\mathbf{v}_k^i \cdot \mathbf{n}^i) \mathbf{n}^i$  that yields  $\mathbf{v}_s^\tau - \mathbf{v}_g^\tau = \mathbf{v}_s^i - \mathbf{v}_g^i$  due to  $\mathbf{v}_s^i \cdot \mathbf{n}^i = \mathbf{v}_g^i \cdot \mathbf{n}^i$  from the jump condition (5.12) together with the continuity assumption of the solid volume fraction across the interface. It follows that the non-dimensional components of relation (5.15) in the downslope, cross-slope and normal directions are given by the following,

$$\epsilon \sigma_{e(xx)}^i \psi^i \frac{\partial s_i}{\partial x} + \epsilon \mu_s^b \sigma_{e(xy)}^i \frac{\partial s_i}{\partial y} - \mu_s^b \sigma_{e(xz)}^i \quad (5.38)$$

$$\begin{aligned}
&= (\mathbf{n}^i \cdot \boldsymbol{\sigma}_e^i \mathbf{n}^i) \left( \epsilon \psi^i \frac{\partial s_i}{\partial x} - \Delta_i \frac{u_s^i - u_g^i}{|\mathbf{v}_s^i - \mathbf{v}_g^i|} \mu_s^i \right) - k_s^i \phi_g \Delta_i (u_s^i - u_g^i), \\
\epsilon \mu_s^b \sigma_{e(yx)}^i \psi^i \frac{\partial s_i}{\partial x} + \epsilon \sigma_{e(yy)}^i \frac{\partial s_i}{\partial y} - \mu_s^b \sigma_{e(yz)}^i
\end{aligned} \tag{5.39}$$

$$\begin{aligned}
&= (\mathbf{n}^i \cdot \boldsymbol{\sigma}_e^i \mathbf{n}^i) \left( \epsilon \frac{\partial s_i}{\partial y} - \Delta_i \frac{v_s^i - v_g^i}{|\mathbf{v}_s^i - \mathbf{v}_g^i|} \mu_s^i \right) - k_s^i \phi_g \Delta_i (v_s^i - v_g^i), \\
\epsilon \mu_s^b \sigma_{e(zx)}^i \psi^i \frac{\partial s_i}{\partial x} + \epsilon \mu_s^b \sigma_{e(zy)}^i \frac{\partial s_i}{\partial y} - \sigma_{e(zz)}^i
\end{aligned} \tag{5.40}$$

$$= (\mathbf{n}^i \cdot \boldsymbol{\sigma}_e^i \mathbf{n}^i) \left( -1 - \Delta_i \frac{\epsilon (w_s^i - w_g^i)}{|\mathbf{v}_s^i - \mathbf{v}_g^i|} \mu_s^i \right) - \epsilon k_s^i \phi_g \Delta_i (w_s^i - w_g^i),$$

respectively, where  $|\mathbf{v}_s^i - \mathbf{v}_g^i| = \left[ (u_s^i - u_g^i)^2 + (v_s^i - v_g^i)^2 + \epsilon^2 (w_s^i - w_g^i)^2 \right]^{1/2}$ .

## 5.3 Ordering and Depth-averaged theory

### 5.3.1 Ordering

To perform the depth-averaged technique, we need to reasonably define orderings of the non-dimensional parameters arising in the aforementioned non-dimensional equations.

Based on the flow characteristics, a shallow flow is taken into account. It follows that the typical down- and cross-slope lengths are much larger than the typical thickness, which implies that the aspect ratio  $\epsilon$  is small, i.e.,  $\epsilon \ll 1$ . Additionally, relation (3.41) for orders of non-dimensional  $\lambda$  and  $\mu_s^b$ , (3.42) for order of  $\psi$ , (3.43) for orders of  $N_R^b$  and  $N_R^i$ , (3.44) for orders of  $\Delta_b$  and  $\Delta_i$  are employed.

### 5.3.2 Depth-averaged theory

Integrating the mass equation (5.17) for the pure granular mass of the upper layer by applying the Leibnitz rule to interchange the orders of differentiation and integration, one can obtain

$$\begin{aligned}
\frac{\partial}{\partial t} (h_g \phi_g) + \frac{\partial}{\partial x} (h_g \overline{\phi_g u_g}) + \frac{\partial}{\partial y} (h_g \overline{\phi_g v_g}) - \overline{\epsilon \lambda \phi_g \kappa' z u_g \psi^2} - \overline{\epsilon \lambda \phi_g \kappa w_g \psi} \\
- \left[ \phi_g \left( \frac{\partial z}{\partial t} + u_g \psi \frac{\partial z}{\partial x} + v_g \frac{\partial z}{\partial y} - w_g \right) \right]_i^s = 0,
\end{aligned} \tag{5.41}$$

where the depth-averaged value of a quantity  $q(x, y, z, t)$  throughout the upper layer is defined by  $\bar{q} = (1/h_g) \int_{s_i}^s q dz$  with  $h_g = s - s_i$ . The expression within  $[\cdot]$  can be

further handled by the kinematic boundary condition (5.21) at the top surface, and jump condition (5.33). Approximating (5.41) to order  $1 + \mathcal{O}(\epsilon^\alpha)$ , one can obtain

$$\frac{\partial}{\partial t}(h_g \phi_g) + \frac{\partial}{\partial x}(h_g \phi_g \bar{u}_g) + \frac{\partial}{\partial y}(h_g \phi_g \bar{v}_g) = \mathcal{M} + \mathcal{O}(\epsilon^{1+\alpha}). \quad (5.42)$$

Similarly, integrating the mass equations (5.3) and (5.4) for the fluid and solid components in the lower layer, and approximating the results to order  $\mathcal{O}(\epsilon^{1+\alpha})$ , one can obtain the following depth-averaged equations

$$\frac{\partial}{\partial t}(h_m \bar{\phi}_f) + \frac{\partial}{\partial x}(h_m \bar{\phi}_f \bar{u}_f) + \frac{\partial}{\partial y}(h_m \bar{\phi}_f \bar{v}_f) = \mathcal{O}(\epsilon^{1+\alpha}), \quad (5.43)$$

$$\frac{\partial}{\partial t}(h_m \bar{\phi}_s) + \frac{\partial}{\partial x}(h_m \bar{\phi}_s \bar{u}_s) + \frac{\partial}{\partial y}(h_m \bar{\phi}_s \bar{v}_s) = -\mathcal{M} + \mathcal{O}(\epsilon^{1+\alpha}), \quad (5.44)$$

where we define the depth-averaged value of a quantity  $q$  throughout the lower layer by  $\bar{q} = (1/h_m) \int_b^{s_i} q dz$  with  $h_m = s_i - b$ .

Integrating the non-dimensional momentum equations (5.18)-(5.20) for the pure granular mass in the upper layer can yield

$$\begin{aligned} & \frac{\partial}{\partial t}(h_g \phi_g \bar{u}_g) + \frac{\partial}{\partial x}(h_g \phi_g \overline{u_g^2 \psi}) + \frac{\partial}{\partial y}(h_g \phi_g \overline{u_g v_g}) - \epsilon \lambda \kappa' h_g \overline{z \phi_g u_g^2 \psi^2} - 2\epsilon \lambda \kappa \phi_g h_g \overline{u_g w_g \psi} \\ &= -(\mathbf{n}^i \cdot \boldsymbol{\sigma}_e^i \mathbf{n}^i) \left[ \Delta_i \frac{u_g^i - u_s^i}{|\mathbf{v}_s^i - \mathbf{v}_g^i|} \mu_s^i + \epsilon \psi^i \frac{\partial s_i}{\partial x} \right] + k_s^i \phi_g \Delta_i (u_s^i - u_g^i) + \Delta_i \cdot \mathcal{M} u_s^i \\ & - \epsilon \frac{\partial}{\partial x}(h_g \overline{\sigma_{g(xx)} \psi}) - \epsilon \mu_s^b \frac{\partial}{\partial y}(h_g \overline{\sigma_{g(xy)}}) + \epsilon^2 \lambda \kappa' h_g \overline{z \sigma_{g(xx)} \psi^2} + 2\epsilon \lambda \mu_s^b \kappa h_g \overline{\sigma_{g(xz)} \psi} \\ & + h_g \phi_g \sin \zeta, \end{aligned} \quad (5.45)$$

$$\begin{aligned} & \frac{\partial}{\partial t}(h_g \phi_g \bar{v}_g) + \frac{\partial}{\partial x}(h_g \phi_g \overline{u_g v_g \psi}) + \frac{\partial}{\partial y}(h_g \phi_g \bar{v}_g^2) - \epsilon \lambda \kappa' h_g \phi_g \overline{z u_g v_g \psi^2} - \epsilon \lambda \kappa h_g \phi_g \overline{v_g w_g \psi} \\ &= -(\mathbf{n}^i \cdot \boldsymbol{\sigma}_e^i \mathbf{n}^i) \left[ \Delta_i \frac{v_g^i - v_s^i}{|\mathbf{v}_g^i - \mathbf{v}_s^i|} + \epsilon \psi^i \frac{\partial s_i}{\partial y} \right] + k_s^i \phi_g \Delta_i (v_s^i - v_g^i) + \Delta_i \cdot \mathcal{M} v_s^i \\ & - \epsilon \mu_s^b \frac{\partial}{\partial x}(h_g \overline{\sigma_{g(yx)} \psi}) - \epsilon \frac{\partial}{\partial y}(h_g \overline{\sigma_{g(yy)}}) + \epsilon^2 \lambda \mu_s^b \kappa' h_g \overline{z \sigma_{g(xy)} \psi^2} + \epsilon \lambda \mu_s^b \kappa h_g \overline{\sigma_{g(yz)} \psi}, \end{aligned} \quad (5.46)$$

$$\begin{aligned} & \epsilon \left[ \frac{\partial}{\partial t}(h_g \phi_g \bar{w}_g) + \frac{\partial}{\partial x}(h_g \phi_g \overline{u_g w_g \psi}) + \frac{\partial}{\partial y}(h_g \phi_g \overline{v_g w_g}) \right] - \lambda \kappa \phi_g h_g (\overline{\epsilon^2 w_g^2} - u_g^2) \psi \\ &= -(\mathbf{n}^i \cdot \boldsymbol{\sigma}_e^i \mathbf{n}^i) \left[ \epsilon \Delta_i \frac{w_g^i - w_s^i}{|\mathbf{v}_g^i - \mathbf{v}_s^i|} - 1 \right] + \epsilon k_s^i \phi_g \Delta_i (w_s^i - w_g^i) + \epsilon \Delta_i \cdot \mathcal{M} w_s^i \\ & - \epsilon \mu_s^b \frac{\partial}{\partial x}(h_g \overline{\sigma_{g(xx)} \psi}) - \epsilon \mu_s^b \frac{\partial}{\partial y}(h_g \overline{\sigma_{g(zy)}}) + \epsilon^2 \lambda \mu_s^b \kappa' h_g \overline{z \sigma_{g(xz)} \psi^2} + \epsilon^2 \lambda \kappa' h_g \overline{z \phi_g u_g w_g \psi^2} \\ & - h_g \phi_g \cos \zeta + \epsilon \lambda \kappa h_g (\overline{\sigma_{g(zz)}} - \overline{\sigma_{g(xx)}}) \psi. \end{aligned} \quad (5.47)$$



Similarly, rewriting the momentum equation (5.5) for the solid phase in the lower layer in component forms and then integrating the components can formulate the depth-integrated forms of the momentum balances of the lower-layer solid phase. They are given by

$$\begin{aligned}
& \frac{\partial}{\partial t}(h_m \bar{\phi}_s \bar{u}_s) + \frac{\partial}{\partial x}(h_m \bar{\phi}_s \overline{u_s^2 \psi}) + \frac{\partial}{\partial y}(h_m \bar{\phi}_s \overline{u_s v_s}) - \epsilon \lambda \kappa' h_m \overline{z \phi_s u_s^2 \psi^2} - 2\epsilon \lambda \kappa h_m \overline{\phi_s u_s w_s \psi} \\
&= (\mathbf{n}^i \cdot \boldsymbol{\sigma}_\epsilon^i \mathbf{n}^i) \left[ -\Delta_i \frac{u_s^i - u_g^i}{|\mathbf{v}_s^i - \mathbf{v}_g^i|} \mu_s^i + \epsilon \psi^i \frac{\partial s_i}{\partial x} \right] - k_s^i \phi_g \Delta_i (u_s^i - u_g^i) - \Delta_i \cdot \mathcal{M} u_s^i \\
&\quad - (\mathbf{n}^b \cdot \boldsymbol{\sigma}_\epsilon^b \mathbf{n}^b) \left[ \Delta_b \frac{u_s^b}{|\mathbf{v}_s^b|} \mu_s^b + \epsilon \psi^b \frac{\partial b}{\partial x} \right] - k_s^b \phi_s^b \Delta_b u_s^b - \epsilon \gamma \bar{\phi}_s p_f^b \psi^b \frac{\partial b}{\partial x} \\
&\quad - \epsilon \frac{\partial}{\partial x}(h_m \overline{\sigma_{e(xx)} \psi}) - \epsilon \mu_s^b \frac{\partial}{\partial y}(h_m \overline{\sigma_{e(xy)} \psi}) - \epsilon \gamma \bar{\phi}_s \frac{\partial}{\partial x}(h_m \overline{p_f \psi}) + h_m \bar{\phi}_s \sin \zeta \\
&\quad + \epsilon^2 \lambda \kappa' h_m \overline{z \sigma_{e(xx)} \psi^2} + 2\epsilon \lambda \kappa \mu_s^b \overline{\sigma_{e(xz)} \psi} + \gamma C_d h_m \bar{\phi}_s \bar{\phi}_f (\bar{u}_f - \bar{u}_s), \tag{5.48}
\end{aligned}$$

$$\begin{aligned}
& \frac{\partial}{\partial t}(h_m \bar{\phi}_s \bar{v}_s) + \frac{\partial}{\partial x}(h_m \bar{\phi}_s \overline{u_s v_s \psi}) + \frac{\partial}{\partial y}(h_m \bar{\phi}_s \overline{v_s^2}) - \epsilon \lambda \kappa' h_m \overline{z \phi_s u_s v_s \psi^2} - \epsilon \lambda \kappa h_m \overline{\phi_s v_s w_s \psi} \\
&= (\mathbf{n}^i \cdot \boldsymbol{\sigma}_\epsilon^i \mathbf{n}^i) \left[ -\Delta_i \frac{v_s^i - v_g^i}{|\mathbf{v}_s^i - \mathbf{v}_g^i|} \mu_s^i + \epsilon \psi^b \frac{\partial s_i}{\partial y} \right] - k_s^i \phi_g \Delta_i (v_s^i - v_g^i) - \Delta_i \cdot \mathcal{M} v_s^i \\
&\quad - (\mathbf{n}^b \cdot \boldsymbol{\sigma}_\epsilon^b \mathbf{n}^b) \left[ \Delta_b \frac{v_s^b}{|\mathbf{v}_s^b|} \mu_s^b + \epsilon \psi^b \frac{\partial b}{\partial y} \right] - k_s^b \phi_s^b \Delta_b v_s^b - \epsilon \gamma \bar{\phi}_s p_f^b \psi^b \frac{\partial b}{\partial y} \\
&\quad - \epsilon \mu_s^b \frac{\partial}{\partial x}(h_m \overline{\sigma_{e(yx)} \psi}) - \epsilon \frac{\partial}{\partial y}(h_m \overline{\sigma_{e(yy)} \psi}) - \epsilon \gamma \bar{\phi}_s \frac{\partial}{\partial y}(h_m \overline{p_f}) \\
&\quad + \epsilon^2 \lambda \mu_s^b \kappa' h_m \overline{z \sigma_{e(yx)} \psi^2} + \epsilon \lambda \mu_s^b \kappa h_m \overline{\sigma_{e(yz)} \psi} + \gamma C_d h_m \bar{\phi}_s \bar{\phi}_f (\bar{v}_f - \bar{v}_s), \tag{5.49}
\end{aligned}$$

$$\begin{aligned}
& \epsilon \left[ \frac{\partial}{\partial t}(h_m \bar{\phi}_s \bar{w}_s) + \frac{\partial}{\partial x}(h_m \bar{\phi}_s \overline{u_s w_s \psi}) + \frac{\partial}{\partial y}(h_m \bar{\phi}_s \overline{v_s w_s}) \right] + \lambda \kappa h_m \bar{\phi}_s \overline{u_s^2 \psi} - \epsilon^2 \lambda \kappa h_m \bar{\phi}_s \overline{w_s^2 \psi} \\
&= (\mathbf{n}^i \cdot \boldsymbol{\sigma}_\epsilon^i \mathbf{n}^i) \left[ -\epsilon \Delta_i \frac{w_s^i - w_g^i}{|\mathbf{v}_s^i - \mathbf{v}_g^i|} \mu_s^i - 1 \right] - \epsilon k_s^i \phi_g \Delta_i (w_s^i - w_g^i) - \epsilon \Delta_i \cdot \mathcal{M} w_s^i \\
&\quad - (\mathbf{n}^b \cdot \boldsymbol{\sigma}_\epsilon^b \mathbf{n}^b) \left[ \Delta_b \frac{\epsilon w_s^b}{|\mathbf{v}_s^b|} \mu_s^b - 1 \right] - \epsilon k_s^b \Delta_b w_s^b + \epsilon \gamma C_d h_m \bar{\phi}_s \bar{\phi}_f (\bar{w}_f - \bar{w}_s) \\
&\quad - \epsilon \mu_s^b \frac{\partial}{\partial x}(h_m \overline{\sigma_{e(zx)} \psi}) - \epsilon \mu_s^b \frac{\partial}{\partial y}(h_m \overline{\sigma_{e(zy)} \psi}) + \epsilon^2 \lambda \mu_s^b \kappa' z h_m \overline{\sigma_{e(xz)} \psi} \\
&\quad + \epsilon \lambda \kappa h_m (\overline{\sigma_{e(zz)} \psi} - \overline{\sigma_{e(xx)} \psi}) + \epsilon^2 \lambda \kappa' h_m \overline{z \phi_s u_s w_s \psi^2} - h_m \bar{\phi}_s \cos \zeta - \gamma \bar{\phi}_s p^b. \tag{5.50}
\end{aligned}$$

Similarly, rewriting the momentum equation (5.6) for the fluid phase in the lower layer in component forms, and then integrating the components can yield

$$\begin{aligned}
& \frac{\partial}{\partial t}(h_m \bar{\phi}_f \bar{u}_f) + \frac{\partial}{\partial x}(h_m \bar{\phi}_f \overline{u_f^2 \psi}) + \frac{\partial}{\partial y}(h_m \bar{\phi}_f \overline{u_f v_f}) - \epsilon \lambda \kappa' h_m \overline{z \phi_f u_f^2 \psi^2} - 2\epsilon \lambda \kappa h_m \bar{\phi}_f \overline{u_f w_f \psi} \\
&= \epsilon (\mathbf{n}^b \cdot \boldsymbol{\sigma}_f^b \mathbf{n}^b) \psi^b \frac{\partial b}{\partial x} - h_m \bar{\phi}_f C_d (\bar{u}_f - \bar{u}_s) + h_m \bar{\phi}_f \sin \zeta - k_f^b \Delta_b u_f^b / (\epsilon N_R^b)
\end{aligned}$$

$$\begin{aligned}
 & -\epsilon \bar{\phi}_f \frac{\partial}{\partial x} (h_m \overline{p_f \psi}) + \frac{\epsilon}{N_R} \frac{\partial}{\partial x} (h_m \bar{\tau}_{f(xx)}) + \frac{\epsilon}{N_R} \frac{\partial}{\partial y} (h_m \bar{\tau}_{f(xy)}) \\
 & + \frac{\epsilon^2}{N_R} \lambda \kappa' h_m \overline{z \tau_{f(xx)} \psi^2} + \frac{2\epsilon}{N_R} \lambda \kappa h_m \overline{\tau_{f(xz)} \psi},
 \end{aligned} \tag{5.51}$$

$$\begin{aligned}
 & \frac{\partial}{\partial t} (h_m \bar{\phi}_f \bar{v}_f) + \frac{\partial}{\partial x} (h_m \bar{\phi}_f \overline{u_f v_f \psi}) + \frac{\partial}{\partial y} (h_m \bar{\phi}_f \bar{v}_f^2) - \epsilon \lambda \kappa' h_m \overline{z \phi_f u_f v_f \psi^2} - \epsilon \lambda \kappa h_m \overline{\phi_f v_f w_f \psi} \\
 & = \epsilon (\mathbf{n}^b \cdot \boldsymbol{\sigma}_f^b \mathbf{n}^b) \psi^b \frac{\partial b}{\partial y} - h_m \bar{\phi}_f^2 C_d (\bar{v}_f - \bar{v}_s) - k_f^b \Delta_b v_f^b / (\epsilon N_R^b) \\
 & - \epsilon \bar{\phi}_f \frac{\partial}{\partial y} (h_m \bar{p}_f) + \frac{\epsilon}{N_R} \frac{\partial}{\partial x} (h_m \bar{\tau}_{f(yx)}) + \frac{\epsilon}{N_R} \frac{\partial}{\partial y} (h_m \bar{\tau}_{f(yy)}) \\
 & + \frac{\epsilon}{N_R} \lambda \kappa \overline{\tau_{f(yz)} \psi} + \frac{\epsilon}{N_R} \epsilon^2 \lambda \kappa' h_m \overline{z \tau_{f(yx)} \psi^2},
 \end{aligned} \tag{5.52}$$

$$\begin{aligned}
 & \epsilon \left[ \frac{\partial}{\partial t} (h_m \bar{\phi}_f \bar{w}_f) + \frac{\partial}{\partial x} (h_m \bar{\phi}_f \overline{u_f w_f \psi}) + \frac{\partial}{\partial y} (h_m \bar{\phi}_f \overline{v_f w_f \psi}) \right] + \lambda \kappa h_m \bar{\phi}_f \overline{u_f^2 \psi} - \epsilon^2 \lambda \kappa' h_m \bar{\phi}_f \overline{z u_f w_f \psi^2} \\
 & = -(\mathbf{n}^b \cdot \boldsymbol{\sigma}_f^b \mathbf{n}^b) - \epsilon h_m \bar{\phi}_f^2 C_d (\bar{w}_f - \bar{w}_s) - h_m \bar{\phi}_f \cos \zeta - k_f^b \Delta_b w_f^b / N_R^b \\
 & + \frac{\epsilon}{N_R} \frac{\partial}{\partial x} (h_m \bar{\tau}_{f(zx)}) + \frac{\epsilon}{N_R} \frac{\partial}{\partial y} (h_m \bar{\tau}_{f(zy)}) + \epsilon^2 \lambda \kappa h_m \bar{\phi}_f \overline{w_f^2} \\
 & + \frac{\epsilon^2}{N_R} \lambda \kappa' h_m \overline{z \tau_{f(zx)} \psi^2} + \frac{\epsilon^2}{N_R} \lambda \kappa \overline{\tau_{f(zz)} \psi} + \bar{\phi}_f p_f^b.
 \end{aligned} \tag{5.53}$$

### 5.3.3 Evaluation of the unknown terms

As mentioned above, the traction-free condition is defined at the interface for the fluid. As a result, relation (3.60) can be taken for the expression of the pore fluid pressure, relation (3.62) can be used for the fluid basal normal stress, relation (3.63) can be used for the integrations of the gradients of the pore pressure, and relations (3.64) and (3.65) can be used for the integrations of the fluid shear stress.

Moreover, to simplify the momentum balances (5.45)-(5.50), it is necessary to clearly express the stress ( $\mathbf{n}^i \cdot \boldsymbol{\sigma}_e^i \mathbf{n}^i$ ) at the interface, the upper-layer granular depth-averaged lateral stresses  $\bar{\sigma}_{g(xx)}$  and  $\bar{\sigma}_{g(yy)}$ , the stress ( $\mathbf{n}^b \cdot \boldsymbol{\sigma}_e^b \mathbf{n}^b$ ) at the bottom, and the lower-layer solid depth-averaged lateral stresses  $\bar{\sigma}_{e(xx)}$  and  $\bar{\sigma}_{e(yy)}$ , which will be presented in the following.

Applying the order arguments (3.41), (3.42), and (3.44), the normal component (5.20) of the upper-layer granular momentum balance reduces to

$$\lambda \kappa \phi_g u_g^2 + \phi_g \cos \zeta + \frac{\partial \sigma_{g(zz)}}{\partial z} = \mathcal{O}(\epsilon). \tag{5.54}$$

Integrating relation (5.54) leads that  $\sigma_{g(zz)}$ , corrected to order  $\mathcal{O}(\epsilon)$ , is

$$\sigma_{g(zz)} = (s - z)\phi_g(\cos \zeta + \lambda\kappa u_g^2) + \mathcal{O}(\epsilon). \quad (5.55)$$

and corrected to order  $\mathcal{O}(\epsilon^\alpha)$  is

$$\sigma_{g(zz)} = (s - z)\phi_g \cos \zeta + \mathcal{O}(\epsilon^\alpha). \quad (5.56)$$

Similar to formulate (3.73), the normal stress  $\sigma_{g(zz)}$  can be linked with the lateral stresses  $\sigma_{g(xx)}$  and  $\sigma_{g(yy)}$  as follows

$$\sigma_{g(xx)} = K_x^g \sigma_{g(zz)} + \mathcal{O}(\epsilon^\nu), \quad \sigma_{g(yy)} = K_y^g \sigma_{g(zz)} + \mathcal{O}(\epsilon^\nu), \quad (5.57)$$

by introducing earth pressure coefficients  $K_x^g$  and  $K_y^g$ , where  $K_x^g$  and  $K_y^g$  satisfy the following relation

$$\begin{aligned} K_x^g = K_{x_{act/pass}}^g &= 2 \sec^2 \varphi \left( 1 \mp \sqrt{1 - \cos^2 \varphi \sec^2 \varphi} \right) - 1, & \frac{\partial \bar{u}_g}{\partial x} &\geq 0, \\ K_y^g = K_{y_{act/pass}}^g &= \frac{1}{2} \left( K_x^g + 1 \mp \sqrt{(K_x^g - 1)^2 + 4 \tan^2 \varphi} \right), & \frac{\partial \bar{v}_g}{\partial y} &\geq 0. \end{aligned} \quad (5.58)$$

It should be noted that relation (5.58) uses the internal friction angle  $\varphi$  instead of the bed friction  $\delta$ , when compared with relations (3.74) and (3.75). Moreover, combining relation (5.56) with (5.57) and integrating the result, one can obtain the following depth-averaged lateral normal stresses

$$\bar{\sigma}_{g(xx)} = \frac{1}{2} K_x^g h_g \phi_g \cos \zeta + \mathcal{O}(\epsilon^\nu), \quad \bar{\sigma}_{g(yy)} = \frac{1}{2} K_y^g h_g \phi_g \cos \zeta + \mathcal{O}(\epsilon^\nu). \quad (5.59)$$

Moreover, approximating relation (5.47) to order  $\mathcal{O}(\epsilon)$ , one can obtain

$$(\mathbf{n}^i \cdot \boldsymbol{\sigma}_e^i \mathbf{n}^i) = h_g \phi_g \cos \zeta + h_g \phi_g \lambda \kappa \bar{u}_g^2 + \mathcal{O}(\epsilon). \quad (5.60)$$

Similarly, approximating the normal component (3.23) of the lower-layer granular momentum balance to order  $\mathcal{O}(\epsilon^\alpha)$ , one can secure

$$\phi_s \cos \zeta + \frac{\partial \sigma_{e(zz)}}{\partial z} + \gamma \phi_s \frac{\partial p_f}{\partial z} = \mathcal{O}(\epsilon^\alpha), \quad (5.61)$$

which indicates

$$\sigma_{e(zz)} = (s_i - z) \bar{\phi}_s \cos \zeta + \sigma_{e(zz)}^i - \gamma \bar{\phi}_s p_f(z) + \mathcal{O}(\epsilon^\alpha). \quad (5.62)$$

To determine the normal stress  $\sigma_{e(zz)}$ , it is necessary to explicitly express the stress  $\sigma_{e(zz)}^i$  at the interface. Relation (5.37), corrected to order  $\mathcal{O}(\epsilon)$ , reduces to

$$\sigma_{e(zz)}^i = \sigma_{g(zz)}^i + \mathcal{O}(\epsilon). \quad (5.63)$$

Combining relation (5.56) with (5.63), one can secure

$$\sigma_{e(zz)}^i = h_g \phi_g \cos \zeta + \mathcal{O}(\epsilon^\alpha). \quad (5.64)$$

Substitutions of the pore pressure (3.61) and the normal stress (5.64) at the interface into relation (5.62) can derive the normal stress  $\sigma_{e(zz)}$  as follows

$$\sigma_{e(zz)} = (1 - \gamma)(s_i - z)\bar{\phi}_s \cos \zeta + h_g \phi_g \cos \zeta + \mathcal{O}(\epsilon^\alpha). \quad (5.65)$$

Moreover, the earth pressure coefficients are introduced to connect the normal stress  $\sigma_{e(zz)}$  with lateral stresses  $\sigma_{e(xx)}$  and  $\sigma_{e(yy)}$ . Referring to Savage & Hutter (1989) and its modifications (see e.g., Hutter, Siegel, Savage & Nohguchi (1993) and Gray et al. (1999)), the following relations

$$\sigma_{e(xx)}^b = K_x^s \sigma_{e(zz)}^b + \mathcal{O}(\epsilon^\nu), \quad \sigma_{e(yy)}^b = K_y^s \sigma_{e(zz)}^b + \mathcal{O}(\epsilon^\nu), \quad (5.66)$$

hold at the bottom, where the bed earth pressure coefficients  $K_x^s$  and  $K_y^s$  are defined in (3.74) and (3.75). At the interface, we stipulate the following relations

$$\sigma_{e(xx)}^i = \sigma_{g(xx)}^i + \mathcal{O}(\epsilon^\alpha), \quad \sigma_{e(yy)}^i = \sigma_{g(yy)}^i + \mathcal{O}(\epsilon^\alpha), \quad (5.67)$$

which do not violate the momentum jump conditions (5.35) and (5.36). Since relations  $\sigma_{g(xx)}^i = K_x^g \sigma_{g(zz)}^i + \mathcal{O}(\epsilon^\nu)$  and  $\sigma_{g(yy)}^i = K_y^g \sigma_{g(zz)}^i + \mathcal{O}(\epsilon^\nu)$  hold at the interface that are employed to derive (5.57), relations

$$\sigma_{e(xx)}^i = K_x^g \sigma_{e(zz)}^i + \mathcal{O}(\epsilon^\nu), \quad \sigma_{e(yy)}^i = K_y^g \sigma_{e(zz)}^i + \mathcal{O}(\epsilon^\nu), \quad (5.68)$$

can be obtained due to relation (5.63) and (5.67). To proceed, we postulate that the horizontal stresses vary linearly with normal stress throughout the depth of the lower layer. However, the factors are linear with the  $z$  coordinate instead of constant values used previously (see e.g., Savage & Hutter (1989)). This more flexible approach leads to

$$\begin{aligned} \sigma_{e(xx)} &= \left( \frac{K_x^g - K_x^s}{h_m} (z - b) + K_x^s \right) \sigma_{e(zz)} + \mathcal{O}(\epsilon^\nu), \\ \sigma_{e(yy)} &= \left( \frac{K_y^g - K_y^s}{h_m} (z - b) + K_y^s \right) \sigma_{e(zz)} + \mathcal{O}(\epsilon^\nu), \end{aligned} \quad (5.69)$$

which is a generalization of the S-H theory. When  $K_x^g = K_x^s$  and  $K_y^g = K_y^s$ , relation (5.69) reproduces the form used in the S-H theory. Additionally, relation (5.69) will reduce to  $\sigma_{e(xx)}^i = K_x^g \sigma_{e(zz)}^i + \mathcal{O}(\epsilon^\nu)$  and  $\sigma_{e(yy)}^i = K_y^g \sigma_{e(zz)}^i + \mathcal{O}(\epsilon^\nu)$  at the interface, and (5.66) at the bottom.

If the bed elevation  $b(x, y)$  is negligible, the depth-averaged lateral stresses,  $\bar{\sigma}_{e(xx)}$  and  $\bar{\sigma}_{e(yy)}$ , can be derived by combining relation (5.65) with relation (5.69). They take the forms

$$\begin{aligned}\bar{\sigma}_{e(xx)} &= \frac{1}{2}h_g\phi_g(\cos\zeta)(K_x^s + K_x^g) + \frac{1}{6}(1-\gamma)(\cos\zeta)h_m\bar{\phi}_s(2K_x^s + K_x^g) + \mathcal{O}(\epsilon^\nu), \\ \bar{\sigma}_{e(yy)} &= \frac{1}{2}h_g\phi_g(\cos\zeta)(K_y^s + K_y^g) + \frac{1}{6}(1-\gamma)(\cos\zeta)h_m\bar{\phi}_s(2K_y^s + K_y^g) + \mathcal{O}(\epsilon^\nu).\end{aligned}\quad (5.70)$$

Moreover, it is necessary to explicitly formulate  $(\mathbf{n}^b \cdot \boldsymbol{\sigma}_e^b \mathbf{n}^b)$  in order to streamline the momentum balances (5.48) and (5.49). Relation (5.50), corrected to order  $\mathcal{O}(\epsilon)$ , reduces to

$$(\mathbf{n}^b \cdot \boldsymbol{\sigma}_e^b \mathbf{n}^b) = \lambda\kappa h_m \bar{\phi}_s \bar{u}_s^2 + h_m \bar{\phi}_s \cos\zeta - \gamma \bar{\phi}_s p_f^b + (\mathbf{n}^i \cdot \boldsymbol{\sigma}_e \mathbf{n}^i) + \mathcal{O}(\epsilon). \quad (5.71)$$

Substitution of the pore pressure (3.61) and the normal stress (5.60) at the interface into relation (5.71) yields

$$\begin{aligned}(\mathbf{n}^b \cdot \boldsymbol{\sigma}_e^b \mathbf{n}^b) &= h_m \bar{\phi}_s \cos\zeta + \lambda\kappa h_m \bar{\phi}_s \bar{u}_s^2 - h_m \gamma \bar{\phi}_s (\cos\zeta + \lambda\kappa \bar{u}_f^2) \\ &\quad + h_g \phi_g \cos\zeta + \lambda\kappa h_g \phi_g \bar{u}_g^2 + \mathcal{O}(\epsilon).\end{aligned}\quad (5.72)$$

### 5.3.4 Evaluation of the mass-exchange rate $\mathcal{M}$

The mass-exchange rate  $\mathcal{M}$  across the layer interface cannot be calculated directly by field quantities, and must be postulated as a closure condition. The non-dimensional  $J$ , whose dimensional form is defined in (5.12), can be written as,

$$\mathcal{M} = \phi_g (\mathbf{v}_g^i \cdot \mathbf{n}^i - \mathcal{U}) = \phi_g (\mathbf{v}_s^i \cdot \mathbf{n}^i - \mathcal{U}), \quad (5.73)$$

Furthermore, relation (5.28) can yield that the non-dimensional interfacial normal velocity is formulated as

$$\mathcal{U} = \frac{\partial s_i}{\partial t} / |\nabla \mathcal{F}^i|. \quad (5.74)$$

To determine  $\mathcal{M}$ , it remains to postulate  $\mathbf{v}_g^i \cdot \mathbf{n}^i$  or  $\mathbf{v}_s^i \cdot \mathbf{n}^i$ , whose explicit calculation is impossible due to the information lost by the depth integration. In relation (5.73), it is indicated that  $\mathbf{v}_g^i \cdot \mathbf{n}^i = \mathbf{v}_s^i \cdot \mathbf{n}^i$  holds. Additionally, for shallow flows, we assume  $w_k^i \approx \mathbf{v}_k^i \cdot \mathbf{n}^i$  ( $k \in \{g, s\}$ ) which yields  $w_s^i \approx w_g^i \approx \mathbf{v}_g^i \cdot \mathbf{n}^i$ . We empirically model  $w_g^i$  as the contributions of both a mass drift velocity  $w_m^i$  due to gravitational settling and a deformation velocity  $w_d^i$  described by the convective motion

$$w_g^i = w_m^i + w_d^i. \quad (5.75)$$

$w_m^i$  can be postulated by setting  $w_m^i = -c(\phi_{\max} - \phi_s)$ , where the parameter  $c$  may depend on the density ratio  $\gamma$ , fluid viscosity  $\mu_f$ , etc. On the one hand, the settling process takes place when the mean solid volume fraction  $\phi_s$  of the lower layer is be-

low the possible maximum fraction  $\phi_{\max}$  for the solid skeleton. On the other hand, the grains in the lower layer will be extruded to the upper layer, if  $\phi_s$  exceeds  $\phi_{\max}$ . The second contribution  $w_d^i$  in relation (5.75) results from the deformation of the granular material body, in which a linear distribution of the granular normal velocity, from its maximum at the top free surface to the zero value at the bottom, is assumed. Consequently, we postulate

$$w_g^i = -c(\phi_{\max} - \phi_s) + \frac{h_m}{h_m + h_g} w_g^s, \quad (5.76)$$

where  $w_g^s$  is the non-dimensional normal velocity of the granular mass at the top free surface and expressed as  $w_g^s = \partial_t s + u_g^s \partial_x s + v_g^s \partial_y s$  due to kinematic boundary condition (5.21). The combination of (5.73)-(5.76) yields

$$\mathcal{M} = -\phi_g \left[ \frac{\partial s_i}{\partial t} + c(\phi_{\max} - \phi_s) - h_m w_g^s / (h_m + h_g) \right] + \mathcal{O}(\epsilon^2). \quad (5.77)$$

It should be noted that the form (5.77) is only a first postulation, and a more sophisticated formulation needs to be conducted in future.

## 5.4 Summary of depth-averaged equations

### 5.4.1 Assumption of velocity profiles

To factorize the coupling terms  $\overline{u_\eta u_\eta}$ ,  $\overline{u_\eta v_\eta}$ , etc. ( $\eta \in \{g, s, f\}$ ) arising in momentum balances (5.45), (5.46), (5.48), and (5.49), we stipulate a plug-flow velocity profile for the pure granular mass in the upper layer and for the two components in the lower layer. The plug flow indicates that relations  $u_\eta = \bar{u}_\eta + \mathcal{O}(\epsilon^{1+\nu})$  and  $v_\eta = \bar{v}_\eta + \mathcal{O}(\epsilon^{1+\nu})$ , and the following relations

$$\overline{u_\eta u_\eta} = \bar{u}_\eta \bar{u}_\eta + \mathcal{O}(\epsilon^{1+\nu}), \quad \overline{u_\eta v_\eta} = \bar{u}_\eta \bar{v}_\eta + \mathcal{O}(\epsilon^{1+\nu}) \quad (5.78)$$

hold. Additionally, volume fractions and velocities at the boundaries, arising in equations (5.45), (5.46), (5.48), and (5.49), are assumed to equal the depth-averaged volume fractions and the corresponding depth-averaged velocities.

### 5.4.2 Depth-averaged model equations

1. For the pure granular mass in the upper layer, the depth-averaged mass equation takes the form

$$\frac{\partial}{\partial t}(h_g \phi_g) + \frac{\partial}{\partial x}(h_g \phi_g u_g) + \frac{\partial}{\partial y}(h_g \phi_g v_g) = \mathcal{M} + \mathcal{O}(\epsilon^{1+\nu}), \quad (5.79)$$

where the overbar representing depth-averaged values is dropped for simplicity.

By approximating the momentum equations (5.45) and (5.46) to order  $\mathcal{O}(\epsilon^{1+\nu})$ , using relation (5.78) to factorize the averages, and substituting relations (5.59) and (5.60) into the results, one can obtain the depth-averaged momentum equations for the pure granular mass in the upper layer. They take the forms

$$\begin{aligned} & \frac{\partial}{\partial t}(h_g \phi_g u_g) + \frac{\partial}{\partial x}(h_g \phi_g u_g^2) + \frac{\partial}{\partial y}(h_g \phi_g u_g v_g) + \frac{\partial}{\partial x} \left( \frac{1}{2} \beta_g^x h_g^2 \phi_g^2 \right) \\ & = \mathcal{M} u_s - \epsilon h_g \phi_g (\cos \zeta) \frac{\partial h_m}{\partial x} + s_{x(g)} + \mathcal{O}(\epsilon^{1+\nu}) \end{aligned} \quad (5.80)$$

in the downslope direction and

$$\begin{aligned} & \frac{\partial}{\partial t}(h_g \phi_g v_g) + \frac{\partial}{\partial x}(h_g \phi_g u_g v_g) + \frac{\partial}{\partial y}(h_g \phi_g v_g v_g) + \frac{\partial}{\partial y} \left( \frac{1}{2} \beta_g^y h_g^2 \phi_g^2 \right) \\ & = \mathcal{M} v_s - \epsilon h_g \phi_g (\cos \zeta) \frac{\partial h_m}{\partial y} + s_{y(g)} + \mathcal{O}(\epsilon^{1+\nu}) \end{aligned} \quad (5.81)$$

in the cross-slope direction. The factors appearing in equations (5.80) and (5.81) are

$$\beta_g^x = \epsilon K_x^g \cos \zeta / \phi_g, \quad \beta_g^y = \epsilon K_y^g \cos \zeta / \phi_g, \quad (5.82)$$

$$s_{x(g)} = h_g \phi_g \sin \zeta \quad (5.83)$$

$$- \epsilon h_g \phi_g (\cos \zeta) \frac{\partial b}{\partial x} + k_s^i \phi_g (u_s - u_g) + \frac{u_s - u_g}{|\mathbf{v}_s - \mathbf{v}_g|} \mu_s^i (h_g \phi_g \cos \zeta + \lambda \kappa h_g \phi_g u_g^2),$$

$$s_{y(g)} = - \epsilon h_g \phi_g (\cos \zeta) \frac{\partial b}{\partial y} + k_s^i \phi_g (v_s - v_g) + \frac{v_s - v_g}{|\mathbf{v}_s - \mathbf{v}_g|} \mu_s^i (h_g \phi_g \cos \zeta + \lambda \kappa h_g \phi_g u_g^2). \quad (5.84)$$

In the mass equation (5.79), a positive mass-exchange rate,  $\mathcal{M} > 0$ , indicates a granular mass transfer across the interface from the two-phase lower layer into the pure granular upper layer. If no mass exchange takes place at the interface,  $\mathcal{M} = 0$  and the interface will become a material surface for the granular phase as well as the fluid.

The left-hand side of equation (5.80) contains the inertial term and the gradient of the granular stress. The terms on the right-hand side delineate the momentum exchange between the two layers due to the mass exchange, the nonconservative term, and the source terms consecutively. The nonconservative term  $-\epsilon h_g \phi_g (\cos \zeta) \partial h_m / \partial x$  represents the force due to the spatial non-uniform effect of the lower-layer height. The source terms defined in (5.83) is composed of the gravity down-slope component, the bed gradient term, and the viscous and the Coulomb frictions between the two layers consecutively. In the Coulomb friction, the effect of the basal curvature  $\kappa$  is taken into account which causes that the basal normal stress is enhanced by the centrifugal force. The physical clarifications of the terms emerging in the cross-slope momentum equation (5.81) are fully equivalent.

2. For the solid constituent in the lower layer, the resulting depth-averaged conservation equation for mass reads

$$\frac{\partial}{\partial t}(h_m \phi_s) + \frac{\partial}{\partial x}(h_m \phi_s u_s) + \frac{\partial}{\partial y}(h_m \phi_s v_s) = -\mathcal{M} + \mathcal{O}(\epsilon^{1+\nu}). \quad (5.85)$$

Moreover, the resulting depth-averaged solid conservation equations for the momentum are, in the downslope direction

$$\begin{aligned} & \frac{\partial}{\partial t}(h_m \phi_s u_s) + \frac{\partial}{\partial x}(h_m \phi_s u_s^2) + \frac{\partial}{\partial y}(h_m \phi_s u_s v_s) + \frac{\partial}{\partial x} \left( \frac{1}{2} \beta_s^{x1} h_m h_g \phi_g + \frac{1}{2} \beta_s^{x2} h_m^2 \phi_s \right) \\ &= -\mathcal{M} u_s - \frac{\partial}{\partial x} \left( \frac{1}{2} \epsilon \gamma \phi_s h_m^2 \cos \zeta \right) + \frac{\epsilon \gamma}{2} h_m^2 (\cos \zeta) \frac{\partial \phi_s}{\partial x} + \epsilon h_g \phi_g (\cos \zeta) \frac{\partial h_m}{\partial x} \\ &+ s_{x(s)} + \mathcal{O}(\epsilon^{1+\nu}), \end{aligned} \quad (5.86)$$

and in the cross-slope direction

$$\begin{aligned} & \frac{\partial}{\partial t}(h_m \phi_s v_s) + \frac{\partial}{\partial x}(h_m \phi_s u_s v_s) + \frac{\partial}{\partial y}(h_m \phi_s v_s^2) + \frac{\partial}{\partial y} \left( \frac{1}{2} \beta_s^{y1} h_m h_g \phi_g + \frac{1}{2} \beta_s^{y2} h_m^2 \phi_s \right) \\ &= -\mathcal{M} v_s - \frac{\partial}{\partial y} \left( \frac{1}{2} \epsilon \gamma \phi_s h_m^2 \cos \zeta \right) + \frac{\epsilon \gamma}{2} h_m^2 (\cos \zeta) \frac{\partial \phi_s}{\partial y} + \epsilon h_g \phi_g (\cos \zeta) \frac{\partial h_m}{\partial y} \\ &+ s_{y(s)} + \mathcal{O}(\epsilon^{1+\nu}), \end{aligned} \quad (5.87)$$

where the factors are given by

$$\beta_s^{x1} = \epsilon(K_x^s + K_x^g) \cos \zeta, \quad \beta_s^{x2} = \frac{1}{3} \epsilon(1 - \gamma)(2K_x^s + K_x^g) \cos \zeta, \quad (5.88)$$

$$\beta_s^{y1} = \epsilon(K_y^s + K_y^g) \cos \zeta, \quad \beta_s^{y2} = \frac{1}{3} \epsilon(1 - \gamma)(2K_y^s + K_y^g) \cos \zeta, \quad (5.89)$$

$$\begin{aligned} s_{x(s)} &= h_m \phi_s \sin \zeta + \gamma C_d h_m \phi_s \phi_f (u_f - u_s) - \epsilon h_m \phi_s (\cos \zeta) \frac{\partial b}{\partial x} - k_s^b \phi_s u_s \\ &- \frac{u_s}{|\mathbf{v}_s|} \mu_s^b \left[ \cos \zeta \left( h_m \phi_s (1 - \gamma) + h_g \phi_g \right) + \lambda \kappa \left( h_m \phi_s (u_s^2 - \gamma u_f^2) + h_g \phi_g u_g^2 \right) \right] \\ &- \frac{u_s - u_g}{|\mathbf{v}_s - \mathbf{v}_g|} \mu_s^i (h_g \phi_g \cos \zeta + \lambda \kappa h_g \phi_g u_g^2) - k_s^i \phi_g (u_s^i - u_g^i), \end{aligned} \quad (5.90)$$

$$\begin{aligned} s_{y(s)} &= \gamma C_d h_m \phi_s \phi_f (v_f - v_s) - \epsilon h_m \phi_s (\cos \zeta) \frac{\partial b}{\partial y} - k_s^b \phi_s v_s \\ &- \frac{v_s}{|\mathbf{v}_s|} \mu_s^b \left[ \cos \zeta \left( h_m \phi_s (1 - \gamma) + h_g \phi_g \right) + \lambda \kappa \left( h_m \phi_s (u_s^2 - \gamma u_f^2) + h_g \phi_g u_g^2 \right) \right] \\ &- \frac{v_s - v_g}{|\mathbf{v}_s - \mathbf{v}_g|} \mu_s^i (h_g \phi_g \cos \zeta + \lambda \kappa h_g \phi_g u_g^2) - k_s^i \phi_g (v_s - v_g). \end{aligned} \quad (5.91)$$

The left-hand side of equation (5.86) includes the inertial terms and the gradients of the solid effective lateral stress. In comparison with the corresponding terms in (5.80) for the pure granular mass in the upper layer, the depth-averaged solid effective lateral stress  $\bar{\sigma}_{e(xx)} = (\beta_s^{x1} h_m h_g \phi_g + \beta_s^{x2} h_m^2 \phi_s)/2$ , on the one hand, is



intensified due to the existence of pure granular upper layer; on the other hand it is reduced by the buoyancy force from the fluid phase.

Moreover, the momentum exchange with the upper layer due to the mass exchange appears in the first term on the right-hand side of equation (5.86). The second and third terms together delineate contributions of the fluid pressure. Specifically, the second term represents the effect of the fluid pressure on the solid stress, and the third term serves as the buoyancy force. As described in Iverson (1997) and Pitman & Le (2005), the fluid pressure can mitigate the solid stress, thereby enhances the mobility of grains. In Pitman & Le (2005), the second and third terms together, are called as the buoyancy force. Furthermore, the fourth term  $\epsilon h_g \phi_g (\cos \zeta) \partial h_m / \partial x$  indicates the integrated contribution between the normal stress of pure granular upper layer and non-uniform state of the lower-layer height.

For the source terms described in equation (5.90), the gravity down-slope component, the drag force, the gradient of the bed surface, and the bed viscous friction are stated consecutively in the first line. The bed viscous friction indicates a fluid-like behavior of the solid phase, while the bed Coulomb friction, indicated in the second line of equation (5.90), describes a solid-like behavior. The normal traction in the bed Coulomb friction comprises the overburden pressure (the first terms in the square bracket) plus a contribution due to the bed curvature (the second terms in the square bracket). The last line of relation (5.90) represents the interfacial Coulomb and viscous frictions between the two layers. Similar explanations are also suitable for the cross-slope momentum equation (5.87).

3. For the fluid constituent in the lower layer, the resulting depth-averaged conservation equation for mass reads

$$\frac{\partial}{\partial t}(h_m \phi_f) + \frac{\partial}{\partial x}(h_m \phi_f u_f) + \frac{\partial}{\partial y}(h_m \phi_f v_f) = \mathcal{O}(\epsilon^{1+\nu}). \quad (5.92)$$

The depth-averaged momentum conservation equations read, in the downslope direction

$$\begin{aligned} \frac{\partial}{\partial t}(h_m \phi_f u_f) + \frac{\partial}{\partial x}(h_m \phi_f u_f u_f) + \frac{\partial}{\partial y}(h_m \phi_f u_f v_f) + \frac{\partial}{\partial x} \left( \frac{1}{2} \beta_f^x \phi_f h_m^2 \right) \\ = -\frac{\epsilon}{2} h_m^2 (\cos \zeta) \frac{\partial \phi_s}{\partial x} + s_{x(f)} + \mathcal{O}(\epsilon^{1+\nu}), \end{aligned} \quad (5.93)$$

and in the cross-slope direction

$$\begin{aligned} \frac{\partial}{\partial t}(h_m \phi_f v_f) + \frac{\partial}{\partial x}(h_m \phi_f u_f v_f) + \frac{\partial}{\partial y}(h_m \phi_f v_f v_f) + \frac{\partial}{\partial y} \left( \frac{1}{2} \beta_f^y \phi_f h_m^2 \right) \\ = -\frac{\epsilon}{2} h_m^2 (\cos \zeta) \frac{\partial \phi_s}{\partial y} + s_{y(f)} + \mathcal{O}(\epsilon^{1+\nu}), \end{aligned} \quad (5.94)$$

where the source terms are written as

$$s_{x(f)} = h_m \phi_f \sin \zeta - C_d h_m \phi_s \phi_f (u_f - u_s) - \epsilon h_m \phi_f (\cos \zeta) \frac{\partial b}{\partial x} - \frac{1}{\epsilon N_R} k_f^b u_f^b, \quad (5.95)$$

$$s_{y(f)} = -C_d h_m \phi_s \phi_f (v_f - v_s) - \epsilon h_m \phi_f (\cos \zeta) \frac{\partial b}{\partial y} - \frac{1}{\epsilon N_R} k_f^b v_f^b. \quad (5.96)$$

In the source terms (5.95) and (5.96), the diffusion terms are neglected due to the fact that they have a negligible effect on dynamics.

## 5.5 Conclusion

In this Chapter, a two-layer model have been proposed to describe unsaturated flows when the pore fluid cannot fill all the voids between particles. The upper pure granular mass is described by the theory of Savage & Hutter (1989), the lower mixture is accounted for by the mixture theory presented in Chapter 3, and the two layers are interacting at an interface which is a material surface for the fluid. The interface is a singular surface for the granular mass, and therefore jump conditions are employed to define boundary conditions for the granular mass at the interface. The derived depth-averaged equations describe evolutions of the upper height, the upper-layer depth-averaged velocity, the lower height, the lower-layer depth-averaged volume fractions, and the lower-layer depth-averaged velocities. The evolutions of these dynamical quantities will be exhibited next Chapter.

## 6 Dynamical modelling of unsaturated grain-fluid mixtures: simulation part

This section focuses on the simulation of a grain-fluid mixture of finite mass flowing on a slope. To demonstrate the capability of the present two-layer model to describe dynamics of unsaturated flows, we concentrate on two typical cases. One case is to probe into the transition process of an initially saturated mixture into a partially saturated state during flows, which is presented in Section 6.1, and the second case aims to investigate dynamical process of an initially unsaturated mixture. The second case consists of two subcases, in which the first subcase postulates that the fluid phase in the mixture has a large viscosity to account for the fact in natural debris flows that the fine grains increase the viscosity of the fluid phase by suspending in the fluid phase. The second subcase assumes that the fluid phase in the mixture has the small viscosity like the water. Both subcases are presented in Section 6.2

### 6.1 Transition of an initially saturated mixture into unsaturated state

Let us consider a grain-fluid mixture sliding down an inclined plane with a slope angle of  $45^\circ$ . The slope is connected with a horizontal run-out plane by a smooth transition zone (see Fig. 5.1). A rectangular domain  $x \in [-10, 120]$  and  $y \in [-25, 25]$  in non-dimensional length units is chosen as the computational domain, where the inclined part lies in  $x \in [-10, 40]$  and the horizontal area in  $x \geq 54.5$ . The transition zone is  $x \in [40, 54.5]$ . We prescribe the inclination angle as follows

$$\zeta(x) = \begin{cases} \zeta_0, & x \leq 40, \\ \zeta_0(1 - (x - 40)/14.5), & 40 < x < 54.5, \\ 0^\circ, & x \geq 54.5, \end{cases} \quad (6.1)$$

where  $\zeta_0 = 45^\circ$ .

Furthermore, the grain-fluid mixture is originally held within a hemispherical shell of radius  $r_0 = 2$ . The saturated grain-fluid mixture has an initial height of

$$h_m(x, y, t = 0) = \sqrt{2} \left( 1 - \frac{(x - x_0)^2}{r_0^2} - \frac{(y - y_0)^2}{r_0^2} \right)^{1/2}, \quad (6.2)$$

where the center of the shell is initially located at  $(x_0, y_0) = (5, 0)$ . The initial volume fractions are assumed to be homogeneously distributed with  $\phi_s = \phi_{\max}$  and  $\phi_f = 1 - \phi_{\max}$ .

In the numerical simulations, we choose:  $C_d = 3$ ,  $k_s^i = 0$ ,  $k_s^b = 0.0013$ ,  $k_f^b = 30$ ,  $c = 1$ ,  $N_R = 19265$ ,  $\delta = 27^\circ$ ,  $\gamma = 0.4$  (corresponding to  $\tilde{\rho}_f = 1000 \text{ kg/m}^3$  and  $\tilde{\rho}_s = 2500 \text{ kg/m}^3$ ),  $\phi_{\max} = 0.675$  corresponding to a closest packing of identical spherical grains, and  $K_x^g = K_x^s = 1$  and  $K_y^g = K_y^s = 1$ . Given that we attempt to probe into the phase-separation phenomenon between the two components of the mixture, moderate values of  $C_d$  and  $k_f^b$  are used. The other parameters are similar to those used in chapter four. Additionally,  $\epsilon = 1$  and  $\lambda = 1$  are chosen.

This flow case is numerically simulated, respectively, by the two-layer model and the single-layer model, though the latter is not appropriate when the unsaturated state occurs. In the two-layer model, the initial condition of saturation indicates that the upper-layer initial height is zero. Once the condition  $\phi_s > \phi_{\max}$  occurs which is non-physical and implies that the mixture becomes partially saturated, the pure granular upper layer develops. For this case, the model equations (5.79)-(5.81) of the upper-layer pure granular mass separating from the lower layer will be also calculated.

Fig. 6.1 indicates that a blunt snout is developed in both two-layer and single-layer models when the mixture driven by the gravity force is released. The development of the blunt head is in agreement with the result in Iverson (1997) where a single-

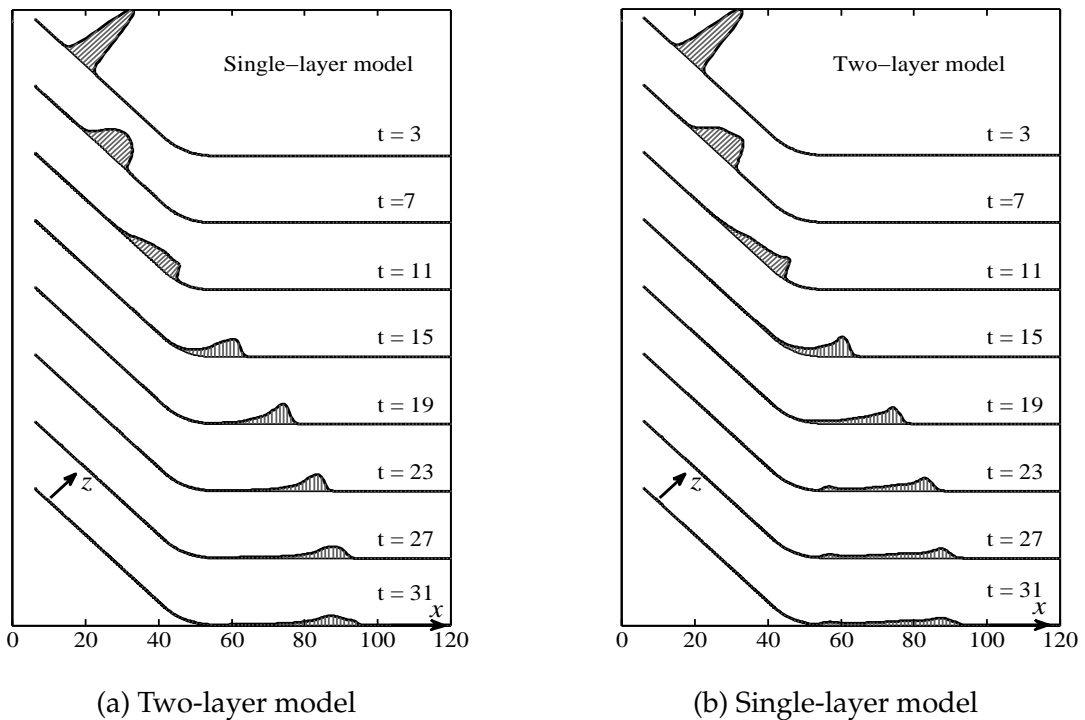


Figure 6.1: Comparison of the total height profiles along the longitudinal section of the flows,  $y = 0$ , between the two-layer and single-layer models. The heights are enlarged by sixty times.

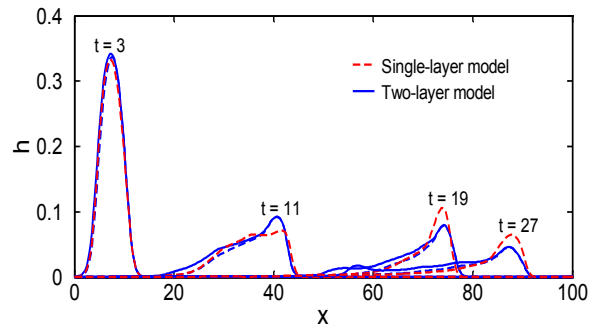


Figure 6.2: Comparison of the depth profiles along the longitudinal section of the flows,  $y = 0$ , obtained by the present two-layer and single-layer model. The red lines denote total heights computed by the single-layer model. The blue solid and dash lines represent the total two-layer height and the lower-layer mixture height, respectively, obtained by the two-layer model.

layer model assuming the same velocity for the solid and fluid constituents was employed. Because the front is accelerating more rapidly than the tail, the mixture body is therefore continuously elongated until it reaches the horizontal plane. Once the mass reaches the horizontal plane, it decelerates due to the basal friction and the absence of the driving force. Then, the blunt snout begins to diffuse and becomes flattened. These phenomena are similar to the observations in nature and experiments (see Iverson (1997)).

Moreover, on the one hand, Fig. 6.1 shows that the two-layer and single-layer models predict almost the same speed for the flowing front. However, this conclusion from this case can perhaps not be generalized to all cases. On the other hand, Fig. 6.1 also indicates different predictions of the height profiles between these two kinds of models. As time increases, the two-layer model predicts a smaller height at the front and a larger height at the tail than the single-layer model from  $t = 19$  onwards, which is more clearly shown in Fig. 6.2. It may be explained as follows. In the two-

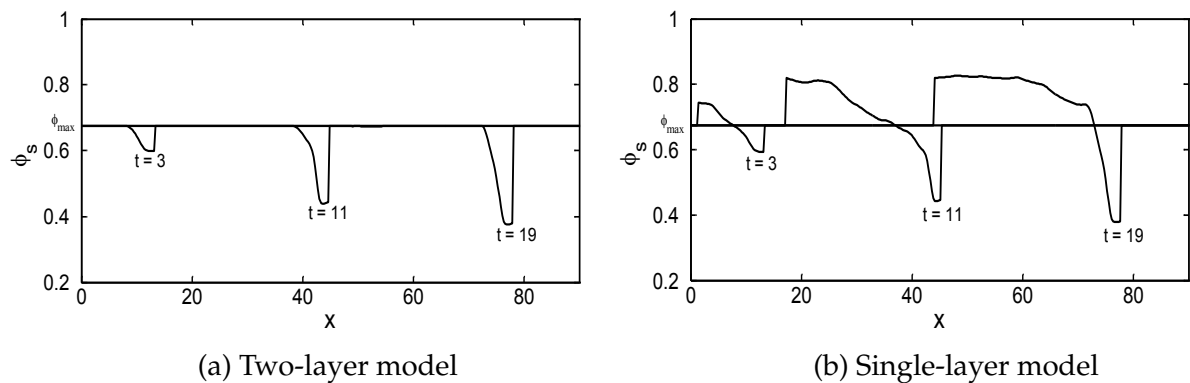
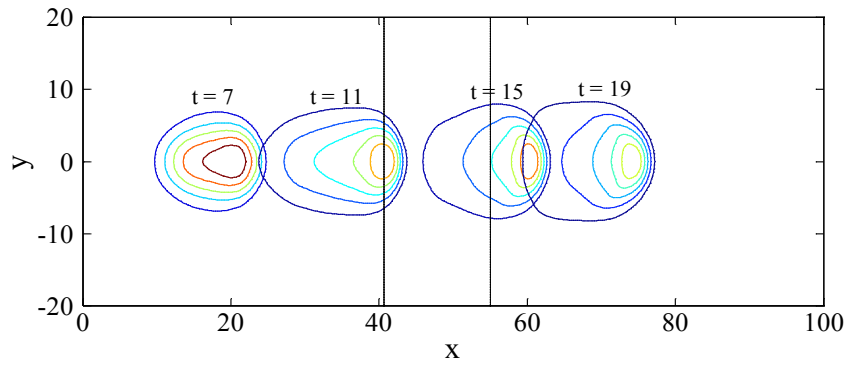
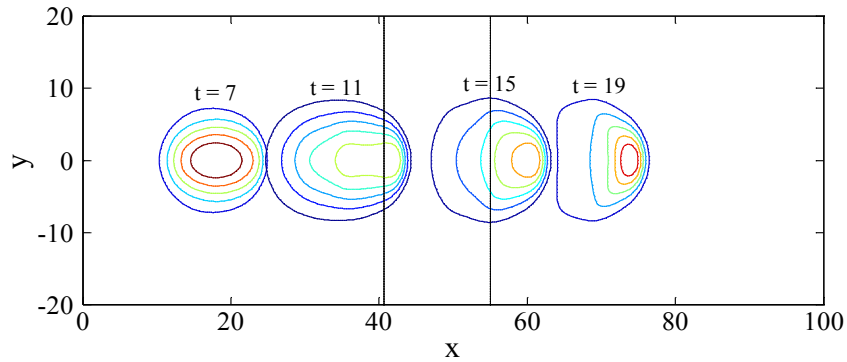


Figure 6.3: Profiles of solid volume fraction along the central line of the flow,  $y = 0$ , obtained from the two-layer model (panel (a)) and single-layer model (panel (b)) where  $C_d = 3$  is used.



(a) Contour plots from two-layer model



(b) Contour plots from single-layer model

Figure 6.4: Contour plots of the total height of a grain-fluid mixture down a curved plane obtained by a two-layer (panel a) and single-layer models (panel b), respectively. The regions between two transverse lines represent transition zone between inclined and horizontal parts.

layer model, the pure granular layer emerges at the tail separating from the lower saturated layer. These pure granular mass subjected to a larger internal friction, to a certain extent, pulls the lower layer backward and as a result yields a thicker tail and smaller front.

Additionally, the dynamic variation of the solid volume fraction  $\phi_s$  is investigated in Fig. 6.3. The two-layer model predicts  $\phi_s < \phi_{\max}$  where the condition of saturation is satisfied and hence the pure granular upper layer is absent, and  $\phi_s = \phi_{\max}$  in the lower-layer regions covered by the pure granular upper layer where the flow is unsaturated. This result is in agreement with the postulation of Berzi (2008) where he postulated  $\phi_s = \phi_{\max}$  according to the analytical solution for a dense saturated flows (see Berzi & Jenkins (2008)). Conversely, when the single-layer model is employed for this case, the non-physical result  $\phi_s > \phi_{\max}$  can be evolved from the saturated condition  $\phi_s + \phi_f = 1$ , as indicated in Fig. 6.3(b). This non-physical result indicates that the two-layer model is necessary to investigate the transition process of a saturated mixture into undersaturated state. In this case the proposed two-layer model may provide more reasonable investigations to the temporal and spatial evolutions of the flow height.

Fig. 6.4 depicts the contour plots of the total flow height. After the material is released, the body of mass starts to stretch in the longitudinal direction and spread in the transverse direction, which is also revealed by Pudasaini et al. (2005). Additionally, it is noted that the two-layer model predicts a longer tail than the single-layer model. It may be explained as follows. As indicated in Fig. 6.2, the two-layer model predicts a pure granular layer emerging at the tail. This solid-dominated tail is prone to be pulled longer by the front where more fluid is accumulated.

## 6.2 Dynamics of an initially unsaturated mixture

With aims of predicting the dynamics of unsaturated flows, we take an initially unsaturated mixture into account. The lower-layer height profile at the initial is defined by (6.2), and the upper-layer height profile at the initial is prescribed as

$$h_g(x, y, t = 0) = (2 - \sqrt{2}) \left( 1 - \frac{(x - x_0)^2}{r_0^2} - \frac{(y - y_0)^2}{r_0^2} \right)^{1/2}. \quad (6.3)$$

### 1. Case I: Dynamics of a high viscous fluid interacting with grains

In this case, it is assumed that the fluid phase in the mixture has a large viscosity, representing the enhancement of the fluid viscosity by suspension of fine parti-

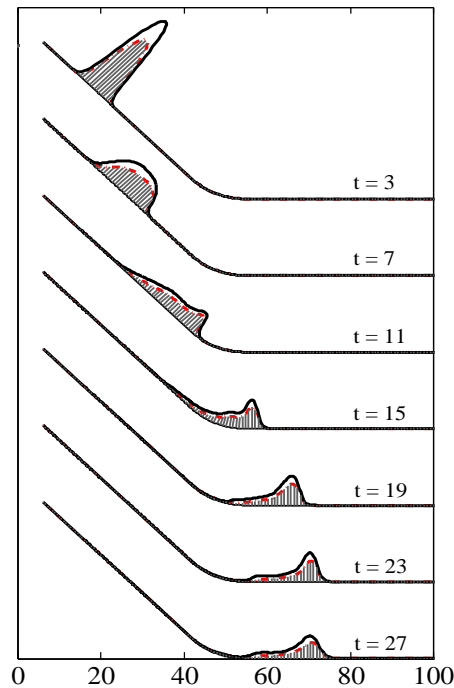


Figure 6.5: Profiles of both heights along the center line of the flow,  $y = 0$ . The upper layer is indicated by the blank area, and the lower layer is indicated by the shaded area. The heights are enlarged sixty times.

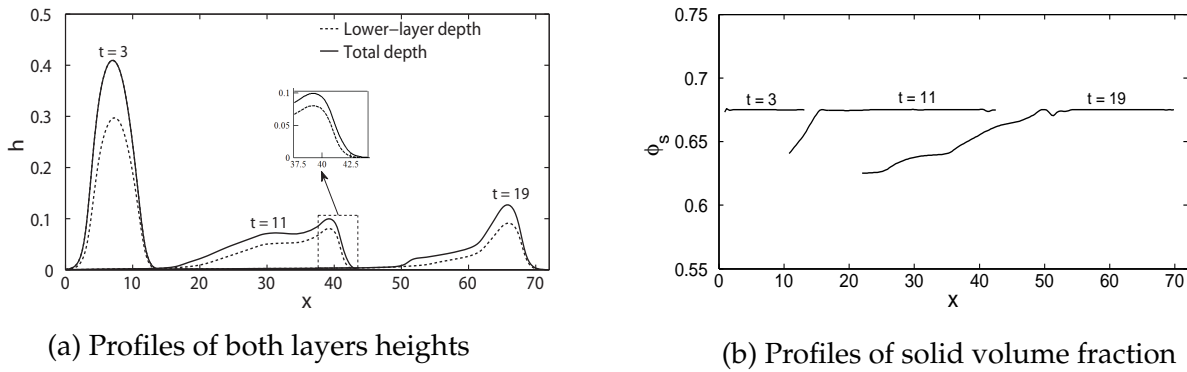


Figure 6.6: Profiles of height and solid volume fraction along the center line of the flow,  $y=0$

cles. Furthermore, a larger  $C_d = 6$  and a larger  $k_f^b = 120$  are used for this case, and the rest of parameters are the same as in case I.

Fig. 6.5 shows the evolution of the two-layer heights along the central line of the flow,  $y = 0$ , at several dimensionless time steps. Once the material is released from a hemispherical shell, the two-layer materials start accelerating down the slope, in which no obvious separation between the upper layer and lower layer is observed at the initial stage. As the mass slides farther downslope, the upper-layer grains are transported to the front due to the fact that the lower-layer grains are experiencing larger friction than the the upper-layer grains, such that a grain-enriched front develops followed by a fluid-dominated thin tail (see the profile at  $t = 11$  in Fig. 6.6). As the mass approaches the horizontal run-out plane, the mass slows down due to the absence of driven force, especially for the granular phase. As a result, the grain-enriched front disappears, and the mixture contracts and heaps up. These phenomena are consistent with the experiments of Iverson et al. (2010).

## 2. Case II: Dynamics of a low viscous fluid interacting with grains

In this case, we still focus on the dynamics of an initially two-layer material defined by (6.2) and (6.3). This case distinguishes from case II in the fact that the fluid phase in the mixture has a small viscosity. Therefore, a smaller  $C_d = 1$  and  $k_f^b = 30$  due to a small fluid viscosity are chosen. The rest parameters are the same as case I.

In Fig. 6.7, the evolution of the mixture height along the central line of the flow,  $y = 0$ , at various non-dimensional time is shown. Once the two-layer mixture driven by the gravity force is released, it accelerates downslope and extends. The fluid phase moves faster due to smaller internal and bed frictions than the solid constituent for this case, and hence a larger fraction of fluid is accumulated in the front than in the tail (see Fig. 6.8). The lower-layer fluid in the tail is not sufficient to maintain the lower-layer mixture saturated, such that the granular mass of the lower layer is partially transferred to the pure granular upper layer



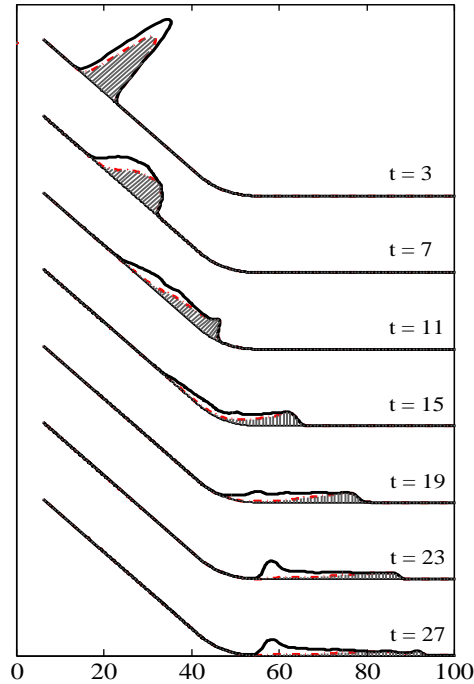
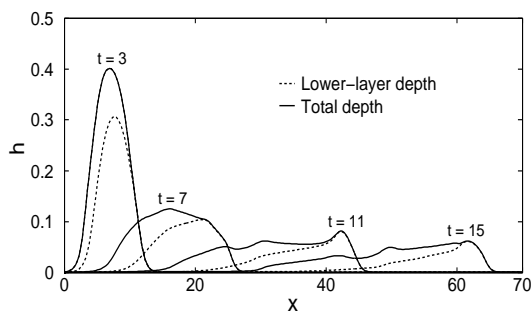


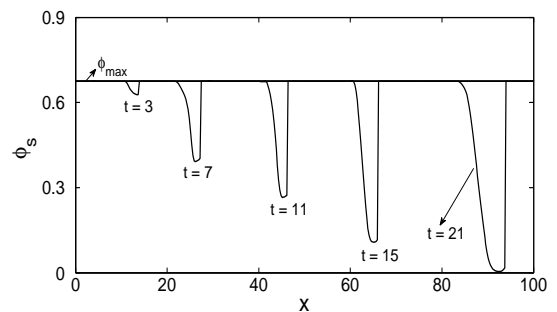
Figure 6.7: Profiles of heights for a two-layer partially saturated mixture along the longitudinal section of the flow,  $y = 0$ . The lower-layer two-phase grain-fluid saturated mixture is indicated by the shaded region, and the upper-layer pure granular mass is indicated by the blank region. The heights are enlarged sixty times.

across the fluid surface (interface). Even in the tail almost just the pure granular upper layer exists and the mixture lower layer nearly vanishes from  $t = 7$  onwards. A counter process occurs in the front, where the lower layer prevails and the upper layer vanishes.

Fig. 6.7 further demonstrates that when the frontal part of the layered mixture reaches the horizontal run-out zone, the mixture decelerates due to the decrease of driven force and contracts, especially for the granular mass in both layers



(a) Profiles of heights



(b) Profiles of solid volume fraction

Figure 6.8: Profiles of heights and solid volume fraction along the longitudinal section of the flow,  $y = 0$ .

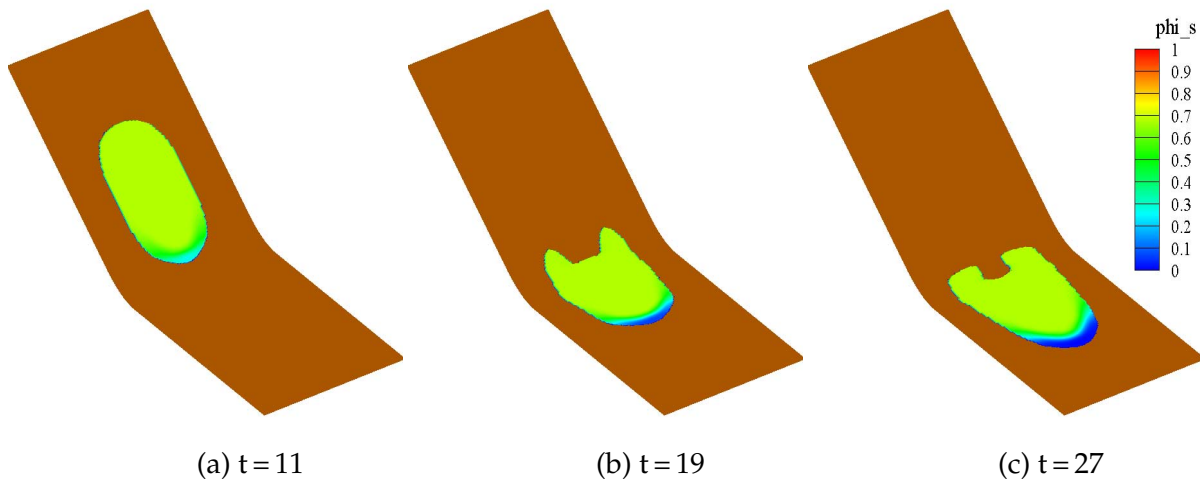


Figure 6.9: Three dimensional geometries of the partially saturated mixture at non-dimensional times  $t = 11$ ,  $19$  and  $t = 27$ . The colors indicate the solid volume fraction. The corresponding animation is enclosed in the supplementary material.

that is experiencing a greater friction. The granular mass of the tail starts to heap up, whereas the fluid is continuously moving such that a finely tapered shape develops from the tail to the front, which is similar to that found in the simulation of pure granular flows (see (Wang et al. 2004)).

### 6.3 Conclusion

In this Chapter, two typical cases, including dynamics of an initially saturated mixture and dynamics of an initially layered mixture, are investigated. Additionally, two subcases in case II are probed, in which the first subcase assumes that the pore fluid has a large viscosity to account for the fact in natural debris flows that the fine grains increase the viscosity of the fluid phase by suspending in the fluid phase. The second subcase in case II assumes that the fluid phase in the mixture has the small viscosity like the water. It should be note that the present model used for the cases above have not considered the granular dilatancy, which will be considered next Chapter.

# 7 Dynamical modelling of grain-fluid mixtures by considering dilatancy

Recent experiments found that the granular dilatancy may play an important role in the dynamics of grain-fluid mixtures by influencing the pore fluid pressure that can enhance or mitigate the granular frictions, see Iverson (2005), Pailha, Nicolas & Pouliquen (2008), Iverson et al. (2010), and Rondon, Pouliquen & Aussillous (2011). Consequently, based on the two-phase saturated model presented in Chap. 3, this Chapter aims to extend this saturated model by taking the granular dilatancy into account.

In this Chapter, the mixture theory is coupled with the modified critical-state theory of Pailha & Pouliquen (2009) relating the granular dilatation or compaction to shear rate, to define the governing equations. This aspect is presented in Section 7.1. By using the thin-layer approximation to simplify the governing equations, an equation describing the relationship between the granular dilatancy and the pore fluid pressure can be derived, in addition to the mass and momentum equations. This equation on the pore fluid pressure reveals that when a densely packed wet granular medium is subject to shear, the pore pressure drops and the fluid as a result is sucked into the voids between the grains. These aspects are presented in Section 7.2. To validate the present model with the granular dilatancy into account, we use this model to revisit the experimental case of Iverson et al. (2010), and compare the model results with experimental data. These aspects are presented in Section 7.3.

## 7.1 Field equations

### 7.1.1 Governing equations

In this Chapter, we focus on a two-phase grain-fluid mixture, and idealize that the fluid phase in the mixture fills all the voids between the grains. Consequently, the saturated condition (2.14) can be applied. Additionally, the fluid and granular components of the mixture are thought to be incompressible, such that the intrinsic densities of the fluid and granular components are constant with time. With these descriptions, the mass and momentum equations can be given by equations (2.44)-(2.47).

### 7.1.2 Dilatancy law

A key feature of the present model lies in the introduction of the critical-state theory to describe the granular dilatancy. The original critical-state theory, proposed by Roux &

Radjai (1998), is valid for quasi-static flows of dry granular media, and it is modified later by Pailha & Pouliquen (2009) for a submarine granular rapid flow. This modified theory of Pailha & Pouliquen (2009) relates the dilatation or the compaction of grains to the dilatancy angle  $\pi$  by

$$-\frac{1}{\phi_s} \frac{d\phi_s}{dt} = \nabla \cdot \mathbf{v}_s = \dot{\gamma} \tan \pi, \quad (7.1)$$

$$\tan \pi = k_1(\phi_s - \phi_{eq}), \quad (7.2)$$

$$\phi_{eq} = \phi_c - k_2 I_v, \quad (7.3)$$

when a granular medium is sheared with a shear rate  $\dot{\gamma}$  ( $\dot{\gamma}/2$  is the square root of the second principal invariant of the deviatoric deformation-rate tensor). In relations (7.1)-(7.3),  $k_1$  and  $k_2$  are positive parameters,  $\phi_{eq}$  is the solid volume fraction associated with steady state, and  $\phi_c$  is the critical solid volume fraction observed when a continuous quasi-static deformation takes place. Usually,  $\phi_c$  determines that the initial packing is dense (above  $\phi_c$ ) or loose (below  $\phi_c$ ). Another parameter  $I_v = \mu_f \dot{\gamma} / \sigma_0$  represents the timescale ratio between the grain-rearrangement timescale ( $\mu_f / \sigma_0$ ) and characteristic time ( $1/\dot{\gamma}$ ) for bulk shear deformation, where  $\sigma_0$  denotes the solid effective normal stress and equals the total stress of the mixture minus the pore pressure by its definition.

Additionally, relation (7.1) can be recast into

$$-\frac{1}{\phi_s} \frac{d\phi_s}{dt} = \nabla \cdot \mathbf{v}_s = \nabla \cdot \phi_f (\mathbf{v}_s - \mathbf{v}_f) = \dot{\gamma} \tan \pi, \quad (7.4)$$

by using the mass equations (2.44) and (2.45). As previous studies, e.g. Pailha & Pouliquen (2009), Iverson & George (2014) and Bouchut, Fernandez-Nieto, Mangeney & Narbona-Reina (2016), showed, relations (7.2)-(7.4) unveil an important coupling between the dilatation and the pore pressure. If  $\phi_s > \phi_{eq}$ , the granular matrix will dilate ( $\nabla \cdot \mathbf{v}_s > 0$ ) when sheared, such that the pore pressure will decline, and as a result, the fluid will be sucked into the voids between the grains ( $\nabla \cdot \phi_f (\mathbf{v}_s - \mathbf{v}_f) > 0$ ). On the contrary, if  $\phi_s < \phi_{eq}$ , the granular matrix, subject to a shear, will compact ( $\nabla \cdot \mathbf{v}_s < 0$ ) such that the pore pressure will elevate and the fluid will be expelled from the voids between the grains ( $\nabla \cdot \phi_f (\mathbf{v}_s - \mathbf{v}_f) < 0$ ).

### 7.1.3 Boundary conditions

We assume that the granular and fluid phases separately satisfy non-penetration boundary condition (3.3) at the bottom. Additionally, a Navier bed slip law (3.4) is proposed for the fluid phase, and a Coulomb-like bed friction law

$$\boldsymbol{\sigma}_e^b \mathbf{n}^b - (\mathbf{n}^b \cdot \boldsymbol{\sigma}_e^b \mathbf{n}^b) \mathbf{n}^b = -\frac{\mathbf{v}_s^b}{|\mathbf{v}_s^b|} (\mathbf{n}^b \cdot \boldsymbol{\sigma}_e^b \mathbf{n}^b) \hat{\mu}_s^b - k_s^b \phi_s^b \mathbf{v}_s^b, \quad (7.5)$$

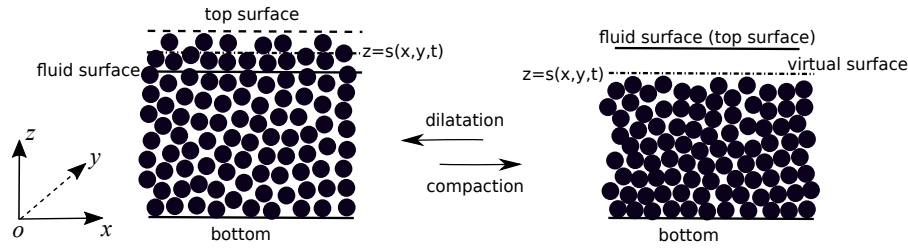


Figure 7.1: Sketch of the variance in the position of a virtual surface ( $z = s(x, y, t)$ ) due to the dilatation and compaction of grains.

is proposed for the granular phase, where  $\mathbf{n}^b$  is the normal vector of the bed topography. It should be noted that (7.5) is different from (5.9) due to the fact that  $\hat{\mu}_s^b = \tan(\delta + \pi)$  characterising the effect of dilatancy on the bed Coulomb frictional coefficient, instead of  $\mu_s^b = \tan \delta$  in (5.9), is used herein.

The dilatancy law employed here allows grains to disperse above the fluid surface or accumulate beneath the fluid surface (see Fig. 7.1). This phenomenon poses a challenge to properly define the upper boundary. To circumvent this difficulty, Iverson & George (2014) introduced a virtual free surface that ensures that the mixture mass beneath the virtual surface per unit basal area is the same as the mass between the bottom and the top surface, and the volume fractions can be reasonably assumed to be uniform along the depth direction. As Iverson & George (2014) described, some combination of solid or fluid mass immediately above or below the virtual surface will be replaced by an equivalently massive and homogeneous layer with density  $\rho$  and the upper surface at  $z = s(x, y, t)$ . With these descriptions, a material surface condition can be written in terms of the mixture velocity  $\mathbf{v}_m^s$  at the virtual surface, which is

$$\frac{\partial \mathcal{F}^s}{\partial t} + \mathbf{v}_m^s \cdot \nabla \mathcal{F}^s = 0, \quad \text{and} \quad \mathcal{F}^s = z - s(x, y, t), \quad (7.6)$$

where  $\mathbf{v}_m^s = (\rho_s^s \mathbf{v}_s^s + \rho_f^s \mathbf{v}_f^s) / \rho^s$ . The boundary condition (7.6) can be rewritten as

$$\rho_s^s \left( \mathbf{v}_s^s + \frac{\partial \mathcal{F}^s}{\partial t} \frac{\nabla \mathcal{F}^s}{|\nabla \mathcal{F}^s|} \right) \cdot \mathbf{n}^s + \rho_f^s \left( \mathbf{v}_f^s + \frac{\partial \mathcal{F}^s}{\partial t} \frac{\nabla \mathcal{F}^s}{|\nabla \mathcal{F}^s|} \right) \cdot \mathbf{n}^s = 0, \quad (7.7)$$

where  $\mathbf{n}^s = \nabla \mathcal{F}^s / |\nabla \mathcal{F}^s|$ . Additionally, a dynamic condition needs to be proposed at the virtual surface. Iverson & George (2014) postulated that the fluid and granular phases move with the same velocity in the slope-align direction. With this postulation, the inflow momentum flux and outflow momentum flux across the virtual surface will cancel out in the slope-align direction such that a traction-free dynamic condition for the mixture holds at the virtual surface (see Iverson & George (2014)). In our case,

the velocity of the fluid phase may deviate from the one of the granular phase. Hence a more general dynamic boundary condition is needed. To this end, we propose

$$\left[ \rho_s^s (\mathbf{v}_s^s - \mathbf{v}_m^s) \cdot \mathbf{n}^s \right] (\mathbf{v}_s^s - \mathbf{v}_f^s) = \boldsymbol{\sigma}_f^s \cdot \mathbf{n}^s + \boldsymbol{\sigma}_s^s \cdot \mathbf{n}^s, \quad (7.8)$$

which presents a momentum balance for an infinitesimal element at the virtual free surface. When both phases move with the same velocity as in Iverson & George (2014), relation (7.8) can reproduce the traction-free condition. Moreover, we split (7.8) into the following forms,

$$\boldsymbol{\sigma}_f^s \cdot \mathbf{n}^s = \alpha \left[ \rho_s^s (\mathbf{v}_s^s - \mathbf{v}_m^s) \cdot \mathbf{n}^s \right] (\mathbf{v}_s^s - \mathbf{v}_f^s), \quad (7.9)$$

$$\boldsymbol{\sigma}_s^s \cdot \mathbf{n}^s = (1 - \alpha) \left[ \rho_s^s (\mathbf{v}_s^s - \mathbf{v}_m^s) \cdot \mathbf{n}^s \right] (\mathbf{v}_s^s - \mathbf{v}_f^s), \quad (7.10)$$

to indicate the effects of the net momentum flux across the virtual surface on individual stress, where  $\alpha$  is assumed to be  $\phi_f^s$  here. The choice of  $\alpha = \phi_f^s$  can reproduce the classical single-phase traction-free condition when either phase is absent.

## 7.2 Depth-averaged theory

To properly describe the dynamics of a flowing grain-fluid mixture, a coordinate system must be defined. We define the coordinate system described in Fig. 3.2 as our coordinate system. To avoid lengthy mathematical formulation, we assume a flat bed without any elevation, i.e.  $b(x, y) = 0$ . In this case, the virtual free surface is  $z = h_m(x, y, t)$ , where  $h_m(x, y, t)$  denotes the mixture height. For details of this coordinate system, refer to Section 3.2.

To derive a depth-averaged model, it is necessary to rewrite the aforementioned boundary conditions in a component form, which is given below.

### 7.2.1 Non-dimensional boundary conditions

To non-dimensionalize the aforementioned boundary conditions, it is necessary to define the scalings of physical quantities. To this end, the scalings defined in (3.11) can be referred to. Consequently, the non-dimensional boundary conditions are presented as follows.

1. **At the bottom**, the downslope component, cross-slope component and the normal component of the Coulomb-like friction condition (7.5) can be non-dimensionalized

onized by applying the scalings (3.11) and (5.16), and the non-dimensional components are indicated as follows

$$\mu_s^b \sigma_{e(xz)}^{b*} = -\sigma_{e(zz)}^{b*} \frac{u_s^{b*}}{\sqrt{(u_s^{b*})^2 + (v_s^{b*})^2}} \hat{\mu}_s^b - k_s^{b*} \phi_s^b u_s^{b*}, \quad (7.11)$$

$$\mu_s^b \sigma_{e(yz)}^{b*} = -\sigma_{e(zz)}^{b*} \frac{v_s^{b*}}{\sqrt{(u_s^{b*})^2 + (v_s^{b*})^2}} \hat{\mu}_s^b - k_s^{b*} \phi_s^b v_s^{b*}. \quad (7.12)$$

Similarly, the non-dimensional downslope component, cross-slope component and the normal component of the fluid Navier bed slip condition are indicated in equations (3.34)-(3.36). Additionally, the non-dimensional form of the kinematic boundary condition are indicated in equation (3.33).

2. Before deriving the non-dimensional forms of the boundary conditions **at the virtual free surface**, some definitions are made. Let us define the granular mass flux across the virtual surface as  $\rho_s^s (\mathbf{v}_s^s - \mathbf{v}_m^s) \equiv \mathcal{J}$ . Expanding this expression, one can obtain

$$\mathcal{J} \equiv \rho_s^s (\partial h_m / \partial t + u_s^s \partial h_m / \partial x + v_s^s \partial h_m / \partial y - w_s^s). \quad (7.13)$$

The mass flux principally depends on the normal velocity across the virtual surface, and  $\epsilon \tilde{\rho}_s \sqrt{g\mathcal{L}}$  is therefore chosen as the scaling for the mass flux  $\mathcal{J}$ . As a result, the non-dimensional form of the mass flux  $\mathcal{J}$  is written as

$$\mathcal{J}^* = \phi_s^s \left( \frac{\partial h_m^*}{\partial t^*} + u_s^{s*} \frac{\partial h_m^*}{\partial x^*} + v_s^{s*} \frac{\partial h_m^*}{\partial y^*} - w_s^{s*} \right). \quad (7.14)$$

With the non-dimensional mass flux, relation (7.7) can be non-dimensionalized as

$$\phi_s^s \left( \frac{\partial h_m^*}{\partial t^*} + u_s^{s*} \frac{\partial h_m^*}{\partial x^*} + v_s^{s*} \frac{\partial h_m^*}{\partial y^*} - w_s^{s*} \right) = -\gamma \phi_f^s \left( \frac{\partial h_m^*}{\partial t^*} + u_f^{s*} \frac{\partial h_m^*}{\partial x^*} + v_f^{s*} \frac{\partial h_m^*}{\partial y^*} - w_f^{s*} \right). \quad (7.15)$$

Moreover, by virtue of the scaling (3.11) and the scaling for the mass flux, the dynamic boundary conditions (7.9) and (7.10) can be non-dimensionalized, and the non-dimensional downslope component, the cross-slope component, and the normal component are given by

$$\epsilon \phi_f^s p_f^{s*} \psi^s \frac{\partial h_m^*}{\partial x^*} - \frac{\epsilon}{N_R} \tau_{f(xx)}^{s*} \psi^s \frac{\partial h_m^*}{\partial x} - \frac{\epsilon}{N_R} \tau_{f(xy)}^{s*} \frac{\partial h_m^*}{\partial y^*} + \frac{1}{N_R} \tau_{f(xz)}^{s*} = \frac{1}{\gamma} \phi_f^s \mathcal{J}^* (u_f^{s*} - u_s^{s*}), \quad (7.16)$$

$$-\frac{\epsilon}{N_R} \tau_{f(yx)}^{s*} \psi^s \frac{\partial h_m^*}{\partial x^*} + \epsilon \phi_f^s p_f^{s*} \frac{\partial h_m^*}{\partial y^*} - \frac{\epsilon}{N_R} \tau_{f(yy)}^{s*} \frac{\partial h_m^*}{\partial y^*} + \frac{1}{N_R} \tau_{f(yz)}^{s*} = \frac{1}{\gamma} \phi_f^s \mathcal{J}^* (v_f^{s*} - v_s^{s*}), \quad (7.17)$$

$$-\frac{\epsilon}{N_R} \tau_{f(zx)}^{s*} \psi^s \frac{\partial h_m^*}{\partial x^*} - \frac{\epsilon}{N_R} \tau_{f(zy)}^{s*} \frac{\partial h_m^*}{\partial y^*} - \phi_f^s p_f^{s*} + \frac{\tau_{f(zz)}^{s*}}{N_R} = \frac{\epsilon}{\gamma} \phi_f^s \mathcal{J}^* (w_f^{s*} - w_s^{s*}), \quad (7.18)$$

and

$$\epsilon\gamma\phi_s^s p_f^{s*} \psi^s \frac{\partial h_m^*}{\partial x^*} + \epsilon\sigma_{e(xx)}^{s*} \frac{\partial h_m^*}{\partial x^*} + \epsilon\mu_s^b \sigma_{e(xy)}^{s*} \frac{\partial h_m^*}{\partial y^*} - \mu_s^b \sigma_{e(xz)}^{s*} = \phi_s^s \mathcal{J}^*(u_f^{s*} - u_s^{s*}), \quad (7.19)$$

$$\epsilon\gamma\phi_s^s p_f^{s*} \psi^s \frac{\partial h_m^*}{\partial x^*} + \epsilon\mu_s^b \sigma_{e(yx)}^{s*} \frac{\partial h_m^*}{\partial x^*} + \epsilon\sigma_{e(yy)}^{s*} \frac{\partial h_m^*}{\partial y^*} - \mu_s^b \sigma_{e(yz)}^{s*} = \phi_s^s \mathcal{J}^*(v_f^{s*} - v_s^{s*}), \quad (7.20)$$

$$-\phi_s^s \gamma p_f^{s*} \psi^s + \epsilon\mu_s^b \sigma_{e(zx)}^{s*} \frac{\partial h_m^*}{\partial x^*} + \epsilon\mu_s^b \sigma_{e(zy)}^{s*} \frac{\partial h_m^*}{\partial y^*} - \sigma_{e(zz)}^{s*} = \epsilon\phi_s^s \mathcal{J}^*(w_f^{s*} - w_s^{s*}), \quad (7.21)$$

respectively, where the non-dimensional form of the mass flux  $\mathcal{J}$  is written as

The superscript  $*$  above represents the non-dimensional quantities, and will be dropped in the following for simplicity.

It is necessary to note that the non-dimensional balance equations for mass are indicated in (3.13) and (3.14), and balance equations for fluid momentum are indicated in equations (3.16)-(3.18), and equations for granular momentum are indicated in (3.21)-(3.23).

## 7.2.2 Mass balances

Integrating mass balances (3.13) and (3.14) over the depth and applying the Leibnitz integration rule to interchange the orders of differentiation and integration, one can derive the depth-averaged forms of the mass balances. Furthermore, substituting the boundary conditions (3.33) and relation (7.15), and applying relations (3.41) and (3.42) to approximate the results to the order  $\mathcal{O}(\epsilon^{1+\nu})$ , one can obtain

$$\frac{\partial(h_m \bar{\phi}_f)}{\partial t} + \frac{(h_m \bar{\phi}_f \bar{u}_f)}{\partial x} + \frac{(h_m \bar{\phi}_f \bar{v}_f)}{\partial y} = -\mathcal{J}/\gamma, \quad (7.22)$$

$$\frac{\partial(h_m \bar{\phi}_s)}{\partial t} + \frac{(h_m \bar{\phi}_s \bar{u}_s)}{\partial x} + \frac{(h_m \bar{\phi}_s \bar{v}_s)}{\partial y} = \mathcal{J}, \quad (7.23)$$

where we follow the convention in Chap. 3 to indicate the mean value of a quantity through the depth by the symbol overbar.

Multiplying equations (7.22) and (7.23) by the fluid and the granular intrinsic densities, respectively, and then adding the results can yield the dimensional mass balance for the mixture as a whole, which is given by

$$\frac{\partial(h_m \bar{\rho})}{\partial t} + \frac{(h_m \bar{\rho} \bar{u}_m)}{\partial x} + \frac{(h_m \bar{\rho} \bar{v}_m)}{\partial y} = 0, \quad (7.24)$$



where  $\bar{\rho} = \bar{\rho}_s + \bar{\rho}_f$ ,  $\bar{u}_m = (\bar{\rho}_s \bar{u}_s + \bar{\rho}_f \bar{u}_f) / \bar{\rho}$ , and  $\bar{v}_m = (\bar{\rho}_s \bar{v}_s + \bar{\rho}_f \bar{v}_f) / \bar{\rho}$ .

### 7.2.3 Slope-normal components of the momentum balances

In Chap. 3, the normal components of the momentum balances, (3.18) and (3.23), are reduced to hydrostatic balances when they are subject to the simplifications of the thin-layer approximation. The acceleration terms and the normal component of the drag force are ignored, which implies that the pore fluid pressure is simply hydrostatic. Here the thin-layer approximation is still used to simplify equations (3.18) and (3.23), in which the acceleration terms are ignored, but the normal component of the drag force is kept due to the following aspects. The grains can have a significant motion in the depth direction in relation to the fluid phase, caused by the dilatancy. This means that  $w_f - w_s \sim \mathcal{O}(1)$  in the presence of dilatancy, instead of  $w_f - w_s \sim \mathcal{O}(\epsilon)$  assumed in the third Chapter. Additionally, it is necessary to note that the non-dimensional drag force coefficient  $\vartheta = \mu_f \sqrt{\mathcal{L}} / (\tilde{\rho}_f k \sqrt{g}) \sim 10^3$  is the order of  $\mathcal{O}(\epsilon^{-1})$ , since  $\mu_f = 0.001$  (Pa · s),  $\mathcal{L} = 100$  m,  $\tilde{\rho}_f = 1000$  kg/m<sup>3</sup>,  $g = 9.8$  m<sup>2</sup>/s, and  $k = 1 \times 10^{-9}$  m<sup>2</sup> are typical for geophysical flows. Consequently, the normal component of the drag force,  $\epsilon \vartheta \phi_f^2 (w_f - w_s)$ , is on the order of  $\mathcal{O}(1)$ , and it is kept here during the simplifications of the normal components (3.18) and (3.23). The description above results in

$$-\phi_f \frac{\partial p_e}{\partial z} - \epsilon \vartheta \phi_f^2 (w_f - w_s) = \lambda \kappa \phi_f u_f^2, \quad (7.25)$$

$$-\gamma \phi_s \frac{\partial p_e}{\partial z} - \frac{\partial \sigma_{e(zz)}}{\partial z} + \epsilon \gamma \vartheta \phi_f^2 (w_f - w_s) + (\gamma - 1) \phi_s \cos \zeta = \lambda \kappa \phi_s u_s^2, \quad (7.26)$$

where  $p_e$  is the excess pore pressure that is given by  $p_e = p_f - p_h$  ( $p_h$ : non-dimensional hydrostatic pressure satisfying  $p_h = (h_m - z) \cos \zeta$ ).

Furthermore combining relations (7.25) and (7.26) to replace  $(w_f - w_s)$ , and then integrating the result in the depth direction from the virtual free surface to any position  $z(x, y, t)$ , one can derive the expression for the solid effective normal stress  $\sigma_{e(zz)}(z)$ , (or  $\sigma_0$ ), as

$$\begin{aligned} \sigma_0 = \sigma_{e(zz)}(z) = & (1 - \gamma) \bar{\phi}_s \cos \zeta (h_m - z) + \lambda \kappa (\gamma \bar{\phi}_f \bar{u}_f^2 + \bar{\phi}_s \bar{u}_s^2) (h_m - z) \\ & + \gamma (p_e^s - p_e^z) + \sigma_{e(zz)}^s, \end{aligned} \quad (7.27)$$

where the plug-flow assumption is used, and  $p_e^s$  and  $\sigma_{e(zz)}^s$  represent quantities at the virtual surface, which can be evaluated by simplifying the boundary conditions (7.18) and (7.21). The boundary conditions (7.18) and (7.21) indicate  $p_e^s \sim \mathcal{O}(\epsilon)$  and  $\sigma_{e(zz)}^s \sim \mathcal{O}(\epsilon)$ . Hence, relation (7.27) can be approximated as

$$\sigma_0 = \sigma_{e(zz)}(z) = (1 - \gamma) \bar{\phi}_s \cos \zeta (h_m - z) - \gamma p_e^z + \mathcal{O}(\epsilon^\alpha), \quad (7.28)$$

to the order  $\mathcal{O}(\epsilon^\alpha)$ , or approximated as

$$\sigma_0 = \sigma_{\epsilon(zz)}(z) = (1 - \gamma)\bar{\phi}_s \cos \zeta (h_m - z) + \lambda\kappa(\gamma\bar{\phi}_f\bar{u}_f^2 + \bar{\phi}_s\bar{u}_s^2)(h_m - z) - \gamma p_e^z + \mathcal{O}(\epsilon), \quad (7.29)$$

to the order  $\mathcal{O}(\epsilon)$ .

Similarly, vertically integrating relation (7.25) and approximating the result to order  $\mathcal{O}(\epsilon^\alpha)$  yield

$$p_e^z = \int_z^{h_m} \epsilon \vartheta \phi_f (w_f - w_s) dz + \mathcal{O}(\epsilon^\alpha), \quad (7.30)$$

where the normal velocity difference  $(w_f - w_s)$  can be derived by vertically integrating relation (7.4) from the bottom to any position  $z(x, y, t)$ . Substitution of the result into (7.30) yields

$$p_e^z = -\epsilon \vartheta \int_z^{h_m} \left( \int_0^z \dot{\gamma} \tan \pi dz \right) dz - \frac{\epsilon \vartheta}{2} (h_m^2 - z^2) \left\{ \frac{\partial}{\partial x} \left[ \bar{\phi}_f (\bar{u}_f - \bar{u}_s) \right] + \frac{\partial}{\partial y} \left[ \bar{\phi}_f (\bar{v}_f - \bar{v}_s) \right] \right\} + \mathcal{O}(\epsilon^\alpha). \quad (7.31)$$

Equation (7.31) indicates that the gradient of the difference of the slope-align velocity between the fluid and the granular phases also influence the excess pore pressure in addition to the dilatation. As the gradients of  $(\bar{u}_f - \bar{u}_s)$  and  $(\bar{v}_f - \bar{v}_s)$  increase, there will be a net granular flux out of the fluid surface as in the circumstance of the granular dilatation, which yields a decrease of the excess pore pressure. Moreover, the integration of dilatancy arising in (7.31) can be simplified by the following steps. First, as relation (7.4) reflects,  $\dot{\gamma} \tan \pi$  is independent of  $z$  coordinate when  $\bar{\phi}_s$  is assumed to be uniformly distributed in the depth direction and the velocity profile is plug flow. Then, since the dominant shear occurs in vertical planes parallel to the main flow direction, it is reasonable to express

$$\dot{\gamma} = \sqrt{(\partial u_s / \partial z)^2 + (\partial v_s / \partial z)^2} \quad (7.32)$$

(see Iverson & George (2014)). For parabolic velocity profiles, the bed shear rate can be written as  $\dot{\gamma}_b = 3\sqrt{\bar{u}_s^2 + \bar{v}_s^2}/h_m$  (see Pailha & Pouliquen (2009)), and the function  $\tan \pi_b$  can be evaluated by combining its definition (see (7.2)) with relation (7.27). These arguments yield

$$p_e^z = -\frac{\epsilon \vartheta}{2} (h_m^2 - z^2) \left\{ \frac{\partial}{\partial x} \left[ \bar{\phi}_f (\bar{u}_f - \bar{u}_s) \right] + \frac{\partial}{\partial y} \left[ \bar{\phi}_f (\bar{v}_f - \bar{v}_s) \right] + \dot{\gamma}_b \tan \pi_b \right\} + \mathcal{O}(\epsilon^\alpha),$$

$$\tan \pi_b = k_1 \left( \bar{\phi}_s - \phi_c + k_2 \frac{\mu_f \dot{\gamma}_b}{\sigma_0^b} \right), \quad (7.33)$$

where  $\sigma_0^b = (\bar{\rho} - \tilde{\rho}_f)g_z h_m - p_e^b$  (see relation (7.27)).

Similarly, the excess pore pressure, corrected to order  $\mathcal{O}(\epsilon)$ , can be derived and given by

$$p_e^z = -\frac{\epsilon\vartheta}{2}(h_m^2 - z^2) \left\{ \frac{\partial}{\partial x} \left[ \bar{\phi}_f(\bar{u}_f - \bar{u}_s) \right] + \frac{\partial}{\partial y} \left[ \bar{\phi}_f(\bar{v}_f - \bar{v}_s) \right] + \hat{\gamma}_b \tan \pi_b \right\} + \lambda \kappa \bar{u}_f^2 (h_m - z) + \mathcal{O}(\epsilon). \quad (7.34)$$

## 7.2.4 Slope-align components of the momentum balances

Integrating the  $x$  components of the momentum balances, (3.16) and (3.21), over the depth by applying the Leibnitz rule to interchange the orders of integration and differentiation yields that the left-hand side terms turn into

$$\int_0^{h_m} \left[ \frac{\partial(\phi_s u_s)}{\partial t} + \frac{\partial(\phi_s u_s u_s)}{\partial x} + \frac{\partial(\phi_s u_s v_s)}{\partial y} + \frac{\partial(\phi_s u_s w_s)}{\partial z} \right] dz \quad (7.35)$$

$$= \frac{\partial(h_m \bar{\phi}_s \bar{u}_s)}{\partial t} + \frac{\partial(h_m \bar{\phi}_s \bar{u}_s \bar{u}_s)}{\partial x} + \frac{\partial(h_m \bar{\phi}_s \bar{u}_s \bar{v}_s)}{\partial y} - \mathcal{J} u_s^s,$$

$$\int_0^{h_m} \left[ \frac{\partial(\phi_f u_f)}{\partial t} + \frac{\partial(\phi_f u_f u_f)}{\partial x} + \frac{\partial(\phi_f u_f v_f)}{\partial y} + \frac{\partial(\phi_f u_f w_f)}{\partial z} \right] dz \quad (7.36)$$

$$= \frac{\partial(h_m \bar{\phi}_f \bar{u}_f)}{\partial t} + \frac{\partial(h_m \bar{\phi}_f \bar{u}_f \bar{u}_f)}{\partial x} + \frac{\partial(h_m \bar{\phi}_f \bar{u}_f \bar{v}_f)}{\partial y} + \mathcal{J} u_f^s / \gamma.$$

Integrating the right-hand side terms of the  $x$  component of the granular momentum equations yields

$$\int_0^{h_m} RHS dz = h_m \bar{\phi}_s \sin \zeta + \gamma \vartheta \bar{\phi}_f^2 h_m (\bar{u}_f - \bar{u}_s) - \epsilon \frac{\partial}{\partial x} (h_m \bar{\sigma}_{e(xx)}) - \epsilon \mu_s^b \frac{\partial}{\partial y} (h_m \bar{\sigma}_{e(xy)})$$

$$+ \left[ \epsilon \psi \gamma \bar{\phi}_s p_f \frac{\partial z}{\partial x} + \epsilon \sigma_{e(xx)} \psi \frac{\partial z}{\partial x} + \epsilon \mu_s^b \sigma_{e(xy)} \frac{\partial z}{\partial y} - \mu_s^b \sigma_{e(xz)} \right]_{z=0}^{z=s}$$

$$- \epsilon \gamma \bar{\phi}_s \frac{\partial(h_m \bar{p}_f)}{\partial x} + \mathcal{O}(\epsilon^{1+\nu}), \quad (7.37)$$

where the terms in the square can be simplified as follows by using the boundary conditions (7.11) and (7.19).

$$\left[ \epsilon \psi \gamma \bar{\phi}_s p_f \frac{\partial z}{\partial x} + \epsilon \sigma_{e(xx)} \psi \frac{\partial z}{\partial x} + \epsilon \mu_s^b \sigma_{e(xy)} \frac{\partial z}{\partial y} - \mu_s^b \sigma_{e(xz)} \right]_{z=0}^{z=s} \quad (7.38)$$

$$= \phi_s^s \mathcal{J} (u_f^s - u_s^s) - \sigma_{e(zz)}^b \hat{\mu}_s^b \frac{u_s^b}{\sqrt{(u_s^b)^2 + (v_s^b)^2}} - k_s^b \phi_s^b \Delta_b u_s^b.$$

Furthermore substituting the overburden pressure  $\sigma_{e(zz)}$  into relation (7.38) and applying relations (3.41) and (3.44) to approximate the result to order  $\mathcal{O}(\epsilon^{1+\nu})$ , one can accomplish

$$\begin{aligned} & \left[ \epsilon \psi \bar{\phi}_s p_f \frac{\partial z}{\partial x} + \epsilon \sigma_{e(xx)} \psi \frac{\partial z}{\partial x} + \epsilon \mu_s^b \sigma_{e(xy)} \frac{\partial z}{\partial y} - \mu_s^b \sigma_{e(xz)} \right]_{z=0}^{z=s} \\ &= \phi_s^s \mathcal{J}(u_f^s - u_s^s) - \frac{u_s^b}{\sqrt{(u_s^b)^2 + (v_s^b)^2}} \hat{\mu}_s^b \left[ (1 - \gamma) \hat{h}_m \bar{\phi}_s \cos \zeta + \lambda \kappa h_m (\gamma \bar{\phi}_f \bar{u}_f^2 + \bar{\phi}_s \bar{u}_s^2) - \gamma p_e^b \right] \\ & \quad - k_s^b \phi_s^b u_s^b + \mathcal{O}(\epsilon^{1+\nu}), \end{aligned} \quad (7.39)$$

where by referring to relation (7.34), the bed excess pore pressure  $p_e^b$ , approximated to order  $\mathcal{O}(\epsilon)$ , is

$$p_e^b = \frac{\epsilon \vartheta h_m^2}{2} \left[ -\gamma_b \tan \pi_b - \frac{\partial}{\partial x} \left( \bar{\phi}_f (\bar{u}_f - \bar{u}_s) \right) - \frac{\partial}{\partial y} \left( \bar{\phi}_f (\bar{v}_f - \bar{v}_s) \right) \right] + h_m \lambda \kappa \bar{u}_f^2. \quad (7.40)$$

Moreover, the gradient of the pore pressure in relation (7.37) can be directly formulated as follows by integrating the hydrostatic part  $p_h^z = \cos \zeta (h_m - z)$  and the dynamic part  $p_e^z$  in relation (7.33). This yields

$$\frac{\partial (h_m \bar{p}_f)}{\partial x} = \frac{\partial}{\partial x} \left( \frac{1}{2} h_m^2 \cos \zeta + \frac{2}{3} h_m p_e^b \right). \quad (7.41)$$

As shown in Chap. 3, the stress gradient  $\partial(h_m \bar{\sigma}_{e(xy)})/\partial y$ , arising in relation (7.37), can be ignored, since it is a high-order term with respect to small parameter  $\epsilon$ . The other stress gradient  $\partial(h_m \bar{\sigma}_{e(xx)})/\partial x$  can be formulated by introducing an earth pressure coefficient  $K_x^s$  i.e.  $\sigma_{e(xx)} = K_x^s \sigma_{e(zz)}$ . Then, the following relation

$$\frac{\partial (h_m \bar{\sigma}_{e(xx)})}{\partial x} = \frac{\partial}{\partial x} \left[ \frac{K_x^s}{2} (1 - \gamma) \bar{\phi}_s h_m^2 \cos \zeta - \frac{2K_x^s}{3} \gamma h_m p_e^b \right], \quad (7.42)$$

holds by vertically integrating relation  $\sigma_{e(xx)} = K_x^s \sigma_{e(zz)}$ . For simplicity, we use  $K_x^s = 1$  here.

Similarly, integrating the  $y$  components of the momentum balances, (3.16) and (3.21), over the depth by applying the Leibnitz rule to interchange the orders of integration and differentiation can yield that the left-hand side terms turn into

$$\begin{aligned} & \int_0^{h_m} \left[ \frac{\partial(\phi_s v_s)}{\partial t} + \frac{\partial(\phi_s u_s v_s)}{\partial x} + \frac{\partial(\phi_s v_s v_s)}{\partial y} + \frac{\partial(\phi_s v_s w_s)}{\partial z} \right] dz \\ &= \frac{\partial(h_m \bar{\phi}_s \bar{v}_s)}{\partial t} + \frac{\partial(h_m \bar{\phi}_s \bar{u}_s \bar{v}_s)}{\partial x} + \frac{\partial(h_m \bar{\phi}_s \bar{v}_s \bar{v}_s)}{\partial y} - \mathcal{J} v_s^s, \end{aligned} \quad (7.43)$$

$$\int_0^{h_m} \left[ \frac{\partial(\phi_f v_f)}{\partial t} + \frac{\partial(\phi_f u_f v_f)}{\partial x} + \frac{\partial(\phi_f v_f v_f)}{\partial y} + \frac{\partial(\phi_f v_f w_f)}{\partial z} \right] dz \quad (7.44)$$

$$= \frac{\partial(h_m \bar{\phi}_f \bar{v}_f)}{\partial t} + \frac{\partial(h_m \bar{\phi}_f \bar{u}_f \bar{v}_f)}{\partial x} + \frac{\partial(h_m \bar{\phi}_f \bar{v}_f \bar{v}_f)}{\partial y} + \mathcal{J} v_f^s / \gamma.$$

for the two phases. Integrating the right-hand side terms of the  $y$  component of the granular momentum balance, one has

$$\begin{aligned} \int_0^{h_m} RHS dz = & -\bar{\phi}_s \frac{\partial}{\partial y} \left( \frac{1}{2} h_m^2 \cos \zeta + \frac{2}{3} h_m p_e^b \right) - \frac{\partial}{\partial y} \left[ \frac{K_y^s}{2} (1 - \gamma) \bar{\phi}_s h_m^2 \cos \zeta - \frac{2K_y^s}{3} \gamma h_m p_e^b \right] \\ & - \frac{v_s^b}{\sqrt{(u_s^b)^2 + (v_s^b)^2}} \hat{\mu}_s^b \left[ (1 - \gamma) h_m \bar{\phi}_s \cos \zeta + \lambda \kappa h_m (\gamma \bar{\phi}_f \bar{u}_f^2 + \bar{\phi}_s \bar{u}_s^2) - \gamma p_e^{(b)} \right] \\ & - k_s^b \phi_s^b v_s^b + \gamma \vartheta \bar{\phi}_f^2 h_m (\bar{v}_f - \bar{v}_s) + \phi_s^s \mathcal{J} (v_f^s - v_s^s), \end{aligned} \quad (7.45)$$

where  $K_y^s = 1$  similar to  $K_x^s$ .

Similarly, integrating the right-hand side terms of the  $x$  component of the fluid momentum balance, one has

$$\begin{aligned} \int_0^{h_m} RHS dz = & h_m \bar{\phi}_f \sin \zeta - \bar{\phi}_f \frac{\partial}{\partial x} \left( \frac{1}{2} h_m^2 \cos \zeta + \frac{2}{3} h_m p_e^b \right) + \phi_f^s \mathcal{J} (u_f^s - u_s^s) / \gamma \\ & + \frac{\epsilon h_m}{N_R} \left[ 2 \frac{\partial^2 \bar{u}_f}{\partial x^2} + \frac{\partial}{\partial y} \left( \frac{\partial \bar{v}_f}{\partial x} + \frac{\partial \bar{u}_f}{\partial y} \right) - \frac{k_f^b u_f^b}{\epsilon^2 h_m} \right] - \vartheta \bar{\phi}_f^2 h_m (\bar{u}_f - \bar{u}_s), \end{aligned} \quad (7.46)$$

where the second term  $-\bar{\phi}_f \partial(h_m^2 \cos \zeta / 2 + 2h_m p_e^b / 3) / \partial x$  represents the contributions of the pore pressure, and the third term stands for the momentum flux across the virtual surface, the fourth terms (terms in the square bracket) stem from the viscous forces, and the last term is the viscous drag force. Similarly, integrating the right-hand side terms of the  $y$  component of the fluid momentum balance, one has

$$\begin{aligned} \int_0^{h_m} RHS dz = & -\bar{\phi}_f \frac{\partial}{\partial y} \left( \frac{1}{2} h_m^2 \cos \zeta + \frac{2}{3} h_m p_e^b \right) + \phi_f^s \mathcal{J} (v_f^s - v_s^s) / \gamma \\ & + \frac{\epsilon h_m}{N_R} \left[ 2 \frac{\partial^2 \bar{v}_f}{\partial y^2} + \frac{\partial}{\partial x} \left( \frac{\partial \bar{v}_f}{\partial x} + \frac{\partial \bar{v}_f}{\partial y} \right) - \frac{k_f^b v_f^b}{\epsilon^2 h_m} \right] - \vartheta \bar{\phi}_f^2 h_m (\bar{v}_f - \bar{v}_s). \end{aligned} \quad (7.47)$$

## 7.2.5 Mathematical closure

To complete the model, the quantity  $\mathcal{J}$  needs to be evaluated. As mentioned above, the dilatancy can cause the mass flux out of the virtual surface. We therefore connect  $\mathcal{J}$  with dilatancy-dependent term. Integrating relation (7.4) over the depth, and simplifying the result with the identity  $-u_s^s \partial_x s - v_s^s \partial_y s + w_s^s + u_f^s \partial_x s + v_f^s \partial_y s - w_f^s = -\rho^s \mathcal{J} / (\rho_f^s \phi_s^s)$  (obtained by replacing temporal derivative of (7.15) with  $\mathcal{J}$ ), one has

$$\mathcal{J} = -\frac{\phi_s^s \tilde{\rho}_f}{\rho^s} \left[ h_m \hat{\gamma}_b \tan \pi_b - \frac{\partial}{\partial x} \left( h_m \bar{\phi}_f (\bar{u}_s - \bar{u}_f) \right) - \frac{\partial}{\partial y} \left( h_m \bar{\phi}_f (\bar{v}_s - \bar{v}_f) \right) \right]. \quad (7.48)$$

Relation (7.48) implies that the mass flux through the virtual surface originates from the dilatancy and relative convective motion between the two components in the mixture. Moreover, it is possible connect the mass flux  $\mathcal{J}$  with the bed pore pressure  $p_e^b$ . Combining relation (7.33) with (7.48) yields

$$\mathcal{J} = \frac{2\phi_s^s \tilde{\rho}_f}{\rho^s} \frac{p_e^b}{\epsilon \vartheta h_m} - \frac{\phi_s^s \tilde{\rho}_f}{\rho^s} \phi_f (\bar{u}_f - \bar{u}_s) \frac{\partial h_m}{\partial x} - \frac{\phi_s^s \tilde{\rho}_f}{\rho^s} \phi_f (\bar{v}_f - \bar{v}_s) \frac{\partial h_m}{\partial y}. \quad (7.49)$$

## 7.2.6 Summary of depth-averaged equations

Combining relation (7.35) with (7.37), one can generate the depth-averaged  $x$ -direction component of the granular momentum balance. The  $y$ -direction component of the granular momentum balance can be derived by combining (7.43) with (7.45). Similarly, combining relation (7.36) with (7.46), one can obtain the depth-averaged  $x$ -direction component of the fluid momentum balance. The  $y$ -direction component can be derived by combining (7.44) with (7.47). Moreover, the boundary velocities and volume fractions in the depth-averaged equations are assumed to equal the depth-averaged ones. With these descriptions, the final model equations for the granular phase are given by

$$\frac{\partial(h_m \phi_s)}{\partial t} + \frac{\partial(h_m \phi_s u_s)}{\partial x} + \frac{\partial(h_m \phi_s v_s)}{\partial y} = \mathcal{J}, \quad (7.50)$$

$$\frac{\partial(h_m \phi_s u_s)}{\partial t} + \frac{\partial}{\partial x} \left( h_m \phi_s u_s u_s + \frac{\epsilon}{2} h_m^2 \phi_s \cos \zeta + \frac{2\epsilon\gamma\phi_f}{3} h p_e^b \right) + \frac{\partial(h_m \phi_s u_s v_s)}{\partial y} = s_{x(s)}, \quad (7.51)$$

$$\frac{\partial(h_m \phi_s v_s)}{\partial t} + \frac{\partial(h_m \phi_s u_s v_s)}{\partial x} + \frac{\partial}{\partial y} \left( h_m \phi_s v_s v_s + \frac{\epsilon}{2} h_m^2 \phi_s \cos \zeta + \frac{2\epsilon\gamma\phi_f}{3} h p_e^b \right) = s_{y(s)}, \quad (7.52)$$

where we have dropped the averaged bar symbol for simplicity. The depth-averaged pressure  $p_t$ , arising in (7.50)-(7.52), is  $p_t = \tilde{\rho}_f g_z h_m / 2 + 2p_e^b / 3$ , and the source terms  $s_{x(s)}$  and  $s_{y(s)}$  are

$$s_{x(s)} = h_m \phi_s \sin \zeta + \left( \frac{1}{2} \epsilon \gamma h_m^2 \cos \zeta + \frac{2\epsilon\gamma}{3} h_m p_e^b \right) \frac{\partial \phi_s}{\partial x} + h_m \gamma \phi_f^2 \vartheta (u_f - u_s) \quad (7.53)$$

$$- \frac{u_s}{\sqrt{u_s^2 + v_s^2}} \hat{\mu}_s^b \left[ (1 - \gamma) h_m \phi_s \cos \zeta - \gamma p_e^b + \lambda \kappa h_m (\phi_s u_s^2 + \gamma \phi_f u_f^2) \right] - k_s^b \phi_s u_s$$

$$+ (\phi_s u_f + \phi_f u_s) \mathcal{J},$$

$$s_{y(s)} = \left( \frac{1}{2} \epsilon \gamma h_m^2 \cos \zeta + \frac{2\epsilon\gamma}{3} h_m p_e^b \right) \frac{\partial \phi_s}{\partial y} + h_m \gamma \phi_f^2 \vartheta (v_f - v_s) \quad (7.54)$$

$$- \frac{v_s}{\sqrt{u_s^2 + v_s^2}} \hat{\mu}_s^b \left[ (1 - \gamma) h_m \phi_s \cos \zeta - \gamma p_e^b + \lambda \kappa h_m (\phi_s u_s^2 + \gamma \phi_f u_f^2) \right] - k_s^b \phi_s v_s$$

$$+ (\phi_s v_f + \phi_f v_s) \mathcal{J}$$

The final model equations for the fluid phase are given by

$$\frac{\partial(h_m\phi_f)}{\partial t} + \frac{\partial(h_m\phi_f u_f)}{\partial x} + \frac{\partial(h_m\phi_f v_f)}{\partial y} = -\mathcal{J}/\gamma, \quad (7.55)$$

$$\frac{\partial(h_m\phi_f u_f)}{\partial t} + \frac{\partial}{\partial x} \left( h_m\phi_f u_f u_f + \frac{\epsilon}{2} h_m^2 \phi_f \cos \zeta + \frac{2\epsilon\phi_f}{3} h_m p_e^b \right) + \frac{\partial(h_m\phi_f u_f v_f)}{\partial y} = s_{x(f)}, \quad (7.56)$$

$$\frac{\partial(h_m\phi_f v_f)}{\partial t} + \frac{\partial(h_m\phi_f u_f v_f)}{\partial x} + \frac{\partial}{\partial y} \left( h_m\phi_f v_f v_f + \frac{\epsilon}{2} h_m^2 \phi_f \cos \zeta + \frac{2\epsilon\phi_f}{3} h_m p_e^b \right) = s_{y(f)}, \quad (7.57)$$

where

$$s_{x(f)} = h_m\phi_f \sin \zeta + \left( \frac{\epsilon}{2} h_m^2 \cos \zeta + \frac{2\epsilon}{3} h_m p_e^b \right) \frac{\partial\phi_f}{\partial x} - \vartheta\phi_f^2 h_m (u_f - u_s) \quad (7.58)$$

$$\begin{aligned} & + \frac{\epsilon h_m}{N_R} \left[ 2 \frac{\partial^2 u_f}{\partial x^2} + \frac{\partial}{\partial y} \left( \frac{\partial v_f}{\partial x} + \frac{\partial u_f}{\partial y} \right) - \frac{k_f^b u_f^b}{\epsilon^2 h_m} \right] - (\phi_s u_f + \phi_f u_s) \mathcal{J}/\gamma, \\ s_{y(f)} = & \left( \frac{\epsilon}{2} h_m^2 \cos \zeta + \frac{2\epsilon}{3} h_m p_e^b \right) \frac{\partial\phi_f}{\partial y} - \vartheta\phi_f^2 h_m (v_f - v_s) \quad (7.59) \\ & + \frac{\epsilon h_m}{N_R} \left[ 2 \frac{\partial^2 v_f}{\partial y^2} + \frac{\partial}{\partial x} \left( \frac{\partial u_f}{\partial y} + \frac{\partial v_f}{\partial x} \right) - \frac{k_f^b v_f^b}{\epsilon^2 h_m} \right] - (\phi_s v_f + \phi_f v_s) \mathcal{J}/\gamma. \end{aligned}$$

The granular momentum equations (7.51) and (7.52) delineate the balance of inertial terms, the granular stress-gradient term  $\partial(\epsilon h_m^2 \phi_f \cos \zeta / 2 + 2\epsilon \gamma \phi_f h_m p_e^b / 3) / \partial x$ , respectively, on the left-hand side, and the source terms  $s_{x(s)}$  and  $s_{y(s)}$ , on the right-hand side, defined in (7.53) and (7.54). The granular source terms (7.53) and (7.54) consecutively characterize the effects of the gravitational force, the buoyancy force, the viscous drag force between the granular and fluid components, the bed Coulomb friction resistance, the bed viscous friction resistance, and the momentum flux across the virtual surface. Similarly, the fluid momentum equations (7.56) and (7.57) delineate the balance of inertial terms, the pressure gradient term, respectively, on the left-hand side, and the source terms  $s_{x(f)}$  and  $s_{y(f)}$  defined in (7.58) and (7.59). The fluid source terms (7.58) and (7.59) consecutively characterize the effects of the gravitational force, the buoyancy force, the viscous drag force, the viscous forces, and the momentum flux across the virtual surface.

### 7.3 Numerical simulation of unsteady flows

To validate the present model, simulations involving unsteady flows are presented in this section. The model equations (7.50)-(7.52) and (7.55)-(7.57) present challenges for the numerical discretization because spurious oscillations could take place at a shock and improper treatments of nonconservative products (multiplicative products of derivative and non-derivative terms) may yield a wrong convergent solution (see Castro, LeFloch, Muñoz-Ruiz & Parés (2008)). To accomplish an accurate and reli-

able solution, the central-upwind scheme, presented in the fourth Chapter, is adopted. Through numerical tests, it is found that the central-upwind scheme is more robust and effective when compared with N-T scheme to solve this model. Additionally, it is important to note that the nonconservative products in equations (7.50)-(7.52) and (7.55)-(7.57) are relatively small quantities compared to the inertial forces, since the small parameter  $\epsilon$  appears in the nonconservative products. The numerical tests of Kurganov & Miller (2014) show that the numerical solutions are insensitive to the choice of discretization of non-conservative products, when the nonconservative products are relatively small quantities.

The numerical results obtained by the present model with and without the basal excess pore pressure  $p_e^b$  are shown, respectively, and compared with experimental data of Iverson et al. (2010). In the absence of  $p_e^b$ , the mass and momentum fluxes across the virtual surface have a negligible influence on dynamics, and therefore the present model reduces to the previous two-phase type model presented in Chap. 3. In the experiment, the initial sand-gravel-mud mixture, placed behind a gate with an initial geometry as shown in Fig. 4.8, was suddenly released as the gate was opened, and then accelerated down the chute until it approached a horizontal run-out plane. The transverse dimension of the chute is wide enough so that the flow across the transverse section is considered as uniform. The settings and details of the experiment can be seen in Iverson et al. (2010). The experimental and computational parameters used to validate the present model are presented in Table 4.1. Besides, the values of parameters  $k_s^b$ ,  $k_f^b$ ,  $k_1$ , and  $k_2$  are needed. Since the experiment does not provide values for the fluid and solid bed frictional coefficients,  $k_s^b = 0$  and  $k_f^b = 75 \text{ N} \cdot \text{s}/\text{m}^3$  are chosen. Such conditions represent a dry Coulomb bed friction for the granular phase and a moderate bed slip for the fluid phase, respectively. For the dilatancy parameters,  $k_1 = 1.1$  and  $k_2 = 3$  are used, which assures a reasonable value for the basal excess pore pressure.

### 7.3.1 Comparison between the model results with $p_e^{(b)}$ and without $p_e^{(b)}$

This section aims to investigate the effects of the excess pore pressure on the profiles of flow height and solid volume fraction. The results obtained by the present model with and without  $p_e^{(b)}$  are reflected in Fig. 7.2. The present model with  $p_e^{(b)}$  predicts that a blunt front quickly develops (roughly at  $t = 4$  s) followed by a spatially tapered rear part, due to the following fact. For initially loosely packed wet grains as in the present case, the grains will compact and squeeze the interstitial fluid as soon as they are subject to a shear after the release of the material. This process leads to an increase of the basal pore pressure and an alleviation of internal friction between grains, and therefore the grains come to the front quickly, leading to a blunt front. As the flow goes down farther, the blunt front and tapered tail only moderately change. The present model without taking  $p_e^{(b)}$  into account predicts that most of the granular mass concentrates in the rear part at the initial stage of the flow (at  $t = 2$  s). Driven by the gravity force, the rear part starts attenuating, but it takes more time to develop a



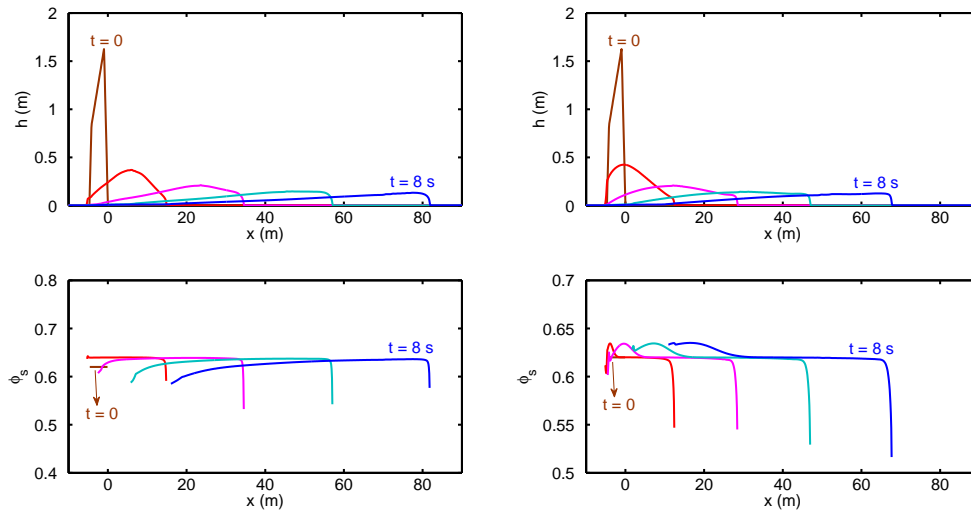


Figure 7.2: Long-term evolutions of  $h_m$  and  $\phi_s$  computed by the present model with and without  $p_e^b$ . The longitudinal profiles of  $h_m$  and  $\phi_s$  are demonstrated for  $t = 0$  s, 2 s, 4 s, 6 s, 8 s. The left figures reflect the results obtained by with  $p_e^b$ , and the right figures represent the results obtained by without  $p_e^b$ .

real thin tail (roughly 6 s from the initial onwards), when compared to 4 s predicted by the present model with  $p_e^{(b)}$ . Once the blunt front and tapered tail develop, the body translates downslope, which is consistent with the prediction of the present model with  $p_e^{(b)}$ .

In addition, the present model taking  $p_e^{(b)}$  into account indicates that  $\nu_s$  in the flow front and flow tail is below those in the middle part of flow (see Fig. 7.2), since high shear rate at the front and tail induces dilatant behavior for grains. However, the present model without taking into account  $p_e^{(b)}$  predicts that the fluid phase moves faster than the granular phase due to the fact that the fluid phase is experiencing smaller bed friction than the granular phase, and as a result  $\nu_s$  in the middle of flow is above that at the flow front and below that at the flow tail.

### 7.3.2 Comparison with experimental data

Fig. 7.3 compares the measured time series of depth at  $x = 2$  m,  $x = 32$  m, and  $x = 66$  m downslope from the gate with the results obtained by the present model with and without  $p_e^b$ . Both computed results show reasonable predictions, among which the present model with  $p_e^b$  gives better predictions in terms of the peak flow depth and flow-front arriving time. The more reasonable prediction with respect to peak flow depth by the present model with  $p_e^b$  should result from the fact that more grains are transported to the front when  $p_e^b$  is taken into account.

Some discrepancies also exist, especially for the predictions at  $x = 2$  m and  $x = 66$  m. The predictive discrepancy for  $x = 2$  m results from the ignorance of the normal accel-

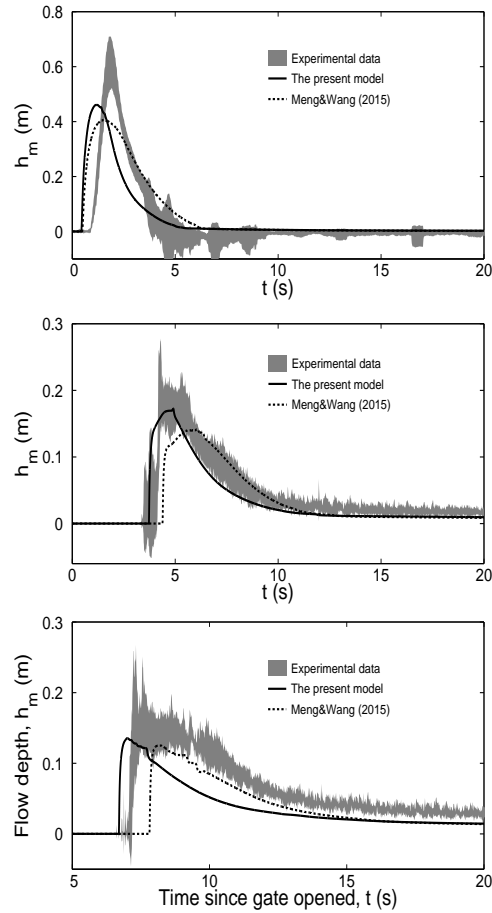


Figure 7.3: Comparison between the measurements and the model predictions. Grey shading represents the mean  $\pm 1$  standard deviation measured in eight experiments. The solid line indicates the predicted result by the present model with  $p_e^b$ , while the dash line characterizes the predicted result by the present model without  $p_e^b$ .

eration, because considerable normal motion develops when the gate is opened. Another discrepancy lies in the time series of depth at section  $x = 66$  m. Fig. 7.3 reflects that the curves (time series of depth) predicted by the model with the consideration  $p_e^b$  are narrower than the experimental curves, which results from the discrepancy of the predicted velocities. The overall velocities predicted with the consideration of  $p_e^b$  are larger than the experimental ones, so that the predicted arriving time of the mass front to section  $x = 66$  m is earlier than the experimental data. One possible explanation for this is the following. In the experiment, a depleted pore pressure is found in the flow front, which is caused by the grain-size segregation yielding the accumulation of high permeable coarse grains in the flow front (see Iverson et al. (2010) and Iverson & George (2014)). Consequently, the granular internal friction and bed friction are enhanced in the flow front that impedes the downslope motion of the mass behind. The predicted pore pressure in the flow front, obtained by the present model with the consideration of  $p_e^b$ , relaxes to hydrostatic state after  $t = 0.6$  s and remains hydrostatic due to the ignorance of the grain-size segregation, and the pore pressure obtained by without  $p_e^b$  is always hydrostatic, because both pore pressure feedback and grain-

size segregation are not considered. The discrepancies in the predictions of the pore pressure cause the deviations of the predicted velocities from the experimental ones.

### 7.3.3 Conclusion

Based on the saturated depth-averaged model presented in Chapter 3, this Chapter aims to improve the previous saturated model by including the granular dilatancy into the model. The improved model equations describe evolutions of flow height, depth-averaged volume fractions, and depth-averaged velocities of the two phases. To validate the improved model, we revisit to the experiment of Iverson et al. (2010). The comparison between the model results and the experimental data demonstrate that the improved model can give better predictions in terms of peak depth and flow speed of the flow front.



## 8 Conclusion and Outlook

In the present work, the dynamics of two-phase grain-fluid mixtures are focused on. The depth-averaged models, gaining advantages of less computational burden compared with three-dimensional models, are proposed and numerically resolved. The aim of this work is to gain deeper insight into the physical mechanisms underlying flowing grain-fluid mixtures by the following approaches:

1. The present work starts with assuming that the interstitial fluid fills all the voids between the grains, i.e. the mixture is saturated. Therefore, standard two-phase mixture theory can be applied to define the governing equations. To make the problem mathematically well-posed, it is postulated that the flow of a grain-fluid mixture is not affected by the ambient air and comes to rest due to bed Coulomb friction for the granular phase and bed Navier friction for the fluid phase. By virtue of thin-layer approximation, a set of depth-averaged equations are derived. The derived model equations are capable to investigate the characteristic shape of the flow front and roll waves commonly observed in fields, and evolutions of dynamical quantities, for instance flowing height and solid volume fraction.
2. Based on the formulated saturated model, unsaturated grain-fluid mixtures are focused on, especially the phase-separation phenomenon. In unsaturated mixtures, the interstitial fluid cannot fill all the voids between the grains. Consequently, a two-layer approach is proposed to describe their dynamics, in which the fluid-grain saturated mixture is overlain by a pure granular upper layer. The two-layer materials are separated by an interface that is a material surface for the fluid phase, whereas the granular mass exchange takes place at the interface. The thin-layer approximation is adopted again to derive a depth-averaged model. Through simulating typical geophysical cases, it is found that the formulated model is capable to reproduce and explain some phenomena commonly observed in nature and experiments, for instance, the elongation of the mixture body, the development and evolution of blunt head, etc. Additionally, the numerical simulation demonstrates that the present model can qualitatively predict the phenomenon of phase separation.
3. Moreover, we aim to extend the formulated depth-averaged model that handles the mixture as a saturated medium by taking the granular dilatancy into account. To this end, the mixture theory is coupled with the critical-state theory. The derived model equations describe the evolutions of flow thickness, depth-averaged volume fractions, and depth-averaged velocities of the two phases. Such quantities are coupled with the basal excess pore pressure occurring owing to the dilated or compacted behavior of grains and the relative motion between

both phases in the mixture. The formulated model is applied to simulate the experimental case documented in Iverson et al. (2010). The comparison with the experimental data demonstrates that the model with the dilatancy into account can give better predictions in term of peak flow depth and the speed of flowing front than the depth-averaged model without the dilatancy into account.

Additionally, it is necessary to stress that some modifications are needed in future, though the formulated depth-averaged models can reasonably describe the dynamics. The possible modifications are presented below:

1. In the present depth-averaged models, the normal acceleration term that may play an important role in the beginning of flows is not considered. Consequently, it may be necessary to include the normal acceleration term in order to improve the numerical predictions in the short-time scale. The way in the works of Castro-Orgaz, Hutter, Giraldez & Hager (2015) and Denlinger & Daniel (2008) to include the normal acceleration may be promising.
2. In the two-layer model, the granular mass-exchange rate across the interface (fluid free surface) is parametrically modelled instead of rigorously theoretical reasoning. This difficulty can be coped with by combining the mixture theory with the critical-state theory. In this way, the mass-exchange rate can be modelled as a function of the granular dilatancy. It implies that the dilatancy yields that the granular mass in the lower layer goes out of the fluid surface and then comes into the pure granular upper layer. Similarly, when the granular compaction takes place, the pure granular mass in the upper layer comes down into the lower mixture layer.
3. In the present depth-averaged model with the granular dilatancy into account, the virtual surface is introduced to describe the phenomenon that the grains can protrude the free surface. The virtual surface does not physically exist, though it is defined to satisfy the conservation of the total mixture mass along the depth direction. A more convinced approach needs to be adopted instead of introducing a virtual surface to describe that the grains, subject to dilatation, protrude the free surface or the grains, subject to contraction, accumulate below the free surface.
4. The proposed depth-averaged models are based on the theory of Savage & Hutter (1989), which postulates that the grains are experiencing a rate-independent Coulomb friction between each other. The absence of a rate-dependent viscous friction prevents the present model from investigating some subtle cases, for instance investigating the cross-stream profile of the downslope velocity for dry granular chute flows. To tackle this problem, the rate-dependent rheology, such as  $\mu(I)$ -rheology described by Jop, Forterre & Pouliquen (2006), can be referred to.

## 9 Bibliography

- ANDERSON, T., JACKSON, R. (1967): A fluid mechanical description of fluidized beds. *Ind. Eng. Chem. Fundam.* 6, 527–539.
- ARAI, M., HUEBL, J., KAITNA, R. (2013): Occurrence conditions of roll waves for three grain-fluid models and comparison with results from experiments and field observation. *Geophys. J. Int.* 195, 1464–1480.
- BAGNOLD, R. (1954): Experiments on a gravity-free dispersion of large solid spheres in a Newtonian fluid under shear. *Proc. R. Soc. A.* 225, 49–63.
- BARTELT, P., SALM, B., GRUBER, U. (1999): Calculating dense-snow avalanche runout using a voellmy-fluid model with active/passive longitudinal straining. *J. Glaciol* 45, 150, 242–254.
- BERZI, D. (2008): Approximate analytical solutions in a model for high concentrated granular-fluid flows. *Phy. Rev. E* 78, 011304.
- BERZI, D., JENKINS, J. (2008): A theoretical analysis of free-surface flows of saturated granular-liquid mixtures. *J. Fluid Mech.* 608, 393–410.
- BOER, R., EHLERS, W. (1990): The development of the concept of effective stresses The development of the concept of effective stresses. *Acta Mech.* 83, 77–92.
- BOUCHUT, F., FERNANDEZ-NIETO, E., MANGENEY, A., NARBONA-REINA, G. (2014): A two-phase shallow debris flow model with energy balance. *Math. Modell. Numer. Anal* 49, 1, 101–140.
- BOUCHUT, F., FERNANDEZ-NIETO, E., MANGENEY, A., NARBONA-REINA, G. (2016): A two-phase two-layer model for fluidized granular flows with dilatancy effects. *J. Fluid Mech.* 801, 166–221.
- CASTRO, M., LEFLOCH, P., MUÑOZ-RUIZ, M., PARÉS, C. (2008): why many theories of shock waves are necessary: Convergence error in formally path-consistent schemes. *J. Comput. Phys.* 227, 8107–8129.
- CASTRO-ORGAZ, O., HUTTER, K., GIRALDEZ, J., HAGER, W. (2015): nonhydrostatic granular flow over a 3-D terrain: New Boussinesq-type gravity waves? *J. Geophys. Res.* 120, 1, 1–28.
- CHEN, C. (1988): Generalized viscoplastic modeling of debris flow. *J Hydraul. Res.* 114, 237–258.
- CHERTOCH, A., KURGANOV, A., WU, T. (2015): Well-balanced positivity preserving central-upwind scheme for the shallow water system with friction terms. *Int J. Numer. Meth. Fl.* 78, 355–383.

- CHIOU, M. C., WANG, Y., HUTTER, K. (2005): Influence of obstacles on rapid granular flows. *Acta Mech.* 175, 105–122.
- CHUGUNOV, V., GRAY, J. M., HUTTER, K. (2003): Group theoretic methods and similarity solutions of the Savage-Hutter equations. *Dynamic response of granular and porous materials under large and catastrophic deformations*, 251–261.
- DENLINGER, R., DANIEL, R. (2008): Computing nonhydrostatic shallow-water flow over steep terrain. *J. Hydraul. Eng.* 134, 11, 1590–1602.
- DENLINGER, R., IVERSON, R. (2001): Flow of variably fluidized granular mass across three-dimensional terrain 2. Numerical predictions and experimental tests. *J. Geophys. Res.* 106, B1, 553–566.
- DREW, D. (1983): Mathematical modeling of two-phase flow. *Ann. Rev. Fluid Mech.* 15, 261–291.
- EGASHIRA, E., ITOH, T., TAKEUCHI, H. (2001): Transition mechanism of debris flows over rigid bed to over erodible bed. *Phys. Chem. Earth B* 26, 2, 169–174.
- EINFELDT, B., MUNZ, C., ROE, P., SJOGREEN, B. (1991): On Godunov-type methods for near low densities. *J. Comput. Phys.* 92, 273–295.
- ENWALD, H., PEIRANO, E., ALMSTEDT, A. (1996): Eulerian two-phase flow theory applied to fluidization. *Int. J. Multiph. Flow* 22, 21–66.
- FACCANONI, G., MANGENEY, A. (2012): Exact solutions for granular flows. *Int. J. Num. Anal. Met.* 37, 1408–1433.
- FRANCO, M. C. (2012): *Continuum mechanics: constitutive modeling of structural and biological*. Cambridge university press.
- GEORGE, D. (2008): Augmented Riemann solvers for the shallow water equations over variable topography with steady states and inundation. *J. Comput. Phys.* 227, 3089–3113.
- GEORGE, D., IVERSON (2011): A two-phase debris flow model that includes coupled evolution of volume fractions, granular dilatancy, and pore-fluid pressure. In Genevois, R., Hamilton, D., and Prestininzi, A., editors, *The 5th intl. conf. on debris-flow hazards, Padova, Italy*. *Ital. J. Eng. Geol. Environ*, 415–424.
- GEORGE, D., IVERSON, R. (2014): A depth-averaged debris-flow model that includes the effects of evolving dilatancy. II. numerical predictions and experimental tests. *Phil. Trans. R. Soc. A* 470, 20130820.
- GODUNOV, S. (1959): A finite difference scheme for numerical computation of the discontinuous solutions of equations of fluid dynamics. *Math. Sb.* 47, 271–306.
- GRAY, J., EDWARDS, A. (2014): A depth-averaged  $\mu(I)$ -rheology for shallow granular free-surface flows. *J. Fluid Mech.* 755, 503–534.
- GRAY, J., WIELAND, M., HUTTER, K. (1999): Gravity-driven free surface flow of granular avalanches over complex basal topography. *Proc. R. Soc. A* 445, 1841–1874.



- HARTEN, A. (1983): High-resolution schemes for hyperbolic conservation laws. *J. Comput. Phys.* 49, 357–393.
- HARTEN, A., LAX, P., VAN LEER, B. (1983): Upstream differencing and Godunov-type schemes for hyperbolic conservation laws. *SIAM Rev.* 25, 35–61.
- HARTEN, A., OSHER, S. (1982): Uniformly high order accurate non-oscillatory scheme. I. *SIAM J. Numer. Anal.* 24, 229–309.
- HARTEN, A., OSHER, S., ENGQUIST, B., CHAKRAVARTHY, S. (1986): Some results on uniformly high-order accurate essentially non-oscillatory schemes. *J. Appl. Num. Math.* 2, 347–377.
- HUNGR, O. (2000): Analysis of debris flow surges using the theory of uniformly progressive flow. *Earth Surf. Process. Landforms* 25, 483–495.
- HUTTER, K., GREVE, R. (1993): Two-dimensional similarity solutions for finite-mass granular avalanches with Coulomb- and viscous-type frictional resistance. *J. Glaciol* 39, 357–372.
- HUTTER, K., JÖHNK, K. (2004): *Continuum methods of physical modeling - Continuum Mechanics, Dimensional Analysis, Turbulence*. Springer, Berlin, Germany.
- HUTTER, K., SIEGEL, M., SAVAGE, S. B., NOHGUCHI, Y. (1993): Two-dimensional spreading of a granular avalanche down an incline plane Part I. Theory. *Acta Mech.* 100, 37–68.
- ISHII, M. (1975): *Thermo-fluid Dynamic Theory of Two-phase Flow*. Eyrolles.
- IVERSON, R. (1997): The physics of debris flows. *Rev. Geophys.* 35, 3, 245–296.
- IVERSON, R. (2005): Regulation of landslide motion by dilatancy and pore pressure feedback. *J. Geophys. Res.* 110, F02015.
- IVERSON, R., DENLINGER, R. (2001): Flow of variably fluidized granular mass across three-dimensional terrain 1. Coulomb mixture theory. *J. Geophys. Res.* 106, 537–552.
- IVERSON, R., GEORGE, D. (2014): A depth-averaged debris-flow model that includes the effects of evolving dilatancy. I. physical basis. *Phil. Trans. R. Soc. A* 470, 20130819.
- IVERSON, R., LOGAN, M., LAHUSEN, R., BERTI, M. (2010): The perfect debris flow? aggregated results from 28 large-scale experiments. *J. Geophys. Res.* 115, F03005.
- JIANG, G., SHU, C. (1996): Efficient implementation of weighted ENO schemes. *J. Comput. Phys.* 126, 202–228.
- JIANG, G., TADMOR, E. (1998): Non-oscillatory central schemes for multidimensional hyperbolic conservation laws. *SIAM. J. Sci. Comput* 19, 1892–1917.
- JOP, P., FORTERRE, Y., POULIQUEN, P. (2006): A constitutive law for dense granular flows. *Nature* 441, 727–730.

- KOWALSKI, J., MCELWAIN, J. (2013): Shallow two-component gravity-driven flows with vertical variation. *J. Fluid Mech.* 714, 434–462.
- KURGANOV, A., MILLER, J. (2014): Central-upwind scheme for SavageHutter type model of submarine landslides and generated tsunami waves. *Comput. Methods Appl. Math* 14, 2, 177–201.
- KURGANOV, A., NOELLE, S., PETROVA, G. (2001): Semidiscrete central-upwind schemes for hyperbolic conservation laws and Hamilton-Jacobi equations. *SIAM J. Sci. Comput.* 23, 3, 707–740.
- KURGANOV, A., PETROVA, G. (2007): A central-upwind scheme for nonlinear water waves generated by submarine landslides. In: *Hyperbolic Problems: Theory, Numerics, Applications*, S. Benzoni-Gavage, D. Serre, Herausgeber, Proceedings of the 11th international conference, Springer, 635–642.
- KURGANOV, A., TADMOR, E. (2000): New high-resolution central schemes for nonlinear conservation laws and convectiondiffusion equations. *J. Comput. Phys.* 160, 241–282.
- LAX, P. (1954): Weak solutions of nonlinear hyperbolic equations and their numerical computation. *Comm. Pure Appl. Math.* 15977, 159.
- VAN LEER, B. (2006): Upwind and high-resolution methods for compressible flow: from donor cell to residual-distribution schemes. *Commun. Comput. Phys.* 1, 2, 192–206.
- LEVEQUE, R. (1997): Wave propagation algorithms for multi-dimensional hyperbolic systems. *J. Comput. Phys.* 131, 327–353.
- LIU, I.-S. (2014): A solid-fluid mixture theory of porous media. *Int. J. Eng. Sci.* 84, 133–146.
- LIU, X., OSHER, S., CHAN, T. (1994): Weighted essentially non-oscillatory schemes. *J. Comput. Phys.* 115, 200–212.
- MENG, X., WANG, Y. (2015a): *Investigations of gravity-driven two-phase debris flows*, Springer Series in Geomechanics and Geoengineering. 119–130.
- MENG, X., WANG, Y. (2015b): Modelling and numerical simulation of two-phase debris flows. *Acta Geotech.* , 1–19.
- MENG, X., WANG, Y. (2016): Modelling dynamic flow of grain-fluid mixtures by coupling mixture theory and dilatancy law. *submitted* .
- MENG, X., WANG, Y., WANG, C., FISCHER, J.-T. (2016): Modeling of unsaturated granular flow by a two-layer approach. *submitted* .
- NEEDHAM, D., MERKIN, J. (1984): On roll waves down an open iincline channel. *Proc. R 394*, 259–278.
- NESSYAHU, H., TADMOR, E. (1990): Non-oscillatory central differencing for hyperbolic conservation laws. *J. Comput. Phys.* 87, 408–463.

- PAILHA, M., NICOLAS, M., POULIQUEN, O. (2008): Initiation of underwater granular avalanches: influence of the initial volume fraction. *Phys. Fluids* 20, 111701.
- PAILHA, M., POULIQUEN, O. (2009): A two-phase flow description of the initiation of underwater granular avalanches. *J. Fluid Mech.* , 115–135.
- PELANTI, M., BOUCHUT, F., MANGENEY, A. (2008): A Roe-type scheme for two-phase shallow granular flows over variable topography. *ESAIM Math Model Numer. Anal.* 42, 05, 851–885.
- PITMAN, E., LE, L. (2005): A two-fluid model for avalanche and debris flows. *Phil. Trans. R. Soc. A* 363, 1573–1601.
- PITMAN, E., PATRA, A., KUMAR, D., NISHIMURA, K., KOMORI, J. (2013): Two phase simulations of glacier lake outburst flows. *J Comput. Sci.* 4, 71–79.
- POIVERSON, O., FORTERRE, Y. (2002): Friction law for dense granular flows: application to the motion of a mass down a rough inclined plane. *J. Fluid Mech.* 453, 133–151.
- PROCHNOW, M., CHEVOIR, F., ALBERTELLI, M. (2000): Dense granular flows down a rough inclined plane. In: *XIIIth Intl Congr. on Rheology, Cambridge, UK., Cambridge,, UK.*
- PUDASAINI, S. (2012): A general two-phase debris flow model. *J. Geophys. Res.* 117, F3, 1–28.
- PUDASAINI, S. (2014): Dynamics of submarine debris flow and tsunami. *Acta Mech.* 225, 2423–2434.
- PUDASAINI, S., MILLER, S. (2012): Buoyancy induced mobility in two-phase debris flow. *Am. Inst. Phys. Proc.* , 149–152.
- PUDASAINI, S., WANG, Y., HUTTER, K. (2005): Modelling debris flows down general channels. *Nat. Hazard Earth Sys.* 5, 799–819.
- PUDASAINI, S. P., HUTTER, K. (2007): *Avalanche dynamics: dynamics of rapid flows of dense granular avalanches.* Springer-VerlSp, Berlin.
- QUE, Y.-T., XU, K. (2006): The numerical study of roll-waves in inclined open channels and solitary wave run-up. *Int. J. Numer. Mech. Fluids* 50, 1003–1027.
- ROE, P. L. (1981): Approximate Riemann solvers, parameter vectors and difference schemes. *J. Comput. Phys.* 43, 357–372.
- RONDON, L., POULIQUEN, O., AUSSILLOUS, P. (2011): Granular collapse in a fluid: role of the initial volume fraction. *Phys. Fluids* 23, 073301.
- ROUX, S., RADJAI, F. (1998): Texture-dependent rigid plastic behavior. In: *Physics of dry granular media*, H. J. Herrmann, Hrsg., Kluwer, Cargèse, France, 305–311.
- SAVAGE, S. B., HUTTER, K. (1989): The motion of a finite mass of granular material down a rough incline. *J. Fluid. Mech.* 199, 177–215.

- SCHONFELD, B. (1996): *Roll waves in granular flows and debris flows*. Diplomarbeit, McGill University, Civil Engineering and Applied Mechanics.
- SEBASTIAN, N., XING, Y., SHU, C. (2007): High-order well-balanced finite volume WENO schemes for shallow water equation with moving water. *J. Comput. Phys.* 226, 1, 29–58.
- SHU, C., OSHER, S. (1988): Efficient implementation of essentially non-oscillatory shock-capturing schemes. *J. Comput. Phys.* 77, 439–471.
- TAI, Y., NOELLE, S., GRAY, J., HUTTER, K. (2001): Shocking-capturing and front-tracking methods for granular avalanches. *J. Comput. Phys.* 175, 269–301.
- TERZAGHI, K. (1925): *Erdbaumechanik auf Bodenphysikalischer Grundlage*. Franz Deuticke, Liepzig-Vienna.
- TRUESDELL, C. (1984): *Rational thermodynamics*. New York: Springer.
- VAN WACHEM, B., SCHOUTEN, J., VAN DEN BLEEK, C. (2001): Comparative analysis of CFD model of dense gas-solid systems. *AIChE Journal* 47, 1035–1051.
- WANG, Y. (2016): *Kontinuumsmechanische Modellierung von Mehrphasenströmungen und Mischungstheorie*. Techn. Ber., Fachgebiet Strömungsdynamik, Technische Universität Darmstadt.
- WANG, Y., HUTTER, K., PUDASAINI, S. P. (2004): The Savage-Hutter theory: A system of partial differential equations for avalanche flows of snow, debris, and mud. *J. App. Math. Mech.* 84, 8, 507–527.
- XING, Y., SHU, C. (2005): High order finite difference WENO schemes with the exact conservation property for the shallow water equations. *J. Comput. Phys.* 208, 206–227.

# A Comparison between mixture theory and averaging theories

It is meaningful to compare the present governing equations based on mixture theory with those based on averaging approaches, e.g. Enwald, Peirano & Almstedt (1996) and Anderson & Jackson (1967). Both mixture theory and averaging approaches start with equations (2.27) and (2.28) to formulate conservation laws. The differences between mixture theory and averaging approaches are the choice of constitutive laws for the fluid and the granular phases and the choice of interaction forces between the two phases. The averaging theory of Enwald et al. (1996) is based on the theory of Ishii (1975) who derived an averaging theory for a fluid-droplets system. Enwald et al. (1996) postulated  $\boldsymbol{\sigma}_f = -\phi_f p_f \mathbf{I} + \phi_f \tilde{\boldsymbol{\tau}}_f$  and  $\mathbf{f}_s = p_f \nabla \phi_s + \mathbf{f}_d$ . Substitution into equations (2.27) and (2.28) yields

$$\frac{\partial(\rho_s \mathbf{v}_s)}{\partial t} + \nabla \cdot (\rho_s \mathbf{v}_s \otimes \mathbf{v}_s) = -\nabla \cdot \boldsymbol{\sigma}_s - \phi_s \nabla p_f + \rho_s \mathbf{g} + \mathbf{f}_d, \quad (\text{A.1})$$

$$\frac{\partial(\rho_f \mathbf{v}_f)}{\partial t} + \nabla \cdot (\rho_f \mathbf{v}_f \otimes \mathbf{v}_f) = -\phi_f \nabla p_f + \nabla \cdot (\phi_f \tilde{\boldsymbol{\tau}}_f) + \rho_f \mathbf{g} - \mathbf{f}_d, \quad (\text{A.2})$$

where  $\boldsymbol{\sigma}_s$  can be interpreted as  $\boldsymbol{\sigma}_e$ , since both of them represent the particle-particle interactions. Equations (A.1) and (A.2) have the same form as the present conservation equations (2.46) and (2.47). Enwald et al. (1996) formulated  $\tilde{\boldsymbol{\tau}}_f = \mu_f [\nabla \mathbf{v}_f + (\nabla \mathbf{v}_f)^T - 2(\nabla \cdot \mathbf{v}_f) \mathbf{I}/3]$  that slightly differs from the present  $\tilde{\boldsymbol{\tau}}_f = \mu_f [\nabla \mathbf{v}_f + (\nabla \mathbf{v}_f)^T]$ . The difference is the form of  $\tilde{\boldsymbol{\tau}}_{f(ij)}$ ,  $i \in (x, y, z)$ . When geophysical flow is considered like the case in the present thesis, the fluid shear stress  $\tilde{\boldsymbol{\tau}}_f$  actually has a negligible effect compared to the inertial forces. Consequently, there should be the same numerical predictions for typical natural geophysical flows between the present theory and the averaging theory of Enwald et al. (1996).

The local averaging theory of Anderson & Jackson (1967) stipulated the following relations

$$\boldsymbol{\sigma}_f = -p_f \mathbf{I} + \tilde{\boldsymbol{\tau}}_f, \quad \mathbf{f}_s = \phi_s \nabla \cdot \boldsymbol{\sigma}_f + \mathbf{f}_d. \quad (\text{A.3})$$

Substitution of relation (A.3) into equations (2.27) and (2.28) can formally derive the momentum conservation equations,

$$\frac{\partial(\rho_s \mathbf{v}_s)}{\partial t} + \nabla \cdot (\rho_s \mathbf{v}_s \otimes \mathbf{v}_s) = -\nabla \cdot \boldsymbol{\sigma}_s - \phi_s \nabla p_f + \phi_s \nabla \cdot \tilde{\boldsymbol{\tau}}_f + \rho_s \mathbf{g} + \mathbf{f}_d, \quad (\text{A.4})$$

$$\frac{\partial(\rho_f \mathbf{v}_f)}{\partial t} + \nabla \cdot (\rho_f \mathbf{v}_f \otimes \mathbf{v}_f) = -\phi_f \nabla p_f + \phi_f \nabla \cdot \tilde{\boldsymbol{\tau}}_f + \rho_f \mathbf{g} - \mathbf{f}_d. \quad (\text{A.5})$$

Equations (A.4) and (A.5) primarily distinguish from the present conservation equations (2.46) and (2.47) with the inclusion of fluid shear stress. Equation (A.4) seemingly indicates that  $\tilde{\tau}_f$  has an influence on granular flow behavior, but the fluid internal and bed shear stresses are actually much smaller than the bed Coulomb friction obtained by simplifying the solid stress (see Iverson & Denlinger (2001)). The difference between equations (A.5) and (2.46) is trivial for nature large-scale flows, since the fluid diffusion terms are actually small relatively to the inertial forces. The study of van Wachem, Schouten & van den Bleek (2001) for fluidized beds also shows that the averaging theories of Anderson & Jackson (1967) and Enwald et al. (1996) predict the same macroscopic flow behavior, though there are different prediction on a microscopic scale.

# Lebenslauf

## Xiannan Meng

### Personal Data:

Date of birth: 12. July 1986  
Place of birth: Yi An, Heilongjiang, China  
Nationalities: Chinese  
Family state: Single

### Educations:

09/93 - 07/97 Elementary school in Yi An  
09/98 - 07/01 Middle school in Yi An  
09/01 - 07/04 Daqing high school in Daqing city  
09/04 - 07/05 the first high school of Daqing city

### Studies:

09/05 - 07/09 Harbin Engineering University  
Subject: Naval architecture and ocean engineering  
Degree: Bachelor  
09/09 - 03/12 Shanghai Jiaotong University  
Subject: Naval architecture and ocean engineering  
Degree: Master

### Professional activities:

09/12 - 12/16 PhD candidate at the chair of fluid Dynamics (FDY),  
Technischen Universität Darmstadt

### Peer-Reviewed Journal Papers:

1. Xiannan Meng and Yongqi Wang, 2016. Modelling dynamic flow of grain-fluid mixtures by coupling mixture theory and dilatancy law, submitted.
2. Xiannan Meng and Wang, Y. and Wang, C. and Fischer, J-T. 2017. Modeling of unsaturated granular flow by a two-layer approach. DOI 10.1007/s11440-016-0509-x
3. Xiannan Meng and Yongqi Wang, 2015. Modelling and numerical simulation of two-phase debris flows. Acta Geotechnica: 1-19.

4. Xiannan Meng and Zaojian Zou, 2013. Radiation and diffraction of water waves by an infinite horizontal structure with a sidewall using SBFEM. *Ocean Engineering* (60): 193-199.
5. Xiannan Meng and Zaojian Zou, 2012. Wave interaction with a uniform porous cylinder of arbitrary shape. *Ocean Engineering* (44): 90-99.
6. Chun Wang, Yongqi Wang, Chong Peng, and Xiannan Meng, 2016. Two-fluid smoothed particle hydrodynamics simulation of submerged granular column collapse. *Mechanics Research Communication*, in press. <http://dx.doi.org/10.1016/j.mechrescom.2016.12.001>
7. Chun Wang, Yongqi Wang, Chong Peng, and Xianna Meng, 2016. Smoothed particle hydrodynamics simulation of water-soil mixture flows. *Journal of hydraulic Engineering*, 04016032.

**Book Chapter:**

1. Xiannan Meng and Yongqi Wang, 2014. Investigations of gravity-driven two-phase debris flows. In: W. Wu (ed.), *Recent Advances in Modeling Landslides and Debris Flows*, Springer Series in Geomechanics and Geo-engineering, DOI: 10.1007/978-3-319-11053-0\_11

**Conference contributions:**

1. Xiannan Meng and Yongqi Wang, 2014. Numerical simulation of two-phase debris flow model. In: IV International Conference on Particle-Based Methods. *Fundamentals and Applications (Particle 2015)*, 28. - 30. September 2015, Barcelona, Spain.
2. Xiannan Meng and Yongqi Wang, 2014. Modeling and numerical simulation of two-layer debris flows. Abstract in 11th World Congress on Computational Mechanics (WCCM XI). <http://www.wccm-eccm-ecfd2014.org/frontal/ProgSesion.asp?id=769>.
3. Xiannan Meng and Yongqi Wang, 2013. Numerical simulation of two-phase debris flow model. Abstract in III International Conference on Particle-Based Methods. *Fundamentals and Applications Particle*. <http://congress.cimne.com/particles2013/frontal/ProgSesion.asp?id=88>